Sergio González Horcas

CFD Methodology for Wind Turbines Fluid-Structure Interaction

Thesis submitted for the degree of doctor in applied sciences

Jury

Prof. Georges Kouroussis, Université de Mons (President)
Prof. Laurent Bricteux, Université de Mons (Secretary)
Prof. Grégory Coussement, Université de Mons (Supervisor)
Prof. Piotr Paweł Doerffer, Institute of Fluid Flow Machinery, Polish Academy of Sciences
Dr.Ir. Benoît Tartinville, NUMECA International
Prof. Jeroen van Beeck, von Karman Institute for Fluid Dynamics & Vrije Universiteit Brussel
Prof. Axelle Viré, Delft University of Technology

Thesis defended on 28/10/2016

This dissertation is dedicated to the memory of Hernando Rayo Calleja, professor at the University of Barcelona and at the Autonomous University of Barcelona, and my mentor during the high school years at the Institut Infanta Isabel d'Aragó. He inoculated me the virus of science, which I am pleasantly hosting till the present day.

"*Pero yo ya no soy yo, ni mi casa es ya mi casa.*"

Federico García Lorca, Romance Sonámbulo (1924)

Acknowledgements

To succeed in the endeavor of completing a thesis dissertation, it is in the interest of the PhD candidate to be surrounded by brilliant and encouraging people. This was definitely the case for this work. I will never be at the point of submitting this document without the help of a significantly large amount of people. In this section I will try to *render unto Caesar the things which are Caesar's*.

First of all I want to thank Dr.Ir. Benoît Tartinville and Dr.Ir. François Debrabandere for their enthusiasm and patience. From them I learned most of the things that are compiled in this thesis, and many others that I carry with me for the next adventures. I am also grateful to Prof. Grégory Coussement for accepting me as one of his students and for believing in this project till the end. Special thanks go to the members of my thesis supervision committee for their time and their constructive criticisms. I also acknowledge all my colleagues of NUMECA International, in particular the members of FINE™/Turbo, for sharing their experience, *IPAs* and *guezes* with me. *Gros merci* to Dr. Stéphane Monté for preparing the cover of this document and to MSc. Thanos Poulos for his meticulous remarks.

This thesis would not have been possible without the funding of the *European Commission* (EC) through the *initial training network* project MAREWINT. My deepest gratitude to this organization and to Prof. Charles Hirsch for selecting me for this scholarship. Being part of MAREWINT was a fantastic opportunity to discover several top-noch European research centers and to meet some of the most talented minds of my generation.

Last but not the least, I would like to thank everyone that supported me before and/or during this PhD thesis. In the first place my parents and Rita for their love and stoicism. Thanks to Prof. Daniel Crespo, Prof. Josep Ignasi Rojas and Prof. Adeline de Villardi de Montlaur from EETAC for their unconditional guidance. To David Duchez from *Lycée Gustave Eiffel* for showing me that there was life beyond the Pyrenees. To Prof. Xavier Carbonneau from ISAE for introducing me to the world of industrial CFD. To Dr.Ir. Makhlouf Hamide from Arcelormittal for his perseverance and his advices. To all the members of the GiD team from CIMNE and to my friends from Compass, for introducing me in the world of programming and numerical methods. And finally to all my brothers and sisters from S4WT, who shared with me the passion for wind energy.

Abstract

Horizontal axis wind turbines (HAWT) are one of the most efficient renewable energy sources. In order to extract the maximum power per machine and reduce the overall energy extraction cost, the main design solution is the increase of the rotor size. Modern designs account for rotor diameters up to 160 m, and even longer blades are expected for next the generation of machines. Due to the attached design constraints, this rotor up-scaling implies the consideration of more flexible blades. Under the action of the aerodynamic loading this leads to considerable blade deformations, that can influence the rotor performance. This coupled phenomenon linking *fluid* and *structure* physics is generally referred to as *Fluid Structure Interaction* (FSI), or in this case as aeroelasticity. The aeroelasticity of HAWT blades cannot be considered as a static phenomenon. Indeed the presence of the tower induces an important flow unsteadiness, that leads to a dynamic deformation of the blades. This phenomenon is known as the dynamic aeroelasticity.

Industry standards for the aeroelastic simulations of wind turbine rotors have historically relied on simplified engineering models. For classical machine designs, these approaches offer a very good computational efficiency and an acceptable accuracy in the flow prediction. The precision of engineering models is however limited when dealing with large HAWT rotors, due to the existence of highly skewed flows and heavy flow detachments. The main motivation of this PhD thesis was to develop a set of high flow fidelity numerical tools to be used for the study of large rotor HAWT aeroelasticity. A *Computational Fluid Dynamics* (CFD) methodology was implemented and tested within the FINE™/Turbo software, edited by NUMECA International.

Two new developments resulting from this PhD research work were introduced to extend the capabilities of the solver on wind turbine rotor analysis. On the one hand, a new *mesh deformation* method was developed in order to accommodate wind turbine blades deflection in aeroelastic simulations. An innovative combination of consolidated technologies allowed to achieve a good trade-off between deformed mesh quality, scalability and computational cost. The deformation of multi-million 3D meshes was reduced from several days to several minutes when compared to previously existing approaches. On the other hand, a *2-way coupling* FSI methodology to be applied in the study of HAWTs rotors dynamic aeroelasticity was implemented. In order to maximize the efficiency of the method, both the fluid and the structure were solved in the harmonic domain.

To explore the capabilities of the performed developments in a wind energy context, a comprehensive analysis of the DTU 10MW RWT was carried out. The permutation of structural flexibility and flow unsteadiness modeling lead to four different numerical analyses:

steady aerodynamics, *static aeroelasticity*, *unsteady aerodynamics* and *dynamic aeroelasticity*. The first two types of simulations were carried out on an isolated rotor framework, while for the rest the full machine was considered (also accounting for the tower geometry). *Steady aerodynamics* computations already revealed the complexity of the rotor flow. Important three-dimensional flow patterns were observed around blades and hub geometries. When performing *Static aeroelasticity* computations blade tip displacements up to 8.73% of the total blade radius were predicted. This significant blade deflection had a direct impact on the loads computed at the high span range of the blade. At the maximum studied wind speed, a total reduction of the mechanical power coefficient of 1.34% was found, while the thrust coefficient was decreased in 2.25%. The performed *unsteady aerodynamics* computations were able to capture the complex interaction between rotor and tower flows. The presence of the tower had a direct impact on rotor performance, with a decrease of around 5% of the time-averaged thrust and 8% of the time-averaged power. Due to the flow unsteadiness, relative fluctuation amplitudes of 1% for the thrust and 2% for the power were also observed. Finally, *dynamic aeroelasticity* computations revealed that the blade flexibility decreased the rotor loads fluctuations related to the *blade-tower alignment* event.

The developed methodology was shown to be able to answer to different design questions such as the installation of flow control devices and the definition of the blade prebending law. The reduced computational cost attached to the final platform also enables its direct introduction into the wind energy market.

Table of contents

List of figures

List of tables

Nomenclature

Chapter 2 & Appendix B Symbols

a	Induction factor
C_p	Power Coefficient
C_t	Thrust Coefficient
$\vec{e}$	Unitary vector
E	Total Energy
$\vec{f_e}$	External forces
$\vec{F_I}$	Vector of inviscid fluxes
$\vec{F_V}$	Vector of viscous fluxes
H	Total enthalpy
h	Enthalpy per unit mas
I	Imaginary number
P	Power
p	Pressure
$\vec{q}$	Total turbulent heat flux
Q	Vector of source terms
$\vec{q_c}$	Heat conduction flux
q_h	Heat source
$\vec{q_t}$	Turbulent heat flux
R	Rotor radius
$\vec{S}$	Surface vector
T	Thrust
t	Time
U	Vector of conservative flow variables
u	Rotor velocity
v	Velocity
V_0	Free stream fluid velocity
v_{axial}	Axial velocity
V_r	Relative velocity
$\vec{x}$	Position vector
χ	Inverse of Eddies length scale
μ	Dynamic viscosity
Ω	Volume
ω	Angular velocity
ρ	Density
ρ_0	Free stream fluid density
$\boldsymbol{\tau}$	Total shear stress tensor
$\boldsymbol{\tau}^R$	Reynolds stress tensor
$\boldsymbol{\tau}^v$	Viscous shear stress tensor
υ	Pitch angle
ς	Pseudo-time

Chapter 3 Symbols

E	Young modulus
$\boldsymbol{I}$	Unit tensor

J	Jacobian of the transformation
$\vec{u}$	Deformation vector
$\vec{x}$	Position vector
$\gamma_1, \gamma_2, \gamma_3$	Metric coefficients
λ	Lamé’s first parameter
μ	Lamé’s second parameter
ν	Poisson ratio
ω	Local diffusivity factor
ψ	Relaxation factor of linear solver
ρ	Density
$\boldsymbol{\sigma}$	Structural stress
$\boldsymbol{\varepsilon}$	Structural strain
ξ, η, ζ	Computational coordinates

Chapter 4 Symbols

$\mathbf{C}$	Damping matrix
C_D	Drag coefficient
$\mathbf{C_g}$	Generalized damping matrix
C_L	Lift coefficient
Cp	Pressure coefficient
D	Diameter
D_y	Cylinder displacement
f_F	Forced motion frequency
f_k	Structure frequency
f_{shed}	Shedding frequency
f_{shnat}	Natural shedding frequency
$\boldsymbol{I}$	Unit tensor
$\mathbf{K}$	Stiffness matrix
k^*_{eff}	Effective stiffness
L	Span
$\mathbf{M}$	Mass matrix
m	Cylinder mass
N_h	Number of harmonics
N_n	Millions of mesh nodes
N_p	Number of processors
p	Pressure
q	Generalized displacement
Re	Reynolds number
St	Strouhal number
T_h	Hours of computational time
$\vec{u}$	Deformation vector
U_∞	Freestream velocity
β	Rayleigh damping parameters
γ	Relaxation factor
α	Phase angle
ν	Kinematic viscosity
ω	Angular velocity
$\vec{\phi}_k$	Deformed shape
ρ	Density
ξ	Damping ratio

Chapter 5 Symbols

C_p	Power Coefficient

C_t	Thrust Coefficient
R	Rotor radius
r	Radial position

Chapter 6 Symbols

f_{shed}	Shedding frequency
N_h	Total number of harmonics
Q_c	Q-Criterion
R	Rotor radius
r	Radial position
$\boldsymbol{S}$	Rate of strain tensor
St	Strouhal number
T	Period of revolution
t	Current revolution time
U_∞	Freestream velocity
$\vec{v}$	Velocity
$\boldsymbol{\Omega}$	Rate of rotation tensor

Superscripts

$\bar{}$	Time-averaged value
$\wedge$	Density weighted averaged
$'$	Perturbation
“	Fluctuations around density weighted average
T	Transpose
$\tilde{}$	Harmonic complex amplitude

Subscripts

b	Domain Boundary
$call$	Call of mesh deformation process
def	Mesh deformation process
i	Inner node
Im	Imaginary part
NLH	Related to a Non-Linear Harmonic computation
pre	Preprocessing of mesh deformation process
Re	Real part
ref	Original mesh
sim	Fluid simulation
$Steady$	Related to a steady computation

Acronyms / Abbreviations

ALE	Arbitrary Lagrangian Eulerian
AR	Mesh Aspect Ratio
BEM	Blade Element Momentum
BPF	Blade Passing Frequency
CFD	Computational Fluid Dynamics
CPU	Central Processing Unit
CSM	Computational Structural Mechanics
DDES	Delayed Detached Eddy Simulation
DES	Detached Eddy Simulation
DLC	Design Load Case
DOF	Degree of freedom

DTI	Direct Time Integration
EC	European Comission
ELA	Elastic Analogy
ER	Mesh Expansion Ratio
FEM	Finite Element Method
FFT	Fast Fourier Transform
FSI	Fluid-Structure Interaction
GLS	Garlekin Least Squares
HAWT	Horizontal Axis Wind Turbine
IGA	Isogeometric Analysis
LES	Large Eddy Simulation
MBD	Multi-Body Dynamics
OR	Cell orthogonallity
NLH	Non-Linear Harmonic
OR	Cell orthogonallity
PIV	Particle Image Velocimetry
RANS	Reynolds-Averaged Navier Stokes
RBF	Radial Basis Function
RPM	Revolutions per minute
RMS	Root mean square
ROM	Reduced-Order Model
TFI	Transfinite Interpolation
URANS	Unsteady Reynolds-Averaged Navier Stokes
VIV	Vortex Induced Vibrations
VMS	Variational Multiscale

Chapter 1

Motivation and global thesis goal

1.1 Motivation

Horizontal axis wind turbines (HAWTs) are one of the most efficient renewable energy sources. In order to extract the maximum power per machine and reduce the overall energy extraction cost, the main design solution is the increase of the HAWT rotor size. Figure 1.1 shows the historical and predicted rotor diameter evolution from 1985. As it can be observed, modern big rotor diameters are bigger than the biggest commercial airplane ever manufactured.

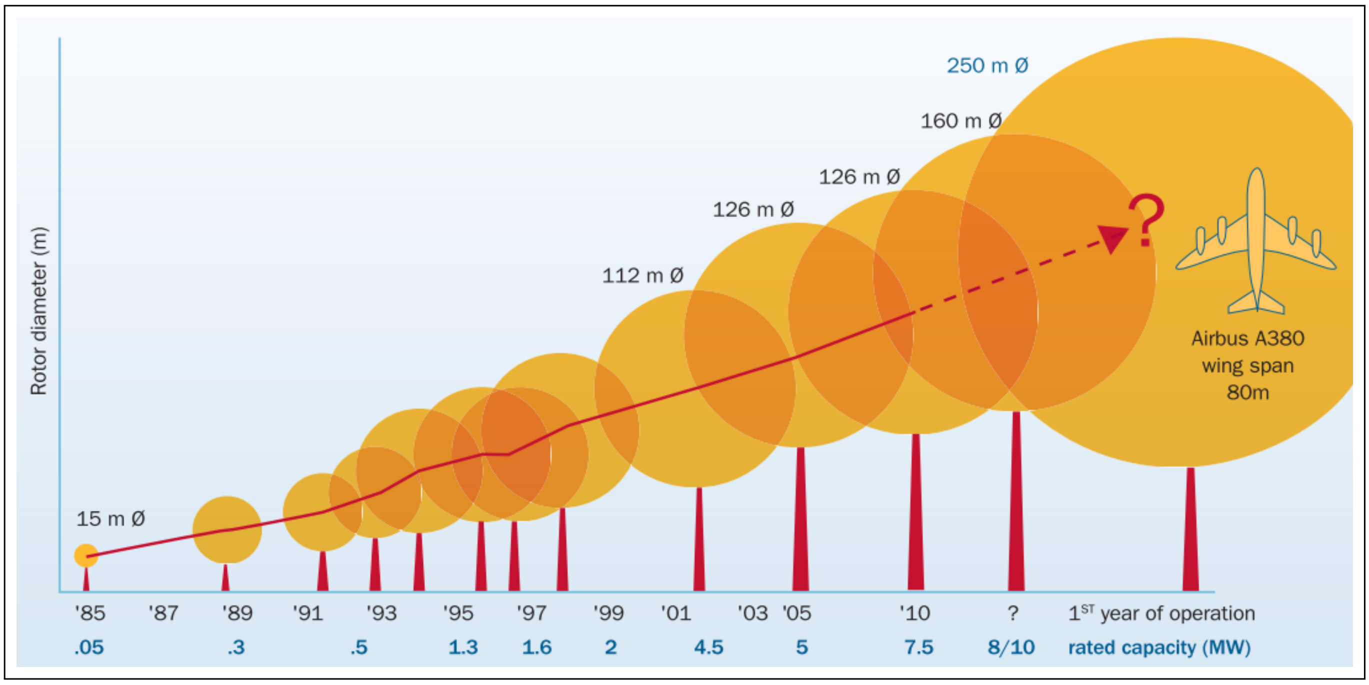

Figure 1.1: Wind turbines rotor evolution [source: UpWind Consortium (2011)]

A HAWT implies a very complex aerodynamic scenario for designers, since it is a highly three-dimensional and rotatory flow problem. In addition and due to the nature of the wind, the inflow conditions are constantly varying. This makes very difficult their estimation, requiring the use of physical or statistical models built from data coming from the wind turbine potential locations [Azad et al. (2014)]. The resulting dynamic loading conditions are very constraining from a structural point of view. Blade manufacturers should certify that their design will withstand the expected dynamic loads, both in *extreme* and *fatigue* conditions during the whole machine lifetime, which typically ranges from 20 to 30 years [Hau (2006)]. Modern blades are mainly manufactured with composite fiber materials, due to their benefits in terms of mechanical properties and weight [Hau (2006)]. Indeed a special attention is put in the last design parameter, which has a direct impact both in the manufacturing and installation costs and in the final power production. This is specially true for big rotor wind turbines, since the weight of the blades scales approximately with the cubic of the radius. To illustrate this relation, Figure 1.2a shows the results of the WindPACT project obtained by Griffin and Zuteck (2001). Available data for commercial HAWTs up to a rotor radius of 40 m is included (triangular markers), together with a numerical prediction of higher radius values (straight and dashed lines). An approximately cubic evolution is observed, and the predicted blade designs accounting for a 60 m length were related to a weight of 30 tones. To minimize the blade weight and increase its performance regarding the flapwise bending, structural engineers will tend to equip HAWTs with thick airfoils, specially at low span range [Schubel and Crossley (2012)]. The impact of the airfoils thickness on the total blade mass predicted by Griffin and Zuteck (2001) is depicted in Figure 1.2b. A reduction of the blade weight of 10% was expected when increasing the airfoils thickness of approximately 30%. This preference for thicker airfoils is inevitably in conflict with the flow performance of the blade, since they show less aerodynamic efficiency. This classical *structure* versus *aerodynamics* trade-off, also present in other industries such as automotive or aeronautics, is complexified in the framework of modern HAWTs by two additional factors. First, a strongly coupled physics is expected due to the low-weight and the slenderness of the blades. Indeed, the aerodynamic loading resulting from the flow around the rotor blades is highly influenced by the elastic blades deformation, and *vice versa*. This interaction between flow and structure physics is often referred to as *Fluid Structure Interaction* (FSI). For modern designs, due to this aerodynamic loading, blade tip deflections up to 10% of the blade length are expected [Resor (2013); Wirz and Johnson (2011)]. Hence, aerodynamic loads can not be computed by assuming a rigid structure. In addition, the structural response is highly influenced by the blade aerodynamic loading to consider. Secondly, modern HAWT rotors are designed to work at higher *Reynolds* numbers (in the range $[10^7, 1.5 \times 10^7]$), where little experimental data is available. Current aerodynamic loads prediction techniques are based on scaling of previous experiences at lower *Reynolds* numbers and the results of *Computational Fluid Dynamics* (CFD) models.

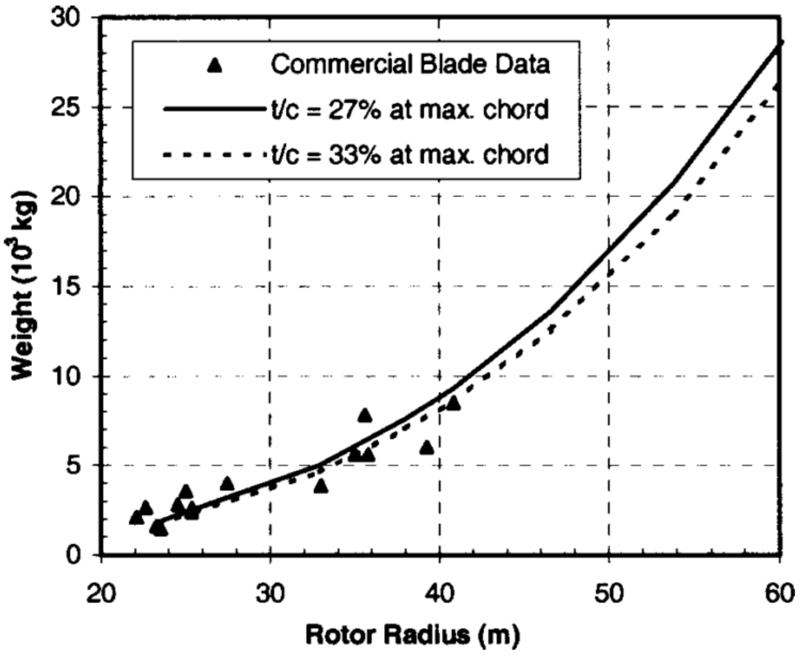

(a) Observed (triangles) and estimated (straight and dashed lines) blade weight in tones. Results are expressed as a function of rotor radius in meters

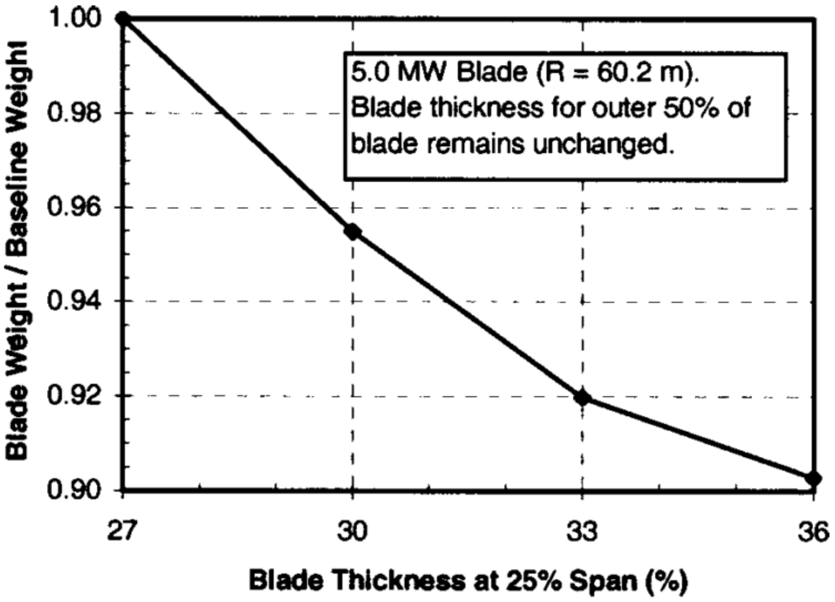

(b) Estimated blade weight reduction factor as a function of the blade thickness at 25% of the span. Results refer to a 5MW blade with a radius of 60.2 m

Figure 1.2: Results of the WindPACT project [source:Griffin and Zuteck (2001)]

1.2 Global thesis goal

In order to approach this highly coupled problem, industry standards for multi-physics wind turbine rotors aeroelastic simulations have historically relied on simplified engineering models. For classical machine designs, these approaches offer a very good computational efficiency and an acceptable accuracy in the flow prediction. The precision of engineering models is however limited when dealing with big HAWT rotors, due to the existence of highly skewed flows and heavy flow detachments. The main motivation of this PhD thesis is to develop a set of high flow fidelity numerical tools to be used during the HAWT rotor design stage. This methodology should be able to take into account the blade deformation due to the FSI and the unsteadiness of the flow due to the rotor-tower flow interactions. Special attention is put in the industrialization of the method, both from a robustness and efficiency point of view. In order to contextualize the subjects covered by this work, a brief literature survey is included in Section 2.1. A description of the flow solver used in this study can be found in Section 2.2. The main objectives of this PhD thesis are then discussed in Section 2.3.1. Finally, Section 2.3.2 contains an outline of this document.

1.3 PhD funding and dissemination

The content of this PhD covers the research performed at NUMECA International under the academic supervision of the University of Mons, during the period from April 2013 to April 2016. This work was funded by the *European Commission* (EC) through a *Marie Skłodowska-Curie* scholarship and in the framework of the project FP7-PEOPLE-2012-ITN 309395 MAREWINT (*new MAterials and REliability in offshore WINd Turbines technology*), see: http://marewint.eu/. The main objective of the MAREWINT project is to promote transversal research in the fields on structural mechanics, fluid mechanics, risk analysis and reliability analysis in order to increase the competitiveness of next generation wind turbines. As dissemination is another important milestone of the MAREWINT project, the results of this research were partially published in several conferences and technical papers. In the publications *Mesh deformation tool for Offshore Wind Turbines fluid-structure interaction* [Horcas et al. (2014)] and *Hybrid Mesh Deformation Tool for Offshore Wind Turbines Aeroelasticity Prediction* [Horcas et al. (2015b)], the theoretical basis of a new mesh deformation algorithm were presented and applied to the deflection of a large HAWT blade. In *A new, high fidelity offshore wind turbines aeroelasticity prediction method with significant CPU time reduction* [Horcas et al. (2015a)] and *CFD Study of DTU 10MW RWT Aeroelasticity and Rotor-Tower Interactions* [Horcas et al. (2016a)], a complete characterization of the static aeroelasticity of a HAWT rotor was shown, together with the first unsteady results of a full machine configuration. A comprehensive analysis of these unsteady computations was finally published in *Rotor-tower interactions of DTU 10MW reference wind turbine with a non-linear harmonic method* [Horcas et al. (2016b)], including a comparison between both time marching and harmonic methodologies.

Chapter 2

Literature review

2.1 Literature review

Following literature review covers most part of the subjects related to this research. Firstly, the basic principle of wind power extraction of a horizontal axis wind turbine is presented in Section 2.1.1. An overview of the computational tools used for HAWT aerodynamic loads prediction is then provided in Section 2.1.2, including simplified *engineering models* and the more sophisticated Computational Fluid Dynamics (CFD) approach. The concept of aeroelasticity and *Fluid Structure Interaction* (FSI) is introduced by means of its influence on HAWT applications in Section 2.1.3. The different structural models used for HAWT simulations are described in Section 2.1.4. Final sections are strictly related to CFD applications, which is the focus of the present research. An exhaustive description of mesh deformation algorithms in given in Section 2.1.5. In Section 2.1.6, previous HAWT CFD studies are compiled, focusing in two particular problems: *aeroelasticity* and *rotor-tower interactions*.

2.1.1 Basic principle of a Horizontal Axis Wind Turbine

The main objective of a turbine is the extraction of kinetic energy from the wind passing through the rotor, and its *a posteriori* transformation into electricity [Burton et al. (2001)]. Its basic principle, as for most part of rotating machines, can be explained by means of the airfoil theory [Hau (2006)], as it is illustrated in Figure 2.1a. At every radial position of the blade r, the relative incoming flow velocity V_r can be understood as a combination of an axial velocity v_{axial} and a tangential driven velocity component ωr (where ω stands for the angular velocity). This leads to a relative angle of attack α, which has to be considered in combination with the blade pitch angle υ. This incidence will drive the resultant aerodynamic force generated by the airfoil, that can be decomposed in the classical lift and drag contributions (being normal and parallel to V_r, respectively). However, from a rotor point of view it is interesting to express the resulting force in terms of the direction of rotation, leading to the *tangential* and *axial* loads distinction. The role of the former force is to generate the machine *torque*, that will be translated into *power* by the HAWT generator (Figure 2.1b). The integration of the axial load on the blade leads to the so-called rotor *thrust*. The *thrust* can be understood as a residual load, since it will not contribute to the power generation but will be translated as moments on the tower base.

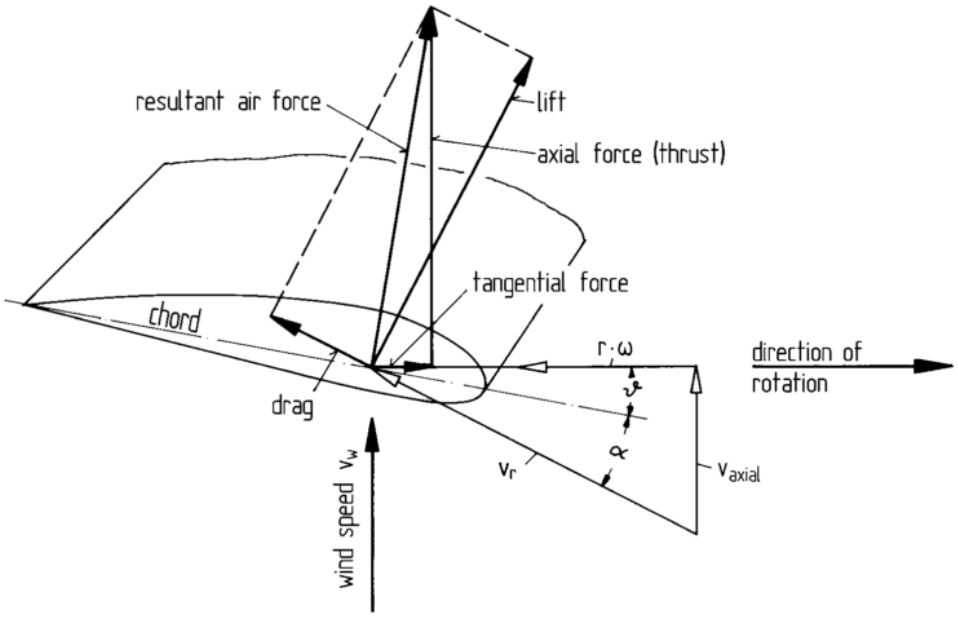

(a) Airfoil detail

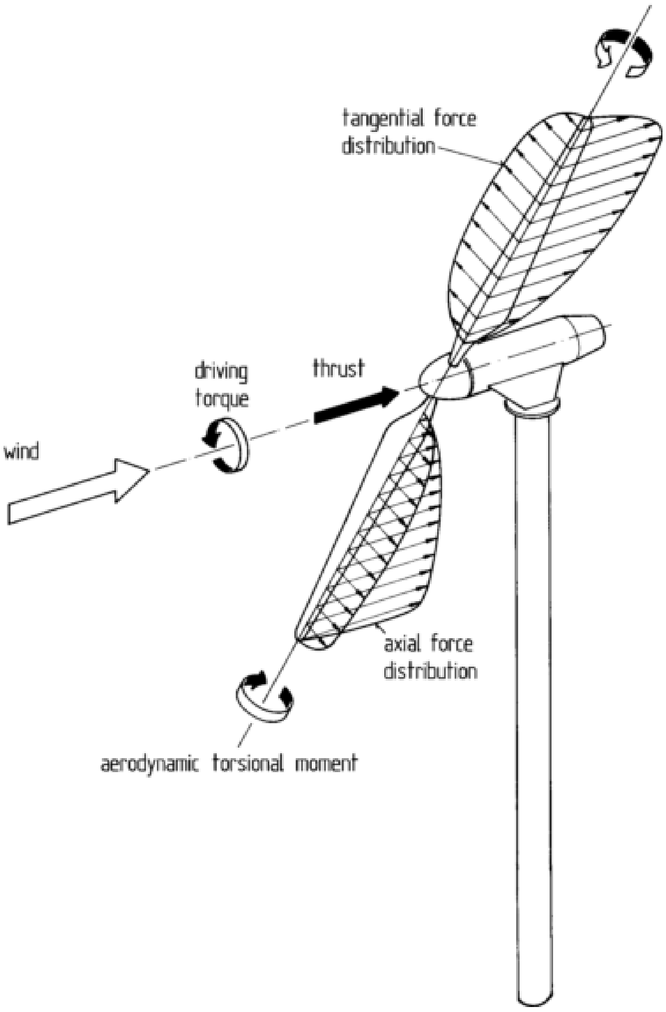

(b) Global overview

Figure 2.1: Basic principle of a horizontal axis wind turbine [source: Hau (2006)]

The so-called *actuator disc model*, originally introduced by Froude (1889) as an extension of the works of Rankine (1865), allows to characterize the fundamental flow phenomena to be expected in a HAWT operation. Let consider a one-dimensional model of an ideal rotor (assuming infinite blades, no hub and no axial thickness), as performed in Hansen (2008). The rotor is modeled by means of a permeable actuator disc, which slows the upstream velocity V_0 to a value of u at the rotor and u_1 at the wake (see Figure 2.2). Assuming no compressibility effects, due to the slow down induced by the extraction of kinetic energy by the rotor the application of the mass conservation implies a divergence of the streamlines. The disc load is obtained by a discontinuous pressure drop over the rotor. The Bernoulli equation can be applied downstream and upstream of the rotor position x_{rotor}, in order to relate pressure and velocity evolutions.

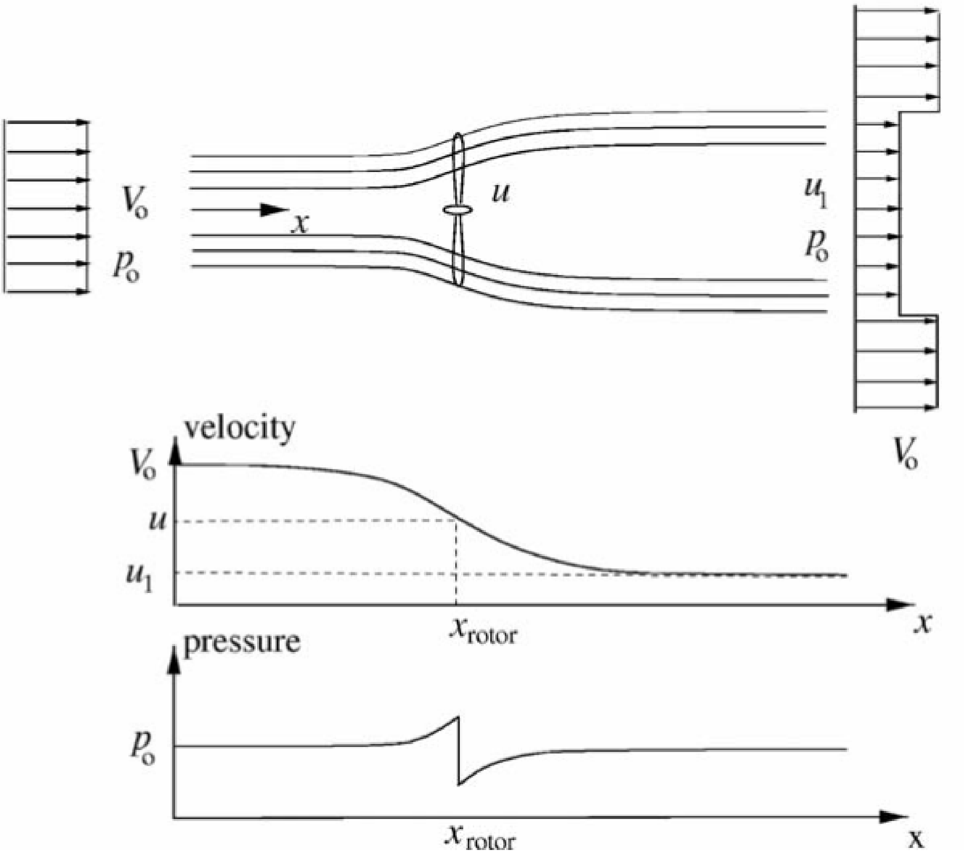

Figure 2.2: Schema of an ideal rotor flow (assuming infinite blades and no hub). Source: Hansen (2008)

The axial induction factor a is defined by the relation between the upstream and the rotor velocities:

$$u = (1-a)V_0 \tag{2.1}$$

In the context of this ideal rotor, expressions for the rotor thrust T and rotor power P can be theoretically derived [see Hansen (2008)], and related to the axial induction factor:

$$T = C_t \frac{1}{2} \rho_0 V_0^2 \pi R^2 \;, \tag{2.2}$$

$$P = C_p \frac{1}{2} \rho_0 V_0^3 \pi R^2 \;, \tag{2.3}$$

with:

$$C_t = 4a\left(1-a\right) \;, \tag{2.4}$$

$$C_p = 4a\left(1-a\right)^2 \;, \tag{2.5}$$

where C_t refers to the rotor thrust coefficient, C_p to the rotor power coefficient and R to the rotor radius.

The maximum power coefficient C_p can be computed by differentiation of its expression:

$$\frac{dC_p}{da} = 4\left(1-a\right)\left(1-3a\right) \tag{2.6}$$

Which becomes null for the non trivial solution $a = \frac{1}{3}$, corresponding to $C_{p,max} = \frac{16}{27} \simeq 0.59$. This theoretical maximum power coefficient for ideal wind turbines is known in the literature as the *Betz limit* [Betz (1920)].

2.1.2 Wind turbine loads prediction

In order to estimate rotor loads, HAWT designers traditionally employ the so-called *engineering models* [Abedi et al. (2013)]. Among others, these approaches include the *Blade element momentum theory* (BEM), the vortex method, the panel method and the actuator models. These approaches are characterized by a reduced computational cost and they rely in the simplification of the rotor aerodynamics by means of different hypothesis. A complete review of these methods was provided in Hansen et al. (2006). Due to the efficiency improvement of the more sophisticated *Computational Fluid Dynamics* (CFD) methods, they start to be considered as an alternative for design purposes. CFD methods, which were initially employed in aeronautics back in the 80's, can account for complex fluid phenomena such as 3D effects, compressibility, turbulence and unsteadiness.

BEM method

The BEM method was first developed by Glauert (1935), combining the one-dimensional momentum theory and blade element concepts in order to locally estimate rotor loads. The distributed aerodynamics loads on the blade are computed at different *cross-sections*, each one related to an airfoil and assumed to be independent. Every airfoil is related to a lift, drag and moment coefficients evolution in function to the *Reynolds* number. Airfoil data is usually based either on wind tunnel experimental results or two-dimensional numerical modes. BEM base formulation has been improved along with wind turbines evolution, thanks the introduction of additional sub-models [Heege et al. (2013); Jonkman and Buhl Jr. (2007)]. These modifications aim to estimate the effect local phenomena as hub and tip losses, dynamic inflow (inertial effects related to pitch control), skewed flow, dynamic stall, etc. The accuracy of BEM method is however limited when dealing with big HAWT rotors due to the existence of highly skewed 3D flows, heavy flow detachments and important blade deflections.

Vortex and panel methods

Both vortex and panel methods were developed in order to obtain a detailed description of the three-dimensional flow around the wind turbine. The common hypothesis for these approaches is the consideration of an inviscid flow, which limits their modeling capabilities. In the vortex method the rotor blades, trailing vorticity and shed vorticity in the wake are modeled by means of lifting lines or lifting surfaces [Thomson (1966)]. Induced velocities around the blades are computed based on the strength and position of the vortices by means of the Biot-Savart law. In the panel method the blade surface is discretized in a set of singularities, consisting in a combination of sources and dipoles. The Green's theorem is then used in order to obtain an integral representation of a potential flow [Hess (1975)].

Actuator models

The classical actuator disc methodology of Froude (1889) and Rankine (1865) was already described in Section 2.1.1. In this approach the rotor is modeled by means of a permeable disc. Many authors have extended this technique in order to work in combination with the solution of the *Navier-Stokes* equations or the *Euler equations* (described in Section 2.1.2), by including the average blade loading predicted by the disc rotor into the momentum equation [Calaf et al. (2010); Meyers and Meneveau (2010); Prospathopoulos et al. (2009)]. This *hybrid* method is often referred as the *generalized actuator disc model.* The geometry of the blades is not resolved, and the aerodynamic forces are computed based on previously determined airfoil characteristics (as for the BEM approach). This is the reason why the *generalized actuator disc model* is mainly used as a high flow fidelity tool for the study of wind turbine wakes and wind farms aerodynamics. Two additional approaches that follow the same *hybrid* philosophy of the generalized actuator disc can be found in the literature, aiming to extend its modeling capabilities: the *actuator line* and the *actuator surface* models. In the actuator line model the loading is not averaged over the complete disk but it is exerted on lines that represent the wind turbine blades, making it time dependent [Sørensen and Shen (2002)]. The actuator surface model has been mainly applied to vertical axis wind turbines and it can be understood as an extension of the actuator line approach. In this case the blades are represented by planar surfaces, requiring as an input the pressure and skin-friction distribution of every airfoil [Shen et al. (2007)]. In order to have a more detailed insight of the aforementioned actuator models, the reader is referred to the review article of Sanderse et al. (2011).

CFD methods

Fluids behavior is governed by the conservation laws of the mass, the momentum and the energy. The mathematical expression of these laws is referred as the *Navier-Stokes equations*, which constitutes a system of five fully-coupled time-dependent differential equations [Hirsch (2007)]. *Navier-Stokes equations*, which are the basis of almost all CFD approaches, can be expressed in a general, integral conservative form for a control volume Ω as:

$$\frac{\partial}{\partial t}\int_{\Omega} U d\Omega + \oint_{S}\left(\vec{F_I} - \vec{F_V}\right)\cdot d\vec{S} = \int_{\Omega} Q d\Omega \tag{2.7}$$

being U the vector of conservative variables of mass, momentum and energy:

$$U = \begin{pmatrix} \rho \\ \rho v_x \\ \rho v_y \\ \rho v_z \\ \rho E \end{pmatrix} \tag{2.8}$$

$\vec{F_I}$ the vector of inviscid fluxes:

$$\vec{F_I} = \begin{pmatrix} \rho\vec{v} \\ \rho\vec{v}v_x + p\vec{e}_x \\ \rho\vec{v}v_y + p\vec{e}_y \\ \rho\vec{v}v_z + p\vec{e}_z \\ \rho\vec{v}E + p\vec{v} \end{pmatrix} \tag{2.9}$$

$\vec{F}_V$ the vector of viscous fluxes, accounting for the contribution of the viscous shear stress tensor $\boldsymbol{\tau}^v$ and the heat conduction flux $\vec{q}_c$:

$$\vec{F}_V = \begin{pmatrix} 0 \\ \tau^v_{xx}\vec{e}_x + \tau^v_{xy}\vec{e}_y + \tau^v_{xz}\vec{e}_z \\ \tau^v_{xy}\vec{e}_x + \tau^v_{yy}\vec{e}_y + \tau^v_{yz}\vec{e}_z \\ \tau^v_{xz}\vec{e}_x + \tau^v_{yz}\vec{e}_y + \tau^v_{zz}\vec{e}_z \\ \boldsymbol{\tau}^v\vec{v} + \vec{q}_c \end{pmatrix} \tag{2.10}$$

and Q the vector of source terms, which can vary depending on the targeted application. In a general form, it includes the *external forces* $\vec{f}_e$ and the *heat source* q_h:

$$Q = \begin{pmatrix} 0 \\ \rho f_{e,x} \\ \rho f_{e,y} \\ \rho f_{e,z} \\ \rho \vec{f}_e \vec{v} + q_h \end{pmatrix} \tag{2.11}$$

To close the *Navier-Stokes* equations, the choice of a fluid constitutive law is required (in order to define an expression of the shear stress module). Under the hypothesis of a Newtonian fluid in local thermodynamic equilibrium, $\boldsymbol{\tau}^v$ can be expressed as:

$$\tau^v_{ij} = \mu \left[\left(\frac{\partial v_j}{\partial x_i} + \frac{\partial v_i}{\partial x_j} \right) - \frac{2}{3} \left(\vec{\nabla} \cdot \vec{v} \right) \delta_{ij} \right] \tag{2.12}$$

Where μ is the dynamic molecular viscosity.

Navier-Stokes equations are fully-coupled and highly non-linear. Different approximations can be made for their solution, depending on the targeted flow complexity and domain of application. Most popular approaches are described in sections below. For a complete and detailed description of each of them, the reader is referred to Hirsch (2007).

Inviscid flow *Navier-Stokes equations* can be simplified supposing zero viscosity and zero thermal conductivity, leading to the so called *Euler equations*. It is equivalent of assuming $\vec{F}_V = 0$ in Equation 2.7. Usually, this assumption is valid in regions located far from wall boundaries, where thin and attached boundary layers are found. If the hypothesis of irrotationality is also made, the flow model can be even more simplified and it can be solved by means of a *potential* solution.

Laminar flow *Navier-Stokes equations* describe both laminar and turbulent flows. For the former case (corresponding to low *Reynolds numbers*), Equation 2.7 can be solved without any additional considerations. The contribution of $\vec{F}_V$ is then carried out exclusively by the laminar viscosity.

Turbulent flow At high *Reynolds numbers*, the solution of the *Navier-Stokes equations* requires the consideration of turbulence [Sagaut et al. (2006)]. This phenomenon can be understood as an instability of the laminar flow, due to the important contribution of the inertial fluid forces. Turbulence starts by the generation of large-scale turbulent eddies, caused by mean velocity gradients. These structures, in their turn, generate smaller eddies. This process is known as the kinetic energy cascade, and it is repeated till the viscous effects of the very small eddies dissipate their turbulence energy into heat (see Figure 2.3). Figure 2.4 shows a typical energy cascade, described by the evolution of the kinetic energy per mass unit E with respect to the wave number χ (defined as the inverse of the eddies length scale).

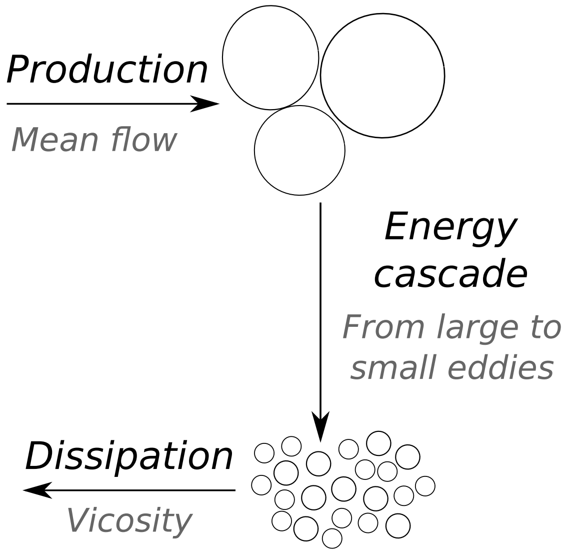

Figure 2.3: Turbulence phenomenon, sketch of eddies evolution

The *Navier-Stokes equations* constitute a system of five equations with five unknown variables. Assuming that the boundary conditions are also known, this system can be directly solved even in a turbulent regime. This approach is referred as *Direct Numerical Simulation* (DNS), which allows to get an accurate three-dimensional and time-dependent description of all the turbulent scales of the kinetic energy cascade without requiring any additional hypothesis [Orszag (1970)]. However, the number of mesh nodes required for the application of such a method scales with $\mathscr{O}\left(Re_L^3\right)$, where Re_L refers to the *Reynolds number* based on the spatial integral scale [Sagaut and Deck (2009)]. This limitation makes impossible the introduction of DNS in the today's study of industrial flows, where typical *Reynolds numbers* range from 10^6 to 10^9. In order to overcome this problem, several numerical approaches based on the modeling of turbulent eddies have been developed. The *Large Eddy Simulation* (LES) method decomposes the flow field between large and small turbulent scales by applying a spatial filter [Smagorinsky (1963)]. While the former are directly resolved, the

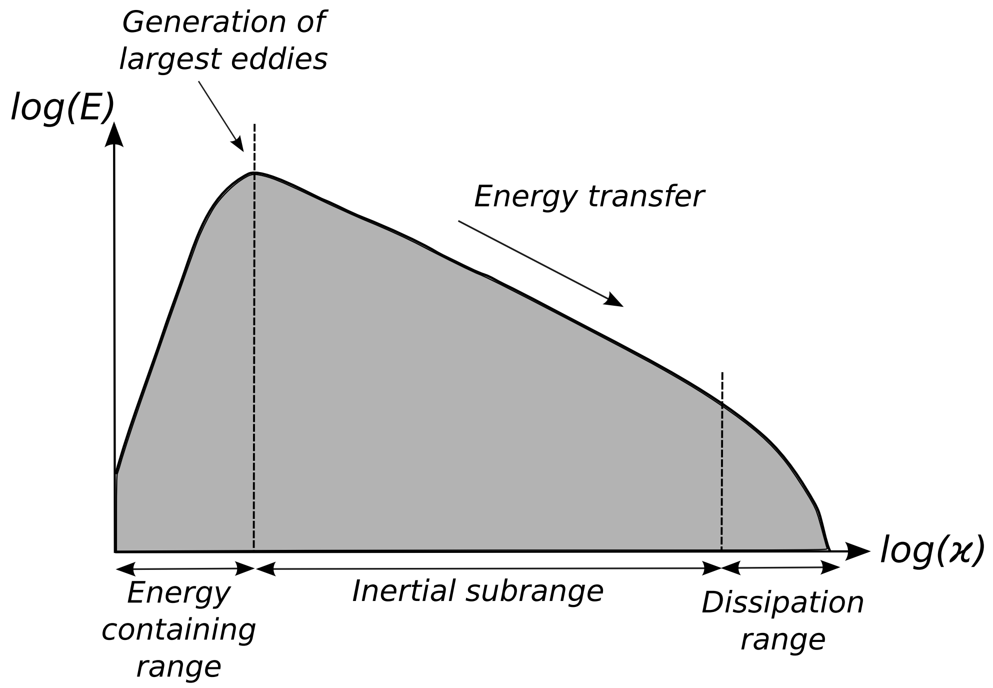

Figure 2.4: Kinetic energy cascade sketch, reproduced from Sagaut et al. (2006)

latter are taken into account through the use of a model. The delimiter between resolved and modeled scales is known as the cut-off wave number. Even if the LES is computationally less expensive that the DNS, its application to industrial flows is also limited by the required computational resources. Indeed, the resolution of the large scales is still very demanding in terms on near-wall mesh refinement [Sagaut and Deck (2009)]. As an affordable alternative for the prediction of turbulence, industrial flows computation traditionally relied in the *Reynolds-Averaged Navier-Stokes* (RANS) approach. This methodology allows to obtain a statistical representation of the time-averaged flow at a reduced computational cost, assuming that the natural frequencies of the aerodynamic loading are much lower than the characteristic frequencies of turbulence. In this case, the resolved part of the kinetic energy cascade of Figure 2.4 corresponds to an empty spectrum, since all the turbulent scales are modeled.

In RANS approach, flow variables A are decomposed into a time averaged $\bar{A}$ and fluctuating part A', with:

$$\bar{A}(\vec{x},t) = \frac{1}{T}\int_{-\frac{T}{2}}^{\frac{T}{2}} A(\vec{x},t+\imath)\,d\imath \tag{2.13}$$

Where the averaging time T should be large enough with respect to the time scale of the turbulent fluctuations, but small enough with respect to all other time-dependent effects. For compressible flows and in order to avoid the product of different flow variables fluctuations, a *density-weighted* averaged use to be introduced [Hirsch (1990)]:

$$A = \hat{A} + A'' = \frac{\overline{\rho A}}{\bar{\rho}} + A'' \tag{2.14}$$

Applying the *time* averaging to the density and pressure variables of Equation 2.7, and the *density-weighted* averaging to the energy, velocity and temperature, the resulting U vector and the fluxes contribution can be written as:

$$U = \begin{pmatrix} \bar\rho \\ \bar\rho\hat v_x \\ \bar\rho\hat v_y \\ \bar\rho\hat v_z \\ \bar\rho\hat E \end{pmatrix}, \tag{2.15}$$

$$\vec F_I - \vec F_V = \begin{pmatrix} \bar\rho\hat{\vec v} \\ \bar\rho\hat{\vec v}\hat v_x + \bar p\vec e_x \\ \bar\rho\hat{\vec v}\hat v_y + \bar p\vec e_y \\ \bar\rho\hat{\vec v}\hat v_z + \bar p\vec e_z \\ \bar\rho\hat{\vec v}\hat E + \bar p\hat{\vec v} \end{pmatrix} - \begin{pmatrix} 0 \\ -\overline{\rho\vec v''v_x''} \\ -\overline{\rho\vec v''v_y''} \\ -\overline{\rho\vec v''v_z''} \\ -\overline{\rho H''\vec v''} \end{pmatrix} - \begin{pmatrix} 0 \\ \bar\tau^v_{xx}\vec e_x + \bar\tau^v_{xy}\vec e_y + \bar\tau^v_{xz}\vec e_z \\ \bar\tau^v_{xy}\vec e_x + \bar\tau^v_{yy}\vec e_y + \bar\tau^v_{yz}\vec e_z \\ \bar\tau^v_{xz}\vec e_x + \bar\tau^v_{yz}\vec e_y + \bar\tau^v_{zz}\vec e_z \\ \overline{\boldsymbol{\tau}^v}\vec v + \bar{\vec q}_c \end{pmatrix} \tag{2.16}$$

The second term of Equation 2.16 introduces complementary stresses with respect to the laminar formulation, due to the consideration of turbulent fluctuations. In particular, the additional components of the momentum equation resulting from the averaging process are referred to as the *Reynolds stresses* $\boldsymbol{\tau}^R = -\overline{\rho v_i'' v_j''}$, while for the energy equation the *turbulent heat flux* vector appeared $\bar{\vec q}_t = -\overline{\rho H''\vec v''}$. The *Reynolds stresses* are usually added to the effects of the viscous shear stress tensor in the so-called *total shear stress vector* $\boldsymbol{\tau} = \boldsymbol{\tau}^v + \boldsymbol{\tau}^R$, so the fluxes can be further simplified as:

$$\vec F_I - \vec F_V = \begin{pmatrix} \bar\rho\hat{\vec v} \\ \bar\rho\hat{\vec v}\hat v_x + \bar p\vec e_x \\ \bar\rho\hat{\vec v}\hat v_y + \bar p\vec e_y \\ \bar\rho\hat{\vec v}\hat v_z + \bar p\vec e_z \\ \bar\rho\hat{\vec v}\hat E + \bar p\hat{\vec v} \end{pmatrix} - \begin{pmatrix} 0 \\ \bar\tau_{xx}\vec e_x + \bar\tau_{xy}\vec e_y + \bar\tau_{xz}\vec e_z \\ \bar\tau_{xy}\vec e_x + \bar\tau_{yy}\vec e_y + \bar\tau_{yz}\vec e_z \\ \bar\tau_{xz}\vec e_x + \bar\tau_{yz}\vec e_y + \bar\tau_{zz}\vec e_z \\ \overline{\boldsymbol{\tau}}\vec v + \bar{\vec q} \end{pmatrix} \tag{2.17}$$

where the *total turbulent heat flux* $\bar{\vec q} = \bar{\vec q}_c - \overline{\rho h''\vec v''}$ combines the effect of the heat conduction flux and the turbulent heat flux.

From a mathematical point of view, the turbulence related contributions add several unknowns to the system without providing any additional equation. Hence, a closure model is needed in order to relate these new quantities to the averaged flow variables. This is the role of the so-called *turbulence models*. RANS *turbulence models* are based on approximations of different complexity, which are tuned thanks to available experimental data. A common solution for all targeted flows has not been found, and the choice of a *turbulence model* still relies on previous experiences on similar flow problems. As a reference, some of the most popular *turbulence models* (ordered by complexity), are summarized in Table 2.1.

Table 2.1: Examples of RANS turbulence models

Type of model	Examples
Algebraic	*Cebeci & Smith* [Smith and Cebeci (1967)], *Baldwin-Lomax* [Baldwin and Lomax (1978)]
One-equation	*Spalart-Allmaras* (SA) [Spalart and Allmaras (1992)]
Two-equations	k-ε [Launder and Sharma (1974)], k-ω [Wilcox (1988)], k-ω SST [Menter1993]
Four-equations	$v^2 - f$ [Durbin (1995)]

When the flow cannot be considered as statistically stationary, Reynolds averaging is not equivalent to time-averaging. This is the reason why several adaptations of the RANS equations in order to account for time dependence have been proposed, often referred as *unsteady* RANS (or URANS). These modifications are only applicable when the flow field is characterized by a separation of time scales between the unsteadiness of the mean field and the unsteadiness of turbulent fluctuations. The new solution algorithm increases the computational time of the RANS approach, but it is required for the solution of unsteady flows. However, the mesh and time-requirements for URANS are less constraining than the ones for the LES method, since the former technique only deals with mean-flow unsteadiness.

Figure 2.5 compiles the presented CFD approaches regarding their cut-off wavenumber in the kinematic energy cascade.

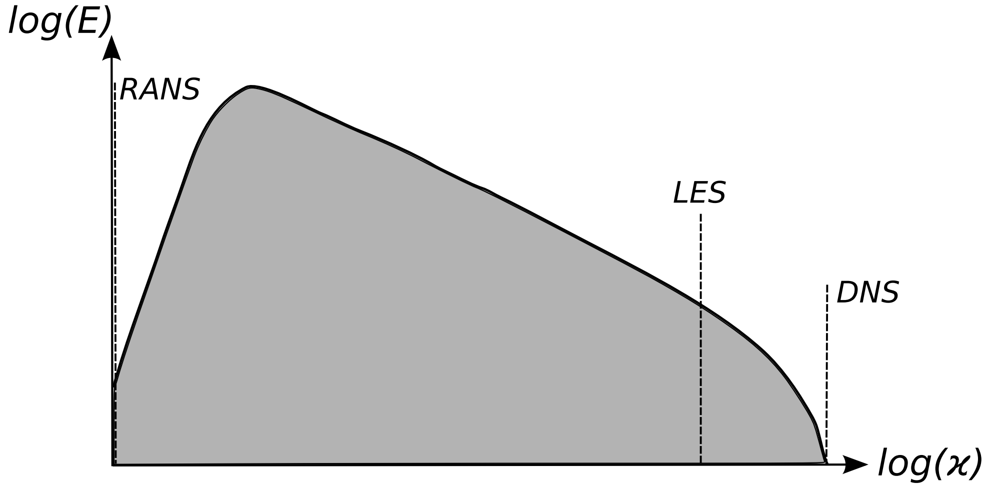

Figure 2.5: Kinetic energy cascade sketch, reproduced from Sagaut et al. (2006). Includes CFD techniques cut-off wavenumbers (left hand region is to be resolved, while right hand is modeled)

In order to provide a CFD solution able to resolve large eddies at an affordable computational time, several authors tried to combine the LES and RANS approaches [Sagaut et al. (2006)]. These methods are known as *hybrid RANS/LES*. One of the most popular algorithms in this category is the so-called *Detached Eddy Simulation* (DES), proposed by Spalart et al. (1997). In the DES method, the small structures attached to the wall are modeled by means of RANS, while large eddies present in the separated region are solved *via* de LES technique.

To illustrate the hardware requirements of each of the introduced CFD approaches, Figure 2.6 depicts the necessary resources in order to perform a simulation of a complete aircraft wing. As it can be observed the DNS methodology is still too computationally expensive, requiring machines operating at speeds in the range of *zetta flops* (which are expected to be available in the 2040s decade).

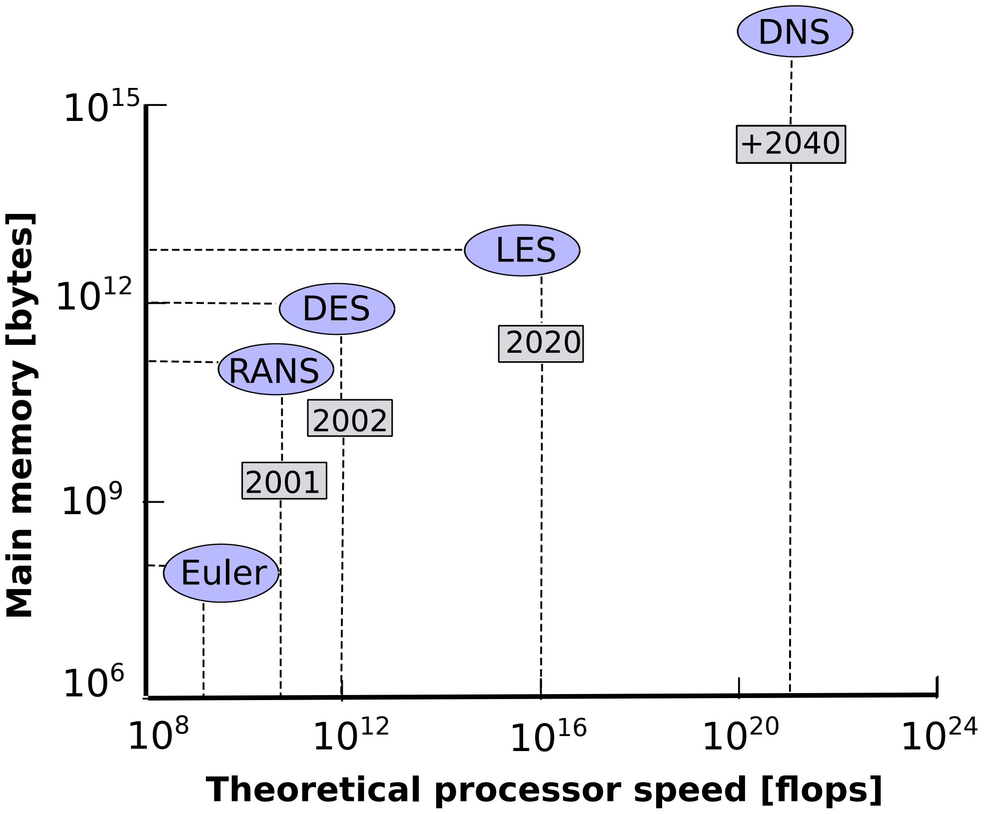

Figure 2.6: Theoretical hardware requirements for the different CFD methods when performing a complete aircraft wing simulation. Includes the year of first performed/expected simulation. Adapted from Biswas (2005)

2.1.3 Aeroelasticity issues in wind turbines

The concept of aeroelasticity refers to all the effects derived from the mutual interaction of aerodynamic loads and solid deformation. It can be seen as a subset of the so-called *Fluid-Structure Interaction* (FSI) field, which considers also other sources of fluid loading (such as hydrodynamics). Collar (1946) proposed to classify the aeroelastic effects depending on the nature of the forces involved in every phenomenon:

- Aerodynamic forces
- Elastic forces
- Inertial forces

If only aerodynamic and elastic forces are involved in a given aeroelastic effect, it is referred as *static* [Bisplinghoff et al. (1995)]. When the action of inertial forces is also to be considered, the effect is *dynamic*. The application of the so-called Collar's diagram for aircraft design purposes is depicted in Figure 2.7.

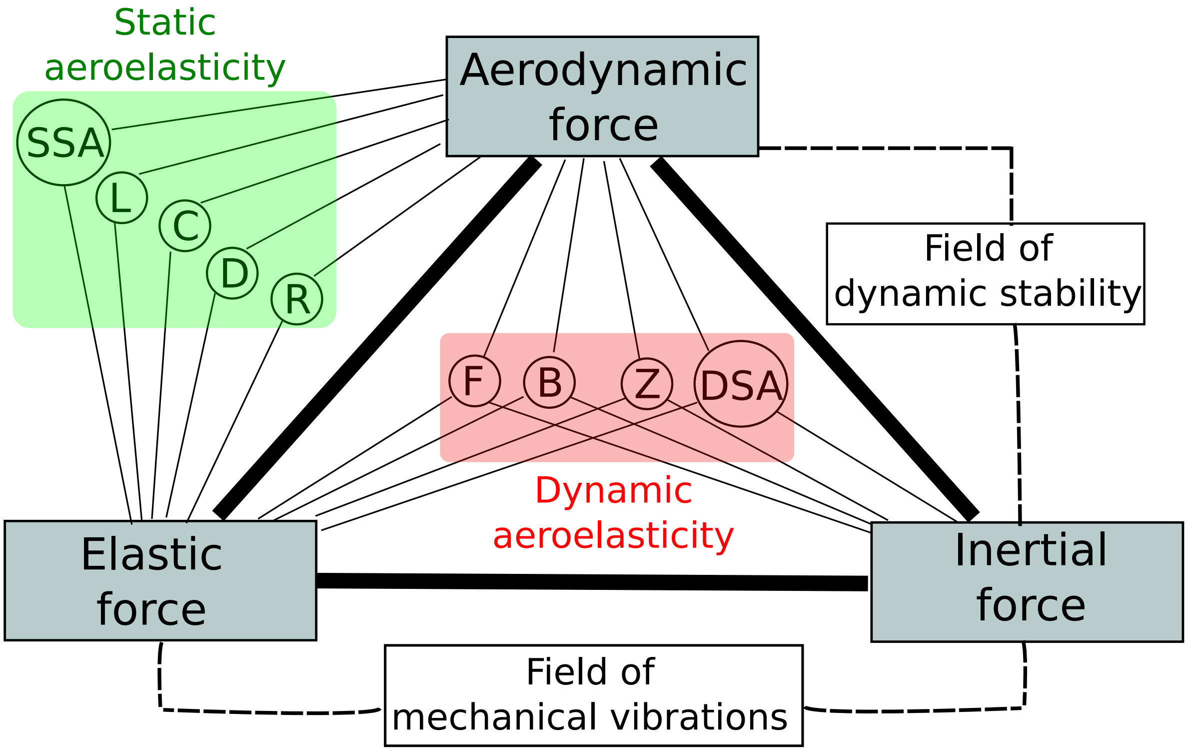

Figure 2.7: Collar's diagram applied to aircraft design, adapted from Bisplinghoff et al. (1995). *SSA*: Aeroelastic effects on static stability, *L*: Load distribution, *C*: Control effectiveness, *D*: Divergence, *R*: Control system reversal, *F*: Flutter, *B*: Buffeting, *Z*: Dynamic response, *DSA*: Aeroelastic effects on dynamic stability

Load distribution refers to the redistribution of aerodynamic loads due to the static deformation of the structure. The concept of *Divergence* appears when the structural deformations under aerodynamic loading induce higher aerodynamic loading itself, and a static equilibrium cannot be reached. Both effects should be considered for HAWTs [Bottasso (2011)].

In the framework of aircraft design, the *Dynamic loading* refers to the transient response of structural components under the application of dynamic loads such as gusts, landing maneuvers, abrupt control motions, etc. For HAWTs, *Dynamic loading* is expected not only for particular loading scenarios (e.g. gusts and wind direction changes), but also during nominal operation. Indeed, both the atmospheric boundary layer and the presence of the tower introduce a considerable azimuthal dependence of blade loading. Therefore flow unsteadiness during the the blade revolution is expected. Wind turbine blades are characterized by having low structural damping, leading to potential problems with regards to the *dynamic aeroelasticity*. In addition, modern rotor blades are made of composite materials, and the structural damping is harder to estimate, depends on meteorological conditions and is substantially modified with aging [Hansen et al. (2006)]. Under certain operational conditions, HAWT *dynamic aeroelasticity* can reach to an instable situation, where the amplitude of blades deflection increases in time. This situation could end up with the structural failure of the blade or with an eventual contact with the tower. In HAWTs most part of these destructive phenomena correspond to the so-called *aeroelastic instabilities*, which are characterized by being excited by the structural deformation itself. Examples of these effects during wind turbines operation are the flapwise instability and the edgewise instability [Hansen et al. (2006)]. Parked conditions are considered to be more problematic due to their particular loading scenario, leading to potential *aeroelastic instabilities* involving side-to-side motion of the tower, edgewise motion of the rotor blades and yawing of the platform [Bir and Jonkman (2007)].

Flutter is a very important aspect to consider during the design stage of a high speed aircraft [Bisplinghoff et al. (1995)]. It is caused by a positive feedback between the structure deformation and the aerodynamic loading. Even if classical *flutter* has not been observed in HAWT blades, the increase in the bending-torsion coupling related to rotor up-scaling motivates the consideration of this phenomenon in modern designs [Hansen et al. (2006)].

2.1.4 Structural modeling of wind turbines

When performing aeroelastic computations, a model of the HAWT structure is required. As for the aerodynamics loads, several approaches can be found in the literature with regards to wind turbines structure modeling, accounting for different levels of complexity. In the *modal approach*, the structure is represented by its natural frequencies and mode shapes [Debrabandere et al. (2011)]. These are determined prior to the aeroelastic simulation, either by computation with a *Finite Element Method* (FEM) structure solver or by experiments. In practice only the first eigen modes are considered, assuming that high frequency modes will not be excited by aerodynamic loads. The main advantage of the *modal approach* is its computational efficiency, since the number of *Degrees Of Freedom* (DOF) to be solved is drastically reduced. In addition, the filtering of high eigen frequencies allows to decrease the time resolution when considering dynamic simulations.

More sophisticated approaches are based on FEM models of the wind turbine components. Most part of these use one-dimensional beam models in order to represent the blades. Both *Euler-Bernoulli* and *Timoshenko* formulations have been used in wind energy [Timoshenko (1921, 1953)]. Other applications of finite elements in this context include the full FEM representation of the blade and the use of super-elements [Heege et al. (2011)].

The impact of the blade deformations linearization hypothesis was assessed by Larsen et al. (2004). Geometrical non-linearities led to more important blade tip deflections, causing a reduction of rotor loads. In particular, for the studied mega-watt sized HAWT a maximum power deviation of 2.5% was computed.

2.1.5 Mesh deformation algorithms in CFD

In the framework of CFD methods, different approaches can be followed in order to model *Fluid-Structure Interaction* (FSI) problems. The most intuitive one is the so-called *monolithic* approach, where fluid *Navier-Stokes* equations are solved together with structural equations at every time-step [Hron and Turek (2006)]. However, this approach faces several implementation problems:

- **Historical reasons**
  - Technological consolidation is a very important issue when dealing with numerical methods applied in the industry. The development of *fluids* and *structures* simulation codes have followed almost independent paths all along their history. Nowadays software industry is offering reliable packages for either *Computational Fluid Dynamics* (CFD) or *Computational Structural Mechanics* (CSM) simulations. The integration of these type of codes in an unified multi-physics package at an industrial level use to be impracticable.
- **Numerical reasons**:
  - Solving the structural problem is usually less computationally expensive than the fluid solution. Mixing both formulations in a *monolithic* scheme prevents the benefit of this computational time saving.
  - The time-scales for the fluid and the structure-related effects can be very different. The implementation of a *monolithic* approach will force to use the smallest required time-step for both physics, adding an unnecessary computational cost to the aeroelastic simulation.

Due to the mentioned limitations, the most commonly used approach in industrial applications is the so-called *staggered scheme* [Felippa et al. (1977)]. In this case, fluid and structural problems are solved separately. Interfaces information is exchanged in order to ensure continuity of the variables and compatibility of the charges.

In the framework of FSI, one of the main challenges is to handle structural deflections during the simulation. Three different methodologies have been identified in the literature when dealing with this problem:

- **Body-fitted approach** [Löhner and Yang (1996); Quaranta et al. (2008)]: In this case, fluid mesh is re-adapted at every time-step following structural deflections.
- **Chimera methods** [Benek et al. (1985)]: In this approach, a body-fitted fine mesh around each object is independently created. Usually, it is employed when dealing

with objects in relative motion compared to each other. The fluid solution is computed by a sequential iteration over the overlapping sub-domains. It allows to reduce the complexity involved in fluid mesh re-adaptation of the classical *body-fitted approach*.

- **Immersed/embedded boundary methods** [Löhner et al. (2004)]: The fluid mesh is considered as fixed and a special formulation is added for moving boundaries. Hence, no mesh re-adaptation is needed.

The present research is focused on a *body-fitted approach*. In this scenario, the modification of the CFD mesh in order to re-adapt to the new fluid domain due to the deformation of the blade wall becomes one of the most important numerical issues to face. The quality of the resulting adapted mesh should ensure a good communication between CFD and CSM codes along the blades wall interface, and fulfill the necessary *fluid solver* requirements for the next flow simulation.

A fast and reliable tool is then needed to carry out this numerical operation at every time step. Two main approaches have been followed in the literature in order to achieve this goal:

- **Mesh deformation**: Structural deflections are propagated into the new fluid domain. Fluid mesh topology and connectivity is kept during this operation (see Figure 2.8).

- **Re-meshing**: A new fluid mesh is generated taken into account the new CFD domain. This approach use to be less efficient from a computational time point of view. In addition, the automation of the mesh generation process and the interpolation of the flow between two consecutive meshing is not a trivial development.

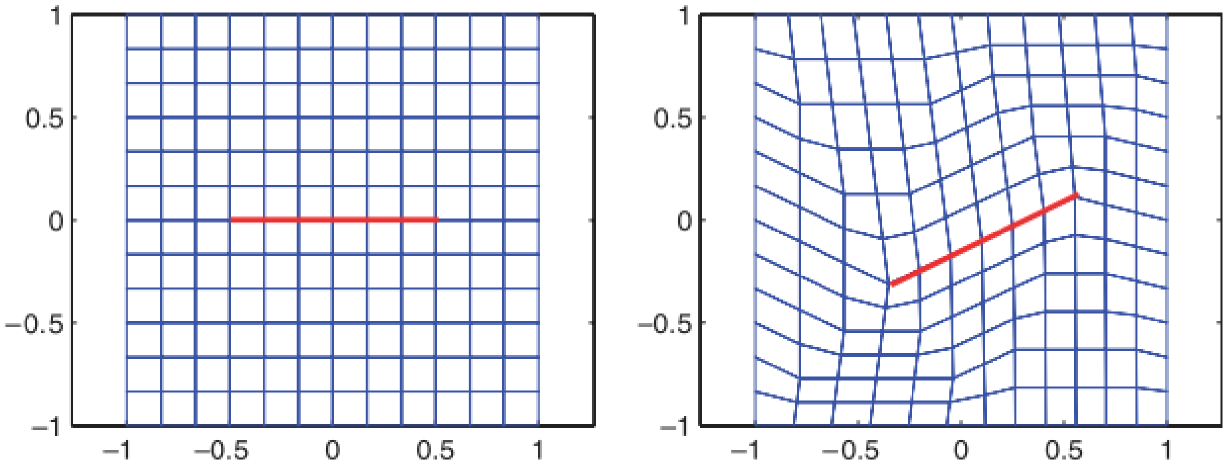

(a) Original mesh **(b)** Deformed mesh after forced pitching

Figure 2.8: Schematic representation of the mesh deformation around a moving boundary (in red). Source: Lefrançois (2008)

Only the *mesh deformation* subject was assessed in this work. Following sections describe the state-of-the art concerning this problem. A main distinction is made between the *mesh connectivity* and the *point-by-point* schemes.

Mesh connectivity schemes

These methods are based on fluid mesh connectivity, so in the notion of *element*. Its implementation use to be topologically and element type dependent. In many cases, the solution of a linear system issued from the numerical discretization of a theoretical model is required. Due to the connectivity notion inherent to these methods, its parallelization is often not trivial in an industrial implementation.

Elliptic smoothing A pure diffusion mechanism is used in this type of fluid mesh deformators. The most simple approach is to apply a *Laplacian* operator to our deformation, in order to isotropically diffuse moving walls movement into the inner fluid mesh. A local variable diffusion coefficient is however needed in order to restrict the diffusion of cells prone to high distortion [Löhner and Yang (1996)]. Even with this model enhancement, mesh folding cannot be prevented. The reason why new and more sophisticated (and computationally costly) approaches were set-up, such us the biharmonic operator [Helenbrook (2003); Wick (2011)].

Spring analogy In this method, fluid mesh nodes are assumed to be connected by a network of springs [Bartels (1999); Batina (1989)]. In order to ensure the deformed mesh quality, a heterogeneous distribution of spring stiffness is set-up, based on a geometric quantity such as the length of the edge. Initial formulation of the method was only accounting for translational springs, hence it was unable to prevent edge cross-overs (see Figure 2.9). Several improvements have been proposed in order to add the concept of mesh rotations in the original formulation:

- Torsional springs [Degand and Farhat (2002); Farhat et al. (1998); Maruyama et al. (2002)]
- Semi-torsional springs [Blom (2000); Zeng and Ethier (2005)]
- Ball-vertex springs [Acikgoz and Bottasso (2007)]
- Ortho-semi-torsional [Markou et al. (2007)]

Even if these methods considerably increase the robustness of the spring analogy, a computational time over-head has to be considered in their implementation.

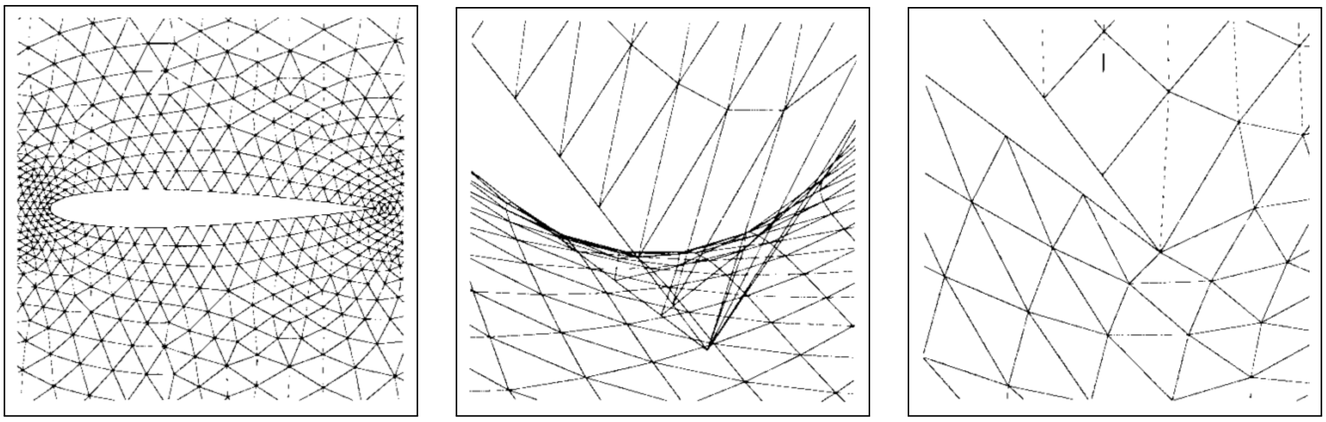

(a) Original mesh (b) Base spring analogy (c) Semi-torsional springs

Figure 2.9: Performance of the spring analogy of Blom (2000) in the mesh deformation of an airfoil unstructured mesh when a 45 deg pitch is imposed. (a): Original mesh. (b): Detail of the trailing edge, base spring analogy mesh deformation. (c): Detail of the trailing edge, enhanced formulation of the spring analogy by introducing semi-torsional springs

Elastic analogy Originally introduced by Lynch and O'Neill (1980), in this approach we assume the mesh as an elastic continuum, with linear elastic properties. In order to prevent mesh folding, an heterogeneous distribution of elastic properties use to be defined (see Figure 2.10). Several criteria have been analyzed in the literature in order to stiffen the cells that are more prone to inversion.

- Cell geometry [Johnson and Tezduyar (1994)]
- Distance to the wall [Chiandussi et al. (2000)]
- Cell distortion [Bar-Yoseph et al. (2001)]
- Strain field [Hsu and Chang (2007)]

The resulting methodology is rated as significantly more robust with respect to the spring analogy approach but more computationally demanding.

Other connectivity-based methods Alternative less mature connectivity-based methods have been studied by several authors:

- Advancing front: Gerhold and Neumann (2008)
- Cell layering technique: Carvallo et al. (1997)
- Bi-elliptic operator: Wang and Hu (2012)

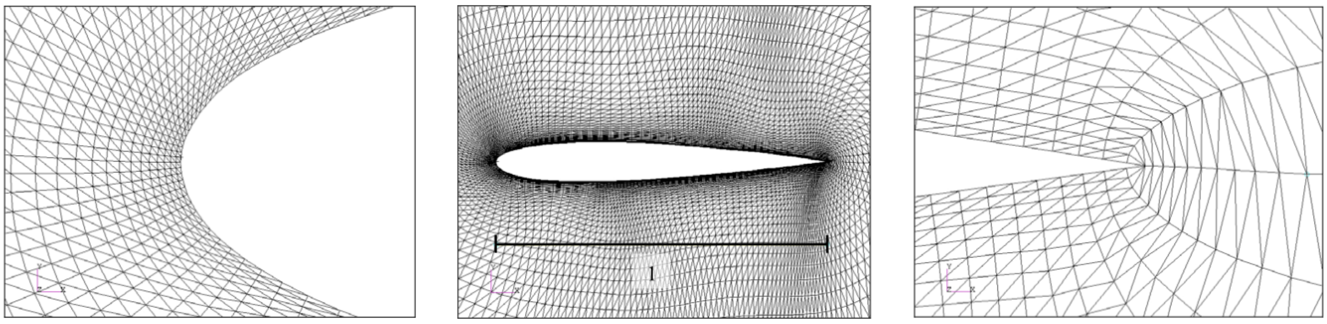

(a) Leading edge, original **(b)** Global view, original **(c)** Trailing edge, original

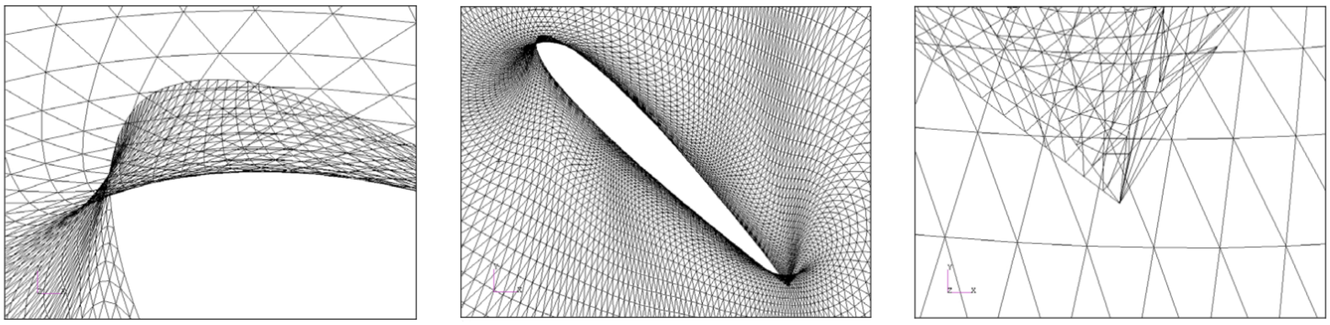

(d) Leading edge, homogeneous **(e)** Global view, homogeneous **(f)** Trailing edge, homogeneous

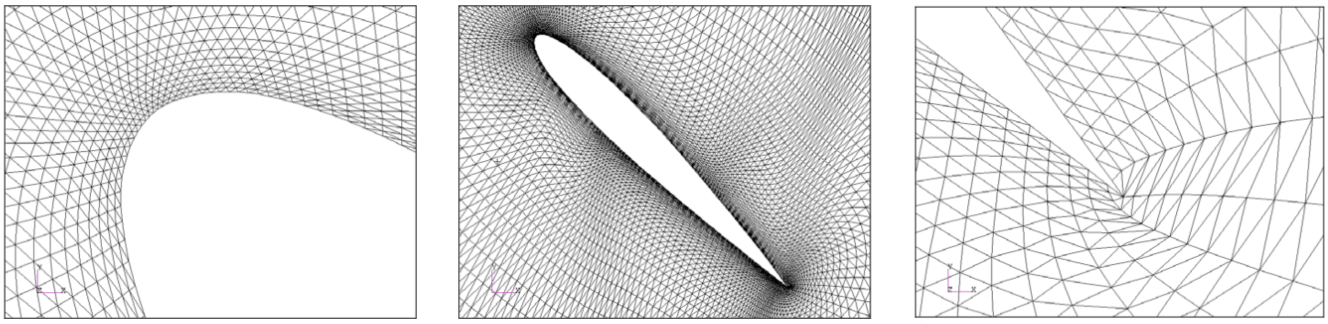

(g) Leading edge, heterogeneous **(h)** Global view, heterogeneous **(i)** Trailing edge, heterogeneous

Figure 2.10: Performance of the elastic analogy of Hsu and Chang (2007) in the mesh deformation of an airfoil unstructured mesh when a 45 deg pitch is imposed. (a), (b), (c): Original mesh. (d), (e), (f): Deformed mesh assuming homogeneous elastic properties. (g), (h), (i): Deformed mesh assuming heterogeneous elastic properties (variable Young's modulus)

Point-by-point schemes

Point-by-point schemes are based on the concept of *nodes*, and no mesh connectivity is required. This is the reason why they use to be topologically independent and easier to parallelize, allowing a more flexible and efficient implementation.

Radial basis functions Originally described by De Boer et al. (2007), this method uses the displacement of the *moving walls* in order to build an interpolation function, expressed as a sum of *radial basis functions*. The method can easily handle big deformations, and the resulting mesh quality use to be very close to the undeformed one. It is also easy to implement and parallelize. However and as it will be shown in this document, its problems of scalability make the cost of this method unaffordable for industrial configurations (where multi-million meshes are expected). Indeed, a matrix inversion is involved in the application of this method, having an attached complexity of $\mathcal{O}(\mathrm{n_b}^3)$, where n_b refers to the number of boundary nodes to consider.

Inverse distance weighting This mesh deformation method was proposed by Witteveen (2010) as an alternative to the *Radial basis functions* interpolation. The theoretical basis of the method were already established by Shepard (1968) in the framework of geographical information systems. As it is based on an explicit interpolation, no matrix inversion is required for this approach. This considerable computational time saving with respect to the *Radial basis functions* interpolation makes this approach very attractive. A moderate reduction in terms of resulting mesh quality should however be considered.

Delaunay graph mapping Introduced by Liu et al. (2006), in this method the *Delaunay* graph of the boundary nodes is used as a basis of the interpolation. This approach offers a very high efficiency for moderate deformations, but limitations has been found when dealing with large displacements and rotations.

Other point-to-point methods Alternative less mature point-to-point methods have been studied by several authors:

- Surface influence technique: Allen (2007)
- Disk relaxation: Zhou and Li (2013)
- Neural networks: Stadler et al. (2011)

Auxiliary algorithms

Several technologies has been developed in order to enhance the performance of the already presented methodologies. These methods cannot be considered as *stand-alone* approaches, but they play an important role in the resulting mesh quality and/or the computational efficiency of the whole mesh deformation process

Transfinite Interpolation *Transfinite Interpolation* (TFI) method was initially developed for mesh generation purposes by Gordon and Hall (1973). Several authors have adapted this technique in the framework of structured multi-block meshes [Ding et al. (2014),Gopalakrishnan and Tafti (2009) and Tsai et al. (2001)]. In this context, the application of the *transfinite* *interpolation* requires the computation of the block corners displacement as an input. This task is usually performed by one of the traditional *mesh deformation* methods presented in this chapter. Block corners displacements are then used in order to compute the new position of block edges by linear interpolation, based on original node clustering information. A similar procedure is followed in order to computed deformed block faces (see Figure 2.11). When dealing with 3D meshes, the TFI can be also applied to compute the displacement of the block inner nodes. The application of the *transfinite interpolation* to mesh deformation problems offers a very fast solution for cases accounting for small displacements. However, due to the purely linear nature of this approach, the quality of the resulting mesh could be highly distorted if important rotations are present in the considered deformation.

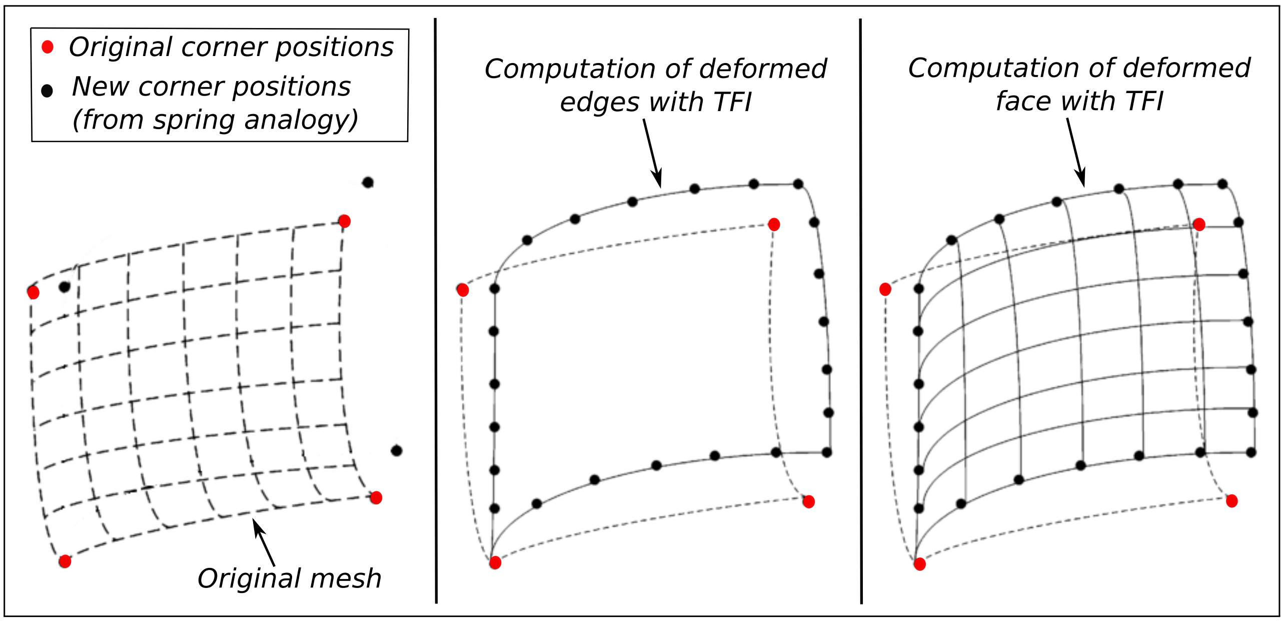

Figure 2.11: Schematization of the transfinite interpolation applied to mesh deformation. Adapted from Gopalakrishnan and Tafti (2009)

Quaternion algebra The quaternions algebra was introduced by Samareh (2002), aiming to consider the concept of rotations on mesh deformation approaches. In this case, the quaternions were applied in combination with *Transfinite Interpolation* and *Spring Analogy* techniques. Quaternion algebra is used to compute the rotations of the elements at the boundary, in order to interpolate this information into the inner mesh.

Hybrid methodologies

Presented methods can be classified based on their performance regarding:

- Computational efficiency
- Topological flexibility

- Resulting mesh quality
- Implementation complexity
- Required input data

As seen in previous sections, there is not an universal mesh deformation method being able to combine both efficiency and resulting mesh quality for every considered mesh. The reason why many authors have focused their effort in combining existing technologies, in order to profit from the benefits of each one of them and to avoid their limitations. Table 2.2 lists some of the *hybrid mesh deformation methods* found in the literature and ordered by date of publication. Among these numerical strategies, three main philosophies can be distinguished:

- Reduce the computational cost of *Elastic analogy* or *Radial Basis Functions* by incorporating sophisticated numerical methods either before or after the application of these classical approaches.
- Application of different algorithms for the movement of *boundary layers* and for the rest of the mesh.
- Deformation based on *Transfinite Interpolation* thanks to the pre-computation of block displacements *via* another technique (most popular approach when dealing with structured grids).

2.1.6 Overview of some CFD applications for Horizontal Axis Wind Turbines analysis

Horizontal Axis Wind Turbine (HAWT) aerodynamics is characterized by massive separation and complex three-dimensional effects. These phenomena cannot be properly modeled by simplified engineering approaches, such as the widely used *Blade Element Momentum* (BEM) method [Heege et al. (2013); Jonkman and Buhl Jr. (2007)]. This limitation has motivated the introduction of high fidelity flow modeling methods based on *Computational Fluid Dynamics* (CFD). Traditional CFD applications to HAWTs analysis are based on steady flow *rotor-only* simulations (where only blades, hub and nacelle geometries are considered). Thanks to the problem periodicity when assuming an incoming wind aligned with the rotor axis and uniform upstream flow conditions, a single *blade passage* is considered. These simulations allow to characterize the local flow behavior around the wind turbine and its impact on global rotor performance with a reduced computational effort. However, by omitting the tower geometry the main source of flow unsteadiness is also neglected. Indeed, due to the proximity of the HAWT rotor to the tower, the generation of complex unsteady flow phenomena is expected.

Table 2.2: Hybrid mesh deformation methods found in the literature

Author/s	Short description
Dubuc et al. (2000)	Vertex interpolation based on rigid body motion + *Transfinite Interpolation*
Gopalakrishnan and Tafti (2009); Tsai et al. (2001)	*Spring analogy* for vertex displacement + *Transfinite Interpolation*
Martineau and Georgala (2004)	Fast rigid body motion initialization followed by the application of the *Elastic analogy* in order to improve resulting mesh quality
Kholodar et al. (2005)	Particular treatment for viscous boundary layers based on *surface vectors readjustment* followed by torsional springs analogy
Lefrançois (2008)	*Elastic analogy* in combination with a sub-mesh approach in order to reduce the total computational cost of this technique
Morton and McDaniel (2009)	The viscous mesh is rigidly moved together with the *moving wall*, followed by either a *surface influence* or *Delaunay graph* method for the rest of the mesh
Ko et al. (2010)	*Elastic Analogy* in a *macro-element* + *Transfinite Interpolation*
Abgrall et al. (2012)	*Elastic analogy* enhanced by NURBS technologies
Kowollik et al. (2013)	*Radial basis function* based on a reduced deformation field + *Delaunay graph mapping* for exact surface reconstruction
Ding et al. (2014)	*Radial basis function* based on *block corners* + *Transfinite Interpolation*

This mechanism is often referred to as *rotor-tower interactions*. A considerable amount of scientific material regarding the application of CFD techniques to HAWT *rotor-only* analysis has been produced. A complete compilation of these works can be found in the review paper of Sumner et al. (2010). The number of publications approaching the study of *rotor-tower interactions* is however very limited. Due to the historical upscaling of HAWTs in order to increase the produced energy per machine, important blade deflections are also expected for modern designs, motivating the need of an *elastic blades* modeling in CFD computations.

Following literature survey compiles the CFD works concerning HAWTs unsteady aerodynamics and HAWTs aeroelasticity. Due to the lack of publicly available industrial configurations, most part of previous work is based on the so-called *academic* or *reference* wind turbines. Only the publications relying on *rotor-resolved* approaches are included in this section due to their potential use for local HAWT design and their direct relation with this PhD work. However, CFD methods are also used in other type of wind turbine analysis such as the study of wake meandering, the effects of the atmospheric boundary layer, the interaction between the different machines integrating a wind farm, etc. In this context the LES methodology has become very popular during the last decade, due to their modeling capabilities regarding anisotropic flows and its less dissipative nature [Mehta et al. (2014)]. Because of hardware limitations, current LES publications in the context of HAWTs use to rely on one of the actuator models described in Section 2.1.2 to simulate the rotor. Examples of these LES-based computations are the study of the atmospheric turbulence of Backaert et al. (2014), the gust impact analysis of Norris et al. (2012), the tandem configuration research performed by Chatelain et al. (2013) or the works of Meyers and Meneveau (2010) and Churchfield et al. (2012) concerning complete wind farms. The last publication was found to be particularly demanding due to the number of HAWTs considered and their proximity, requiring the use of one million of hours and 4096 processors.

In order to contextualize each of the HAWTs mentioned in this literature survey, Table 2.3 compiles their main geometrical and operational parameters. Details of the numerical set-up of the presented works are given in Appendix A.

NREL Phase VI

The first complete *reference* HAWT was the NREL Phase VI, a 10 m rotor diameter model published by the *National Renewable Energy Laboratory* (NREL). A description of the whole NREL Phase VI assembly can be found in Hand et al. (2001), together with the results of an experimental test campaign performed at the NASA Ames wind tunnel. Time-accurate blade pressure measurements were produced in these experiments for a wide range of operating conditions. Five-hole probes were also installed in order to measure local flow angles at different radial locations. Finally, strain-gauge measurements provided information of total torque and flap and edge moments at the blade root. A blind code comparison was carried out in order to compare the predictions of several aeroelastic BEM codes against the obtained experimental data [Simms et al. (2001)]. An important scatter was observed for the different simulations results, even for the most supposedly easy-to-predict operating points. For example for the uniform inflow speed conditions aligned with the rotor axis, rotor power predictions ranged from 25% to 175% with respect to the experimental value. This experience revealed the complexity of the flow and the necessity of high resolution numerical tools in order to characterize the flow. The NREL Phase VI has served as a basis for the validation of almost every CFD code applied to HAWT analysis, confirming the potential of this approach.

A lot of material have been compiled regarding the influence of turbulence and transition modeling, as well as the dependence between the flow behavior and the considered operating point. In this context, three different working regimes were characterized based on the nature of the suction side separation bubble: *pre-stall* or *low speed*, *transitional* and *deep-stall* or *high speed* (see Figure 2.12). A complete overview of the already performed works concerning NREL Phase VI *rotor-only* studies can be found in the review paper of Hansen et al. (2006) , and in the more recent works of Aranake (2013); Potsdam and Mavriplis (2009); Suárez and Doerffer (2015); Yelmule and Anjuri (2013).

(a) *Pre-stall* regime (wind speed of 7 m.s^{-1})

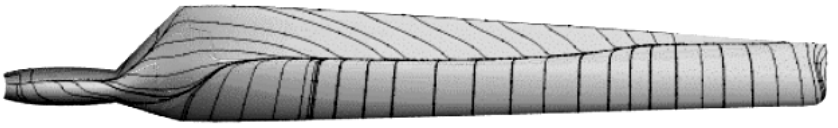

(b) *Transitional* regime (wind speed of 10 m.s^{-1})

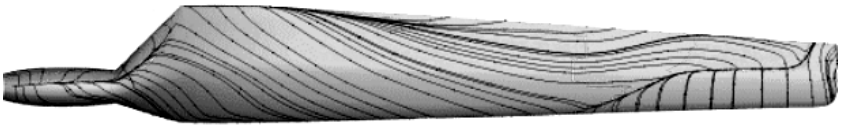

(c) *Deep-stall* regime (wind speed of 13 m.s^{-1})

Figure 2.12: Friction streamlines of the NREL Phase VI simulations performed by Suárez and Doerffer (2015) for the different operating regimes

First studies concerning unsteady CFD simulations of this HAWT were carried out by Le Pape and Lecanu (2004). Initial RANS simulations were performed using the multigrid multi-block structured solver elsA, developed by Onera [Cambier and Gazaix (2002)]. Even if the tower was not included in the computational domain, the convergence problems encountered for high wind speeds required the use of an URANS approach. A three-dimensional behavior of the flow was observed (in particular, the spreading of low span range stall towards the blade tip due to the radial centrifugal forces). A frequency analysis of the computed results identified clear vortex shedding related to the blade flow separation. A more complete characterization of the NREL Phase VI unsteadiness was performed by Zahle et al. (2009). URANS computations were performed using the multigrid multi-block structured solver Ellypsis3D, developed in collaboration between DTU and Risø [Sørensen (1995)]. In this work the whole wind turbine assembly in a *downwind* configuration was considered, including the tower. The shedding phenomenon was not only observed for the rotor blades, but also all along the tower height. Significant blade load fluctuations due to the existence of the tower were computed, reaching up to 40% of the freestream level. Lynch (2011) studied the whole HAWT *upwind* assembly in the framework of his PhD thesis. Both URANS and zonal hybrid RANS/LES technologies were compared. The unstructured solver FUN3D, developed by NASA Langley, was used [NASA (2015)]. For nominal operation conditions, both approaches offered a good agreement with respect to experimental data, even if the URANS solution was found to be more dissipative. While tower vortex shedding was found in all the studied working points, this phenomenon was only clearly identified on the blade for high wind speeds (see Figure 2.13). Wang et al. (2012) also performed URANS simulations of the *upwind* configuration for the whole HAWT operating range. The pimpleDyMFoam solver from the open source code OpenFoam was used [Weller et al. (1998)]. Wind speeds from 5 m.s^{-1} to 25 m.s^{-1} were studied. Especially at high wind, a strong interaction between blade tip vortices and tower vortices was observed. Vortex shedding was also identified on the blades. Hsu et al. (2014) studied the *rotor-tower interactions* of the *upwind* configuration. An in-house code was used, based on an *Arbitrary Lagrangian Eulerian* residual-based *Variational Multiscale* formulation of the Navier–Stokes equations (ALE-VMS) [Bazilevs et al. (2007)]. First steady *rotor-only* computations showed a good agreement with respect to available experimental data. Same situation was reproduced when introducing the tower and comparing the simulation results against the measured azimuthal evolution of the mechanical power. For this unsteady computation, a 8% of mechanical power decay was predicted due to the *blade/tower alignment* event. Li (2014) also based his analysis in an *upwind* configuration, including the

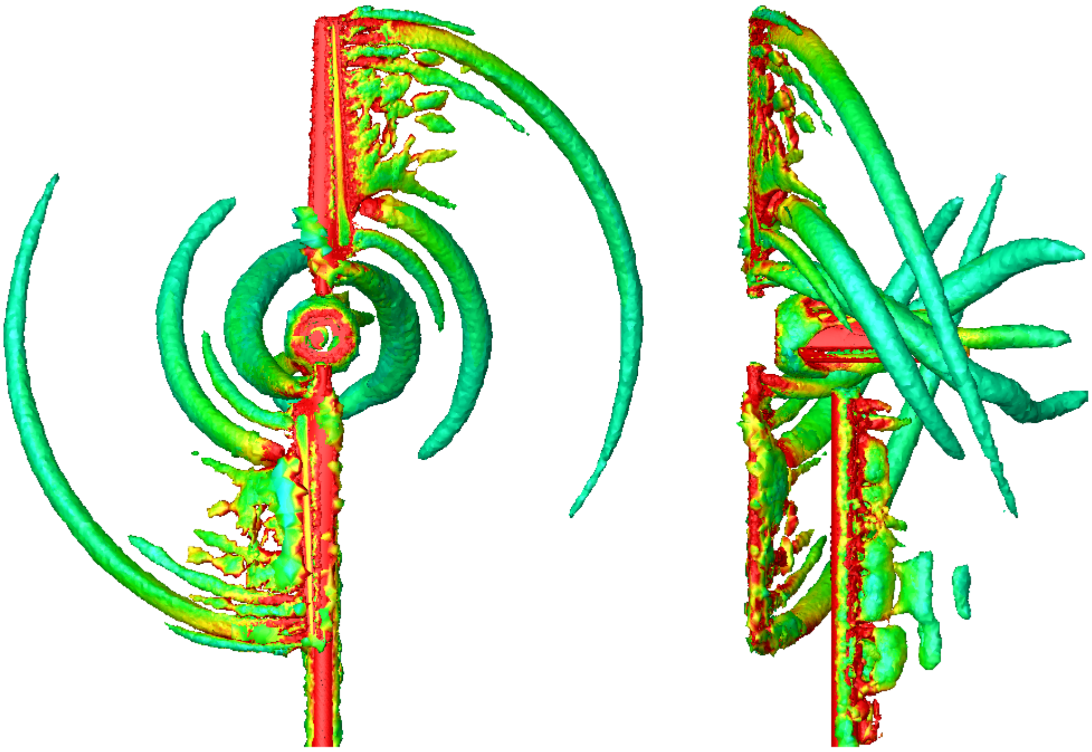

Figure 2.13: Vorticity of the NREL Phase VI, illustrated by means of the Q-criterion isosurfaces for a value of 0.1. URANS computation of Lynch (2011) at 15 m.s^{-1}.

tower. The multi-block structured solver CFDShip-Iowa was used, which is developed by the University of Iowa [Paterson et al. (2003)]. Results from URANS and DES approaches were compared and validated against experimental data. A good agreement between both methodologies was found at low wind speed. When assessing a *deep-stall* operating point, URANS approach was unable to model the periodic shedding of the blade suction surface separation bubble predicted by the DES. The only works accounting for a structural model of the NREL PHASE VI blade were performed by Carrión (2014). A mesh of the whole assembly in *upwind* configuration was studied. URANS computations were performed using the multi-block structured solver HMB2, developed by the University of Liverpool [Barakos et al. (2005)]. The structure was modeled by means of the *modal approach*. As expected for the size of this HAWT and the mechanical properties of the equipped blades, simulations showed very small blade tip displacement fluctuations (in the order of millimeters).

MEXICO

The 4.5 m rotor diameter MEXICO wind turbine was defined in a project founded by the European Commission [Schepers and Snel (2007)]. Open section wind tunnel experiments were performed in order to provide experimental data of the HAWT operation. Blade pressure and loads were computed, together with a description of the flow field around the rotor and in the near-wake region obtained by means of *Particle Image Velocimetry* (PIV) techniques. This wind turbine model extended the possibilities for CFD code validation purposes, especially when focusing in wake analysis. A complete review of the performed simulations can be found in Schepers et al. (2012), and more recently in the PhD thesis of Carrión (2014). In this last publication, the static aeroelasticity of the MEXICO rotor was studied. RANS simulations were performed using HMB2, and modeling the rotor blades as beams. As expected, small blade deflections were computed (with out-of-plane blade tip deflections in the order of millimeters), and a negligible impact on total rotor loads is presumed.

NREL 5MW

With a diameter of 126 m, the NREL 5MW was the first big rotor *reference* HAWT [Jonkman et al. (2009)]. It has been used for both research and code validation purposes. In particular, the NREL 5MW has served as a basis for a series of aeroelastic packages code-to-code comparison projects focused in the study of bottom-fixed and floating offshore configurations. These actions are referred as OC3, OC4 and OC5 projects [Jonkman and Musial (2010); Jonkman et al. (2012); Robertson et al. (2013, 2015)]. Due to the important aeroelastic effects expected during the operation of this machine, previous unsteady CFD computations included a structural model of the rotor. In this context we can find the dynamic aeroelasticity works of Hsu and Bazilevs (2012). The adopted computational approach was based on the combination of ALE-VMS formulation of the Navier–Stokes equations and a NURBS-based *Isogeometric Analysis* (IGA) for structure modeling. Due to blade flexibility, approximate blade deflection amplitudes of 0.5 m were observed for the blade tip out-of-plane displacement (see Figure 2.14). Yu and Kwon (2014) performed aeroelastic computations of the NREL 5MW assembly using an in-house code. Both RANS and URANS methods were employed, accounting for a beam-based blade model. For the former approach, an out-of-plane blade tip deformation of approximately 4.7 m was computed for the *rated speed* operating point. When passing to time marching simulations, a maximum value of 5 m was observed. A significant reduction of blade loads was also found due to blade deflection. Li (2014) studied this HAWT mounted on a spar buoy platform designed in the framework of the OC3 project [Jonkman (2010)]. Blade flexibility was modeled by means of multi-body dynamics elements *via* the commercial software Virtual.Lab Motion [Siemens (2015)]. URANS simulations were performed with the CFDShip-Iowa solver, including both air and water phases. In order to assess the capabilities of the developed methodology, CFD results were compared against other aeroelastic codes from OC3 project participants [Jonkman et al. (2012)]. For the constant inflow of 8 m.s^{-1} operating point, out-of-plane blade tip deflections of the order of 3.5 m were computed. Blade vortex shedding was identified as a lagging mechanism of the rotor loads.

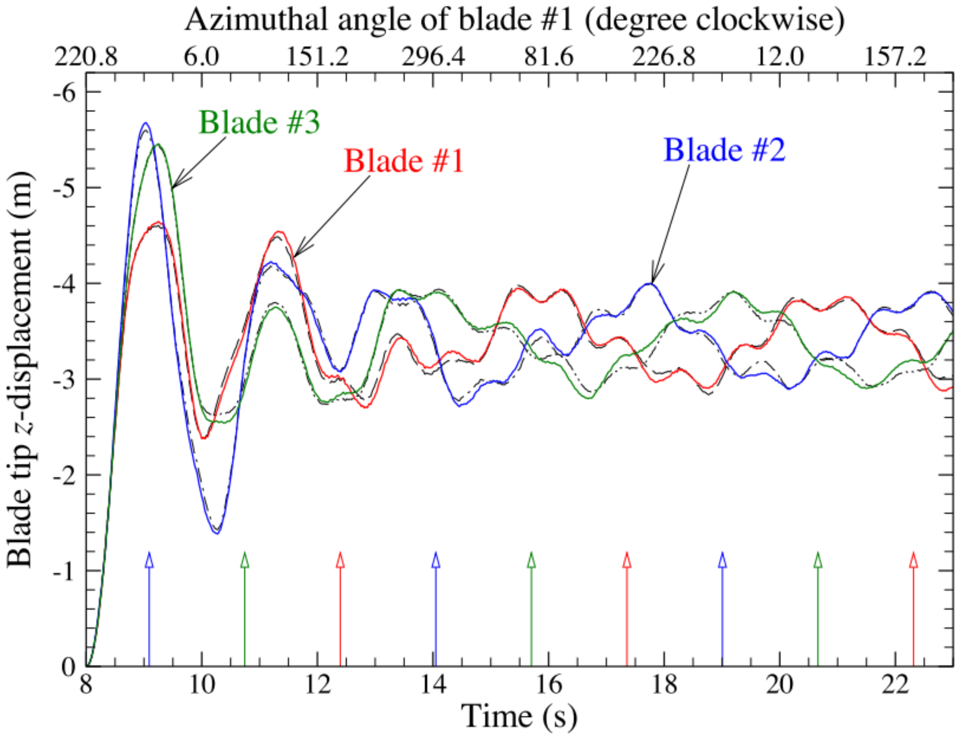

Figure 2.14: Blade tip displacement parallel to the rotor axis for the computations of the NREL 5MW of Hsu and Bazilevs (2012), as a function of the time. Solid lines correspond to full machine simulations, while dashed lines refer to *rotor-only* computations. The arrows displayed at the bottom of the image mark every *blade-tower alignment* event

Industrial wind turbines

Zahle and Sørensen (2008) studied the unsteady aerodynamics of the whole assembly of an industrial HAWT, referenced as SIEMENS 3.6MW. URANS simulations were performed using Ellypsis3D. The two objectives of this work were to analyze the impact of non uniform upstream conditions due to the presence of the atmospheric boundary layer on rotor performance and to characterize the effects of *rotor-tower interactions*. Results showed that the consideration of a non-uniform wind speed inflow leads to an important azimuthal dependence of blade forces. When evaluating flow unsteadiness of the complete rotor and tower assembly, important vortex shedding structures were identified near the blade root, where sections were almost cylindrical. This effect was also observed for the tower region below the rotor disc. Computed rotor thrust and torque showed approximate decays of 1% and 2% due to the *blade-tower alignment* event (see Figure 2.15). Zahle and Sørensen (2011) studied the unsteady flow phenomenon related to blade root separation of the NKT 500/41 rotor. Both RANS and URANS computations were performed using Ellypsis3D. Results were compared against an experimental campaign which results can be found in Diznabi (2009), together with a description of this HAWT. For steady simulations a good agreement with respect to experimental data was found, except for high wind speeds. At this operational range, RANS model showed an overprediction of the mechanical power up to an approximate value of 26%.

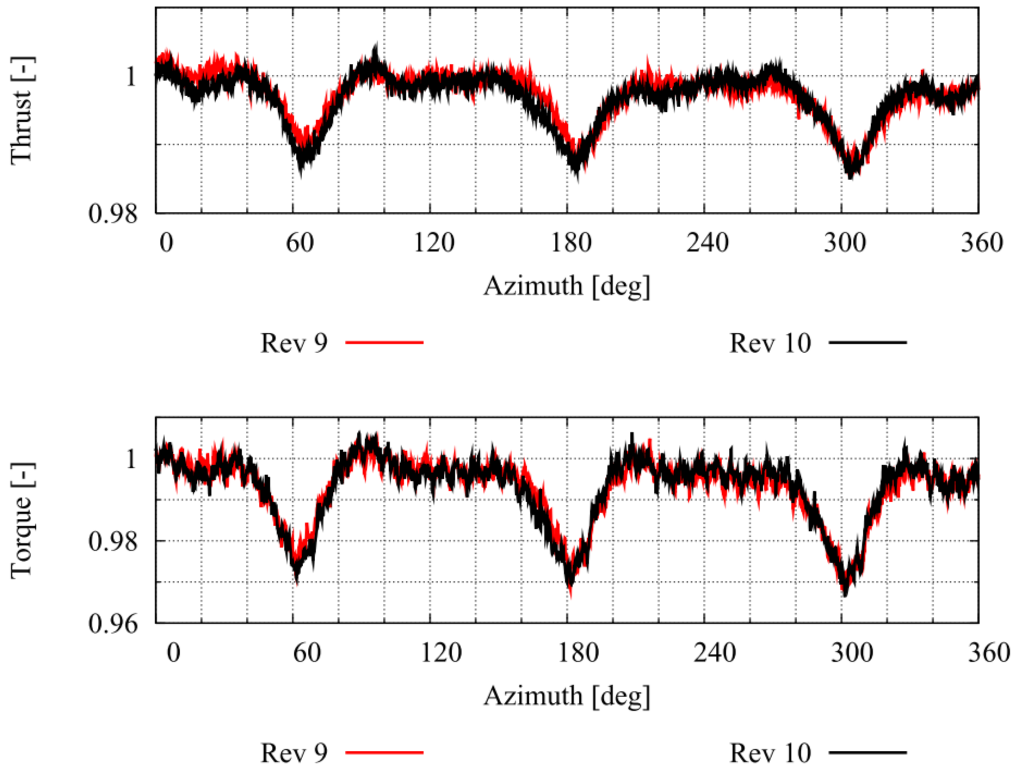

Figure 2.15: Normalized rotor thrust and torque for the last two revolutions of a simulation of the SIEMENS 3.6MW wind turbine [source: Zahle and Sørensen (2008)]

The authors attributed this discrepancy to the inability of RANS models to properly predict stall, in particular at the blade span region equipped with thick airfoils. When analyzing URANS results, important vortex shedding was identified at low blade span range. With this approach, the discrepancy in the predicted mechanical power was found to be even higher than the one computed with RANS.

Next generation HAWTs

Over the past few years, a continuous upscaling of new HAWT rotor diameters has been observed [UpWind Consortium (2011)]. To provide the research community with a representative design of current and near-future big rotor HAWTs, several *reference* wind turbine models have been recently proposed. The first effort in this line was the *Sandia 100-m all-glass baseline blade model* SNL-100-00, a 100 m long blade design published by *Sandia National Laboratories* [Griffith and Ashwill (2011)]. The SNL-100-00 was designed to provide 13.2 MW when being installed in a 3-bladed rotor. A structural model description based on composite materials is also included in the definition document. Corson et al. (2012) performed a numerical analysis in order to study the static and dynamic aeroelasticity of this blade. Both RANS and DES methods were employed, using the commercial unstructured solver AcuSolve, developed by Altair [ACUSIM (2009)]. Important mean blade deflections were computed in static conditions, with a maximum out-of-plane tip deflection of 5.5 m. The performed dynamic simulations aimed to characterize the *flutter* phenomenon on this blade, but no aeroelastic instability could be captured.

Recently, Bak et al. (2013) have presented a complete *reference* wind turbine representative of next generation machines. This model, created from a collaboration between *DTU Wind Energy* and *Vestas*, is referred to as the DTU 10MW RWT. A special attention was put in blade design optimization, in order to increase the stiffness and global rotor performance based on aerodynamic, aero-servo-elastic and structural considerations. The complete geometrical and structural characteristics of this HAWT have been been made publicly available from the site https://dtu-10mw-rwt.vindenergi.dtu.dk, including the blades, the nacelle and the tower for an onshore configuration. Zahle et al. (2014) provided a complete aerodynamic characterization of this machine in a *rotor-only* configuration, using the Ellypsis3D solver. RANS simulations of the whole machine operating range were performed. Results coming from a CFD computation at 10 m.s^{-1} and 8.06 RPM were used to recompute airfoil characteristic curves in a 3D framework. This airfoil data was injected in a BEM-based rotor model in order to evaluate the differences of this method performance with respect to the original 2D CFD based information. Clear improvements on BEM loads prediction capabilities were observed, especially at low span range, where the CFD computations revealed a highly three-dimensional flow (see Figure 2.16). In a second part of the study, the DES method was employed in an off-design operating point. This loadcase corresponded to standstill conditions, and it accounted for important flow misalignment in yaw. Vortex shedding was identified on the blade, having a direct impact on the predicted loads due to its spanwise correlation. This issue was identified by the authors as a potential cause of vortex-induced vibrations.

The DTU 10MW RWT was adopted as a common wind turbine for all the researches performed within the framework of the MAREWINT project. In the D5.4 deliverable [Leble et al. (2015)], the results of the HMB2 simulations performed by the University of Liverpool were compiled. Both *rigid* and *flexible* blades configurations were analyzed. The results of this work are discussed together with the findings of the present research in Section 5. In order to contextualize each of the aforementioned HAWTs, Table 2.3 compiles their main geometrical and operational parameters.

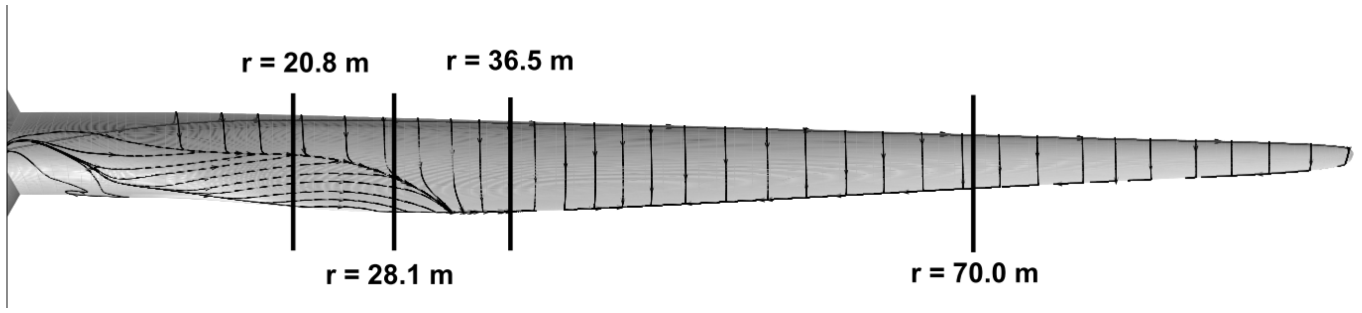

Figure 2.16: Friction streamlines of the DTU 10MW RWT blade suction surface at 10 m.s^{-1} and 8.06 RPM [source: Zahle et al. (2014)]

Table 2.3: Summary of horizontal wind turbines characteristics

	NREL Phase VI†	MEXICO	NREL 5MW	SIEMENS 3.6MW	NKT 500/41‡	SNL-100-00‡	DTU 10MW RWT
Manufacturer	Ref.	Ref.	Ref.	Siemens	Nordtank	Ref.	Ref.
Public experimental data	Yes	Yes	No	No	No	No	No
Number of blades	2	3	3	3	3	3	3
Rotor diameter [m]	10.06	4.5	126	107	41	200	178.3
Rated power [kW]	19.8	14.9	5000	3600	500	13200	10000
Hub height [m]	12.19	5.3	90	90	-	146.4	119
Tower diameter top [m]	0.41	0.5	3.87	3	-	-	5.5
Tower diameter base [m]	0.61	0.5	6	4.5	-	-	8.3
Distance blade tip/tower [m]	1.40	1.85	10.54	9	-	-	18.26

Ref. refers to *reference* wind turbines, not industrially exploited

†: NREL Phase VI parameters refer to the *S sequence* in an *upwind* configuration

‡: Tower not defined/Presented simulations did not include the tower in the computational domain

2.2 Overview of FINE™/Turbo solver

The developments and simulations performed within the scope of this PhD were based in the CFD package FINE™/Turbo [NUMECA International (2013b)]. In order to contextualize the capabilities of the solver prior to this research, a brief description is included in this section. The emphasis is put in the numerical methods concerned by unsteady aerodynamics and FSI analysis. References to previous solver validations concerning both topics are also included.

FINE™/Turbo solver is a three-dimensional, density-based, structured, multi-block finite volume code. The discretization in space is based on a cell centered control volume approach. Both upwind schemes and central schemes are available. The latter method is used in this research, in combination with with Jameson type artificial dissipation [Jameson et al. (1981)]. A four-stage explicit Runge-Kutta scheme is applied for the temporal discretization. Multigrid method [Brandt (1982)], local time-stepping and implicit residual smoothing [Zhu et al. (1993)] are used in order to speed-up the convergence for steady computations.

2.2.1 Unsteady computations

In FINE™/Turbo solver, time marching unsteady computations are performed using the dual time steeping approach described in Jameson (1991). For complex geometries, the required computational time in order to perform this type of simulations is often difficult to fit in an industrial work-flow. This is the reason why an alternative and less costly methodology was implemented. The *Non-linear Harmonic* (NLH) approach, introduced by He and Ning (1998) and industrialized by Vilmin et al. (2006), allows to drastically reduce the required computational time. In the NLH method, the instantaneous conservative flow variables $U = (\rho, \rho v_x, \rho v_y, \rho v_z, \rho E)$ are decomposed into a time-averaged value $\bar{U}$ and a sum of unsteady perturbations U'_n, assumed to be periodic:

$$U(\vec{x},t) = \bar{U}(\vec{x}) + \sum_n U'_n(\vec{x},t) \ , \tag{2.18}$$

A Fourier decomposition is applied to each of the periodic perturbations. Hence, the perturbation U'_n can be written as a finite sum of N_h time harmonics:

$$U'_n(\vec{x},t) = \sum_{k=1}^{N_h} \left[\tilde{U}_k(\vec{x})\, e^{Ik\omega t} + \tilde{U}_{-k}(\vec{x})\, e^{-Ik\omega t}\right] = 2\sum_{k=1}^{N_h} \left[\tilde{U}^k_{Re} cos(k\omega t) - \tilde{U}^k_{Im} sin(k\omega t)\right] \ , \tag{2.19}$$

where the harmonic amplitudes $\tilde{U}_k$ and $\tilde{U}_{-k}$ are complex conjugates defined by the real part $\tilde{U}^k_{Re}$ and the imaginary part $\tilde{U}^k_{Im}$ and related to the n^{th} perturbation. For the particular case of rotating machinery applications the fundamental harmonic, corresponding to $k = 1$, is associated to the so-called *Blade Passing Frequency* (BPF).

The NLH formulation is obtained by introducing this variable decomposition into the unsteady *Reynolds-Averaged Navier-Stokes* equations presented in Section 2.1.2. The resulting expression, that can be found in Appendix B together with a detailed derivation of the NLH method, is referred to as *decomposed Navier-Stokes equations* in this section. Two new sets of equations are then obtained, corresponding to the time-mean and harmonic contributions of every conservation law.

To derive the NLH mean equations, the time-averaged of the *decomposed Navier-Stokes equations* is considered. This procedure is similar to the Reynolds averaging summarized in Section 2.1.2, but in this case the unsteady perturbations are periodic and their magnitude is assumed to be more important than the turbulent fluctuations. The resulting expression can be written using a compact finite-volume formulation as follows:

$$\frac{\partial \bar{U}}{\partial \varsigma}\Omega + \sum_{\text{cell faces}} \left(\overline{\vec{F}_I} - \overline{\vec{F}_V}\right)\cdot\vec{S} = \bar{Q}\Omega\,, \tag{2.20}$$

with:

$$\overline{\vec{F}_I}\cdot\vec{S} = \begin{pmatrix} \overline{\rho\vec{v}}\vec{S} \\ \overline{\rho\vec{v}}\bar{v}_x\vec{S}+\bar{p}S_x \\ \overline{\rho\vec{v}}\bar{v}_y\vec{S}+\bar{p}S_y \\ \overline{\rho\vec{v}}\bar{v}_z\vec{S}+\bar{p}S_z \\ \overline{\rho H}\bar{\vec{v}}\vec{S} \end{pmatrix} + \begin{pmatrix} 0 \\ \overline{(\rho\vec{v})'\,v'_x}\vec{S} \\ \overline{(\rho\vec{v})'\,v'_y}\vec{S} \\ \overline{(\rho\vec{v})'\,v'_z}\vec{S} \\ \overline{(\rho H)'\,\vec{v}'}\vec{S} \end{pmatrix}\ ;\ \overline{\vec{F}_V}\cdot\vec{S} = \begin{pmatrix} 0 \\ \overline{\tau_{xx}}S_x+\overline{\tau_{xy}}S_y+\overline{\tau_{xz}}S_z \\ \overline{\tau_{xy}}S_x+\overline{\tau_{yy}}S_y+\overline{\tau_{yz}}S_z \\ \overline{\tau_{xz}}S_x+\overline{\tau_{yz}}S_y+\overline{\tau_{zz}}S_z \\ \bar{\boldsymbol{\tau}}\bar{\vec{v}}\vec{S}+\bar{\vec{q}}\vec{S} \end{pmatrix} + \begin{pmatrix} 0 \\ 0 \\ 0 \\ 0 \\ \overline{\boldsymbol{\tau}'\vec{v}'}\vec{S} \end{pmatrix} \tag{2.21}$$

where the second terms of $\overline{\vec{F}_I}\cdot\vec{S}$ and $\overline{\vec{F}_V}\cdot\vec{S}$ expressions correspond to the *deterministic stresses*. These are present due to the non-linearity of the formulation, as the *Reynolds stresses* appeared in the derivation of the RANS equations in Section 2.1.2. The role of the *deterministic stresses* is then to account for the contribution of the flow unsteadiness into the time-mean flow equations.

In the baseline formulation, the set of NLH harmonic equations is derived by retaining the first-order fluctuation terms of the *decomposed Navier-Stokes equations*. By casting into the frequency domain, a set of conservation laws is obtained for each harmonic. Using a compact finite-volume formulation as omitting the harmonic index, these can be written as follows:

$$\frac{\partial \widetilde{U}}{\partial \varsigma}\Omega + I\omega\widetilde{U}\Omega + \sum_{\text{cell faces}} \widetilde{\vec{F}}_I\cdot\vec{S} - \sum_{\text{cell faces}} \widetilde{\vec{F}}_V\cdot\vec{S} = \widetilde{Q}\Omega\,, \tag{2.22}$$

with:

$$\widetilde{\vec{F}_I} \cdot \vec{S} = \begin{pmatrix} \widetilde{\rho \vec{v}} \vec{S} \\ \overline{\rho \vec{v}} \tilde{v}_x \vec{S} + \widetilde{\rho \vec{v}} \bar{v}_x \vec{S} + \tilde{p} S_x \\ \overline{\rho \vec{v}} \tilde{v}_y \vec{S} + \widetilde{\rho \vec{v}} \bar{v}_y \vec{S} + \tilde{p} S_y \\ \overline{\rho \vec{v}} \tilde{v}_z \vec{S} + \widetilde{\rho \vec{v}} \bar{v}_z \vec{S} + \tilde{p} S_z \\ \widetilde{\rho H} \bar{\vec{v}} \vec{S} + \overline{\rho H} \widetilde{\vec{v}} \vec{S} \end{pmatrix} ; \ \widetilde{\vec{F}_V} \cdot \vec{S} = \begin{pmatrix} 0 \\ \widetilde{\tau_{xx}} S_x + \widetilde{\tau_{xy}} S_y + \widetilde{\tau_{xz}} S_z \\ \widetilde{\tau_{xy}} S_x + \widetilde{\tau_{yy}} S_y + \widetilde{\tau_{yz}} S_z \\ \widetilde{\tau_{xz}} S_x + \widetilde{\tau_{yz}} S_y + \widetilde{\tau_{zz}} S_z \\ \bar{\boldsymbol{\tau}} \widetilde{\vec{v}} \vec{S} + \widetilde{\boldsymbol{\tau}} \bar{\vec{v}} \vec{S} + \widetilde{\vec{q}} \vec{S} \end{pmatrix} \tag{2.23}$$

Recently, Debrabandere (2014) extended the baseline NLH formulation to the consideration of the interaction between the harmonics of the flow. This was achieved by removing the first-order linearization performed prior to the derivation of Equation 2.22. This enhancement introduced several crossing terms in the harmonic equations, aiming to capture high non-linearities of the flow. However a computational overhead was observed after this extension, reaching up to a factor two for traditional applications.

Being the starting point of the NLH method derivation the *Reynolds-Averaged Navier-Stokes* equations, both $\vec{q}$ and $\boldsymbol{\tau}$ contain stresses related to the turbulent effects that need of a closure model. In the NLH approach implemented in FINE™/Turbo solver, this is task is carried out by means of one of the following linear eddy viscosity turbulence models: Baldwin-Lomax, Spalart-Allmaras, k-ε, k-ω or k-ω SST. Both the laminar and eddy viscosities are computed based on the time-mean flow variables, assuming that they are unaffected by the unsteady fluctuations.

As for the RANS approach, the obtained harmonic equations are only space-dependent. The solution of the system is performed by the integration of the the pseudo-time ς, *via* the introduction of the derivatives $\frac{\partial \overline{U}}{\partial \varsigma}$ and $\frac{\partial \widetilde{U}}{\partial \varsigma}$. This transformation from time-dependent equations into steady ones justifies the computational time saving attributed to the NLH approach. In addition the NLH methodology applied to rotating machinery problems only requires the meshing of a single blade passage, while unsteady time marching computations usually need a full rotor and stator mesh. The NLH belongs to a family of techniques often referred as non-linear frequency methods. Other examples of these approaches are the Harmonic Balance [Hall et al. (2002)] and the Non-Linear Frequency Domain [McMullen (2003)].

2.2.2 Fluid solid interaction

Several developments aiming to extend FINE™/Turbo capabilities in order to deal with FSI problems in turbomachinery applications were performed in the PhD thesis of Debrabandere (2014). Three different methods were implemented, accounting for different approximations regarding the flow and structural models (see Table 2.4). A main distinction was made concerning the type of coupling between both physical models:

- **1-way coupling**: A prescribed deformation is applied to the structure, and a new flow solution is computed based on this new position.
- **2-way coupling**: In this integrated approach, a mutual interaction between the fluid and the structure is assumed. Structural deformation is first computed based on an initial flow solution. Since the updated position of the structure changes the flow properties, a new solution of the *Navier-Stokes equations* is required. This sequence is repeated in an iterative way, till the interaction between both physical models stabilizes.

Table 2.4: FINE™/Turbo methods for FSI computations

	Flow model	Structure model	Coupling
Method_CSM	Steady/Time marching	CSM	2-way coupling
Method_MOD	Steady/Time marching	Modal approach	1-way coupling/2-way coupling
Method_MODH	NLH	Modal approach	1-way coupling

The aim of *Method_CSM* and *Method_MOD* was to provide a 2-way coupling solution for steady and time marching computations. In the *Method_CSM* method, FINE™/Turbo was extended in order to perform FSI simulations in combination with a *Computational Structural Mechanics* (CSM) code. The coupling of both physics was ensured by exchanges of information performed by the MpCCI software, developed by Fraunhofer Institute for ALgorithms and Scientific Computing (SCAI) (2012). In *Method_MOD*, the structural model was simplified by means of the *modal approach*. As the mode shapes were defined on a FEM mesh, some interpolation issues between structure and fluid data may occur [see Fenwick and Allen (2007)]. In order to avoid this, the mode shapes were interpolated onto the fluid mesh prior to the coupled computation as suggested by Sayma et al. (2000). The objective of *Method_MODH* was to provide a 1-way coupling solution for the NLH solver. The structural deformation was prescribed *via* an adaptation of the modal basis of *Method_MOD* in order to work in the harmonic domain. More details about *Method_MODH* are included in Chapter 4. In order to deal with the unsteady time evolution of the fluid mesh deformation, all the aforementioned methods required the adaptation of the solver formulation to an Arbitrary Lagrangian-Eulerian (ALE) framework [Hughes et al. (1981)]. In addition, a mesh deformation approach based on the radial basis functions was developed. This algorithm was first implemented in a steady/time marching context, and then adapted to a harmonic formulation to be used in *Method_MODH*.

2.2.3 Relevant solver validations

The validation of FINE™/Turbo capabilities for HAWTs analysis was previously assessed by other authors, mainly based on the NREL Phase VI *reference* model. In all these publications, *rotor-only* RANS simulations were performed and compared against experimental data (see Appendix A for more details of the numerical set-up). First complete validation was performed by Fan and Kang (2009). A good agreement with experimental results was found for both Spalart-Almaras and k-ω SST turbulence models. A better converge was observed for the latter model when assessing operating points where large separation occurred. The authors also pointed out the necessity of accounting for the nacelle geometry in order to obtain accurate results. The work of Elfarra et al. (2014) aimed to design an optimize a winglet geometry installed at the NREL Phase VI blade tip. An initial validation of FINE™/Turbo capabilities was also performed. A good agreement with experimental data was found for the whole operating range. For the particular case of the 15 m.s^{-1} (*deep-stall* region), important tangential forces discrepancies with respect to the experimental results were observed. These were assumed to be related to either experimental or numerical causes. Indeed, the authors argued that an important measurement error should be considered for the tangential loads, due to its relative low value with respect to the normal loads and to the sparseness of the blade pressure taps. Additionally, the complete flow separation experienced by the blade at this operating point could be limiting for the capabilities of the used turbulence model. The final winglet design proposed by the authors predicted an increase in the mechanical power of around 9%. A more recent validation was described in the works of Suárez and Doerffer (2015) and Suárez et al. (2015). Very small discrepancies with respect to experimental data were computed for low (*pre-stall*) and high (*deep-stall*) wind speeds. Blade separation and rotor wake were also accurately modeled for the mentioned conditions. For the particular case of the 10 m.s^{-1} operating point (*transitional case*) important differences were found, probably due to the fully turbulent nature of the model used. Figure 2.17 compiles the rotor power computed in the aforementioned simulations, where the dispersion of the results for wind speed higher than 10 m.s^{-1} is clearly observed. As pointed out by Fan and Kang (2009), these differences could be explained by the sensitivity of the numerical model to the CFD domain, the mesh and the turbulence model.

The NLH method was validated for a wide range of turbomachinery applications. Johann and Swoboda (2007) studied a 4.5-stage high-speed compressor. The NLH modeling capabilities regarding blade rows interaction was highlighted, as well as its computational efficiency. Kunzelmann et al. (2011) applied the NLH method in a 1.5-stage low-speed compressor. Simulations were able to predict the beneficial effects of air injection observed in the experiments. Crosh et al. (2011) presented a validation of a turbine (including the casing), where NLH computations were able to reproduce the blade surface pressure variations obtained experimentally. Comparisons between NLH and classical time marching unsteady solutions were also performed for compressors [Guidotti and Turner (2009); Hembera et al. (2009)] and turbines [Crosh et al. (2009); Green et al. (2012); Nordwall et al. (2008)]. Good

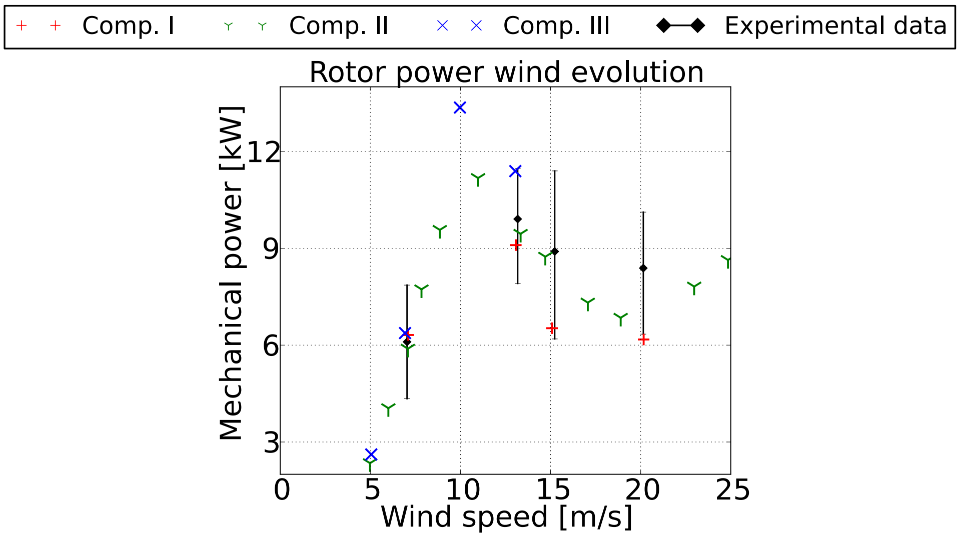

Figure 2.17: Total mechanical power of the NREL Phase VI computed by previous *rotor-only* FINE™/Turbo simulations. Comp. I: Fan and Kang (2009), Comp. II: Elfarra et al. (2014), Comp. III: Suárez and Doerffer (2015). Experimental results account for the considered error bars

comparisons between both approaches were obtained, with considerable computational savings attributed to the NLH approach (ranging from one to two orders of magnitude). In order to exemplify the level of agreement of NLH and time marching simulations, Figure 2.18 depicts the normalized static pressure fluctuations on a high-pressure turbine computed by Crosh et al. (2009). In this particular validation, a time saving factor of 10 could be attributed to the NLH method. Validations of the FSI methodology were included in Debrabandere

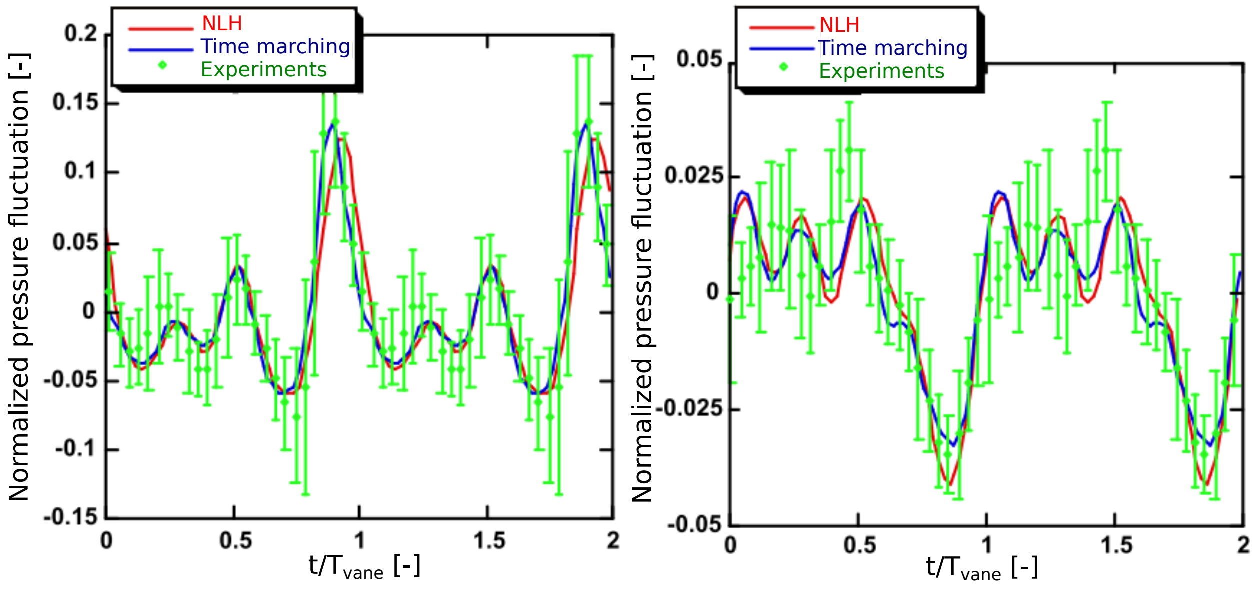

(a) Suction surface **(b)** Pressure surface

Figure 2.18: Normalized static pressure fluctuations transient for a high-pressure turbine, computed with both NLH and time marching methods. Results are compared with experimental data. Source: Crosh et al. (2009)

(2014). The flutter boundary of the AGARD 445.6 wing was studied using *Method_MOD*. Computed results were validated against the experimental data compiled in Yates (1987). *Method_MODH* was used in a flutter investigation of the turbine cascade STFC 11 [Fransson et al. (1999)]. A very good agreement with experimental results was found for the design flow conditions.

2.3 PhD objectives and outline

2.3.1 Objectives

An accurate rotor loads prediction is essential in order to design a HAWT. To reduce the overall costs, the loads estimation at preliminary design phases relies in the virtual prototyping of the machine. For classical wind turbines, simplified engineering methods offer a very good computational efficiency and an acceptable accuracy in the flow prediction. As pointed out by the literature survey, the precision of these approaches is however limited when dealing with big HAWT rotors due to the existence of highly skewed flows, heavy detachments and important blade deflections due to FSI. Hence, the use of more sophisticated *Computational Fluid Dynamics* (CFD) techniques is justified. The introduction of CFD in the wind energy industry is currently facing an important bottleneck: the required engineering and computational time. This last remark brings to the main goal of this PhD research. The CFD package FINE™/Turbo, traditionally used for turbomachinery applications, was extended in order to perform high fidelity HAWT rotor flow analysis at a reduced computational time. In particular, two challenging problems were tackled: the *rotor aeroelasticity* and the *rotor-tower interactions*. While the former issue requires the consideration of blade flexibility in FSI simulations, the introduction of the tower in the computational domain needs of an unsteady flow solution. The permutation of both problems leads to the four types of simulations studied in this work (Table 2.5). To illustrate the performance of the developed solutions, the DTU 10MW RWT reference wind turbine was studied. The expertise issued from this analysis was compiled as set of advices, aiming to guide the use of the developed methodology in future work.

Table 2.5: Relation between numerical models and type of simulations studied in this research

		Flow model	
		Steady	**Unsteady**
Blade model	**Rigid**	Steady aerodynamics	Unsteady aerodynamics
	Flexible	Static aeroelasticity	Dynamic aeroelasticity

RANS methodology was applied for steady flow computations. Regarding unsteady solutions, the use of the NLH approach was considered for the first time in the framework of HAWT analysis. Both technologies correspond to an improvement of the current wind energy standard tools. At the same time, they are computationally less expensive than other CFD approaches implying the partial or complete resolution of the turbulence spectrum (see Figure 2.19). Spalart-Allmaras turbulence model was used in all the performed computations, chosen by its robustness and simplicity [Spalart and Allmaras (1992)]. The study of the influence of turbulence and transition modeling is out of the scope of this work.

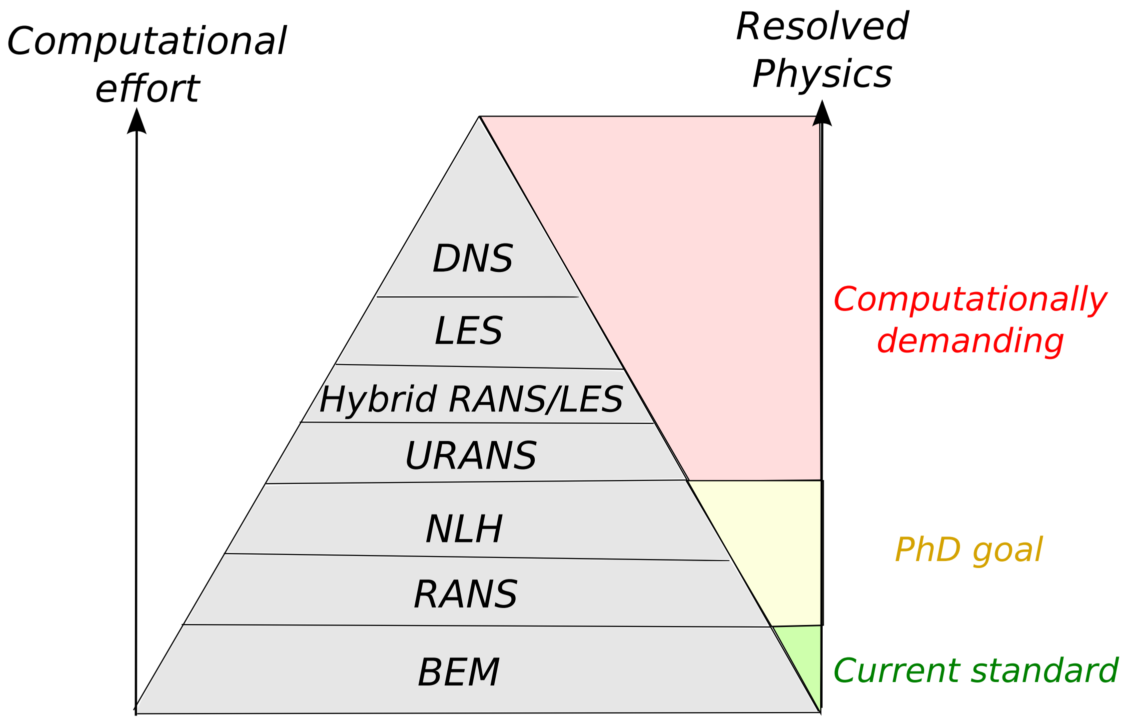

Figure 2.19: Classification of numerical approaches for HAWT rotor loads prediction regarding their computational cost and flow physics modeling capabilities. Adapted from Sagaut et al. (2006)

The assessment of *rotor aeroelasticity* requires the consideration of the blade flexibility. In order to reduce the required computational time of FSI simulations, blade structure was modeled by means of a *Reduced Order Model* (ROM) based on the modal approach. *Static aeroelasticity* was studied by performing 2-way coupling computations with a steady flow formulation. The impact of loads distribution on the blade deflection and the final rotor performance was analyzed. *Dynamic aeroelasticity* was studied by means of an innovative 2-way coupling methodology based on the NLH approach. The aim was to study the effects of dynamic loading on rotor loads and harmonic blade deflections. The analysis of aeroelastic instabilities is out of the scope of this research.

2.3.2 Outline

Even if FINE™/Turbo is already consolidated as a standard in the *turbomachinery* industry, its adaptation to the study of HAWTs requires of additional implementations. In particular, two new developments regarding the *aeroelastic* capabilities of the solver were performed:

- **Improvement of mesh deformation algorithms:** To account for FSI phenomena, the discretized fluid domain needs to be re-adapted to structural deformations, motivating the application of *mesh deformation algorithms*. Strong requirements need to be considered when dealing with the important blade deflections expected for big rotor HAWTs. An efficient *hybrid mesh deformation* algorithm was developed within the framework of this research and described in Chapter 3.

- **2-way coupling harmonic aeroelasticity:** When performing a FSI simulation, blade deformations can be either imposed (1-way coupling) or computed based on the aerodynamic loading (2-way coupling). The implementation of the latter option into the harmonic solver of FINE™/Turbo for its application in HAWT dynamic aeroelasticity analysis is detailed in Chapter 4.

Together with preliminary test cases, the performance of both developments was assessed when being applied to the analysis of the DTU 10MW RWT. The study of this wind turbine is split in two chapters:

- **Rotor-only simulations:** In Chapter 5, the DTU 10MW rotor is analyzed assuming a steady flow relative to the rotor, as well as uniform upstream conditions. In a first approach, rotor blades were considered as *rigid*. In a second step, the implemented *hybrid mesh deformation* method was applied in order to study the static aeroelasticity of the rotor.

- **Full machine simulations:** A set of computations were performed accounting also for the DTU 10MW RWT tower, and included in Chapter 6. In order to properly capture the *rotor-tower interaction* effects, high fidelity unsteady computations were required. As for the isolated rotor configuration, both *rigid* and *flexible* simulations were carried out. For the latter case, the use of all the new developments performed within the framework of this research was needed.

Finally Chapter 7 compiles the main conclusions extracted from this PhD work, along with suggested future work.

Chapter 3

Development of a mesh deformation tool for external aerodynamics applications

In the context of *Fluid-Structures Interaction* (FSI) simulations based on *body-fitted* mesh approaches, the re-adaptation of the fluid mesh following structural deflections is required at every time-step. In order to avoid the computational time and implementation problems attached to a re-meshing process, the so-called *mesh deformation* algorithms have become a popular alternative for most of applications. In terms of *mesh deformation*, the requirements of big rotor HAWTs aeroelastic analysis were away from the capabilities of FINE™/Turbo prior to this PhD work. Indeed, the deformation magnitude to consider in wind energy with respect to the classical *flutter* phenomenon found in turbomachinery field is completely different. Table 3.1 illustrates this fact, by comparing the deflections at the nominal operating points for:

- DTU 10-MW wind turbine [Bak et al. (2013)]: static conditions results issued from this research and included in Section 5
- STCF-11 axial turbine [Fransson et al. (1999)]: results from Debrabandere (2014)

Table 3.1: Comparison of aeroelastic deflections in turbomachinery and wind energy industries. Number of mesh nodes refer to a single blade passage

Parameter	**STCF-11**	**DTU 10-MW**
Number of mesh nodes	2.8×10^5	7.2×10^6
Chord at tip (c)	59 mm	0.6 m
Tip displacement (d)	3.3×10^{-2} mm	7.74 m
Ratio d/c	6.66×10^{-3}	12.9

In addition, the number of mesh nodes typically needed for a wind turbine simulation is considerably higher than the meshes used in turbomachinery. In this chapter, a set of new developments regarding the adaptation of FINE™/Turbo *mesh deformation* methods to this new aeroelastic scenario is presented. As it will be shown, there is always a trade-off between obtained deformed mesh quality and the computational cost attached to every method. Since this trade-off is usually highly affected by the considered application, it uses to drive the choice of the *mesh deformation* method. The numerical context expected for *Horizontal Axis Wind Turbine* (HAWT) rotors deformation can be characterized as:

- Dealing with structured, multi-block and multi-grid meshes (requirements directly coming from FINE™/Turbo)
- External aerodynamics application
- Accounting for multi-million meshes
- Possible existence of *boundary layer* meshes (important near-wall nodes clustering)
- Large displacements and rotations are expected in the blade deflection
- Blade geometry accounting for sharp edges (at the tip and the trailing edge)

3.1 Mesh quality criteria

The role of the *mesh deformation* algorithms is to re-adapt the mesh of the CFD domain to new boundaries displacement without modifying its quality. Hence, it is important to define some qualitative quality criteria *prior* to the description of the methods. In this research, discussions about the mesh quality will be based on the parameters computed by NUMECA International software. Since their definition can vary with respect to other software, they are introduced in this section.

The *orthogonality* (OR) is a criterion ranging from 0 deg to 90 deg that measures the minimum angle between the edges of every cell. When the angle between two edges is greater than 90 deg, the supplementary angle is taken. The *aspect ratio* (AR) is a quality criterion that aims to measure the differences in the edges length for a given cell face (see Figure 3.1a). The best case scenario occurs when all the edges of a face do have the same length, corresponding to an aspect ratio of 1. Finally, the *expansion ratio* (ER) is a criterion that estimates the size variation between every two adjacent cells of a given mesh direction (see Figure 3.1b). As for the aspect ratio, the optimum expansion ratio corresponds to 1. It is not simple to state which are the values of these criteria that ensure a *good quality* mesh, since there is a strong dependence with the targeted application and the CFD solver to be used. As a general rule, a mesh built for industrial purposes can be considered as acceptable when the minimum orthogonality is higher that 15 deg, the maximum aspect ratio is below 5000 and the expansion ratio is smaller than 3. However, there is always a trade-off between the number of grid points and the mesh quality, that is especially constraining for large problems (as most part of external aerodynamics applications). In particular, the maximum aspect ratio for these configurations when using a structured mesh solver use to go above 5000 at the vicinity of the boundary layer. This local deterioration of the mesh quality is assumed to be acceptable since at the boundary layer the gradients in the streamwise direction are relatively small when compared to the transverse gradients.

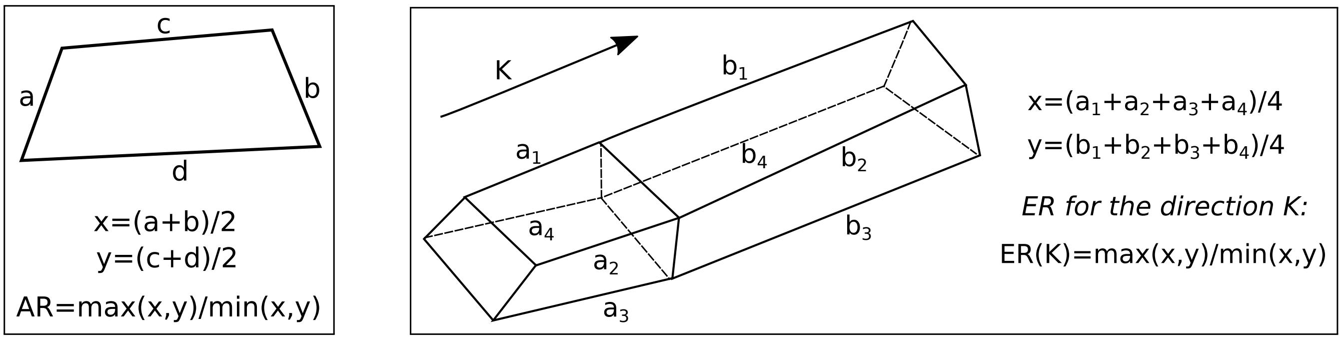

(a) Aspect ratio (AR) **(b)** Expansion ratio (ER)

Figure 3.1: Definition of the mesh quality criteria used in this research

3.2 Base test case

The performance of each mesh deformation method is illustrated through a simple application in following sections. For this purpose, the two-dimensional *Vortex Induced Vibrations* (VIV) test case [Hübner et al. (2004)] was considered. This model established a simplified numerical scenario to test the presented mesh deformation algorithms, and it accounted for large displacements and rotations. The existence of sharp edges and boundary layer clustering was also found to be very constraining, as it is shown further on in this document.

A mesh accounting for 1.2×10^5 nodes and 6 blocks was used, based on previous works of Debrabandere (2014). A first cell of 2.0×10^{-6} m thickness was imposed along the walls, to ensure a proper boundary layer capture. Figure 3.2 illustrates the original considered mesh. In order to impose a geometrical deflection, the 1-way coupling modal approach developed by Debrabandere (2014) and described in Section 2.2.2 was employed. The modal shapes and eigen frequencies of the beam, compiled also in the PhD work of Debrabandere (2014), were used in order to linearize the structure behavior. In particular, a significant deflection was imposed based on the first bending mode. The resulting deformed beam, illustrated in Figure 3.3, is representative of the maximum deflection computed during the VIV analysis performed in the aforementioned PhD work.

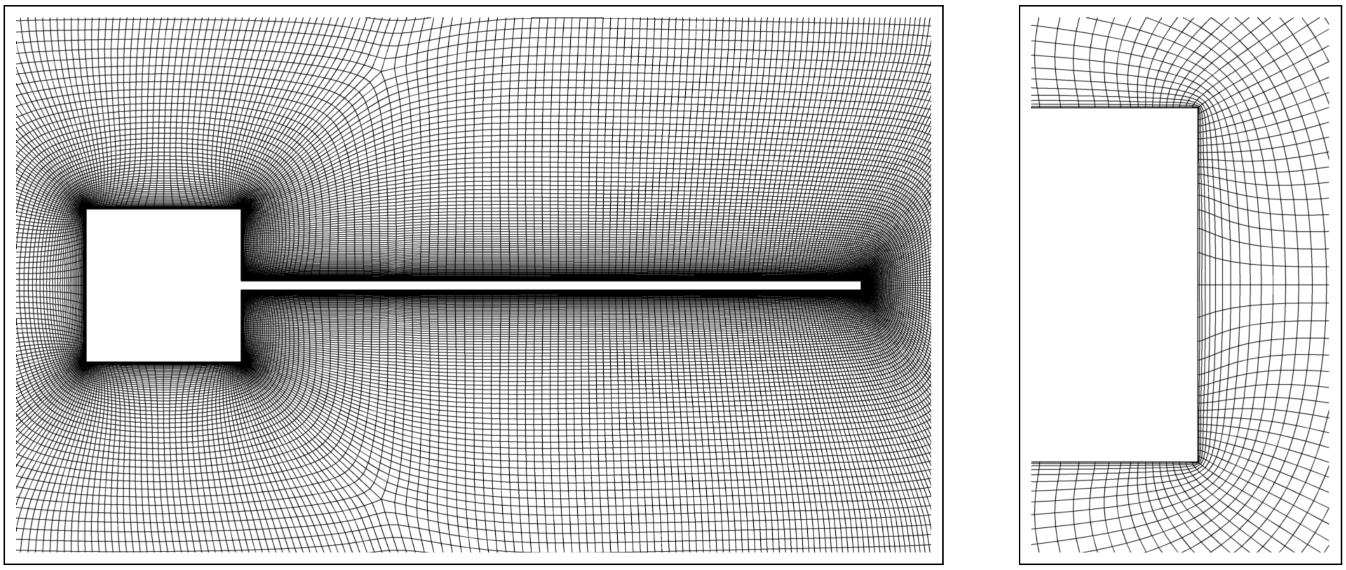

(a) Global view **(b)** Beam tip detail

Figure 3.2: VIV test case, original mesh

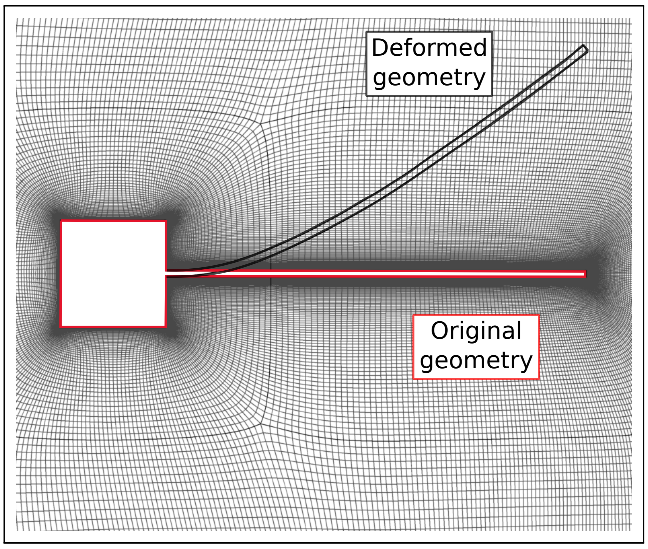

Figure 3.3: VIV test case, original and deformed geometries

3.3 Existing mesh deformation algorithms

Several mesh deformation tools were already present in FINE™/Turbo prior to this research [NUMECA International (2013b)]. In particular, a point-by-point scheme based on *Radial basis function* (RBF) interpolation has been proved as a robust and high quality tool for a wide variety of applications [De Boer et al. (2007)]. The RBF method uses the displacement of the boundary nodes in order to construct an interpolation function $f(\vec{x}_{ref})$ as a sum of *Radial Basis Functions*:

$$\vec{x} = \vec{x}_{ref} + f(\vec{x}_{ref}) = \vec{x}_{ref} + \sum_{b=1}^{n_b} \alpha_b \phi \left(\| \vec{x}_{ref} - \vec{x}_{ref,b} \| \right) + p\left(\vec{x}_{ref}\right) \,, \tag{3.1}$$

with:

- $\vec{x}$ the deformed mesh node position
- $\vec{x}_{ref}$ the original mesh node position
- $\vec{x}_{ref,b}$ the original mesh position of boundary node b
- n_b the total number of boundary nodes
- α_b interpolation coefficients
- ϕ the *Radial Basis Function* (in this case, *Thin Plate spline*)
- $p(\vec{x}_{ref})$ a first order polynomial

The interpolation coefficients α_b are computed based on the displacements of the boundary nodes:

$$\begin{pmatrix} \mathbf{F} & \mathbf{P} \\ \mathbf{P}^T & 0 \end{pmatrix} \begin{pmatrix} \boldsymbol{\alpha} \\ \boldsymbol{\beta} \end{pmatrix} = \begin{pmatrix} \mathbf{\Delta x_b} \\ 0 \end{pmatrix} \tag{3.2}$$

with:

- $\mathbf{F}$ the matrix of RBF evaluated at the boundary nodes
- $\mathbf{P}$ the matrix of the polynomials evaluated at the boundary nodes
- $\boldsymbol{\alpha}$ the vector of interpolation coefficients
- $\boldsymbol{\beta}$ the vector of the polynomial $p(\vec{x})$ coefficients
- $\mathbf{\Delta x_b}$ the vector of the displacements of the boundary nodes $\vec{x_b} - \vec{x_{ref,b}}$

The solution of the linear system of Equation 3.2 is usually performed in FINE™/Turbo *via* the inversion of the coefficients matrix. Figure 3.4 illustrates the performance of the presented RBF approach when dealing with imposed large displacements in the VIV test case (see Section 3.2). A very good mesh quality of the deformed mesh was observed. The RBF method is however limited by its scalability. As stated by Bos et al. (2013), the cost of calculation of the interpolation coefficients scales with $\mathcal{O}(\mathrm{n_b}^3)$ and the new coordinates evaluation with $\mathcal{O}(\mathrm{n_b n_i})$, where $\mathrm{n_i}$ is the number of inner mesh nodes and $\mathrm{n_b}$ the number of boundary mesh nodes. This is the reason why it is hardly applicable to multi-million three-dimensional meshes. Prior to this PhD work, the only alternative of the solver when dealing with big industrial meshes in external aerodynamics applications was the so-called *Laplacian*

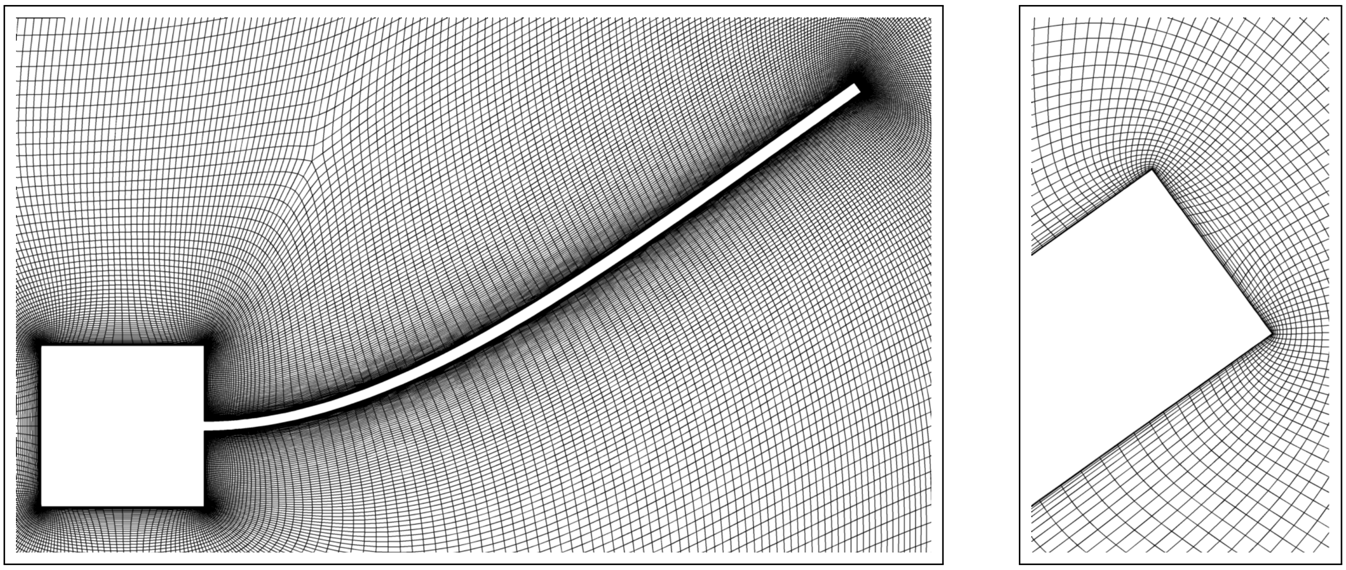

(a) Global view **(b)** Beam tip detail

Figure 3.4: VIV Test Case, *Radial Basis Functions* deformation

smoothing [NUMECA International (2013b)]. With this method, new mesh nodes position are calculated by solving the linear system:

$$\vec{\nabla} \cdot \left(\omega \vec{\nabla}\left(\vec{x}-\vec{x}_{ref}\right)\right) = 0 \, , \tag{3.3}$$

where ω is a local diffusivity factor aiming to preserve the final mesh quality by limiting the deformation of small volume cells.

This method shows a very good scalability with respect to the number of mesh nodes. However and even if the diffusion process is controlled by ω, the limitations of the *Laplacian smoothing* when dealing with large displacements have been extensively described in the literature [Arabi et al. (2012); Hermansson and Hansbo (2003); Karman Jr. (2010)]. In particular the mesh folding is often observed around concave regions as illustrated in Figure 3.5, where the same views of Figure 3.4 were kept. This mesh folding involves the existence of the so-called *negative volume cells* (i.e. one or several edges intersect an opposite face), that can lead to erroneous solutions or to the divergence of the CFD solver.

3.4 Development of an Inverse Elliptic Smoother

In the context of HAWTs rotor blades, two important constraints from the *mesh deformation* point of view are converging:

- *Multi-million nodes, external aerodynamics meshes*: An important number of boundary nodes are expected, decreasing the efficiency of interpolation-based techniques

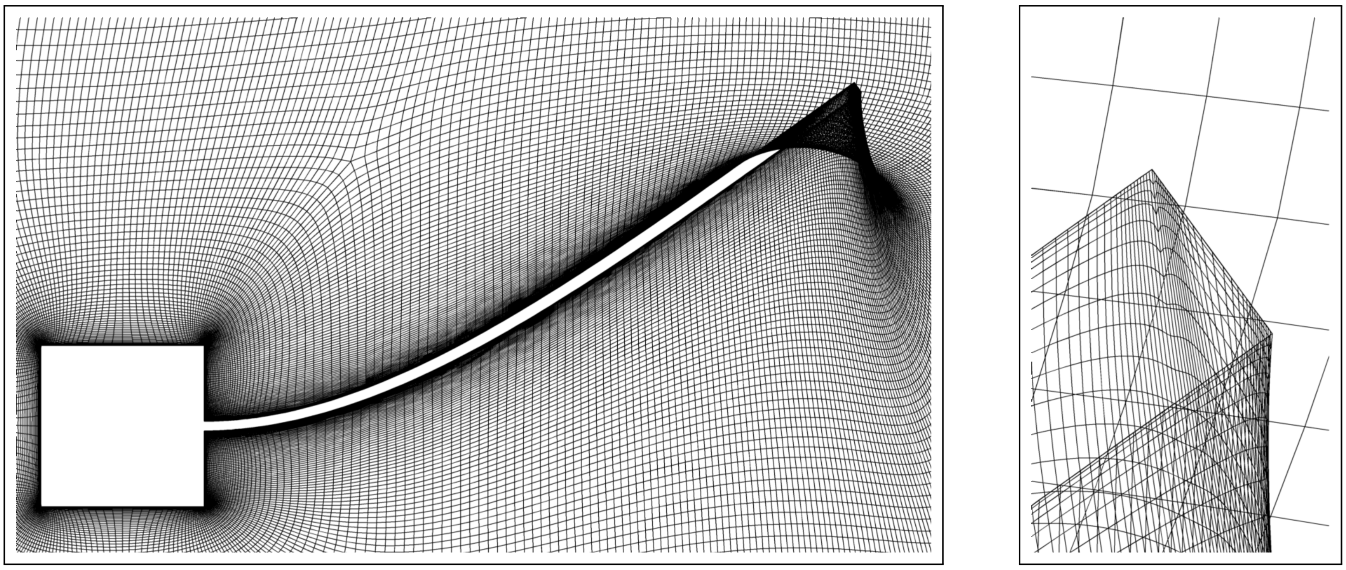
(a) Global view **(b)** Beam tip detail

Figure 3.5: VIV Test Case, *Laplacian Smoothing* deformation

- *Large blade deflections including sharp edges*: Requiring the use of accurate tools in order to avoid mesh folding

This combined numerical scenario does not correspond to the one found in *turbomachinery*, the historical application of FINE™/Turbo. First experiences showed that RBF had a prohibitive cost when applied to HAWT rotors FSI predictions, while the *Laplacian smoothing* could not avoid mesh folding around the blade. The development of a fast and robust method for HAWTs rotor blades *mesh deformation* was then necessary. A connectivity-based approach was chosen from the very beginning, in order to profit from its good scalability properties. In this context, the performance of the already existing *Laplacian smoother* tried to be improved by moving to a formulation based on an *inverse mapping*. This section describes the implemented model and its performance.

3.4.1 Base model

Inspired in the coordinates mapping techniques used in *grid generation*, a curvilinear form of the *Laplacian Smoothing* (Equation 3.3) was obtained. The main philosophy of this technique is the expression of the original problem in physical coordinates (x, y, z) to logical/computational ones (ξ, η, ζ). As stated by Karman Jr. (2010), the solution of the elliptic operator *via* a direct mapping in the computational space leads to possible grid crossing, due to the lack of cross derivative terms:

$$\Delta x = \frac{\partial^2 x}{\partial \xi^2} + \frac{\partial^2 x}{\partial \eta^2} + \frac{\partial^2 x}{\partial \zeta^2} = 0\,, \tag{3.4}$$

$$\Delta y = \frac{\partial^2 y}{\partial \xi^2} + \frac{\partial^2 y}{\partial \eta^2} + \frac{\partial^2 y}{\partial \zeta^2} = 0\,, \tag{3.5}$$

$$\Delta z = \frac{\partial^2 z}{\partial \xi^2} + \frac{\partial^2 z}{\partial \eta^2} + \frac{\partial^2 z}{\partial \zeta^2} = 0\,, \tag{3.6}$$

A so-called *inverse mapping* becomes more interesting from the numerical point of view:

$$\Delta \xi = \frac{\partial^2 \xi}{\partial x^2} + \frac{\partial^2 \xi}{\partial y^2} + \frac{\partial^2 \xi}{\partial z^2} = 0\,, \tag{3.7}$$

$$\Delta \eta = \frac{\partial^2 \eta}{\partial x^2} + \frac{\partial^2 \eta}{\partial y^2} + \frac{\partial^2 \eta}{\partial z^2} = 0\,, \tag{3.8}$$

$$\Delta \zeta = \frac{\partial^2 \zeta}{\partial x^2} + \frac{\partial^2 \zeta}{\partial y^2} + \frac{\partial^2 \zeta}{\partial z^2} = 0\,, \tag{3.9}$$

Figure 3.6 illustrates graphically the aimed coordinates transformation. It should be remarked that one of the advantages of the computational domain is that, in addition to the *Cartesian* topology of the mesh, an homogeneous mesh size is also considered. This numerical property becomes very interesting in order to simplify the involved quantities derivatives.

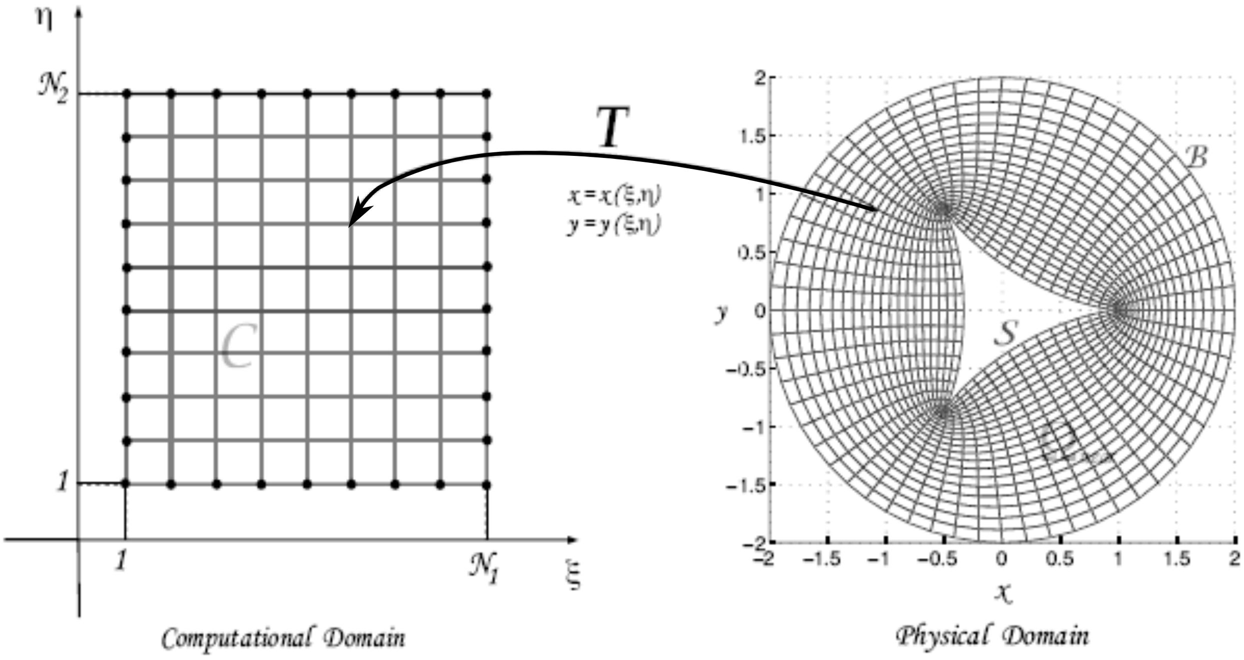

Figure 3.6: Inverse curvilinear transformation overview [source: Acosta and Acosta (2015)]

Let approach Equation 3.7 in its two-dimensional form in order to evaluate the capabilities of this methodology in a simplified numerical scenario:

$$\frac{\partial^2 \xi}{\partial x^2} + \frac{\partial^2 \xi}{\partial y^2} = 0\,, \tag{3.10}$$

$$\frac{\partial^2 \eta}{\partial x^2} + \frac{\partial^2 \eta}{\partial y^2} = 0\,, \tag{3.11}$$

Assuming $x = x(\xi,\eta)$ and $y = y(\xi,\eta)$, the chain derivative rule can be applied to Equation 3.10 in order to get:

$$\beta_1 \frac{\partial^2 x}{\partial \xi^2} + 2\beta_2 \frac{\partial^2 x}{\partial \xi \partial \eta} + \beta_3 \frac{\partial^2 x}{\partial \eta^2} = 0\,, \tag{3.12}$$

$$\beta_1 \frac{\partial^2 y}{\partial \xi^2} + 2\beta_2 \frac{\partial^2 y}{\partial \xi \partial \eta} + \beta_3 \frac{\partial^2 y}{\partial \eta^2} = 0\,, \tag{3.13}$$

with β_1, β_2, β_3 being:

$$\beta_1 = \left(\frac{\partial \xi}{\partial x}\right)^2 + \left(\frac{\partial \xi}{\partial y}\right)^2\,, \tag{3.14}$$

$$\beta_2 = \frac{\partial \xi}{\partial x}\frac{\partial \eta}{\partial x} + \frac{\partial \xi}{\partial y}\frac{\partial \eta}{\partial y}\,, \tag{3.15}$$

$$\beta_3 = \left(\frac{\partial \eta}{\partial x}\right)^2 + \left(\frac{\partial \eta}{\partial y}\right)^2\,, \tag{3.16}$$

In order to express the physical derivatives in terms of computational derivatives, it is interesting to consider the *Jacobian* of the transformation J:

$$J = |\mathbf{J}| = \begin{vmatrix} \frac{\partial x}{\partial \xi} & \frac{\partial x}{\partial \eta} \\ \frac{\partial y}{\partial \xi} & \frac{\partial y}{\partial \eta} \end{vmatrix} = \frac{\partial x}{\partial \xi}\frac{\partial y}{\partial \eta} - \frac{\partial x}{\partial \eta}\frac{\partial y}{\partial \xi}\,, \tag{3.17}$$

Indeed, by introducing Equation 3.17 into the definitions of β_1, β_2 and β_3, the following expression is obtained:

$$\beta_1 = \left(\frac{\partial \xi}{\partial x}\right)^2 + \left(\frac{\partial \xi}{\partial y}\right)^2 = J^2\gamma_1 = J^2\left[\left(\frac{\partial x}{\partial \xi}\right)^2 + \left(\frac{\partial x}{\partial \eta}\right)^2\right]\,, \tag{3.18}$$

$$\beta_2 = \frac{\partial \xi}{\partial x}\frac{\partial \eta}{\partial x} + \frac{\partial \xi}{\partial y}\frac{\partial \eta}{\partial y} = -J^2\gamma_2 = -J^2\left[\frac{\partial x}{\partial \xi}\frac{\partial y}{\partial \xi} + \frac{\partial x}{\partial \eta}\frac{\partial y}{\partial \eta}\right]\,, \tag{3.19}$$

$$\beta_3 = \left(\frac{\partial \eta}{\partial x}\right)^2 + \left(\frac{\partial \eta}{\partial y}\right)^2 = J^2\gamma_3 = J^2\left[\left(\frac{\partial y}{\partial \xi}\right)^2 + \left(\frac{\partial y}{\partial \eta}\right)^2\right]\,, \tag{3.20}$$

Under the hypothesis of $J \neq 0$, Equation 3.12 and Equation 3.13 can be then rewritten in terms of γ_1, γ_2 and γ_3 as:

$$\gamma_1 \frac{\partial^2 x}{\partial \xi^2} - 2\gamma_2 \frac{\partial^2 x}{\partial \xi \partial \eta} + \gamma_3 \frac{\partial^2 x}{\partial \eta^2} = 0\,, \tag{3.21}$$

$$\gamma_1 \frac{\partial^2 y}{\partial \xi^2} - 2\gamma_2 \frac{\partial^2 y}{\partial \xi \partial \eta} + \gamma_3 \frac{\partial^2 y}{\partial \eta^2} = 0\,, \tag{3.22}$$

Equation 3.21 and Equation 3.22 are known as the *Winslow equations*, and the coefficients γ_1, γ_2, and γ_3 are referred to as the *metric coefficients*.

3.4.2 Implementation details

A *linear system* based on Equation 3.21 and Equation 3.22 was built, based on the *finite differences* discretization accounting for centered stencils proposed by Karman Jr. (2010). For the system solution, a *Jacobi* solver based on *Richardson-Iteration* was implemented. Even if it is a simple solution technique, it allowed an easy parallelized implementation. Being the system to solve:

$$A\vec{x} = \vec{b}\,, \tag{3.23}$$

By defining D as the diagonal matrix of A, the update of the solution at every $k+1$ iteration depending on the preceding one can be written as:

$$\vec{x}^{k+1} = \psi D^{-1}(\vec{b} - A\vec{x}^{k}) + \vec{x}^{k}\,, \tag{3.24}$$

Where ψ is a factor <1.0 acting as an *under relaxation factor* of the solution process, and D^{-1} is the preconditioning of the matrix (*Jacobi* preconditioner).

The developed linear solver was enhanced with the following additional features in order to speed-up its convergence:

- **Multi-grid** solution: performed in different mesh *coarsening* levels, transferring their computed residuals at every iteration

- Parallelization based in a **Multi-block** approach: The solution of every block can be performed by a different processor. Residuals at block connections are averaged at every time step thanks to *Message Passage Interface* (MPI) techniques.

Dirichlet boundary conditions were used for both fixed and moving walls. In order to take into account the non-linearity of the system, $\gamma_1, \gamma_2, \gamma_3$ were recomputed at every iteration based on new node coordinates.

3.4.3 Base results

First experiences were devoted to confirm the potential of the new implemented *Winslow smoothing* when dealing with important imposed deflections. Let consider first a *Cartesian* homogeneous grid of 1x1 m where we apply an imposed motion by means of *Dirichlet* boundary conditions (Figure 3.7). Both *Laplacian* and *Winslow* smoothing operators were applied in order to compute the deformed mesh of this simple test case (see Section 3.3 and Section 3.4.1 respectively). The resulting deformed meshes are depicted in Figure 3.8. The existence of mesh folding shown in Figure 3.8a for the *Laplacian smoothing* is coherent with previous observations for the VIV test case (Figure 3.5). As stated before, this numerical limitation is related to the presence of sharp edges and highly concave regions. The spatial coupling introduced in the solution process of the *Winslow* smoother was able to avoid the existence of mesh folding, even if near-wall orthogonality was not kept (Figure 3.8b).

However, when passing to more complex deformation scenarios (accounting for two-dimensional deflections and rotations), the developed *Winslow smoother* was also very limited. Figure 3.9 shows an important mesh folding when considering the VIV test case of Section 3.2.

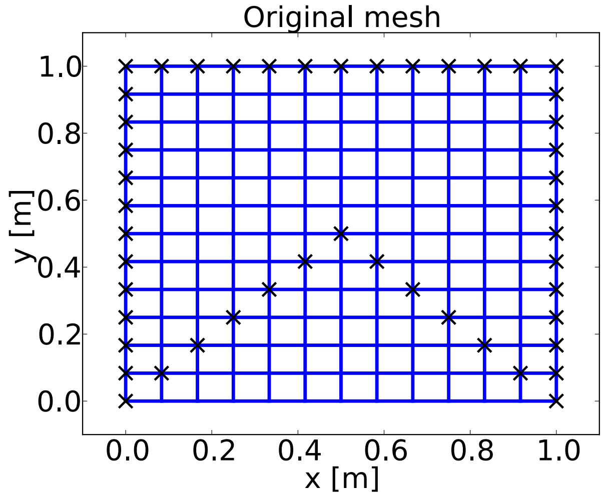

Figure 3.7: Original *Cartesian* mesh (in blue). Black crosses refer to the imposed displacements through Dirichlet boundary conditions

3.4.4 Model improvement: diffusion control

Analogously to the base *Laplacian smoother* of Equation 3.3, a local diffusion positive factor $\omega(x,y)$ was included in the *Inverse Elliptic operator*:

$$\vec{\nabla}\cdot(\omega\vec{\nabla}\xi)=0\,, \tag{3.25}$$

$$\vec{\nabla}\cdot(\omega\vec{\nabla}\eta)=0\,, \tag{3.26}$$

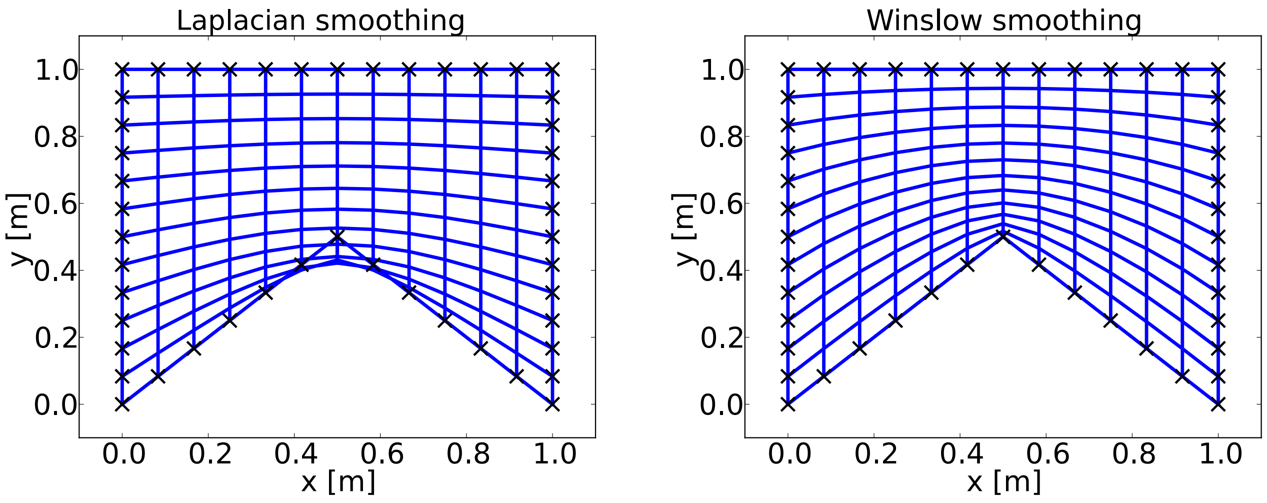

(a) Laplacian smoothing **(b)** Winslow smoothing

Figure 3.8: Deformed *Cartesian* homogeneous meshes. Crosses refer to imposed displacements

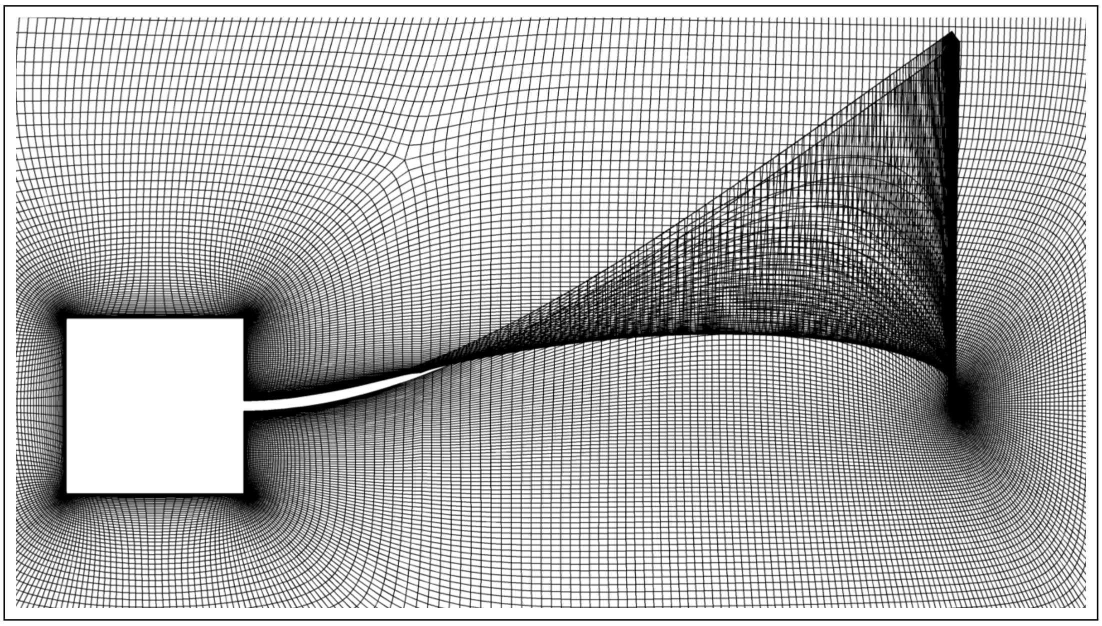

Figure 3.9: VIV test case, deformed mesh with *Winslow smoothing*

That can be written as:

$$\omega\Delta\xi + \frac{\partial\omega}{\partial x}\frac{\partial\xi}{\partial x} + \frac{\partial\omega}{\partial y}\frac{\partial\xi}{\partial y} = 0\,, \tag{3.27}$$

$$\omega\Delta\eta + \frac{\partial\omega}{\partial x}\frac{\partial\eta}{\partial x} + \frac{\partial\omega}{\partial y}\frac{\partial\eta}{\partial y} = 0\,, \tag{3.28}$$

Equation 3.27 corresponds to the inverse mapped form of the well known *Poisson equation*, established by Winslow (1981). Analogously to the derivation of the base model in Section 3.4.1, it can be further simplified under the hypothesis of $J \neq 0$ as:

$$\gamma_1 \frac{\partial^2 x}{\partial \xi^2} - 2\gamma_2 \frac{\partial^2 x}{\partial \xi \partial \eta} + \gamma_3 \frac{\partial^2 x}{\partial \eta^2} = -\frac{J}{\omega}\left(\frac{\partial \omega}{\partial \xi}\frac{\partial y}{\partial \eta} - \frac{\partial \omega}{\partial \eta}\frac{\partial y}{\partial \xi}\right), \tag{3.29}$$

$$\gamma_1 \frac{\partial^2 y}{\partial \xi^2} - 2\gamma_2 \frac{\partial^2 y}{\partial \xi \partial \eta} + \gamma_3 \frac{\partial^2 y}{\partial \eta^2} = \frac{J}{\omega}\left(\frac{\partial \omega}{\partial \xi}\frac{\partial x}{\partial \eta} - \frac{\partial \omega}{\partial \eta}\frac{\partial x}{\partial \xi}\right), \tag{3.30}$$

Equation 3.29 was solved using the procedure described in Section 3.4.2. New terms introduced by ω heterogeneity were understood as *right hand side* terms. As suggested by Masud et al. (2007), the value of ω was chosen to be inversely proportional to the original mesh cells volume. Even if the *mesh folding* was avoided, the impact on the original mesh size distribution did not fulfill the requirements of an *a posteriori* CFD computation (Figure 3.10), due to the significant modification of the boundary layer first cell thickness.

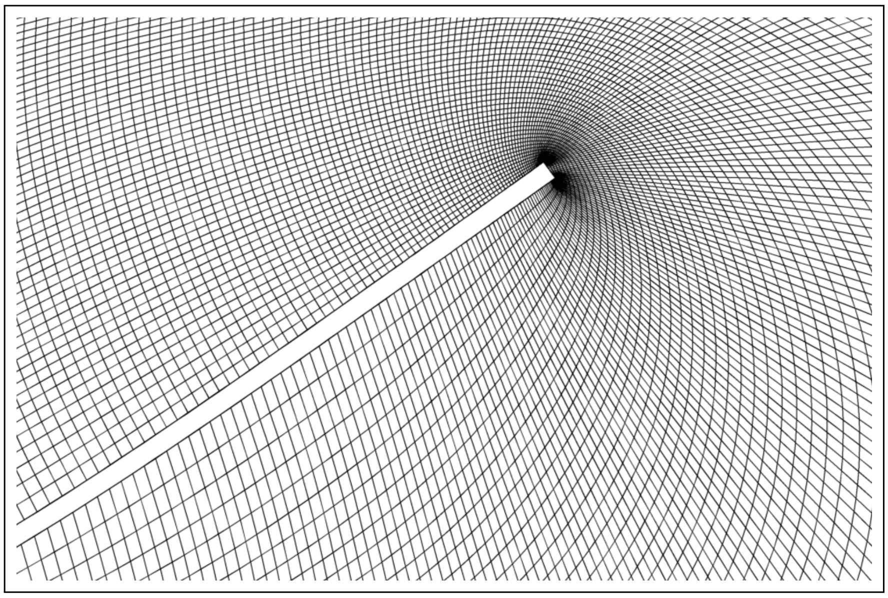

Figure 3.10: VIV test case, deformed mesh with *Winslow smoothing* with local diffusion of Masud et al. (2007)

3.4.5 Related work and conclusion

The limitation in terms of *diffusion* control of the implemented *Winslow Smoothing* are known in other field of applications. In *mesh generation*, the *Thomas-Middlecoff approach* has been taken by many authors [Agoes Moelyadi (2006); Eça (1999); Masters (2011)], modifying

Equation 3.21 and Equation 3.22 as:

$$\gamma_1\left(\frac{\partial^2 x}{\partial \xi^2}+P\frac{\partial x}{\partial \xi}\right)+\gamma_3\left(\frac{\partial^2 x}{\partial \eta^2}+Q\frac{\partial x}{\partial \eta}\right)=0\,, \tag{3.31}$$

$$\gamma_1\left(\frac{\partial^2 y}{\partial \xi^2}+P\frac{\partial y}{\partial \xi}\right)+\gamma_3\left(\frac{\partial^2 y}{\partial \eta^2}+Q\frac{\partial y}{\partial \eta}\right)=0\,, \tag{3.32}$$

with $P(\frac{\partial x}{\partial \xi},\frac{\partial x}{\partial \eta},\frac{\partial y}{\partial \xi},\frac{\partial y}{\partial \eta})$ and $Q(\frac{\partial x}{\partial \xi},\frac{\partial x}{\partial \eta},\frac{\partial y}{\partial \xi},\frac{\partial y}{\partial \eta})$ being the so-called *control functions*.

The role of P and Q is to locally control the diffusion process by imposing the prevalence either of mesh orthogonality, initial cell volume or other parameters. A common practice consists in computing P and Q at the domain boundaries and interpolate their values into the inner mesh. To best of author's knowledge, the only successful adaptation of these *mesh generation* techniques in a pure deformation scenario was carried out by Yigit et al. (2008), inspired by the formulation of Spekreijse (1995). A very good performance when dealing with large displacement and rotations was achieved for two-dimensional applications. However, the complexity of the algorithm was considerably increased, involving several interpolation and solution steps. Due to the high implementation and computational times attached to these sophisticated techniques, new formulations for *near-wall orthogonality* and *mesh folding* control were foreseen in the present PhD work.

3.5 Development of the Elastic Analogy

Previous experiences trying to avoid the limitations of the *Laplacian Smoothing* when dealing with large deformations and sharp edges did not manage to ensure a good quality of the deformed mesh (see Section 3.4). In order to explore the possibilities of other connectivity-based *mesh deformation* methods, an implementation of the *Elastic analogy* (ELA) was foreseen. In this approach, near-wall orthogonality can be controlled thanks to the coupled nature of the linear elastic equations to solve. This section includes details about this implementation, together with a discussion regarding the capabilities of the approach.

3.5.1 Base model

The developed algorithm is based on the *Elastic Analogy* described by Jasak and Weller (2000). In this case, the diffusion mechanism is controlled by considering the CFD mesh as an elastic continuum. Let assume a 3D *Eulerian* notation, together with the following considerations:

- A direct *Cartesian* orthonormal frame, fixed to the reference system attached to the observer and with its origin in O

- A simulation time t
- A fixed positioning vector $\vec{x}$

Considering a force $\mathrm{d}\vec{f}(\vec{n},\vec{x},t,\mathrm{d}S)$ applied to a material surface $\mathrm{d}S$, the *stress vector* over the plan with normal vector $\vec{n}$ can be defined as:

$$\vec{\sigma} = \lim_{\mathrm{d}S \to 0} \frac{\mathrm{d}\vec{f}(\vec{n},\vec{x},t,\mathrm{d}S)}{\mathrm{d}S} , \tag{3.33}$$

As in a real material, these stresses can be propagated in all directions. The *stress tensor* $\boldsymbol{\sigma}$ (also known as *Cauchy tensor*) with respect to R can be then introduced as:

$$\boldsymbol{\sigma}(\vec{x},t) = \begin{bmatrix} \sigma_{xx}(\vec{x},t) & \sigma_{xy}(\vec{x},t) & \sigma_{xz}(\vec{x},t) \\ \sigma_{yx}(\vec{x},t) & \sigma_{yy}(\vec{x},t) & \sigma_{yz}(\vec{x},t) \\ \sigma_{zx}(\vec{x},t) & \sigma_{zy}(\vec{x},t) & \sigma_{zz}(\vec{x},t) \end{bmatrix} , \tag{3.34}$$

In this continuum mechanics context, *Newton*'s second law can be written as:

$$\vec{\nabla} \cdot \boldsymbol{\sigma}(\vec{x},t) + \rho(\vec{x},t)\vec{b}(\vec{x},t) = \rho(\vec{x},t)\vec{a}(\vec{x},t) , \tag{3.35}$$

where:

- $\vec{b}(\vec{x},t)$ refers to the long range forces field (also named as *body forces*). In this category we find electric, magnetic and gravity forces
- $\rho(\vec{x},t)$ refers to the volume masses field
- $\vec{a}(\vec{x},t)$ refers to the accelerations field

Assuming that no *long range* forces are present in the targeted application, the static equilibrium (no accelerations) will be driven by the following simplification of Equation 3.35:

$$\vec{\nabla} \cdot \boldsymbol{\sigma} = \vec{0} , \tag{3.36}$$

The simplest way to relate the *stress tensor* $\boldsymbol{\sigma}$ with the *strain tensor* $\boldsymbol{\varepsilon}$ is the linear hypothesis. This implies that a a completely elastic behavior will be reproduced in the continuum. For structure analysis application, this hypothesis is valid only when dealing with small deformations. However, since in this work the aim was not to accurately solve a solid mechanics problem but to have a robust and efficient mesh deformation method, the linearity assumption did not imply any constraint. If a completely isotropic behavior is also assumed, the *Hooke law* can be established as:

$$\boldsymbol{\sigma} = \lambda Tr(\boldsymbol{\varepsilon})\boldsymbol{I} + 2\mu\boldsymbol{\varepsilon} , \tag{3.37}$$

where $\boldsymbol{I}$ refers to the unit tensor and λ and μ correspond to the so-called *Lame Coefficients*, that can be directly related to the elastic properties (*Young Modulus* and *Poisson Ratio*) given to the continuum:

$$\mu = \frac{E}{2(1+\nu)} , \tag{3.38}$$

$$\lambda = \frac{\nu E}{(1+\nu)(1-2\nu)} , \tag{3.39}$$

Let us define now $\vec{u}$ as the *deformation vector* between an unconstrained situation characterized by $\vec{x}_{ref}$ and the deformed position $\vec{x}$. Under the already assumed hypothesis of small deformations, $\boldsymbol{\varepsilon}$ and $\vec{u}$ can be related as:

$$\boldsymbol{\varepsilon} = \frac{(\nabla\vec{u})^T + \nabla\vec{u}}{2} , \tag{3.40}$$

By introducing Equation 3.40 in Equation 3.37, the *static equilibrium* condition of Equation 3.36 can be expressed in terms of the *deformation vector* $\vec{u}$ as:

$$\vec{\nabla}\cdot[\lambda(\vec{\nabla}\cdot\vec{u})\boldsymbol{I} + \mu((\vec{\nabla}\cdot\vec{u})^T + \vec{\nabla}\cdot\vec{u})] = 0 , \tag{3.41}$$

3.5.2 Implementation details

A finite volume discretization of Equation 3.41 was used in order to reproduce the elastic equations of the fictitious material. By applying this expression all along a control volume V (i.e. the *deforming domain*):

$$\int\int\int_V (\vec{\nabla}\cdot[\lambda(\vec{\nabla}\cdot\vec{u})\boldsymbol{I} + \mu((\vec{\nabla}\cdot\vec{u})^T + \vec{\nabla}\cdot\vec{u})])\,\mathrm{d}V = 0 , \tag{3.42}$$

Using the divergence theorem and assuming a surface S for the control volume and its normal vector $\vec{n}$:

$$\int\int_S (\lambda(\vec{\nabla}\cdot\vec{u})\vec{I} + \mu((\vec{\nabla}\vec{u})^T + \vec{\nabla}\vec{u}))\cdot\vec{n}\,\mathrm{d}\vec{S} = 0 , \tag{3.43}$$

Equation 3.43 can be also expressed in *tensor notation* as:

$$\int\int_S \lambda\frac{\partial u_i}{\partial x_i}\,\mathrm{d}S_j + \mu\frac{\partial u_j}{\partial x_i}\,\mathrm{d}S_i + \mu\frac{\partial u_i}{\partial x_j}\,\mathrm{d}S_i = 0 , \tag{3.44}$$

As it can be seen in Equation 3.44, the *divergence* and *transposed gradient* terms of Equation 3.43 are the responsible of the coupling of spatial directions of the deformation. A linear system was built based on Equation 3.43, and solved with the *Jacobi* approach already described in Section 3.4.2. No coefficients re-computation was needed in this case, since the elastic properties of the material were computed based on the *original mesh*.

3.5.3 Base results

The first application of the developed model to the considered VIV test case also lead to mesh folding around beam tip (see Figure 3.11).

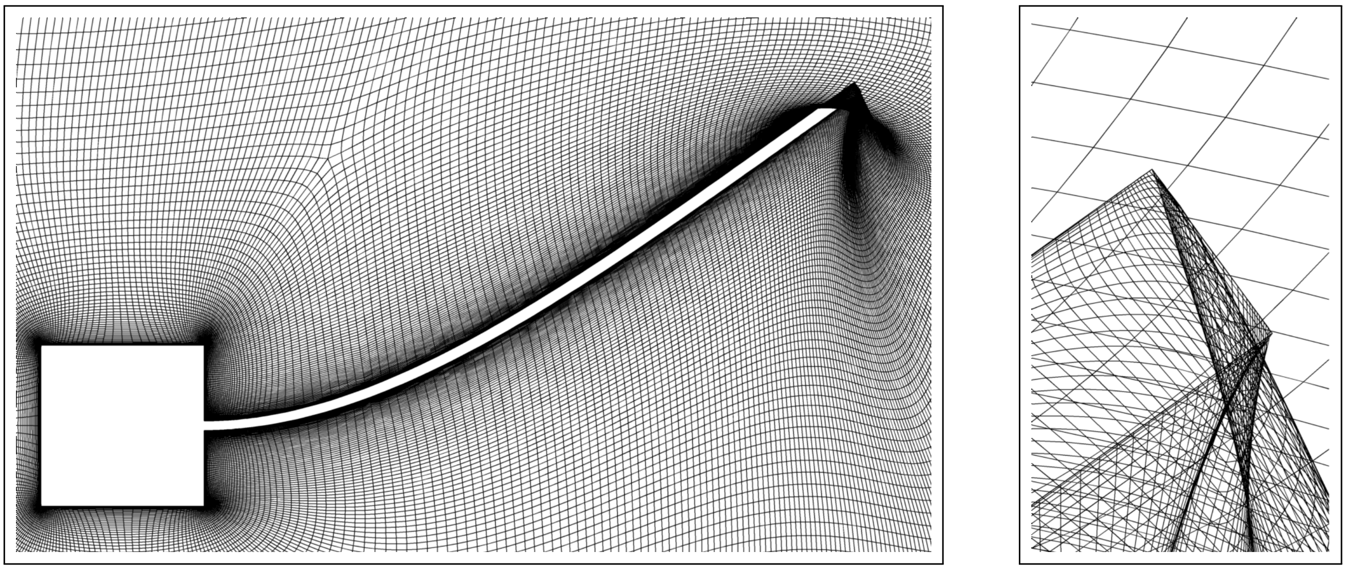

(a) Global view **(b)** Beam tip detail

Figure 3.11: VIV Test Case, *Elastic Analogy* deformation, homogeneous elasticity

As stated by many authors [Stein et al. (2003); Yang and Mavriplis (2005)], a completely elastic material with homogeneous structural properties does not ensure a non-folded deformed mesh. Hence, it was decided to improve the presented model by the implementation of additional elasticity control mechanisms.

3.5.4 Model improvement: heterogeneous elasticity

Under the presence of large displacements, the performance of the base formulation of the *Elastic Analogy* is drastically reduced. The most popular approach found in the literature in order to overcome this limitation consists in replacing the initial *fictitious* homogeneous material by one based on a spatial distribution of its elastic properties. Table 3.2 summarizes previous works performed by other other authors in this context. Four main strategies can be distinguished:

- Distribution of E based on geometrical properties of the original mesh
- Distribution of ν based on geometrical properties of the original mesh

Table 3.2: Elasticity control strategies of the *Elastic Analogy* in the literature

	Young Modulus E	**Poisson Ratio ν**
Quaranta et al. (2008)	$E \propto \frac{1}{l_{min}}$	Constant
Yang and Mavriplis (2005) Biedron and Thomas (2009) Yamazaki et al. (2010)	$E \propto \frac{1}{Vol}, E \propto \frac{1}{d}$	Constant
Truong et al. (2008)	$E \propto \frac{1}{Vol}$	Constant
Stein et al. (2003) Amirante et al. (2012)	$E \equiv f(J, \alpha_s, \alpha_v)$	$\nu \equiv f(J, \alpha_s, \alpha_v)$
Bartels (2005)	$E \propto \frac{1}{1-e^{-a \cdot d}}$	0.0
Lund et al. (2001)	$E \propto \frac{1}{d^a}$	Constant
Nielsen and Anderson (2002)	Constant	$\nu \propto \frac{1}{\Lambda}$
Hsu and Chang (2007) Chiandussi et al. (2000) Hsu et al. (2004)	Based on a first homogeneous simulation	

l_{min}: Minimum edge length in the element, Vol: Cell volume (cell surface in 2D applications)
d: Distance to wall, J: Element Jacobian, Λ: Cell aspect ratio
α_s, α_v: Surface and volume change rate coefficient (user input)

- Computation of E and ν based on the results of a previous homogeneous computation
- Re-computation of the elastic properties during the deformation process based on elements *Jacobian*

In order to reduce the computational time of the developed *elastic analogy*, only the first two strategies were considered in this PhD work. For the presented implementation, the distribution showing a higher robustness for the whole range of expected applications was based on $E \propto \frac{1}{Vol}, E \propto \frac{1}{d}$. The value of ν was set to a constant value.

Since the impact of ν on the deformed mesh quality is case dependent, it is understood as an end-user input in the actual implementation. The *Young modulus* distribution can be controlled by specifying the ratio between its maximum and minimum values in the whole mesh E_{max}/E_{min}. Finally and for flexibility purposes, the end-user can base the distribution of E either on the original *mesh volume* or on the *wall distance* mapping. This choice should be performed according to the topology to study, especially when dealing with the existence of boundary layer meshes.

A good resulting mesh quality could be obtained for the considered VIV test case with $\nu = 0.25$ and $E_{max}/E_{min} = 10^5$ (see Figure 3.12). Since in this case the minimum *cell volumes* were located at the vicinity of our walls, no remarkable differences were observed between the deformed mesh for $E \propto \frac{1}{Vol}$ and $E \propto \frac{1}{d}$ distributions.

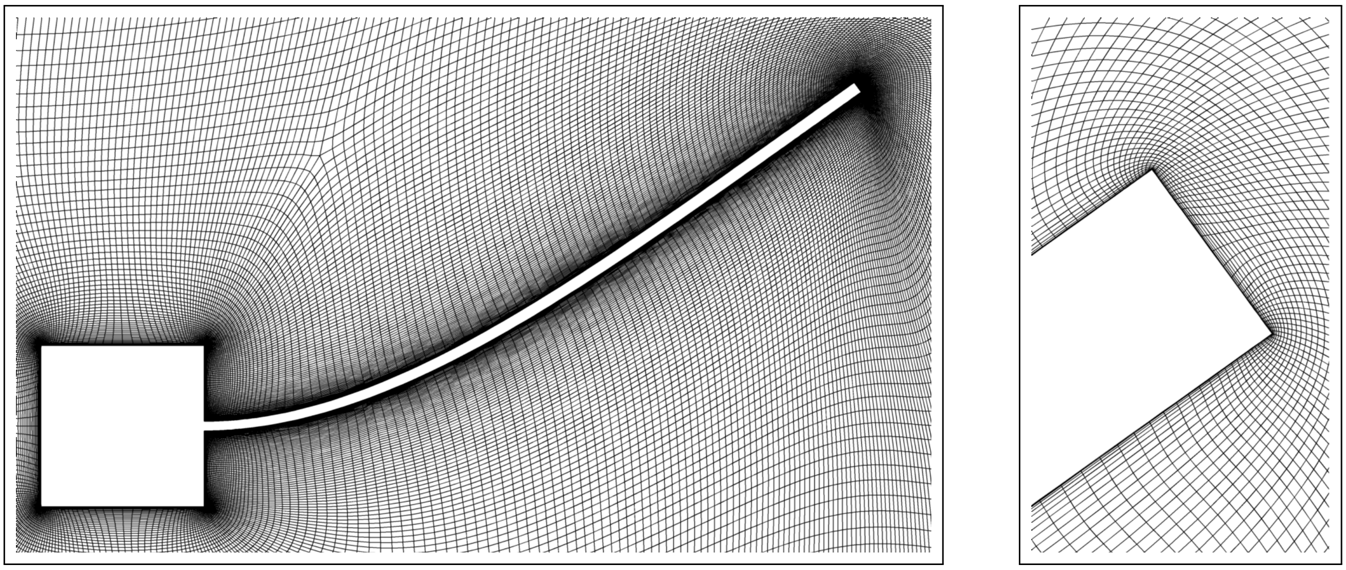

(a) Global view **(b)** Beam tip detail

Figure 3.12: VIV Test Case, *Elastic Analogy* deformation

Table 3.3 illustrates the performance of the developed method against the results of the already existing RBF development (see Section 3.3). Only a slight decrease in the overall *Orthogonality* was observed, corresponding to a relative difference of 3.21%. More interesting remarks could be performed from the computational cost point of view:

- *Computational time prior to the deformation process* ($t_{def,pre}$): Even at this mesh size, the *Elastic Analogy* was considerably less expensive than the RBF method (around 27 times). This fact was related to the required matrix inversion involved in the RBF approach, and could become even more constraining in a multi-million meshes context (see Section 3.3).

- *Allocated memory* (Mem.): Memory consumption was higher for the *Elastic Analogy*, since the whole linear system needed to be allocated. In particular, a relative increase of 26% was observed. However, the *on-disk* memory storage related to the matrix inversion of the RBF approach could become constraining for bigger meshes.

- *Computational time during the deformation process* ($t_{def,call}$): The cost of solving the linear system of the *Elastic Analogy* was still to high, due to the combination of a very simple solution process (i.e. the *Jacobi* solver) and a very important initial excitation. This numerical issue is assessed in future sections.

Table 3.3: Mesh quality of original and deformed VIV mesh, *Elastic analogy* results

Def. method	OR	AR	ER	Computational Data			
	Min.	Max.	Max.	#Proc	$t_{def,pre}$	$t_{def,call}$	Mem.
Original	43.6	1.09×10^4	1.95	-	-	-	-
RBF	43.0	1.09×10^4	1.95	3	0.0300	0.0030	163
ELA	42.2	1.09×10^4	1.95	3	0.0011	1.0670	205

OR: Orthogonality [deg], *AR*: Aspect Ratio, *ER*: Expansion Ratio
Mem.: Max. memory allocated [MB], divided by number of processors *#Proc*
$t_{def,pre}$: Mesh deformation CPU time [min] per Proc spent in *preprocessing* (once per simulation)
$t_{def,call}$: Mesh deformation CPU time [min] per Proc spent at every call of the method

Influence of ν value

In the actual implementation, a simple diagonal matrix preconditioning was implemented (see Section 3.4.2). Since increasing ν reduced the diagonal dominance of the system, numerical instabilities were found for values in the range [0.35,0.5]. In general, a larger value of ν allows a greater deformation of the mesh before the appearance of folding [Baker and Carvallo (1999)]. This numerical behavior was verified for our base test case, as shown in Figure 3.13 (a closer zoom is shown in order to properly analyze the results). A value of $E_{max}/E_{min} = 10^5$ was kept for all the computations.

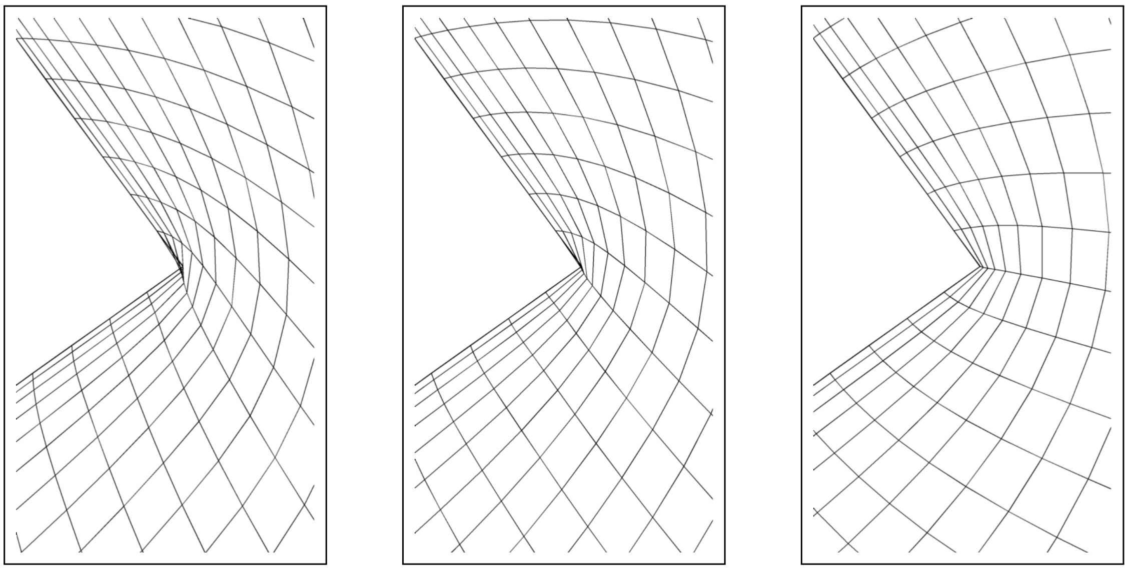
(a) $\nu = 0$ **(b)** $\nu = 0.15$ **(c)** $\nu = 0.25$

Figure 3.13: VIV Test Case, *Elastic Analogy* deformation, impact of ν on beam tip

In this case, increasing the value of ν did not have any important effect on resulting mesh quality for values higher than 0.25.

Influence of E_{max}/E_{min} value

Figure 3.14 shows the impact of E_{max}/E_{min} when fixing $\nu = 0.25$. The mechanism against mesh folding related to the heterogeneous distribution of E was activated from a certain value of E_{max}/E_{min}. Increasing the value of the maximum *Young modulus* did not improve the quality of the deformed mesh, as also observed for ν.

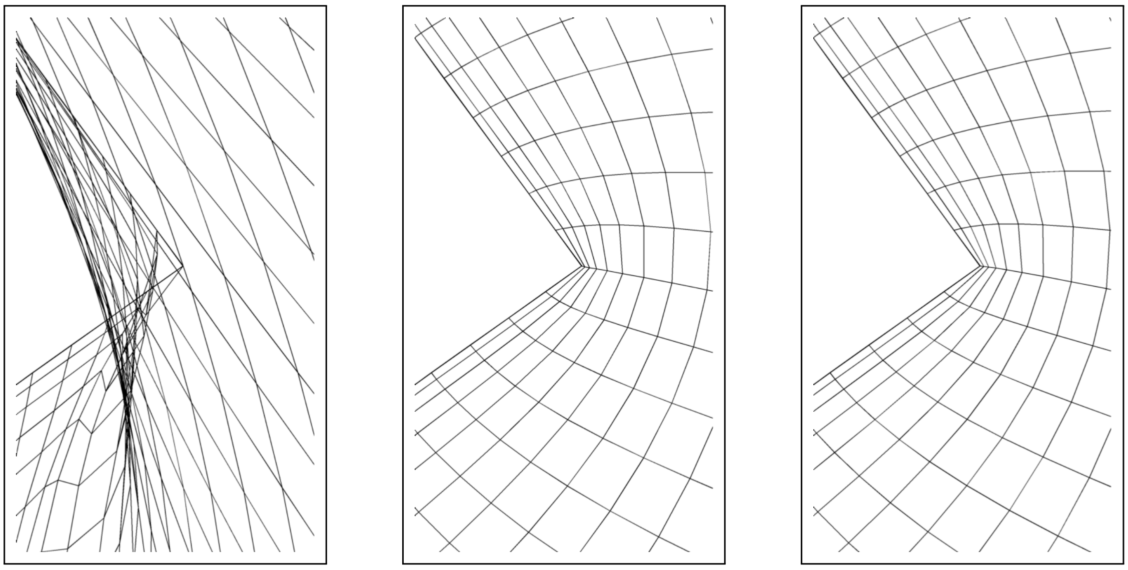

(a) $E_{max}/E_{min} = 10^2$ **(b)** $E_{max}/E_{min} = 10^5$ **(c)** $E_{max}/E_{min} = 10^8$

Figure 3.14: VIV Test Case, *Elastic Analogy* deformation, impact of E_{max}/E_{min} on beam tip

3.5.5 Related work and conclusion

The *Elastic analogy* allowed to accommodate large displacements, including rotations, in a highly demanding two-dimensional numerical scenario. Its performance with respect to the deformed mesh quality was rated as sufficient for the *a posteriori* CFD computations. However, the computational time required for the linear system solution was still constraining for the targeted industrial applications.

Two main strategies can be followed in order to reduce the computational time required by the *Elastic analogy*:

- **Improve linear system solver**: both the matrix preconditioning and the solution process could be improved by adopting more sophisticated approaches [Augarde et al. (2006); Barral et al. (2014)]. This development can be very challenging from an implementation point of view, especially in terms of parallelization.

- **Improve initial solver solution**: The efficiency of the actual solution process was highly reduced when the initial solution was far from the targeted deformed mesh.

> Hence, a fast pre-computation of an initial solution could considerably reduce the actual solution time under the presence of large structural displacements.

In addition, the elastic model could be enhanced by improving the capabilities of the method when dealing with large displacements and/or rotations. In this line, already used concepts in *animation* industry for graphics deformation could be adapted to a CFD environment. Previous experiences in co-rotational elasticity can be found in the works of Bender and Deul (2013), Georgii and Westermann (2008), Hauth and Strasser (2004) and Zhu et al. (2010), while the studies of Gao et al. (2002) and Matthias et al. (2002) were focused in modeling specific material non-linearities.

3.6 Development of a Hybrid mesh deformation method

As seen in Section 3.5, the developed *Elastic Analogy* suffered from a very high numerical cost when dealing with large boundary displacements. Among the suggested possible improvements listed in Section 3.5.5, it was decided to focus the development efforts in providing a better initial solution for the solver in order to speed up its convergence.

Let consider the mesh deformation of the VIV. Figure 3.15 shows the initial solution of the developed *Elastic analogy* method. As it can be observed, only the *Dirichlet* boundary conditions were imposed, while the mesh blocking remained undisplaced. Hence, the solution algorithm had to first diffuse the deformation of the block surrounding the beam, lowering its efficiency. In a more adequate initial solution mesh blocks should be already moved (taking into account boundaries displacement), prior to the start of the *Elastic analogy* iterative solution. This new situation will allow to speed-up the convergence of the *Jacobi* solver.

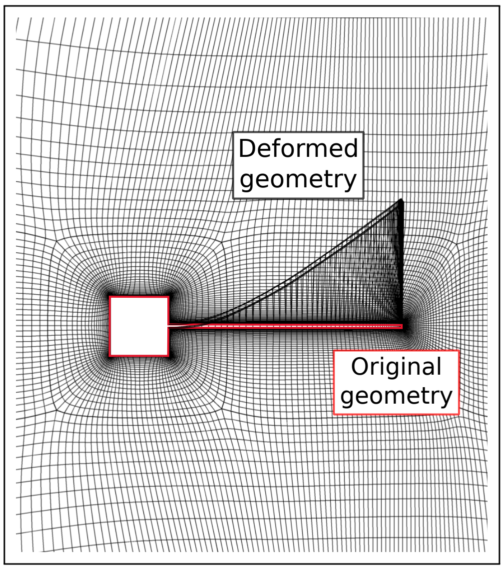

Figure 3.15: Initial solution of the *Elastic Analogy* solver, issued from the application of the imposed Dirichlet boundary conditions. VIV test case

The aim of this development was then to generate an improved initial solution of the *Elastic analogy* solver. For this purpose, a combination of light *mesh deformation* techniques is foreseen, leading to a *hybrid mesh deformation* scheme.

3.6.1 Base model

One of the methods involved in the deformation of structured meshes is the so called *Trans-Finite interpolation* (TFI). This technique, originally implemented for *mesh generation* purposes, can be seen as a three-dimensional linear reconstruction of the original mesh clustering based on blocks displacement. The TFI cannot be considered as a deformation method itself, but as a complementary tool in the whole process. Its reduced computational time makes it very attractive as an intermediate or final step in the complete mesh deformation tool. However and since no rotations are included in the TFI formulation, reduced control on final cells orthogonality can be achieved. Hence, deformed mesh quality is deteriorated in the context of large displacements accounting for rotations. This limitation was overcome in the presented implementation by the application of the *Elastic analogy* solver.

Since the TFI is not able to work as a *stand-alone* mesh deformator, an additional technique was required in order to provide the necessary block deformation input. In this context, the use of the already existing RBF algorithm was foreseen. In order to reduce the computational cost of this step, only block corners were included in the interpolation basis. The position of the inner-mesh block corners was then updated based on the imposed motion, and used as an input for the TFI algorithm.

The whole numerical chain of this new *hybrid method* can be summarized as:

RBF Mesh block corners placed at domain boundaries serve as a base for the *Radial Basis Functions Interpolation* of interior mesh block corners. This topologically-based nodes selection allows us to reduce the important computational time attached to RBF approach.

TFI Block edges, faces and interior points are computed based on *Transfinite Interpolation*, in order to have a complete approximate mesh before improving its quality with the ELA approach.

ELA Interior block nodes are then updated by means of an *Elastic Analogy* based on the reference mesh, in order to improve resulting mesh quality. During this step, the nodes laying on block corners and edges are considered as fixed.

Figure 3.16 illustrates the described methodology trough the VIV test case.

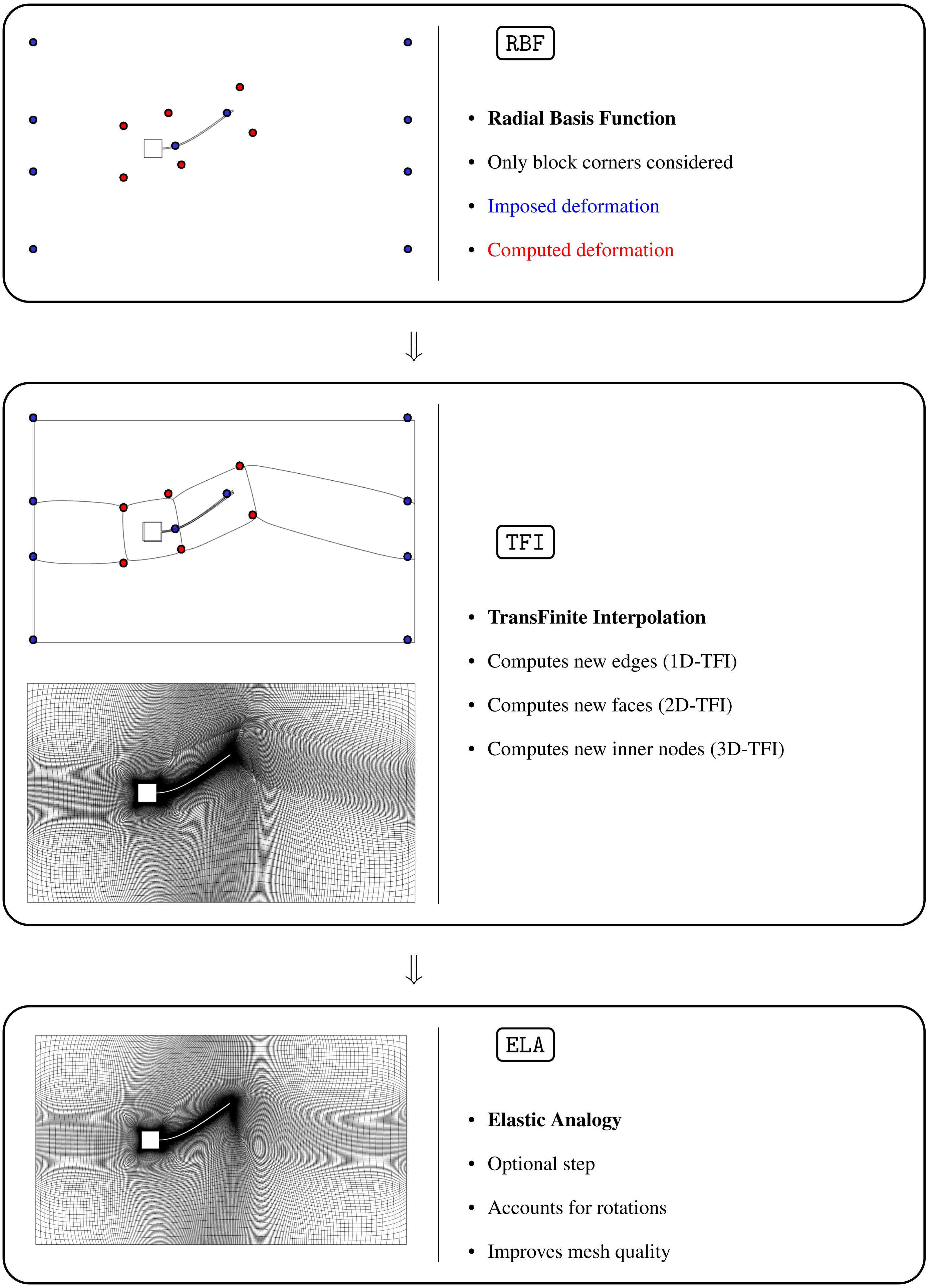

Figure 3.16: Mesh Hybrid method schema

3.6.2 Implementation details

Together with the adaptation of the RBF development in order to work with a block corners basis, the implementation of the TFI approach was required in order set-up the suggested *hybrid methodology*. Details about this development are included in this section.

The arc-length based approach originally suggested by Soni (1985) was implemented. The method has been successfully applied both for mesh generation [Smith (1999)] and mesh deformation purposes [Lai et al. (2003)].

Let us consider a structured mesh segment going from point A to B. The arc-length of an interior point i can be defined as:

$$l_i = \sum_{j=A+1}^{i} |x_{ref,j} - x_{ref,j-1}| \, , \tag{3.45}$$

where x_{ref} corresponds to the first dimension of the nodes reference position vector $\vec{x}_{ref}$. The total arc-length of the segment can be also defined as:

$$L_{BA} = \sum_{j=A+1}^{B} |x_{ref,j} - x_{ref,j-1}| \, , \tag{3.46}$$

Then, new edge interior points coordinates can be computed by performing a linear interpolation:

$$x_i - x_{ref,i} = \left[1 - \frac{l_i}{L_{BA}}\right] \left(x_A - x_{ref,A}\right) + \left[\frac{l_i}{L_{BA}}\right] \left(x_B - x_{ref,B}\right) \, , \tag{3.47}$$

The same methodology was repeated in all the directions.

As performed by Lai et al. (2003), this *1D-edges* interpolation can be easily extrapolated to a *2D-faces* version for block surface interpolation or to *3D-volumes* for block interior nodes recomputation. The combination of these 1D/2D/3D interpolators allows then to remap the blocks starting from the deformed position of block corners as follows:

- **1D-TFI**: Taking as an *input* the new coordinates of the *block corner* nodes, interpolates *new edge* nodes position.
- **2D-TFI**: Taking as an *input* the new coordinates of the *block edge* nodes, interpolates *new face* nodes position.
- **3D-TFI** (only in 3D cases): Taking as an *input* the new coordinates of the *block face* nodes, interpolates *new inner* nodes position.

3.6.3 Base results

In order to increase the efficiency of the developed *hybrid method* in the absence of a violent deformation, it can be launched with or without the optimization step performed by the *Elastic analogy*. In this document, these two possibilities are referred to as:

- **RBF+TFI**: Block corners are moved via RBF, and the TFI is used to generate the final deformed mesh
- **RBF+TFI+ELA**: Block corners are moved via RBF, and the TFI is used to generate an initial solution for the *Elastic analogy* solver, aiming to improve final deformed mesh quality

For the particular application of the VIV test case, the ELA step became necessary in order to preserve near-wall orthogonality (Figure 3.17 and Figure 3.18).

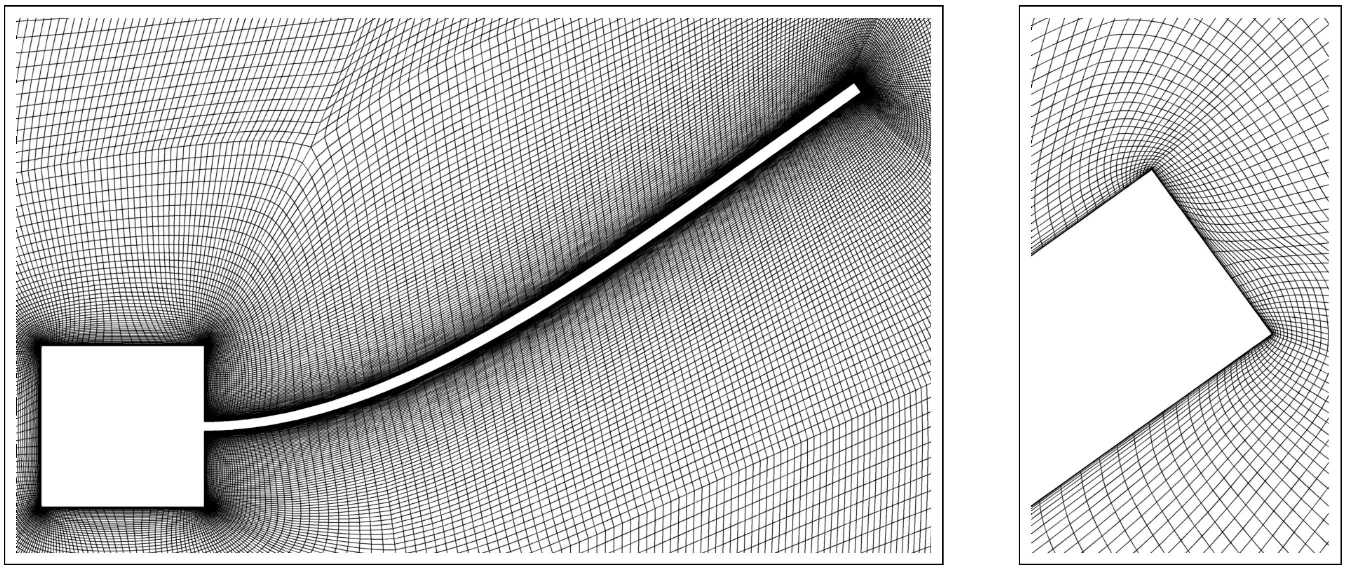

(a) Global view **(b)** Beam tip detail

Figure 3.17: VIV Test Case, RBF+TFI deformation

This fact was verified when analyzing the performance of both RBF+TFI and RBF+TFI+ELA methodologies, compiled in Table 3.4. Indeed, the RBF+TFI numerical chain was not able to keep the original mesh quality, both in terms of *orthogonality* and *aspect ratio*. However, the needed computational resources used were lower than with any other approach. The complete *hybrid method* RBF+TFI+ELA resulted in a higher quality deformed mesh. In addition, its computational cost was considerable lower than the classical *Elastic analogy* approach, which was the objective of this development.

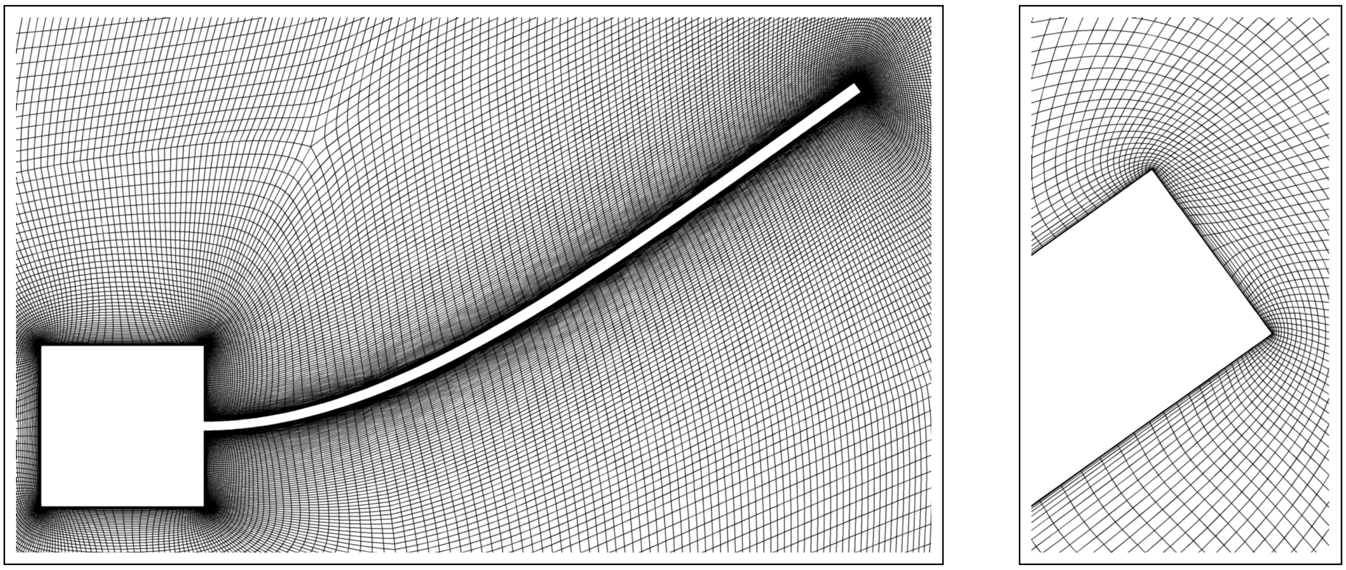
(a) Global view (b) Beam tip detail

Figure 3.18: VIV Test Case, RBF+TFI+ELA deformation

Table 3.4: Mesh quality of original and deformed VIV mesh, *Hybrid method* results

Def. method	OR	AR	ER	Computational Data			
	Min.	Max.	Max.	#Proc	$t_{def,pre}$	$t_{def,call}$	Mem.
Original	43.6	1.09×10^4	1.95	-	-	-	-
RBF	43.0	1.09×10^4	1.95	3	0.0300	0.0030	163
ELA	42.2	1.09×10^4	1.95	3	0.0011	1.0670	205
RBF+TFI	30.5	1.17×10^4	1.95	3	0.0000	0.0001	154
RBF+TFI+ELA	37.3	1.08×10^4	1.95	3	0.0012	0.0233	206

OR: Orthogonality [deg], *AR*: Aspect Ratio, *ER*: Expansion Ratio

Mem.: Max. memory allocated [MB], divided by number of processors *#Proc*

$t_{def,pre}$: Mesh deformation CPU time [min] per Proc spent in *preprocessing* (once per simulation)

$t_{def,call}$: Mesh deformation CPU time [min] per Proc spent at every call of the method

3.6.4 Related work and conclusion

A *hybrid method* based on the combination of existing *mesh deformation* techniques was implemented. The main philosophy was the creation of a fast mesh based on the *TransFinite Interpolation*, which takes into account pre-computed block corners displacement via *Radial Basis Functions* interpolation. The mesh issued from this process can be optionally optimized by the application of an *Elastic analogy* algorithm. For the particular VIV test case, the whole chain RBF+TFI+ELA obtained an acceptable deformed mesh quality at a lower computational cost than the traditional *Elastic Analogy*. The application of the developed methodologies in a wider range of applications is studied in following sections.

Similar *hybrid methods* can be found in the literature:

- Ding et al. (2014): *Radial basis function* based on *block corners* + *Transfinite Interpolation*
- Gopalakrishnan and Tafti (2009); Tsai et al. (2001): *Spring analogy* for vertex displacement + *Transfinite Interpolation*

In all the mentioned publications, the deformed mesh quality issued from the TFI was satisfactory for the considered structural deflections. In the presented development, the ELA step aimed to extend the capabilities of this type of methodologies to a wider range of applications, while ensuring a high deformed mesh quality, especially when considering large imposed rotations.

3.7 Additional test cases

In this section, the performance of the developed mesh deformation methods within the framework of this research are analyzed. In this context, the combination of *test case* and *specific structural deflection* is referred to as *Design Load Case* (DLCs). The choice of the presented DLCs was driven by the final objective of the new algorithms: the deformation of multi-million HAWTs meshes. In order to evaluate the behavior of the different approaches under large displacements, a static moving walls deflection was imposed. The FSI modal approach described in Section 2.2.2 was used for this purpose. The analysis of the different DLCs focuses in the performance of the *mesh deformation* methods, without any consideration regarding the CFD modeling.

3.7.1 FFA-w3-241

This 2D test case was based on the FFA-w3-241 24.1% relative thickness airfoil, which is equipped by the DTU 10MW RWT at the blade tip [Bak et al. (2013)]. This model was found to be very interesting from the development point of view, since it reproduces in two dimensions the problems in mesh deformation that are foreseen for wind turbine blades. The numerical scenario established by the FFA-w3-241 profile can be summarized as:

- External two-dimensional aerodynamics
- Mesh accounting for fine *boundary layer* clustering
- Large moving walls displacements, including sharp edges

The geometry is characterized by asymmetric pressure and suction sides and a blunt trailing edge. A coarser version of the publicly available mesh described in Bak et al. (2013) was used in this study. It consists on a *C-mesh* topology accounting for 1.6×10^4 nodes (see Figure 3.19). A first cell of 2.2×10^{-6}/*chord* thickness was considered in the *boundary layer*, and the farfield was placed at around 30 *chords* from the airfoil.

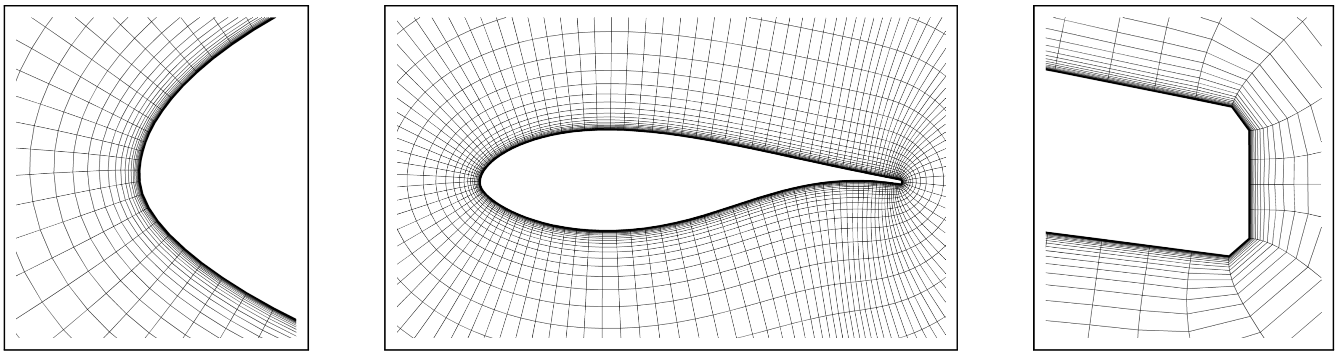
(a) Leading edge **(b)** Global view **(c)** Trailing edge

Figure 3.19: FFA-w3-241 original mesh

Two different DLCs were defined by means of an *imposed rigid motion* of the airfoil geometry. They are referred to as *forced pitch up* and *forced pitch down*, and described in the following sections.

DLC1: Forced Pitch Up

A 30 deg pitch up was imposed to the FFA-w3-241 airfoil, involving an important displacement with respect to the original position (see Figure 3.20).

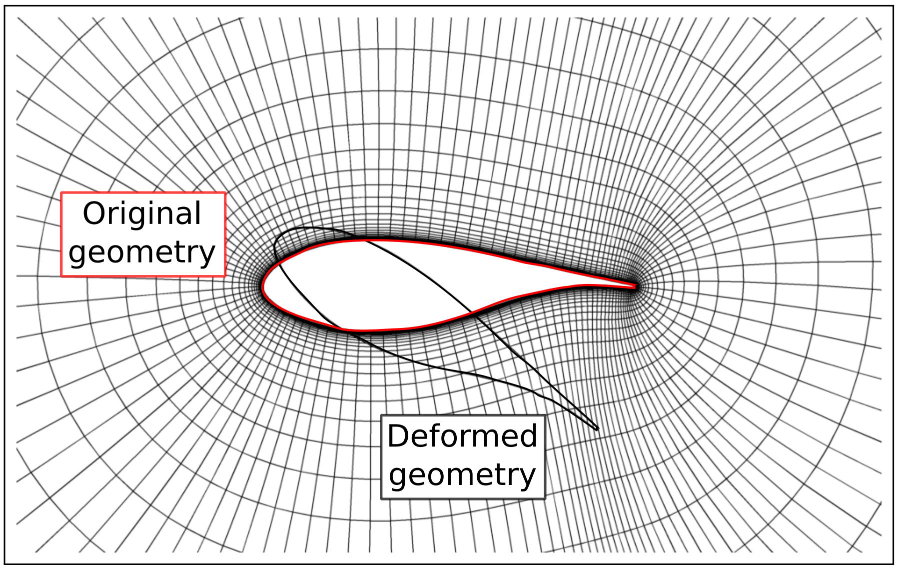

Figure 3.20: Superposition of original FFA-w3-241 mesh and rotated geometry, DLC1

As already observed for the VIV test case, the *Laplacian Smoothing* was not able to avoid the existence of mesh folding near the trailing edge for such an important rotation (Figure 3.21).

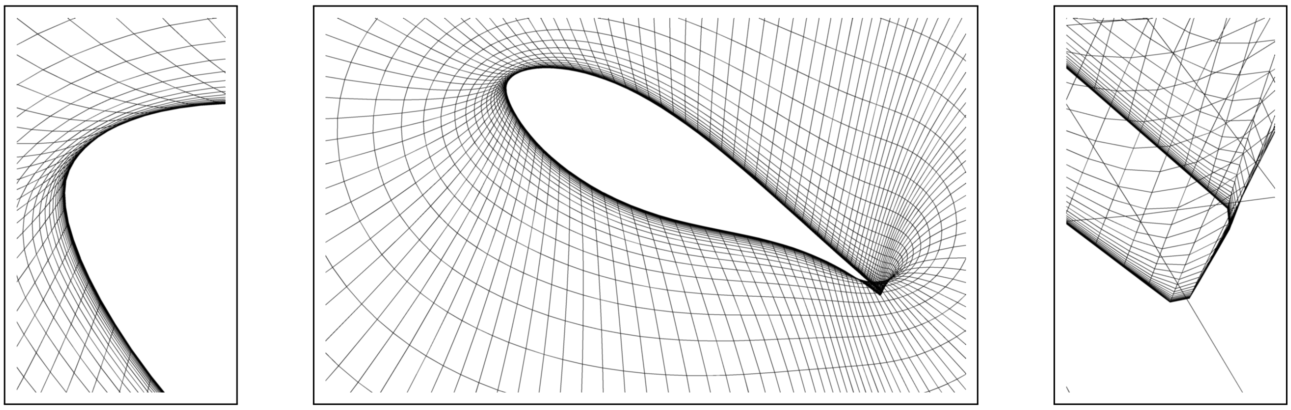

(a) Leading edge **(b)** Global view **(c)** Trailing edge

Figure 3.21: FFA-w3-241 deformed mesh, *Laplacian Smoothing*, DLC1

The rest of studied mesh deformation methodologies were able to provide a non-folded resulting grid. Their performance are summarized in Table 3.5. Information concerning the computational time prior to the deformation process is not included due to the small size of the considered grid.

Table 3.5: Mesh quality of original and deformed FFA-w3-241 mesh, DLC1

Def. method	OR	AR	ER	Computational Data		
	Min.	Max.	Max.	#Proc	$t_{def,call}$	Mem.
Original	43.7	9.19×10^5	1.55	-	-	-
RBF	40.3	9.37×10^5	1.55	1	0.016	33.74
ELA	28.2	8.07×10^5	1.65	1	0.047	43.50
RBF+TFI	14.1	9.17×10^5	1.66	1	0.000	33.48
RBF+TFI+ELA	25.0	9.17×10^5	1.58	1	0.010	43.47

OR: Orthogonality [deg], *AR*: Aspect Ratio, *ER*: Expansion Ratio

Mem.: Max. memory allocated [MB], divided by number of processors *#Proc*

$t_{def,pre}$: Mesh deformation CPU time [min] per Proc spent in *preprocessing* (once per simulation)

$t_{def,call}$: Mesh deformation CPU time [min] per Proc spent at every call of the method

The impact on deformed mesh quality could be mainly observed based on the minimum orthogonality (OR), which was related to the cells near the trailing edge. Indeed, the management of rotations of each deformation method explained this quality reduction. Even if the less computationally expensive method was the RBF+TFI, the lack of rotations of the *linear interpolation* resulted in an unacceptable orthogonality near the walls (Figure 3.22).

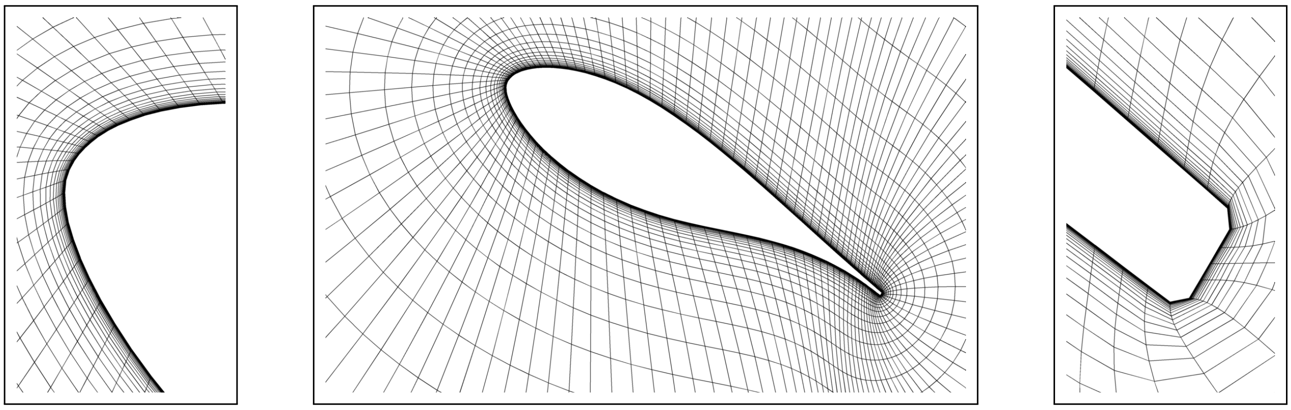

(a) Leading edge **(b)** Global view **(c)** Trailing edge

Figure 3.22: FFA-w3-241 deformed mesh, RBF+TFI, DLC1

Near-wall orthogonality could be improved by adding a final ELA step in the *hybrid* deformation approach (Figure 3.23). The computational time of the whole RBF+TFI+ELA sequence was lower than a direct evaluation of the *Elastic Analogy*, thanks to the proper initialization of the linear system solver.

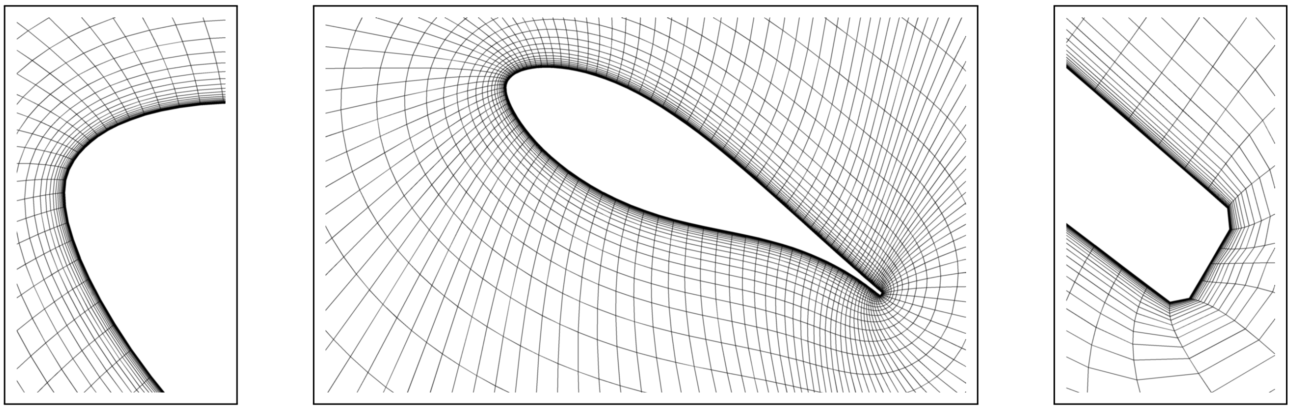

(a) Leading edge **(b)** Global view **(c)** Trailing edge

Figure 3.23: FFA-w3-241 deformed mesh, RBF+TFI+ELA, DLC1

However and due to the small number of nodes of the studied mesh, RBF was offering a computational cost equivalent to RBF+TFI+ELA. Additionally, this method resulted in the highest quality deformed mesh (Figure 3.24).

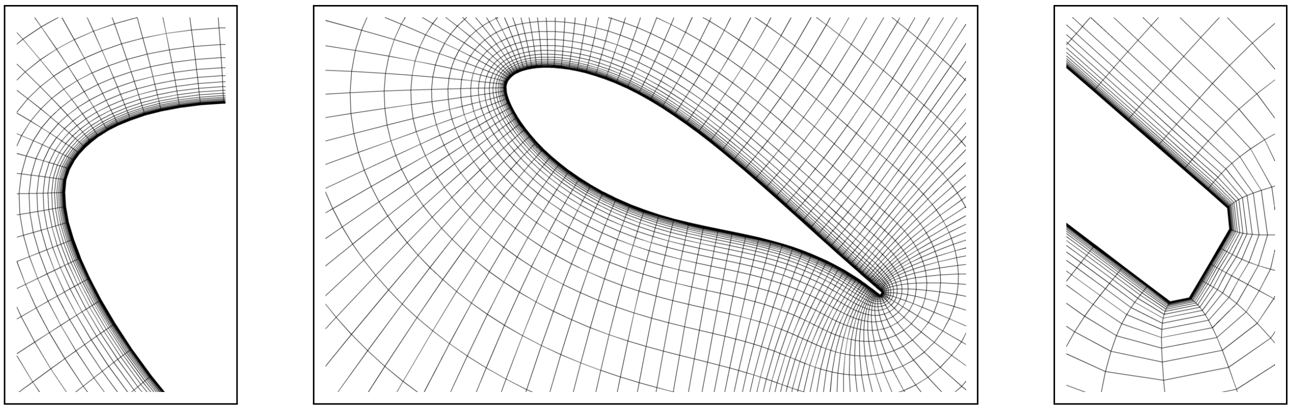

(a) Leading edge **(b)** Global view **(c)** Trailing edge

Figure 3.24: FFA-w3-241 deformed mesh, RBF, DLC1

DLC2: Forced Pitch Down

In order to ensure that the conclusions made in previous DLC were independent on the sign of the rotation, a -30 deg pitch was imposed to the geometry (Figure 3.25). Table 3.6 shows the performance of every mesh deformation method for this DLC. The capabilities of the different *mesh deformation* methods were equivalent to the observed ones for the DLC1 case (see Table 3.5). Same remarks concerning resulting mesh quality could be also made for this DLC (Figure 3.26, 3.27, 3.28). Hence, it could be concluded that the developed algorithms had the same behavior disregarding the rotation sign.

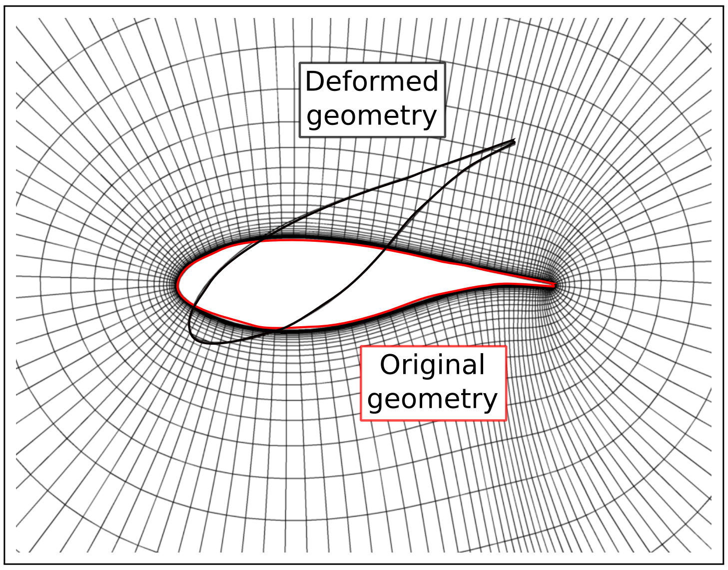

Figure 3.25: Superposition of original FFA-w3-241 mesh and rotated geometry, DLC2

Table 3.6: Mesh quality of original and deformed FFA-w3-241 mesh, DLC2

Def. method	OR	AR	ER	Computational Data			
	Min.	Max.	Max.	#Proc	$t_{def,pre}$	$t_{def,call}$	Mem.
Original	43.7	9.19×10^5	1.55	1	-	-	-
RBF	42.8	9.37×10^5	1.55	1	0	0.016	33.74
ELA	38.5	8.10×10^5	1.49	1	0	0.047	43.50
RBF+TFI	13.9	9.17×10^5	1.65	1	0	0.000	33.48
RBF+TFI+ELA	35.1	9.17×10^5	1.47	1	0	0.010	43.47

OR: Orthogonality [deg], *AR*: Aspect Ratio, *ER*: Expansion Ratio
Mem.: Max. memory allocated [MB], divided by number of processors *#Proc*
$t_{def,pre}$: Mesh deformation CPU time [min] per Proc spent in *preprocessing* (once per simulation)
$t_{def,call}$: Mesh deformation CPU time [min] per Proc spent at every call of the method

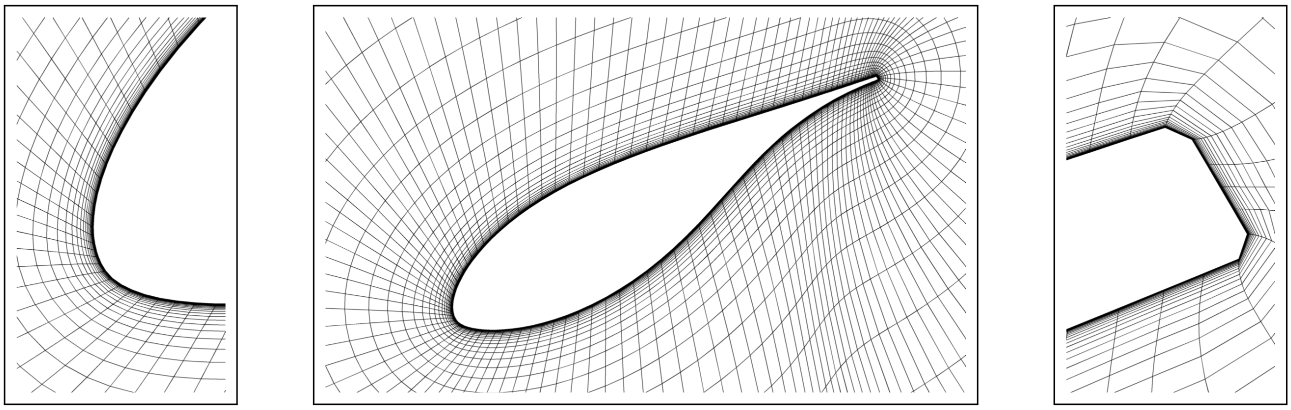

(a) Leading edge **(b)** Global view **(c)** Trailing edge

Figure 3.26: FFA-w3-241 deformed mesh, RBF+TFI, DLC2

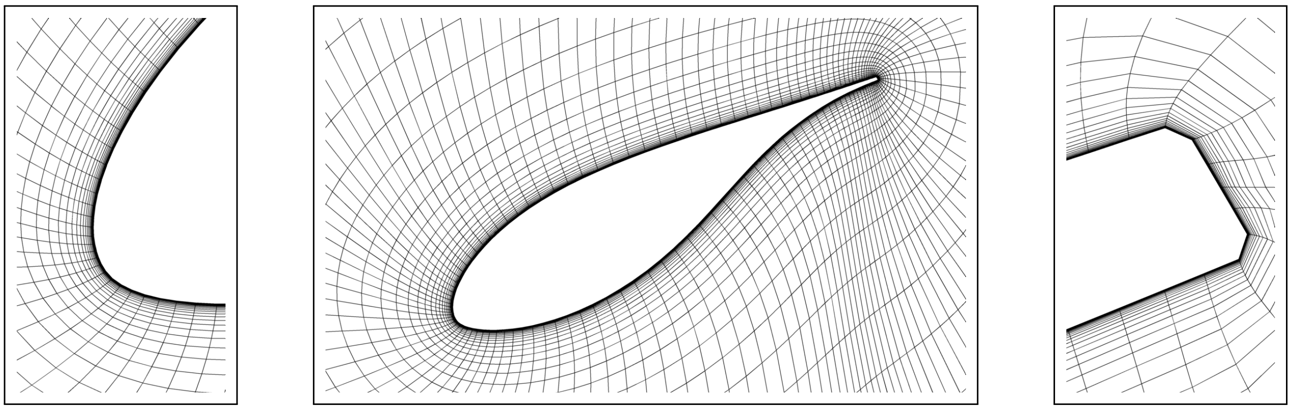

(a) Leading edge **(b)** Global view **(c)** Trailing edge

Figure 3.27: FFA-w3-241 deformed mesh, RBF+TFI+ELA, DLC2

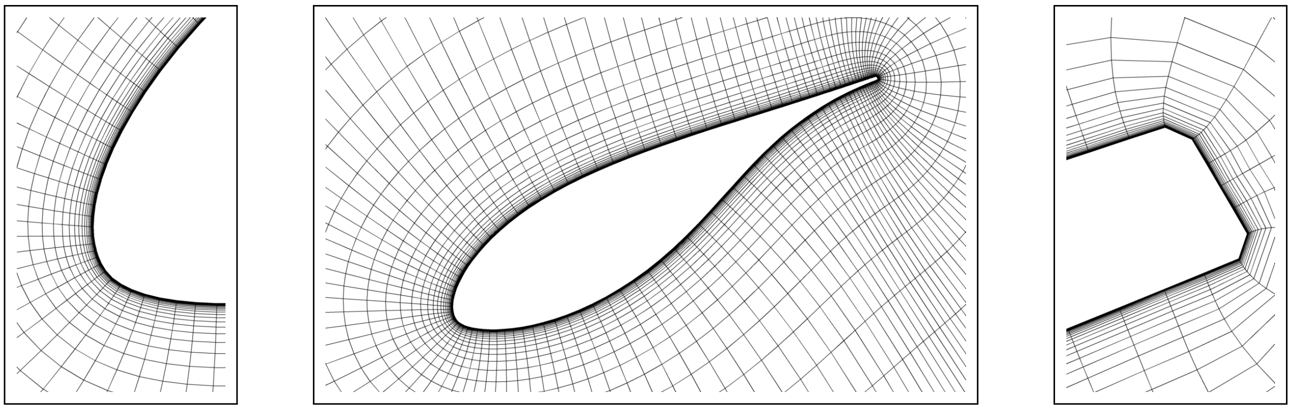

(a) Leading edge **(b)** Global view **(c)** Trailing edge

Figure 3.28: FFA-w3-241 deformed mesh, RBF, DLC2

Concluding Remarks

The FFA-w3-241 test case has illustrated the performance of the different developed methods in 2D configurations, including large moving walls displacement induced by large rotations. Even if at this mesh size the low computational effort of RBF did not require shifting to another mesh deformation method, the numerical chain RBF+TFI+ELA was rated as a good alternative. This *hybrid* approach was able to keep near-wall orthogonality at an equivalent *Central Process Unit* (CPU) cost.

3.7.2 AGARD 445.6 wing

This 3D test case is based on the AGARD 445.6 wing experimentally studied by Yates (1987), and it is representative of a HAWT application. The AGARD 445.6 wing is equipped with a NACA 65A004 airfoil, and it accounts for a root chord of 0.5587 m, a quarter-chord sweep angle of 45 deg, a half wing span L of 0.762 m and a tapper ratio of 0.6. The model aims to analyze the performance of the developed mesh deformation tools in a numerical scenario that can be summarized as:

- External three-dimensional aerodynamics
- Multi-block structured mesh
- Multi-million mesh, accounting for *boundary layer* clustering
- Large moving walls displacements, including sharp edges

A *Navier-Stokes* mesh accounting for 3.0×10^6 nodes and 14 blocks was used, based on previous works of Debrabandere (2014) for *High Reynolds* simulations. A first cell of 10^{-4}m thickness was imposed, corresponding to a factor of 1.79×10^{-4} with respect to the root chord. Figure 3.29 illustrates the created mesh around the wing.

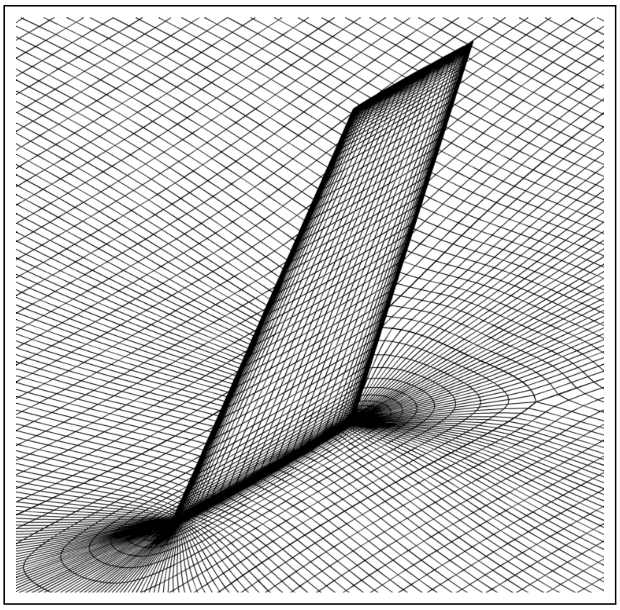

Figure 3.29: AGARD 445.6 mesh detail

Structural model

In order to impose a wing deflection, the 1-way coupling FSI modal approach described in Section 2.2.2 was used. First 4 natural frequencies and mode shapes of the AGARD 445.6 wing were directly obtained from the experimental data published by Yates (1987), see Table 3.7. Two different DLCs were analyzed, referred to as *forced bending* and *forced twist*.

Table 3.7: AGARD 445.6 wing modes

Mode ID.	Frequency [Hz]	Description
1	9.6	1$^{\text{st}}$ bending
2	38.2	1$^{\text{st}}$ torsion
3	48.3	2$^{\text{nd}}$ bending
4	91.5	2$^{\text{nd}}$ torsion

DLC1: Forced bending

A pure bending deflection was imposed, based on the maximum deflections computed by Debrabandere (2014). The 1st bending mode was excited for this purpose (see Table 3.7). A maximum wing tip deflection of 3.95 cm was observed (corresponding to 5.2% of the half span L). Figure 3.30 shows a superposition of original and deflected wing geometries.

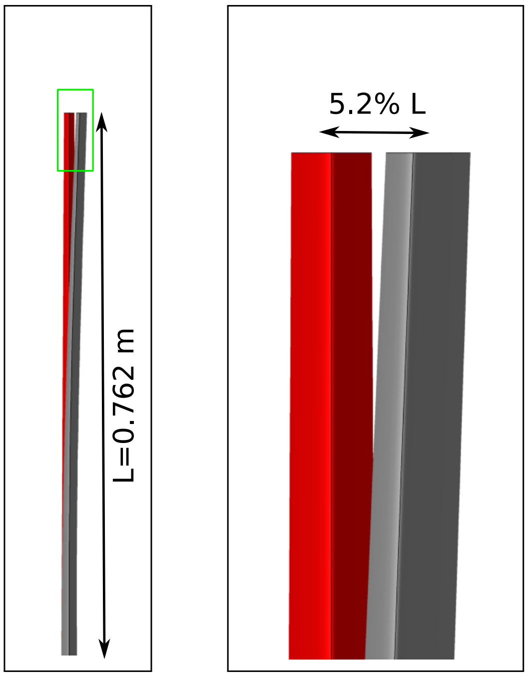

(a) Front **(b)** Detail of blade tip

Figure 3.30: Original (red) and deformed (grey) AGARD 445.6 wing, DLC1

The performance of the developed mesh deformation methods is illustrated in Table 3.8. As already mentioned, classical RBF methods suffered from an unacceptable computational time. This important CPU cost was related to the needed matrix inversion, performed in a *preprocessing* stage. An estimation of this CPU cost, together with the needed memory to store the coefficients matrix is also included in Table 3.8. Both RBF+TFI and RBF+TFI+ELA did not distort original mesh quality. Indeed, due to the low magnitude of the deformation, the resulting meshes of these two methods were equivalent to the original one (Figure 3.31, 3.32, 3.33).

Table 3.8: Mesh quality of original and deformed AGARD 445.6 wing mesh, DLC1

Def. method	OR	AR	ER	Computational Data			
	Min.	Max.	Max.	#Proc	$t_{def,pre}$	$t_{def,call}$	Mem.
Original	77.1	132.0	1.15	-	-	-	-
RBF	-	-	-	-	∼36050	-	∼15700
RBF+TFI	77.1	132.0	1.15	7	0.00	0.04	528
RBF+TFI+ELA	77.1	132.0	1.15	7	0.16	9.5	1530

OR: Orthogonality [deg], *AR*: Aspect Ratio, *ER*: Expansion Ratio
Mem.: Max. memory allocated [MB], divided by number of processors *#Proc*
$t_{def,pre}$: Mesh deformation CPU time [min] per Proc spent in *preprocessing* (once per simulation)
$t_{def,call}$: Mesh deformation CPU time [min] per Proc spent at every call of the method

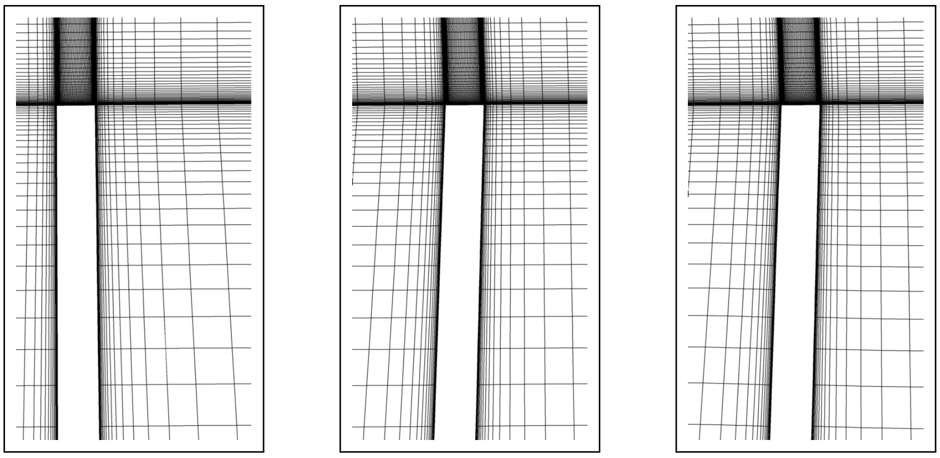

(**a**) Original mesh (**b**) RBF+TFI (**c**) RBF+TFI+ELA

Figure 3.31: AGARD 445.6 spanwise cut at wing tip vicinity, original and deformed meshes (DLC1)

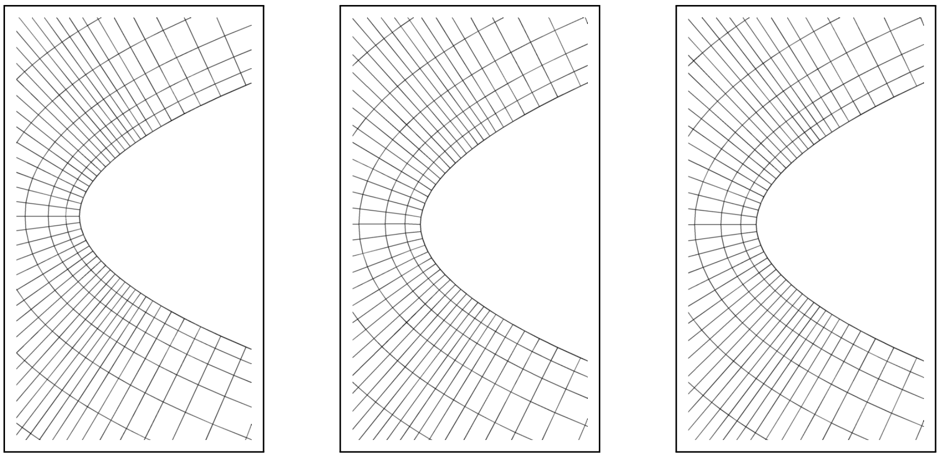

(**a**) Original mesh (**b**) RBF+TFI (**c**) RBF+TFI+ELA

Figure 3.32: AGARD 445.6 leading edge at 90% span, original and deformed meshes (DLC1)

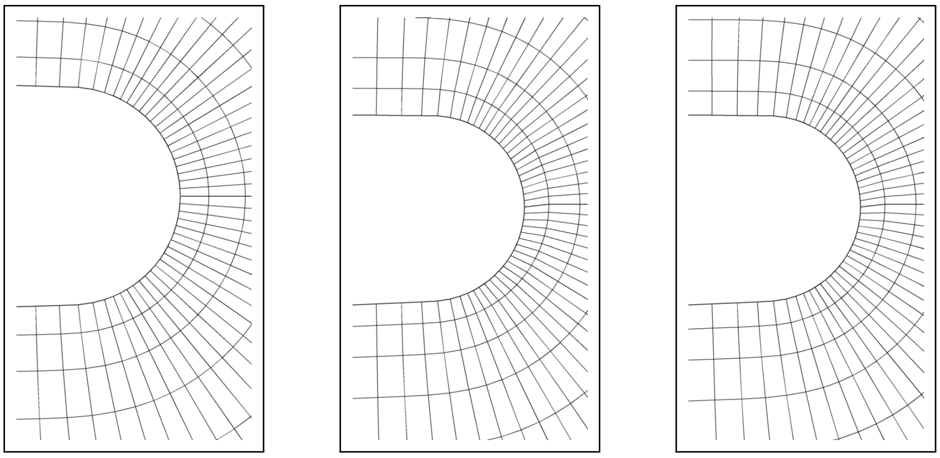

(**a**) Original mesh (**b**) RBF+TFI (**c**) RBF+TFI+ELA

Figure 3.33: AGARD 445.6 trailing edge at 90% span, original and deformed meshes (DLC1)

It can be concluded that for this particular DLC and due to the lack of important induced mesh rotations, the additional computational effort attached to the ELA step of the developed hybrid method is not required. Hence, the RBF+TFI can be seen as a very computationally efficient solution for small to moderate blade deflections. Indeed, only a few seconds were needed in order to deform the mesh with this approach. Due to the important amount of boundary nodes to consider, the inversion of the matrix involved in the application of the full RBF method will require of around 25 days in a single processor.

DLC2: Forced twist

In order to evaluate the performance of the developed methods in an extreme deformation environment, a non-realistic heavy twist deflection was imposed by exciting the 1st twist mode (see Table 3.7). Figure 3.34 shows a superposition of the original and deflected wing geometries. The performance of the developed mesh deformation methods is illustrated in Table 3.9.

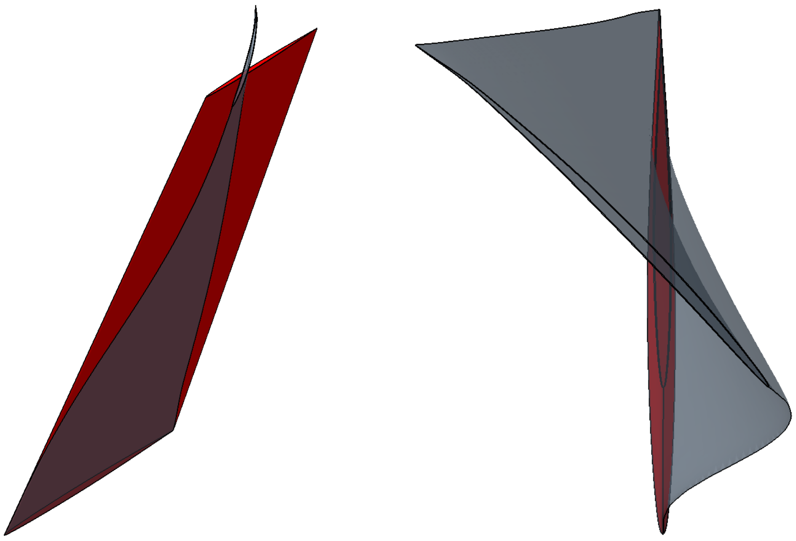

(a) Side view **(b)** Top view

Figure 3.34: Original (red) and deformed (grey) AGARD 445.6 wing, DLC2

As already mentioned, classical RBF methods suffered from an unacceptable computational time. Same remarks done for DLC1 regarding resulting mesh quality and computation details could be made in this case. Even under this important forced deflection, both RBF+TFI and RBF+TFI+ELA hybrid approaches gave overall resulting mesh qualities which were equivalent to the original grid. However a local improvement of the near-wall mesh orthogonality could be attributed to the ELA step. This is illustrated in Figure 3.35, 3.36, 3.37 by means of the cross section meshed at 90% of the wing span.

Table 3.9: Mesh quality of original and deformed AGARD 445.6 wing mesh, DLC2

Def. method	OR	AR	ER	Computational Data			
	Min.	Max.	Max.	#Proc	$t_{def,pre}$	$t_{def,call}$	Mem.
Original	77.1	132.0	1.15	-	-	-	-
RBF	-	-	-	-	∼36050	-	∼15700
RBF+TFI	77.1	132.0	1.15	7	0.00	0.04	528
RBF+TFI+ELA	77.1	132.0	1.15	7	0.16	9.5	1530

OR: Orthogonality [deg], *AR*: Aspect Ratio, *ER*: Expansion Ratio
Mem.: Max. memory allocated [MB], divided by number of processors *#Proc*
$t_{def,pre}$: Mesh deformation CPU time [min] per Proc spent in *preprocessing* (once per simulation)
$t_{def,call}$: Mesh deformation CPU time [min] per Proc spent at every call of the method

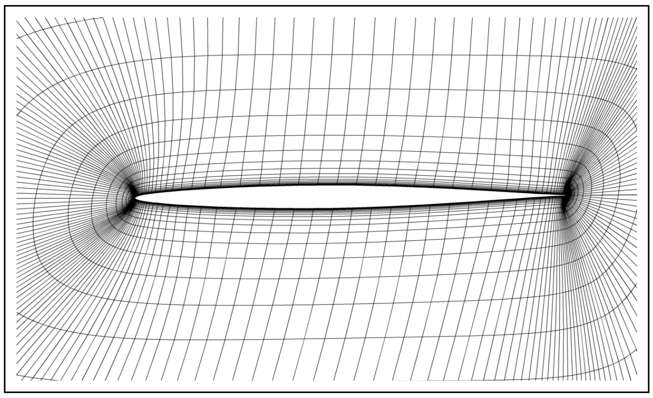

(a) Original mesh

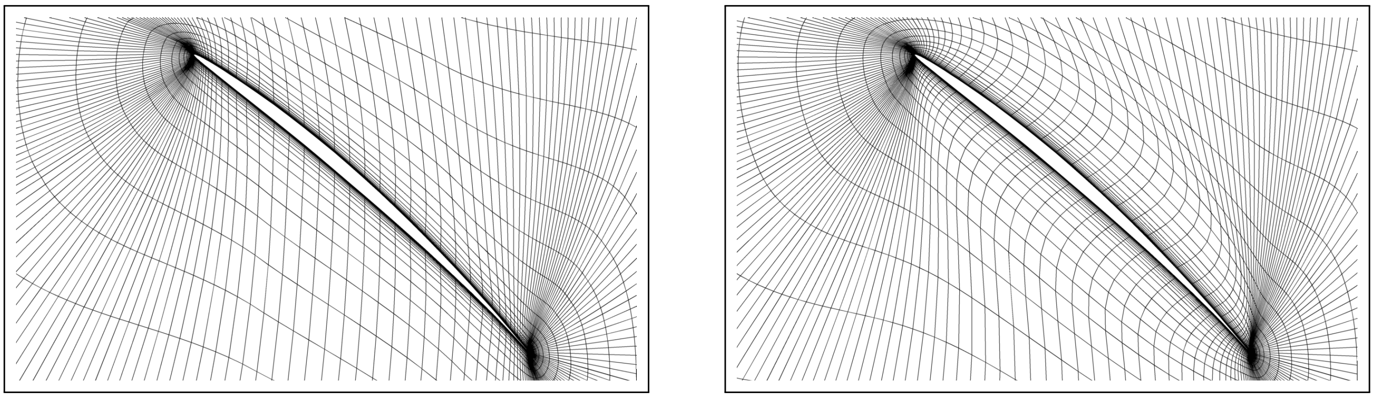

(b) Def. RBF+TFI

(c) Def. RBF+TFI+ELA

Figure 3.35: AGARD 445.6 wing profile at 90% span, deformed meshes (DLC2)

Concluding Remarks

The AGARD 445.6 wing test case has illustrated the benefits of the developed hybrid methods when dealing with multi-million 3D cases. Both RBF+TFI and RBF+TFI+ELA approaches offered a very interesting trade-off between resulting mesh quality and needed computational effort. As a global remark, it could be concluded that under small to moderate deflections (such as structural vibrations), the RBF+TFI did not modify the original near-wall orthog-

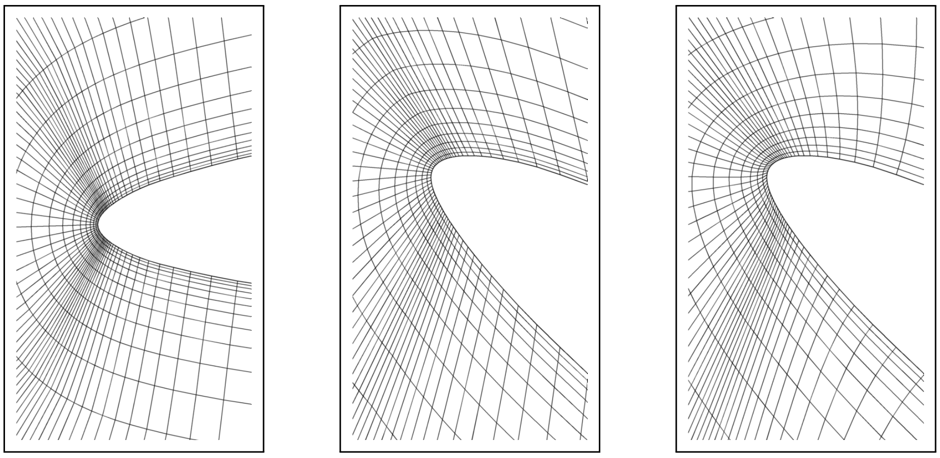

(a) Original mesh **(b)** Def. RBF+TFI **(c)** Def. RBF+TFI+ELA

Figure 3.36: AGARD 445.6 leading edge at 90% span, deformed meshes (DLC2)

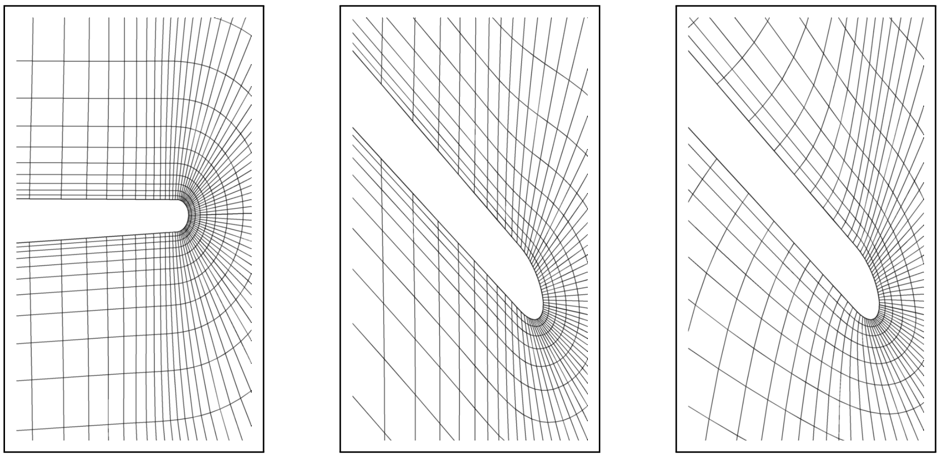

(a) Original mesh **(b)** Def. RBF+TFI **(c)** Def. RBF+TFI+ELA

Figure 3.37: AGARD 445.6 trailing edge at 90% span, deformed meshes (DLC2)

onality of the mesh. When important wing deflections need to be assessed (i.e. extreme DLCs), the last ELA step is required to ensure an accurate *a posteriori* CFD computation.

3.8 Comments about the CPU cost and the mesh size

Table 3.10 compiles the total CPU cost of the mesh deformation process for the developed RBF+TFI and RBF+TFI+ELA *hybrid methods*, together with the results of the traditional RBF approach. All the cases studied in this chapter were listed as a function of the number of mesh nodes: the FFA-w3-241 airfoil (Section 3.7.1), the VIV configuration (Section 3.6) and the AGARD 445.6 wing (Section 3.7.2). Additionally, the results concerning the study of the DTU 10MW RWT wind turbine presented in Section 5.3.2 were also included to have a reacher estimation of the methods scalability. The CPU time is presented in seconds, and it was normalized by the number of nodes of each of the considered grids. It can be observed that for all the meshes, the RBF+TFI was found to be at least two orders of magnitude faster than the rest of approaches. For small meshes such as the FFA-w3-241 or the VIV, the use of the classical RBF approach could still be foreseen, especially when considering its capacity to handle large deflections. However when passing to big 3D meshes like the AGARD 445.6 or the DTU 10MW RWT the problem of scalability of this mesh deformation method became evident. This is illustrated in Figure 3.38, where a graphical representation of the results of Table 3.10 is depicted. The problems of scalability of the RBF motivates the use of the RBF+TFI or the RBF+TFI+ELA approaches as an alternative for this large meshes, when facing small to moderate or large deflections respectively. For the particular case of the DTU 10MW RWT, where the CPU cost of the RBF corresponded to 3.2 s per grid node, a total mesh deformation time of 267 days is to be expected. As it will be shown in Section 5.3.2, the RBF+TFI method was able to deal with the deformation of this wind turbine blade at normal

Table 3.10: Summary of mesh deformation methods CPU cost for each of the studied cases. Values were normalized by the number of nodes of each grid

Considered Grid		**Mesh deformation methods CPU cost [s/node]**		
Case	#Nodes	RBF	RBF+TFI	RBF+TFI+ELA
FFA-w3-241	1.6×10^4	6.00×10^{-5}	3.75×10^{-11}	3.75×10^{-5}
VIV	1.2×10^5	1.65×10^{-5}	5.00×10^{-8}	1.23×10^{-6}
AGARD 445.6	3×10^6	7.21×10^{-1}	8.00×10^{-7}	1.93×10^{-4}
DTU 10MW RWT	7.2×10^6	3.20	2.33×10^{-5}	3.12×10^{-3}

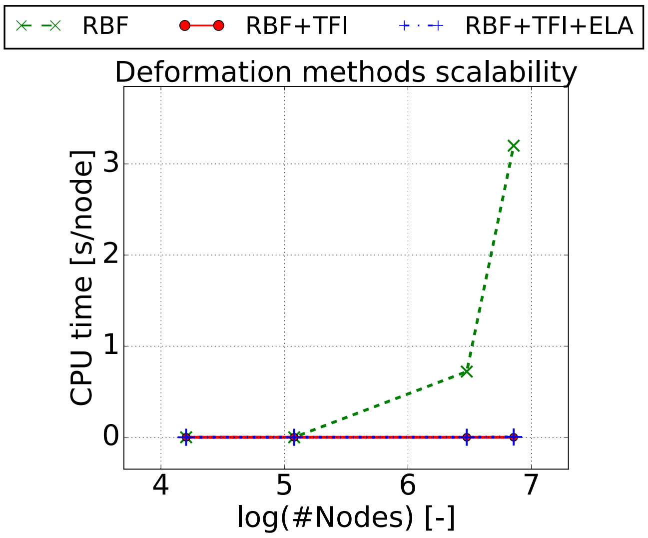

Figure 3.38: CPU cost of the different mesh deformation methods as a function of the number of grid nodes. A logarithmic scale was used for the abscissae

operation with a high quality resulting grid and a total CPU cost of less than 3 minutes.

3.9 Conclusions and future work

A new *hybrid method* for the deformation of multi-block structured meshes of large HAWT rotors was implemented. A combination of consolidated technologies allowed to achieve a good trade-off between deformed mesh quality, scalability and computational cost. In particular, the developed methodology consisted of a first application of the *Radial Basis Function* (RBF), using only the block corners in the interpolation. This allowed to considerably reduce the computational cost attached to the matrix inversion involved in this method when being applied to the whole mesh. The new corner positions of the multi-block structured mesh were used as an input for the *Transfinite Interpolation* (TFI) in order to generate a deformed grid of the whole CFD domain. The quality of this first deformed mesh could be optionally improved by the application of the *Elastic analogy* (ELA). This last step was only necessary when dealing with large displacements and/or large rotations.

An industry-oriented implementation reduced the input needed from the end-user, and ensured the scalability of the method with the number of processors thanks to a MPI-based parallelization. The performance of the developed approach was illustrated in this chapter by means of several mesh deformation scenarios, ranging from academic 2D cases to a 3D mesh around the complete AGARD 445.6 wing. For the latter case the computational cost of the traditional RBF approach in the whole mesh was rated as prohibitive, since the inversion of the coefficients matrix required about 25 days. The developed *hybrid deformation* methodology was found to be a very efficient alternative for this constraining case. Indeed both RBF+TFI and RBF+TFI+ELA approaches were able to deform the whole CFD domain without any mesh folding. A very reduced computational cost was also needed (2 seconds and 10 minutes respectively). The choice between these two *hybrid methods* should be made based on the expected deformations magnitude. Indeed, it was shown that under the existence of large displacements and large rotations, the final ELA step was necessary in order to grantee the near-wall orthogonality of the original mesh. The application of this methodology to a complete HAWT rotor is presented further on in this document in Chapter 5 and Chapter 6.

Future work could be devoted to improve the elastic model included in the method. Additionally, the involved linear interpolator could be also ameliorated in order to take into account mesh induced rotations. This new feature could avoid the use of the last *Elastic analogy* step, that is the most computationally demanding. One of the possibilities in order to model mesh rotations is the implementation of *quaternions algebra*, already used in the *animation* industry by other authors [Johnson (2003); Kavan et al. (2006)].

Chapter 4

Extension of the Non-Linear Harmonic method for 2-way coupling FSI simulations

As introduced in Section 2.1.6, the CFD analysis of big rotor HAWTs requires the consideration of both flow unsteadiness and blade flexibility. The solution of the unsteady flow equations by means of a time marching approach is often too computationally expensive to be fit in the industrial work-flow of a HAWT design. This is the reason why the use of the frequency domain technique referred as the *Non-Linear Harmonic* method (NLH) was adopted in this research [Vilmin et al. (2006)]. In the NLH method the time-dependent Navier-Stokes equations are replaced by a set of harmonic equations, which are less computationally expensive to solve. Due to the strong mutual interaction between the fluid loads and the blade deflections, the consideration of the rotor flexibility requires of a 2-way coupling FSI approach. The integration of such a coupling in a frequency domain flow solver forces the aeroelastic equilibrium equations to be formulated in the harmonic domain as well. While many studies have been conducted regarding the 2-way coupling FSI problem with a time marching approach, only a few researchers have tackled this topic in the harmonic domain. Most part of these publications focused in the study of *Limit Cycle Oscillations* (LCO) by means of the *Harmonic balance* method. In this approach, a harmonic formulation of the aeroelastic equilibrium is included in the CFD solver. Its solution is performed in an iterative way, under the assumption of known structure deformations or known flow conditions (i.e. *Reynolds* and *Strouhal* numbers). To this group belong the works of Dowell et al. (2008) and Besem (2015) about the vortex induced vibrations of cylinders, the F-16 fighter studies of Thomas et al. (2004) and Thomas et al. (2005), and the elastically mounted airfoil analysis included in Thomas et al. (2002) and Liu et al. (2005). A more versatile approach was proposed in Blanc et al. (2010), where the so-called *Time-Harmonic Balance* (THB) method was used. Even if the assumption of periodic flows is still made in the THB technique, the solution of the unsteady Navier-Stokes equations is performed by means of several steady computations running in parallel and coupled by a source term. Each of these simulations represents a given time-step (or snapshot) and they can be solved by means of usual time-domain flow solvers. This allows to solve the aeroelastic equations in a steady-like way for every snapshot. The final deformation transients can be then recomputed by means of harmonic interpolation of each of these solutions.

This chapter describes the development of an innovative 2-way coupling FSI approach integrated in the NLH solver of FINE™/Turbo. The structure was modeled by means of a *Reduced Order Model* (ROM), described by its modal shapes and eigen values. In order to be adaptable to a wide range of potential applications, a generalized formulation of the aeroelastic coupling was adopted. In this way the structure deformations are understood as a set of additional harmonics to be solved by the NLH method, without requiring an *a priori* estimation of their value. The diffusion of these structural deflections into the whole CFD grid was performed with a harmonic adaptation of a *hybrid mesh deformation* method developed within the scope of this PhD and presented in Chapter 3. The works of Debrabandere (2014) regarding the implementation of FSI methods based on the modal approach were taken as an starting point of this development, an they are briefly described in Section 4.1. Due to the lack of experimental data regarding the dynamic aeroelasticity of large rotor HAWTs, the accuracy and performance of the developed methodology are validated in this chapter in the framework of the *Vortex Induced Vibrations* (VIV) of a two-dimensional cylinder in transverse oscillations.

4.1 Existing FSI methods in FINE™/Turbo

As previously introduced in Section 2.2.2, several FSI methods were implemented in FINE™/Turbo in the framework of the PhD thesis of Debrabandere (2014). Of particular interest to this research is the so-called *modal approach*, that assumes a structure model based on a set of eigen frequencies and modal shapes. The *modal approach* was used in FINE™/Turbo in order to perform 1-way and 2-way coupling FSI simulations when dealing with time marching flow solutions. In addition, Debrabandere (2014) extended the capabilities of the NLH method for 1-way coupling computations. The details of these three approaches are briefly described in this section.

4.1.1 Time marching modal approach

In solid mechanics, the inertial reaction of a solid $\mathbf{M}\frac{\partial^2 \vec{u}}{\partial t^2}$ is related to the difference between the external and internal forces ($\vec{f}_S$ and $\vec{i}_S$ respectively):

$$\mathbf{M}\frac{\partial^2 \vec{u}}{\partial t^2} = \vec{f}_S - \vec{i}_S \tag{4.1}$$

where:

- **M** refers to the mass matrix
- $\vec{u}$ is the *deformation* vector, defined from the original node coordinates to the displaced position

When considering a linear system, Equation 4.1 can be written as:

$$\mathbf{M}\frac{\partial^2 \vec{u}}{\partial t^2} + \mathbf{C}\frac{\partial \vec{u}}{\partial t} + \mathbf{K}\vec{u} = \vec{f}_S \tag{4.2}$$

where:

- **C** refers to the damping matrix
- **K** refers to the stiffness matrix

Under the assumption of undamped free vibrations, Equation 4.2 can be written as:

$$\mathbf{M}\frac{\partial^2 \vec{u}}{\partial t^2} + \mathbf{K}\vec{u} = \vec{0} \tag{4.3}$$

In order to have non-trivial solution, Equation 4.3 should satisfy the condition:

$$\det(\mathbf{K} - \lambda \mathbf{M}) = 0 \tag{4.4}$$

Corresponding to an eigenvalue problem, where every solution λ_k can be related to the so-called natural frequencies of the structure f_k:

$$\sqrt{\lambda_k} = 2\pi f_k = \omega_k \tag{4.5}$$

For every eigenvalue λ_k, an associated eigen vector $\vec{\phi}_k$, often referred as the structure mode shape, can be computed by means of:

$$\mathbf{K}\vec{\phi}_k = \lambda_k \mathbf{M}\vec{\phi}_k \tag{4.6}$$

Since we are dealing with a linearized version of the structure, every deformation can be expressed in terms of the mode shapes basis:

$$\vec{u} = \sum_{k=1}^{n_{modes}} q_k \vec{\phi}_k \tag{4.7}$$

Equation 4.7 can be expressed in its matricial form as:

$$\vec{u} = \boldsymbol{\phi} \vec{q} \tag{4.8}$$

By injecting Equation 4.8 into Equation 4.2

$$\mathbf{M}\boldsymbol{\phi} \frac{\partial^2 \vec{q}}{\partial t^2} + \mathbf{C}\boldsymbol{\phi} \frac{\partial \vec{q}}{\partial t} + \mathbf{K}\boldsymbol{\phi} \vec{q} = \vec{f_S} \tag{4.9}$$

Or equivalently:

$$\boldsymbol{\phi}^T \mathbf{M}\boldsymbol{\phi} \frac{\partial^2 \vec{q}}{\partial t^2} + \boldsymbol{\phi}^T \mathbf{C}\boldsymbol{\phi} \frac{\partial \vec{q}}{\partial t} + \boldsymbol{\phi}^T \mathbf{K}\boldsymbol{\phi} \vec{q} = \boldsymbol{\phi}^T \vec{f_S} \tag{4.10}$$

Expressing Equation 4.10 in a basis of scaled mode shapes $\boldsymbol{\phi}_s$ such as $\boldsymbol{\phi}_s^T \mathbf{M} \boldsymbol{\phi}_s = \mathbf{I}$, it can be further simplified [see for instance He and Fu (2001)]:

$$\mathbf{I} \frac{\partial^2 \vec{q}}{\partial t^2} + \boldsymbol{\phi}_s^T \mathbf{C} \boldsymbol{\phi}_s \frac{\partial \vec{q}}{\partial t} + \mathbf{diag}\left[\omega_k^2\right] \vec{q} = \boldsymbol{\phi}_s^T \vec{f_S} \tag{4.11}$$

In the absence of damping Equation 4.11 becomes uncoupled for every mode k, making the solution of the system easier. This simplification is no longer possible with the consideration of the damping through the so-called *generalized damping matrix* or *modal damping matrix* $\mathbf{C_g} = \boldsymbol{\phi}_s^T \mathbf{C} \boldsymbol{\phi}_s$, since generally it is not diagonal. As exposed by Felippa (2016), there are three main approaches to tackle this problem. In the first approach, known as *Direct Time Integration* (DTI), the Equation 4.2 is numerically integrated in time. This allows to keep the original damping matrix without any additional assumption or modal basis transformation. Even if the problem is approached without any loss of generality, the DTI method has the disadvantage of being complex to implement. In addition it requires the complete damping matrix as an input, which may not be available. The second approach for solving this structural problem is referred to as *complex eigen system*, since it usually implies the appearance of complex mode shapes and frequencies. The main philosophy is to transform Equation 4.11 into the *state space* in order to obtain two diagonal matrices that contain the matrices **M**, **C** and **K**. Both the state space transformation and the introduction of the complex mode shapes, which are difficult to physically interpret, significantly difficult the solution of the system. More details regarding this transformation can be found in the PhD thesis of Adhikari (2000). Finally, the third approach works with the original Equation 4.11 but assuming a diagonal damping matrix. On the one hand this *diagonalization* method uncouples the system in a very straightforward manner, simplifying its solution. On the other hand it allows the direct use of the undamped mode shapes and natural frequencies, that can be easily computed with the help of a CSM solver and do have a physical interpretation. These two factors motivated the selection of the *diagonalization* method in Debrabandere (2014). Indeed, for large systems the *diagonalization* approximation was found to be one order of magnitude faster than the *complex eigen system* approach [Adhikari (2000)]. However, the diagonalization of $\mathbf{C_g}$ implies a certain level of approximation. As a general rule, the simplifications performed within this method do not considerably effect the solution when the system is related to a *light damping* (i.e. when $\xi_k << 1$). Several authors have proposed indexes that tried to quantify the error of the *diagonalization* approach by methods based on modal phase difference, modal polygon areas, system response, etc. For a detailed review of this indexes the reader is referred to the PhD thesis of Adhikari (2000). There are two main types of *diagonalization* methods: the *modal damping* and the *Rayleigh damping*. In the *modal damping* the generalized damping matrix is supposed to have the form $\mathbf{C_g} = \mathbf{diag}\,[2\xi_k\omega_k]$, where the ξ_k parameter is known as the *damping ratio* or *damping factor* of the mode k. After the introduction of this simplified expression into Equation 4.11, the system can be uncoupled for every mode k as:

$$\frac{\partial^2 q_k}{\partial t^2} + 2\xi_k\omega_k\frac{\partial q_k}{\partial t} + \omega_k^2 q_k = \vec{\phi}_{k,s}^T\vec{f}_S \tag{4.12}$$

In the absence of experimental results or when the mechanisms of the damping are not completely understood (i.e. the $\mathbf{C}$ matrix is not available), the estimation of ξ_k for every mode remains the only possibility. These guesses rely on previous experiences with similar structures and configurations. Typical damping factors of structures are in the range of 1% to 5%, and they use to increase together with the frequency. In the alternative *diagonalization* technique, the *Rayleigh damping* [Rayleigh (1877)], the damping is assumed to be a linear combination of the mass and stiffness matrix: $\mathbf{C} = \beta_1\mathbf{M} + \beta_2\mathbf{K}$. Introducing this expression into Equation 4.11, it can be decoupled as:

$$\frac{\partial^2 q_k}{\partial t^2} + 2\left[\frac{1}{2}\left(\frac{\beta_1}{\omega_k} + \beta_2\omega_k\right)\right]\omega_k\frac{\partial q_k}{\partial t} + \omega_k^2 q_k = \vec{\phi}_{k,s}^T\vec{f}_S \tag{4.13}$$

The expression $\beta_1/\omega_k + \beta_2\omega_k$ is then acting as the effective damping factor of the *Rayleigh damping*. While the former term aims to damp the lower frequencies of the system, the latter is responsible of the high frequency damping. The main advantage of the *Rayleigh damping* is the estimation of the damping factor of all the modes by choosing its value for two particular frequencies and solving for β_1 and β_2. However, this automatic computation can eventually lead to over-damping of the low or the high frequency range.

Due to its generality, the *modal damping* approach summarized in Equation 4.12 was chosen by Debrabandere (2014). The end user was requested to introduce the linearized behavior of the structure by means of the values of ω_k, ξ_k and $\vec{\phi}_{k,s}$ for every mode. Those were obtained *prior* to the FINE™/Turbo FSI simulation, usually by means of a *modal analysis* performed with a CSM solver. Since the points containing the modal shapes information do not necessarily correspond to the position of the CFD mesh nodes, an additional interpolation step is required. In the implementation of Debrabandere (2014), the *radial basis function* (RBF) interpolation was used for this *pre-processing* task. Two time marching FSI methods based on the *modal approach* were implemented, corresponding to the 1-way coupling (imposed boundary displacements) and 2-way coupling (where the new boundary positions were computed based on the fluid loads). Both methodologies could be easily applied to steady computations by understanding them as unsteady simulations accounting for a single time step.

1-way coupling

For the 1-way coupling approach, the end user is required to enter a set of generalized displacements q_k transients as an input. The solid deformation is directly computed based on Equation 4.8, and diffused into the complete CFD mesh by means of *mesh deformation* algorithms.

2-way coupling

In this case the solid deformation needs to be recomputed based on $\vec{f}_S$, corresponding to the fluid loading. This recomputation is only performed at specific flow inner iterations intervals, chosen by the end-user thanks to the parameter $ITCPL$. The resulting iterative solution procedure for a total number of flow inner iterations $NITE$, a time step Δt and a total simulation time t_{total} is summarized in Figure 4.1.

Different approaches can be used in order to solve Equation 4.12 [Debrabandere (2014)]. For the particular case of an undamped steady application, time derivatives vanish and the direct solution is:

$$q_k = \frac{\vec{\phi}_{k,s}^T \vec{f}_S}{\omega_k^2} \tag{4.14}$$

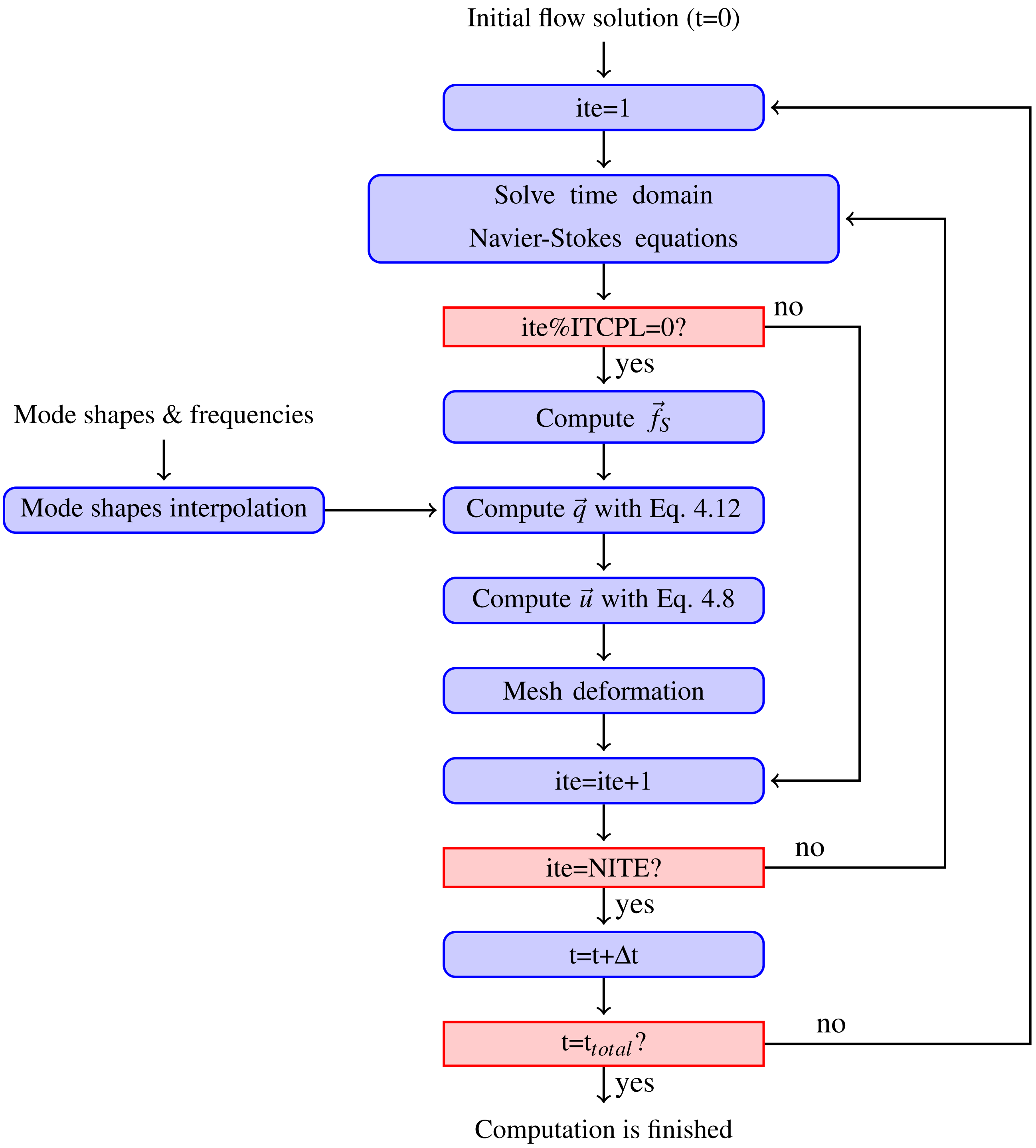

Figure 4.1: Time marching FSI, 2-way coupling with the modal approach

4.1.2 NLH modal approach

The NLH base line formulation was previously adapted to a FSI context by Debrabandere (2014). As a result of the introduction of the mesh deformation, additional terms should be considered for both time mean and harmonic equations during the NLH solution. The time marching 1-way coupling methodology described in Section 4.1.1 was adapted to a NLH formulation, assuming the same modal representation of the structure. Equation 4.8 was re-written in a harmonic context by expressing q_k by means of time-averaged and fluctuation contributions $(\bar{q}_k + q'_k)$. The translation of generalized displacement harmonics into solid boundaries deformation could be then performed as:

$$\bar{\vec{u}} = \sum_{k=1}^{n_{modes}} \overline{q_k}\vec{\phi}_k \tag{4.15}$$

$$\widetilde{u}|_h = \sum_{k=1}^{n_{modes}} \widetilde{q_k}|_h \vec{\phi}_k \tag{4.16}$$

Where $\bar{\vec{u}}$ refers to the time-averaged deformation and $\widetilde{u}|_h$ to the value of the h^{th} harmonic contribution. In the 1-way coupling approach, the user is required to enter the following information for every considered mode k:

- The time-averaged generalized displacement $\bar{q}_k$
- Real and imaginary components of $\widetilde{q_k}|_h$ for every harmonic h

This input allows the direct evaluation of Equation 4.15 for the computation of time-mean and harmonic deformations. In order to diffuse the imposed solid boundaries harmonic displacements into the CFD mesh, the extension of the RBF *mesh deformation* method in the harmonic frequency domain was also required. This was achieved by independently applying the RBF interpolators to time-averaged and harmonic displacements.

4.2 Development of a 2-way coupling NLH method

The implementation of the 2-way coupling approach in the NLH method required the integration of an aeroelastic equilibrium equation. For this development, it was decided to extend the formulation of the time marching 2-way coupling *modal approach* presented in Section 4.1.1 to the harmonic domain. This procedure accounted for two main benefits. On the one hand a generalized formulation was kept, being able to adapt to a wide range of potential applications. On the other hand, it ensured the same aeroelastic coupling for both time marching and NLH approaches. As for the time marching version, the main limitation of this NLH 2-way coupling *modal approach* relies on the linearization of the structure behavior.

The derivation of the NLH method version of the aeroelastic equilibrium equation starts by expressing the generalized displacements and the fluid loads of Equation 4.12 as their time-averaged and harmonic contributions. For the k^{th} mode, the following equation is obtained:

$$\frac{\partial^2 \left(\bar{q}_k + q'_k\right)}{\partial t^2} + 2\xi_k \omega_k \frac{\partial \left(\bar{q}_k + q'_k\right)}{\partial t} + \omega_k^2 \left(\bar{q}_k + q'_k\right) = \vec{\phi}_{k,s}^T \left(\bar{\vec{f_S}} + \vec{f_S}'\right) \tag{4.17}$$

Developing all the terms:

$$\frac{\partial^2 \bar{q}_k}{\partial t^2} + \frac{\partial^2 q'_k}{\partial t^2} + 2\xi_k \omega_k \frac{\partial \bar{q}_k}{\partial t} + 2\xi_k \omega_k \frac{\partial q'_k}{\partial t} + \omega_k^2 \bar{q}_k + \omega_k^2 q'_k = \vec{\phi}^T_{k,s} \overline{\vec{f}_S} + \vec{\phi}^T_{k,s} \vec{f}_S{}' \tag{4.18}$$

Considering that the temporal derivative of a time-averaged quantity is null:

$$\frac{\partial^2 q'_k}{\partial t^2} + 2\xi_k \omega_k \frac{\partial q'_k}{\partial t} + \omega_k^2 \bar{q}_k + \omega_k^2 q'_k = \vec{\phi}^T_{k,s} \overline{\vec{f}_S} + \vec{\phi}^T_{k,s} \vec{f}_S{}' \tag{4.19}$$

4.2.1 Time-mean equations for the aeroelastic equilibrium

Time-mean equation can be derived by time-averaging Equation 4.19:

$$\omega_k^2 \bar{q}_k = \vec{\phi}^T_{k,s} \overline{\vec{f}_S} \tag{4.20}$$

Leading to:

$$\bar{q}_k = \frac{\vec{\phi}^T_{k,s} \overline{\vec{f}_S}}{\omega_k^2} \tag{4.21}$$

4.2.2 Harmonic equations for the aeroelastic equilibrium

By casting into the frequency domain, Equation 4.19 becomes, for the hth harmonic:

$$I^2 \omega_h^2 \widetilde{q}_k|_h + 2I \xi_k \omega_k \omega_h \widetilde{q}_k|_h + \omega_k^2 \widetilde{q}_k|_h = \vec{\phi}^T_{k,s} \widetilde{\vec{f}_S}|_h \tag{4.22}$$

Leading to:

$$\widetilde{q}_k|_h = \frac{\vec{\phi}^T_{k,s} \widetilde{\vec{f}_S}|_h}{\omega_k^2 + I^2 \omega_h^2 + 2I \xi_k \omega_k \omega_h} = \frac{\vec{\phi}^T_{k,s} \widetilde{\vec{f}_S}|_h}{\omega_k^2 - \omega_h^2 + 2I \xi_k \omega_k \omega_h} \tag{4.23}$$

4.2.3 Deformations computation

Once the generalized displacements are computed by means of Equation 4.21 and Equation 4.23, the solid boundaries deformation can be directly recovered as performed for the 1-way coupling NLH approach:

$$\bar{\vec{u}} = \sum_{k=1}^{n_{modes}} \bar{q}_k \vec{\phi}_k \tag{4.24}$$

$$\widetilde{\vec{u}}|_h = \sum_{k=1}^{n_{modes}} \widetilde{q}_k|_h \vec{\phi}_k \tag{4.25}$$

In order to diffuse solid boundaries displacement into the whole CFD mesh, the RBF+TFI *hybrid mesh deformation* method presented in Section 3.6 was extended in order to work in a harmonic framework. As suggested by Debrabandere (2014), developed interpolation routines were independently applied to the time-averaged and real and imaginary harmonic components of computed boundaries deformation. This is illustrated in Figure 4.2. The values of $\widetilde{\vec{u}}|_h$ and $\bar{\vec{u}}$ computed at the boundaries of the structure were used as an input for this *harmonic mesh deformation* process. A first application of the RBF was performed, using only the block corners in the interpolation. The new corner positions of the multi-block structured mesh were then used as an input for the TFI in order to generate a deformed grid of the whole CFD domain. This last process was performed in three-steps: re-computation of the block edges by a 1D version of the TFI, re-computation of the block faces with a 2D extension of this algorithm, and finally the application of a 3D TFI to compute the new position of the block inner nodes.

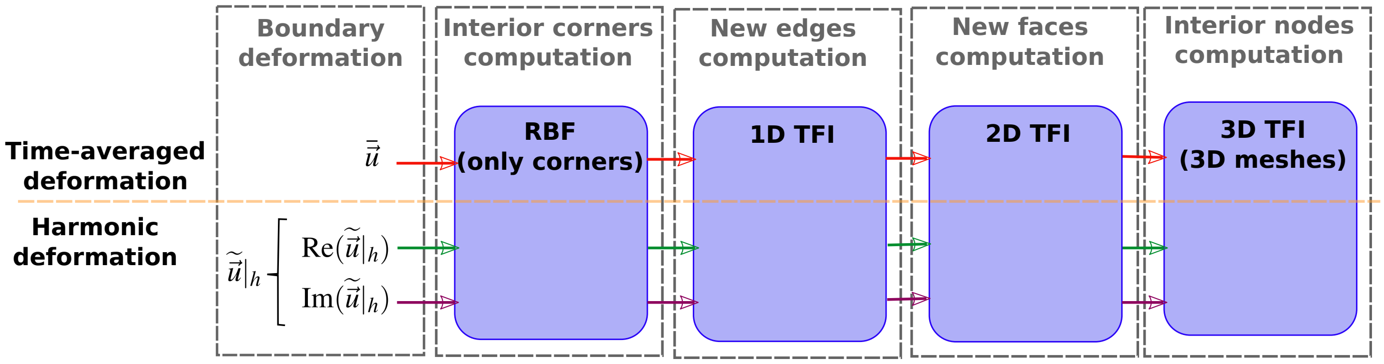

Figure 4.2: Schema of the harmonic adaptation of the *hybrid mesh deformation* method for NLH-based simulations

4.2.4 Implementation details

The harmonic structural equation was implemented in the solver *via* the re-computation of $\bar{q}$ and $\tilde{q}$ based on fluid loads (see Equation 4.21 and Equation 4.23). In order to ensure the stability of the code under the presence of important deformations, an under-relaxation factor $\gamma \leq 1$ was introduced in the update of computed generalized displacements between two consecutive iterations i and $i-1$:

$$\bar{q}_k{}^i = \gamma \bar{q}_k{}^i + (1-\gamma)\,\bar{q}_k{}^{i-1} \tag{4.26}$$

$$\widetilde{q}_k|_h^i = \gamma \widetilde{q}_k|_h^i + (1-\gamma)\,\widetilde{q}_k|_h^{i-1} \tag{4.27}$$

Generalized displacements re-computation was only performed at specific flow iterations intervals, chosen by the end-user thanks to the parameter *ITCPL* in the FINE™/Turbo interface. The solution was rated as converged when the flow variables residuals criteria was satisfied and the generalized displacements were stabilized. The resulting iterative solution procedure for a total number of flow iterations $NITE$, structural modes $NMODES$ and harmonics $NHARMO$ is summarized in Figure 4.4.

4.3 Validation case: 2D cylinder

To the best of author's knowledge, no experimental data regarding the dynamic aeroelasticity of large rotor HAWTs was available when this PhD research was carried out. As an alternative for the validation of the presented harmonic FSI 2-way coupling methodology, the use of a simple two-dimensional geometry was considered. To simplify the numerical set-up, a *non-rotating* problem was targeted. An alternative source of flow unsteadiness was then required for the application of the NLH method, rather than the *rotor/stator* or *rotor/rotor* interactions. In this context the so-called *vortex shedding* phenomenon was selected. In particular, a validation test case consisting on a cylinder mounted on a single degree of freedom elastic system which is excited by *vortex shedding* is presented here (see Figure 4.3). To focus in the testing of the proposed FSI strategy, the eventual influences of the turbulence modeling were avoided by only considering simulations in the laminar regime.

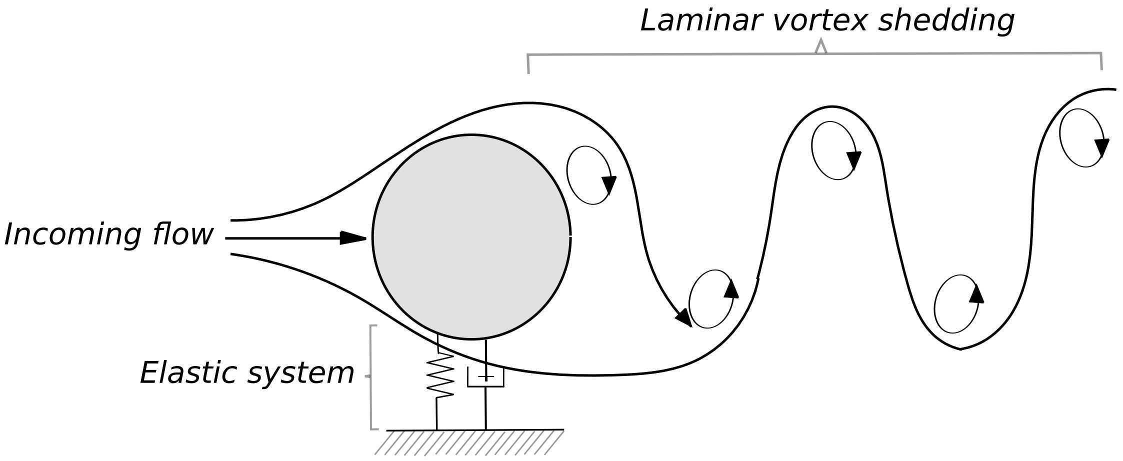

Figure 4.3: Validation test case for 2-way coupled approach

In order to achieve a deep understanding of the flow prior to this final validation, a step-by-step approach was followed. Both the targeted problem and the used numerical methods were complexified as shown in Table 4.1. For all the stages concerning flow unsteadiness, both NLH and time marching computations (based on dual-time stepping of Jameson (1991)) were performed.

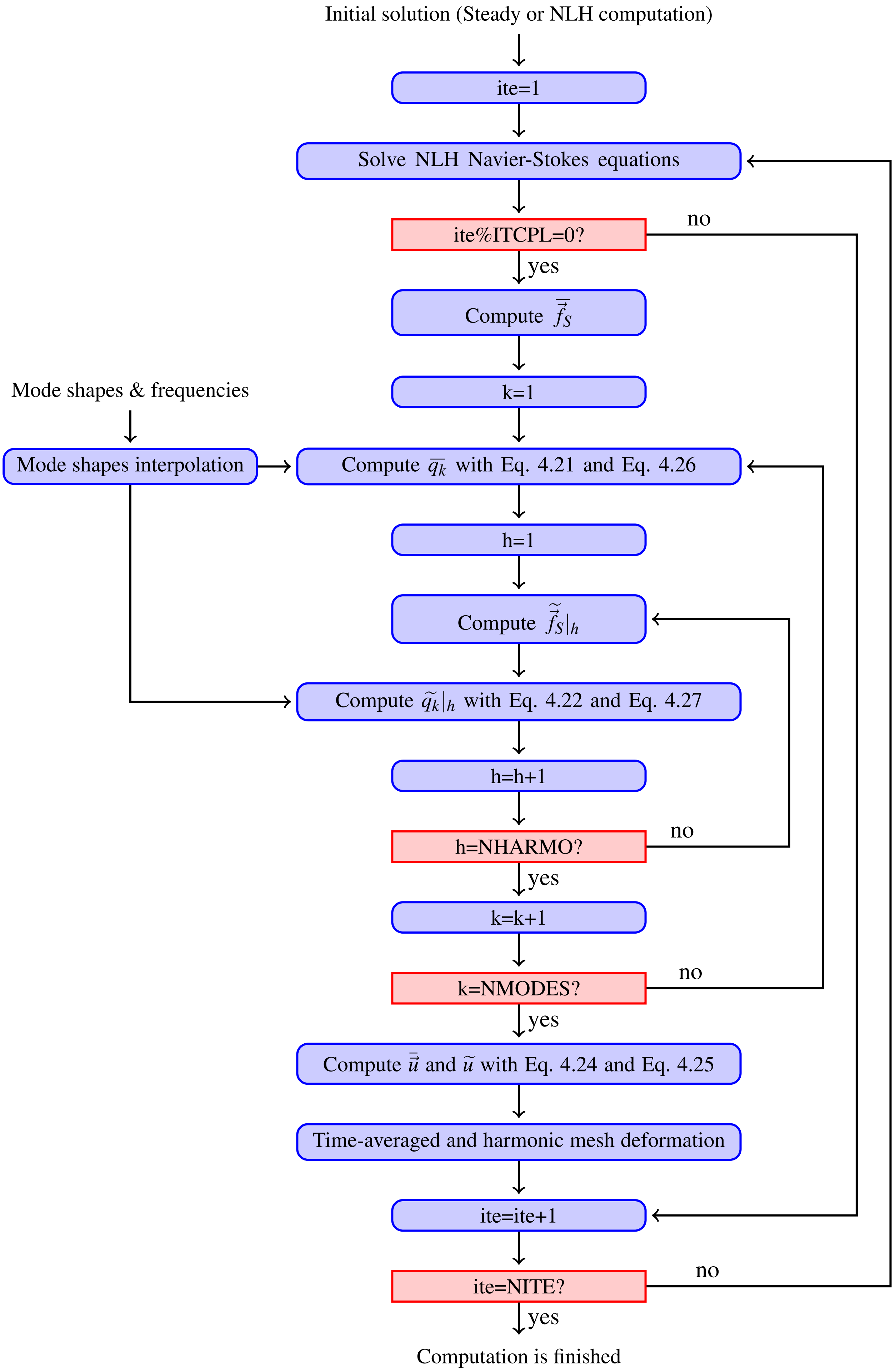

Figure 4.4: NLH FSI, 2-way coupling with the modal approach

Table 4.1: Summary of the step-by-step validation process for the harmonic FSI 2-way coupling approach. LNS acronym refers to *Laminar Navier-Stokes*

Cylinder motion	**Flow**	**Fluid methods**	**FSI methods**	**Reference**
Fixed	Steady	Steady (LNS)	N/A	Section 4.3.3
Fixed	Unsteady	Time marching (LNS), NLH (LNS)	N/A	Section 4.3.4
Forced motion	Unsteady	Time marching (LNS), NLH (LNS)	1-way coupling	Section 4.3.5
Free oscillation (elastic system)	Unsteady	Time marching (LNS), NLH (LNS)	2-way coupling	Section 4.3.6

4.3.1 Scope of the problem

Under certain flow conditions, the flow passing a circular cylinder separates leading to a pattern of unsteady swirling vortices, often referred as *von Karman street* or *vortex shedding*. The nature of this phenomenon is governed by the *Reynolds number* (*Re*), defined as:

$$Re = \frac{DU_\infty}{\nu} \tag{4.28}$$

Where D is the diameter of the cylinder, U_∞ is the freestream velocity and ν is the kinematic viscosity of the fluid.

For *Re* values lower than approximately 5, no recirculation is observed. This situation, sketched in Figure 4.5a, is often referred as *creepy flow*. For $5 \lesssim Re < 40$, stationary downstream vortices are observed, remaining attached to the cylinder (Figure 4.5b). In the range $40<Re<150$, the generation of a laminar *von Karman street* appears (Figure 4.5c). After this value, the shed vortices starts to transition from laminar to turbulent. At approximately $Re=300$, the *von Karman street* is already fully turbulent. The same behavior is observed up to $Re \lesssim 3\times10^5$ (Figure 4.5d). When increasing *Re* after this region, the laminar boundary layer starts to transition towards a turbulent state. The cylinder wake becomes narrower and disorganized, and the *vortex shedding* is not observed (Figure 4.5e). A re-establishment of the turbulent vortex street is found again for $Re \geqslant 3.5\times10^6$, where a turbulent boundary layer is also noticed (Figure 4.5f). In order to avoid the uncertainties that turbulence could introduce in the presented validation, only the *Re* range corresponding to the laminar *von Karman street* generation is considered.

The natural frequency of shed vortices f_{shnat} is determined by the *Strouhal number* (*St*), a dimension-less parameter that in the context of a cylindrical shape can be written as Equation 4.29. The value of *St* has shown a direct dependency with the considered *Reynolds number*, as shown in Figure 4.6. In the laminar vortex shedding region, a monotonic increase

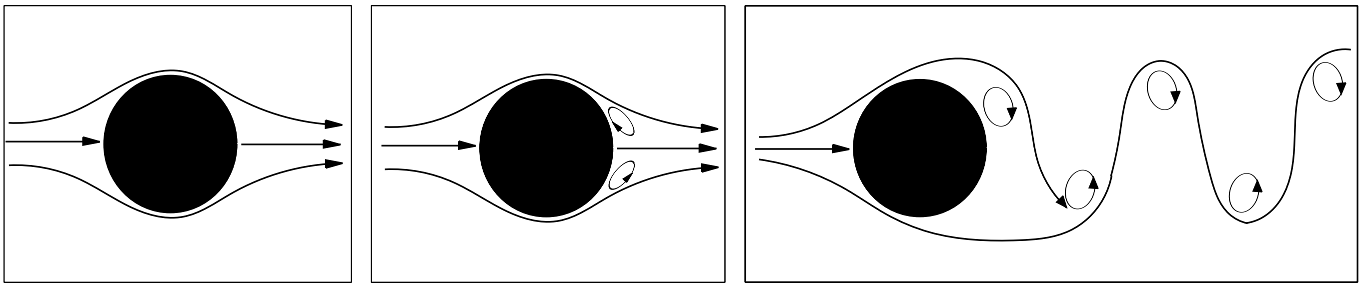

(a) $Re < 5$ **(b)** $5 \lesssim Re < 40$ **(c)** $40 \leq Re < 150$

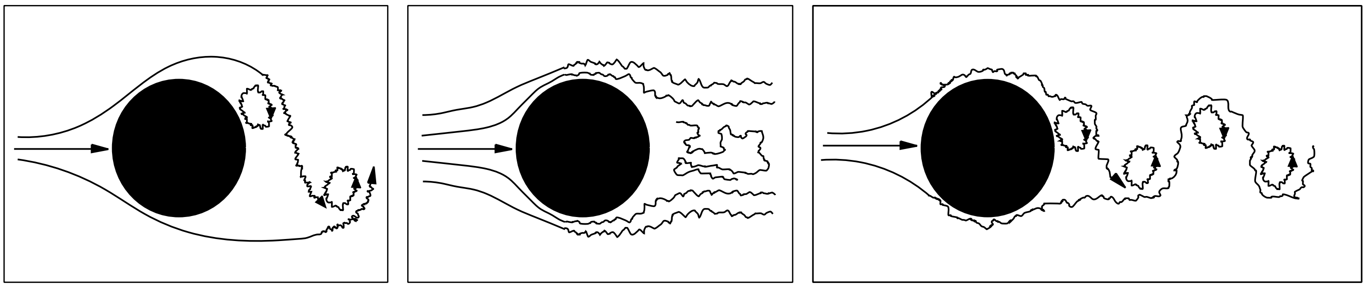

(d) $150 \leq Re \lesssim 3 \times 10^5$ **(e)** $3 \times 10^5 \lesssim Re < 3.5 \times 10^6$ **(f)** $Re \geqslant 3.5 \times 10^6$

Figure 4.5: Regimes of flow across a cylinder, reproduced from Lienhard (1966)

of the *St* value with respect to *Re* is observed. A stabilization of *St* around 0.2 is expected when the turbulence on the wake is completely developed. When the laminar to turbulence transition appears in the boundary layer of the cylinder, the computation of *St* showed an important dispersion (due to the absence of a clear *Von Karman street*). When the *vortex shedding* re-appears for $Re \geqslant 3.5 \times 10^6$, Strouhal numbers higher than 0.2 are to be considered.

$$St = \frac{D f_{shnat}}{U_\infty} \equiv f\left(Re\right) \tag{4.29}$$

Generated vortices can induce unsteady forces, leading to potentially dangerous vibrations on the structure. This problem is known in the literature as *Vortex induced vibrations* (VIV). Many authors have studied the VIV phenomenon by imposing a harmonic cylinder oscillation characterized by an A_F amplitude and a forced frequency f_F [see the review paper by Williamson and Govardhan (2004)]. In this configuration, a regime of synchronization (also referred as *lock-in*) was first observed by Bishop and Hassan (1964). In the *lock-in region*, the *von Karman* shedding frequency f_{shed} synchronizes with f_F, leading to a unique characteristic frequency for the aeroelastic system. Outside of this region, the shedding phenomenon occurs at the natural frequency of shed vortices f_{shnat}, which does not necessarily correspond to f_F. As shown in Figure 4.7, the existence of the lock-in effects depends on both the amplitude of the forced oscillations and the ratio between the forced frequency and f_{shnat}.

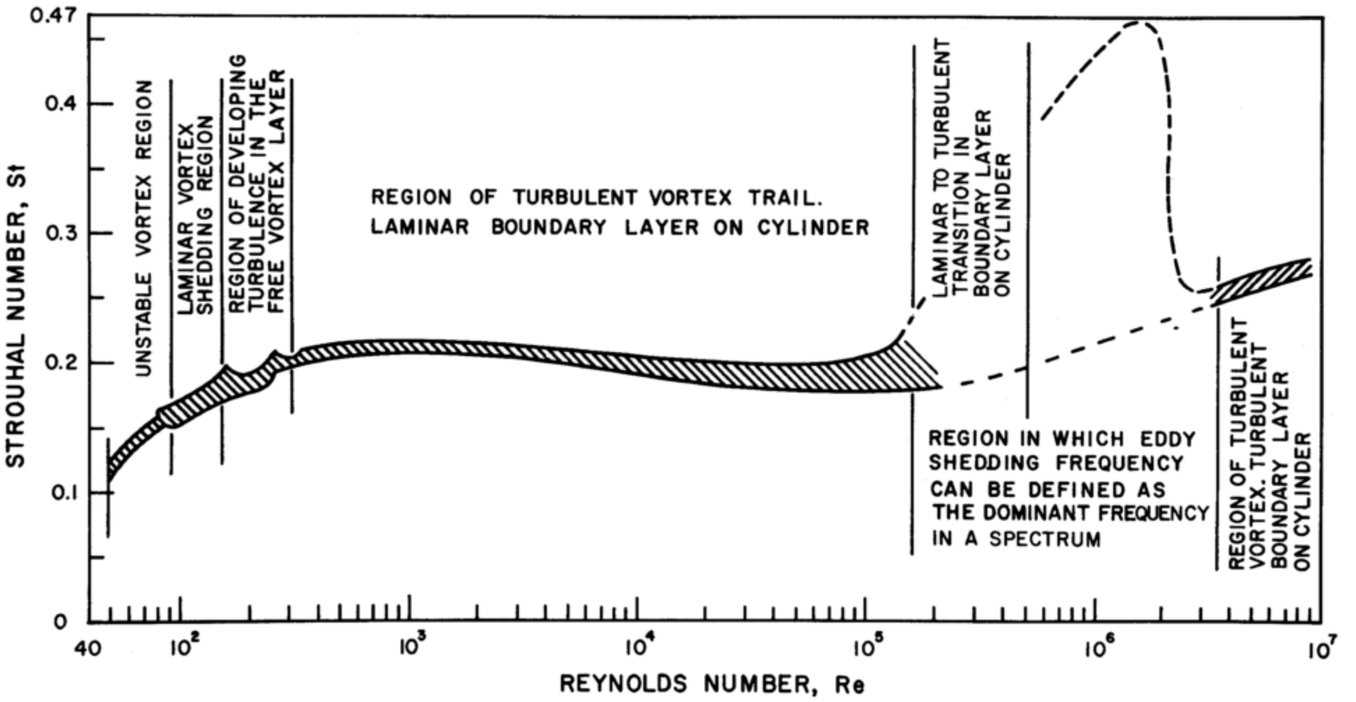

Figure 4.6: Strouhal number evolution with respect to the Reynolds number [source:Lienhard (1966)]

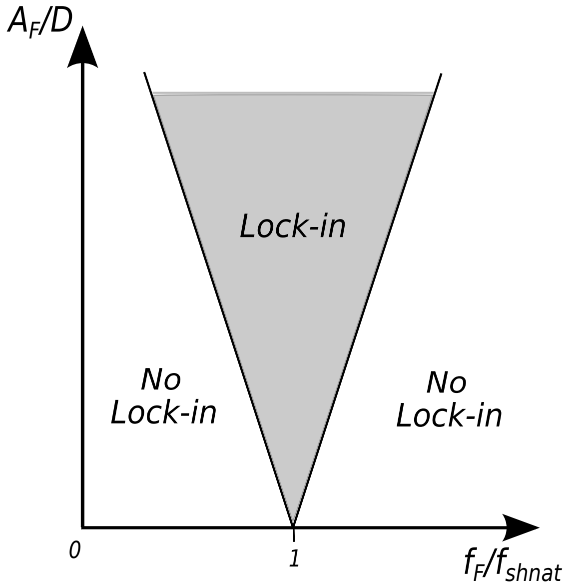

Figure 4.7: Sketch of the lock-in region for a forced oscillation cylinder, adapted from Spiker et al. (2006)

The complexity of the VIV phenomenon is highly increased when considering a *freely oscillating cylinder*. Several authors have assessed this topic, both from experimental and numerical points of view, by attaching a cylinder to an elastic system, composed by one or several springs. Of particular interest to this research are the so-called *transversal oscillations*, where the spring is installed normal to the incoming flow. In such context, the cylinder amplitudes present a strong dependency with the fluid behavior. Maximum amplitude values were found to occur under the so-called *lock-in* conditions, understood here as a synchronization of the oscillator frequency with the shedding frequency of the flow [Griffin et al. (1973)]. In the laminar regime, it was found that the maximum amplitude of a cylinder undergoing transverse oscillations is approximately 60% of its diameter. The existence of a limit in the computed oscillations was justified by Mittal and Kumar (2001) by means of three different mechanisms in the flow. First, the loads exerted by the fluid are reduced under the existence of high amplitude motions. Secondly, the appearance of additional frequencies in the fluid loads spectra. Thirdly, a slight frequency shifting of the shedding frequency with respect to the oscillator frequency (referred as *detuning*). The properties of the elastic system are also an aspect to consider due to its important impact on cylinder oscillations. Williamson and Govardhan (2004) compiled a set of experimental and computational results in the laminar regime that revealed a strong dependency of the structural damping ratio and the cylinder mass on the measured oscillations. The maximum displacements were observed for low values of the product of the reduced mass and the structural damping of the oscillator. Cylinder oscillation amplitudes not only depend on the properties of the oscillator but also on the flow conditions. This fact was highlighted in the experimental works of Anagnostopoulos and Bearman (1992). A strong dependency with the considered *Reynolds number* was showed, since the *lock-in* phenomenon was triggered by the conditions of the flow. The combined impact of the *Reynolds number* and the damping ratio in the aeroelastic response of the system was reviewed in the thesis of Klamo (2007). The use of the so-called *effective stiffness* k^*_{eff} was suggested as a way to compare the results of two different systems undergoing VIV transversal oscillations. This dimensionless parameter accounts for the combined effects of the cylinder mass, as well as the stiffness and damping of the oscillator. The *effective stiffness* was found to collapse the maximum amplitudes of the different performed experiments at a value of k^*_{eff}=2.5, regardless the conditions of the flow or the elastic system. The values of those maximum amplitudes were found to have a dependency on both the Reynolds number and the damping.

4.3.2 Problem set-up

A 2D mesh was generated around a D diameter cylinder, reproduced from the works of Hakimi (1997). This *base* grid accounted for a total of 28.340 nodes and was based on a OH topology (see Figure 4.8). A first cell height of 10^{-4}D was imposed around the cylinder wall. The compressible laminar Navier-Stokes equations were solved for all the presented simulations. A subsonic regime was assumed, with maximum *Mach* numbers of approximately 0.5 for the considered compressible flow conditions. The fluid was considered to be thermodynamically perfect. An arbitrary span of L was assumed for the computation of the cylinder loads.

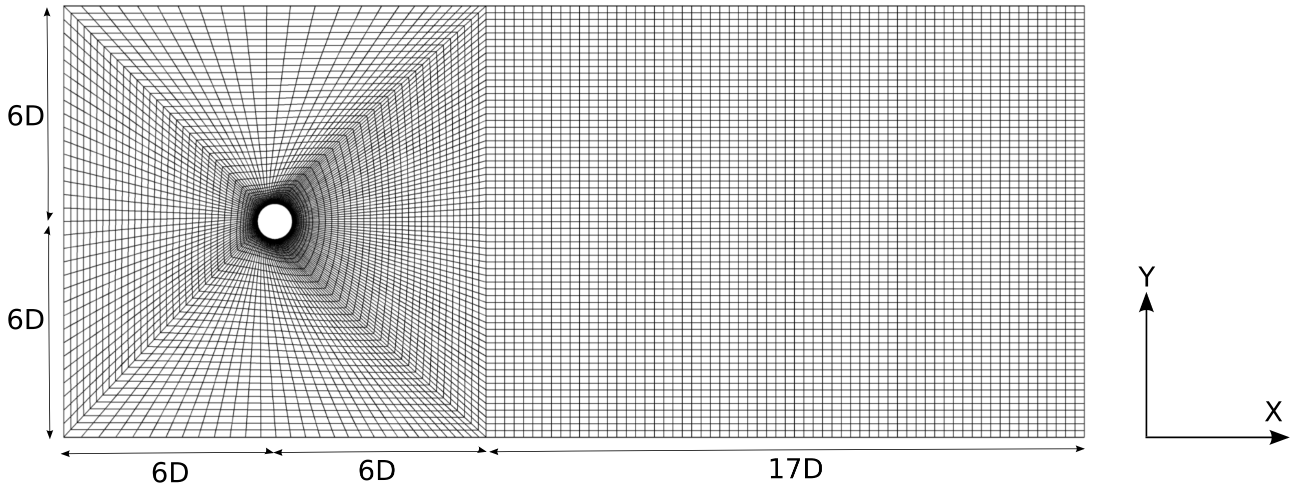

Figure 4.8: Cylinder mesh, D refers to the cylinder diameter

4.3.3 Steady computations, fixed cylinder

In order to analyze the influence of the grid on the computed results, several variants of the *Base* mesh presented in Section 4.3.2 were created. The number of points of the O-block was modified in order to create a finer mesh (referred as *Fine*) and two coarser grids (*Coarse* and *Vcoarse*). The first cell height was also modified according to the number of grid points. A detail of the mesh around the cylinder for each of these configurations is included in Figure 4.9.

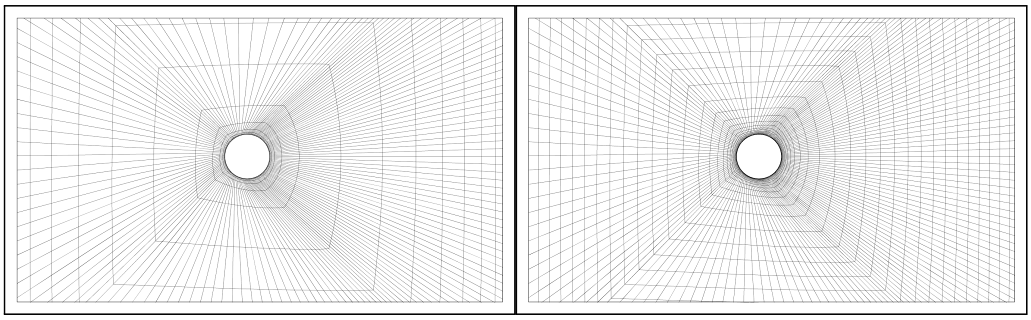

(a) Vcoarse (13652 nodes) **(b)** Coarse (18548 nodes)

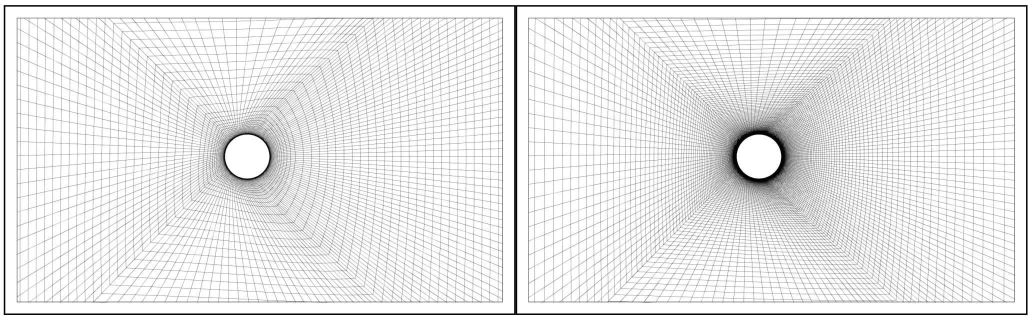

(c) Base (28340 nodes) **(d)** Fine (47924 nodes)

Figure 4.9: Mesh detail around the cylinder for the different considered variants

Steady computations were performed for each variant at Re=75,80,120 and 150. The value of Cp at the wall was computed, being:

$$Cp = \frac{p - p_\infty}{\frac{1}{2}\rho U_\infty} \tag{4.30}$$

where p is the pressure at the wall, p_∞ the free-stream pressure and ρ the fluid density.

Figure 4.10 depicts the predicted Cp values for Re=75 and Re=150 as a function of the angle θ, that is shown in Figure 4.11. The well known solution for a potential flow is also included in Figure 4.10 for reference. The effects of mesh refinement could be noticed when comparing the results of *Vcoarse* with the other grid variants. In fact, an indistinguishable Cp evolution was observed for *Coarse*, *Base* and *Fine* configurations. All simulations exhibited a *plateau* at the vicinity of θ=180 deg. This behavior is not present in the inviscid potential solution, that assumes an irrotational flow. Indeed, downstream flow separation was observed for all the performed simulations. To illustrate this issue, a visualization of the flow corresponding to the *Base* mesh computation at Re=75 is displayed in Figure 4.12.

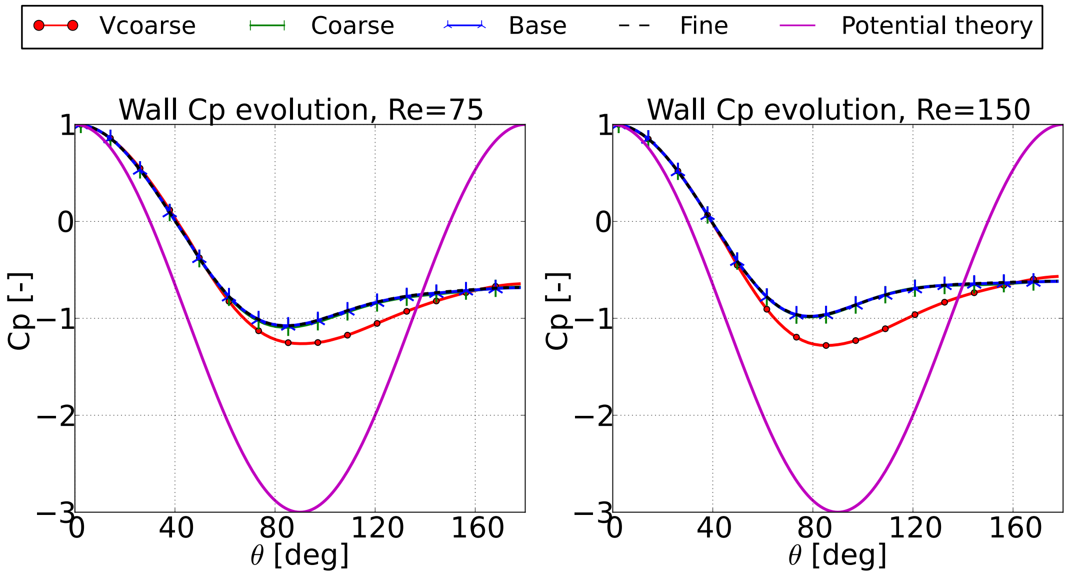

(a) Re=75 **(b)** Re=150

Figure 4.10: Evolution of Cp coefficients at the wall for different mesh variants. Includes analytical solution for potential flow, where $Cp = 4\left(1 - sin^2(\theta)\right)$. Markers do not correspond to data sampling

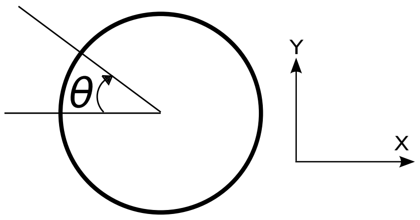

Figure 4.11: Definition of θ

Symmetrical downstream vortices were observed, as it is illustrated in the flow streamlines and the vorticity field $\nabla \times v = \frac{\partial v_y}{\partial x} - \frac{\partial v_x}{\partial y}$ (Figure 4.12a and Figure 4.12b respectively). These recirculations were found to have a direct influence on the pressure around the cylinder, as it is depicted in Figure 4.12c.

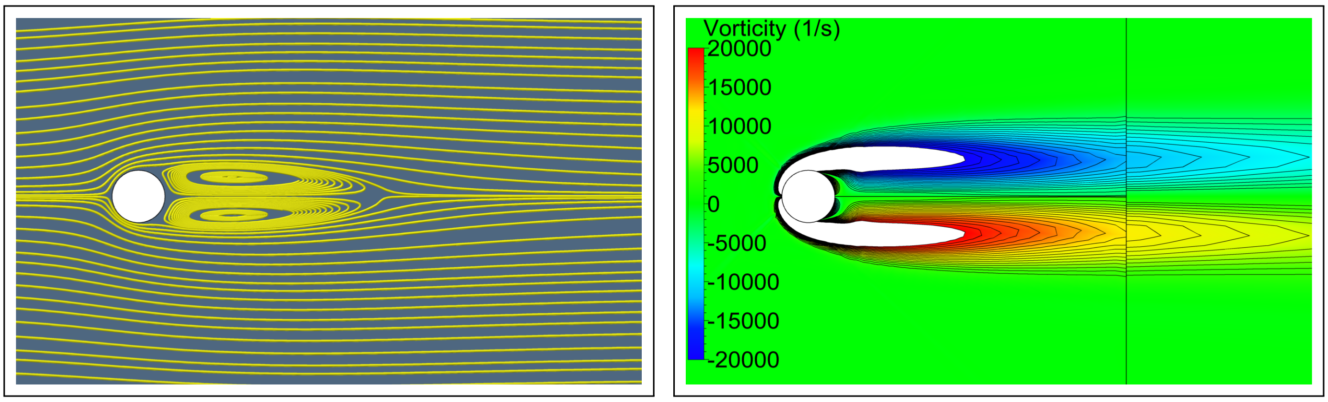

(a) Streamlines

(b) Vorticity

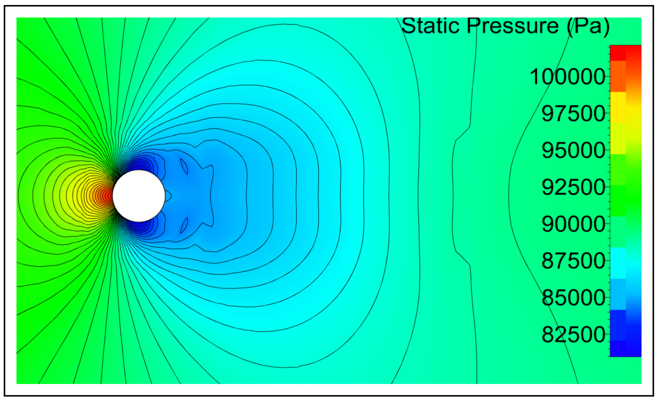

(c) Static Pressure

Figure 4.12: Flow visualization for steady computation at Re=75, *Base* mesh. Vorticity isolines displayed every 1000 s^{-1}. Solid lines represent block lines. Static pressure isolines displayed every 400 Pa.

Table 4.2 compiles the *Drag coefficient* values computed for each of the performed computations, defined as:

$$C_D = \frac{F_x}{\frac{1}{2}\rho U_\infty^2 LD} \tag{4.31}$$

where F_x the force oriented in streamwise direction of the upstream flow.

Stabilized values were observed for *Coarse*, *Base* and *Fine* variants, with differences of less than 0.3%. Figure 4.13 shows a graphical representation of this fact, where the computed values were normalized by the C_D of the *Base* configuration at Re=75. A reduction on the predicted drag was observed when increasing the *Reynolds number*, with a total drop of 17% when passing from Re=75 to Re=150. From the presented results, it can be concluded that the *Base* mesh offered an accurate flow prediction at the studied *Reynolds number* range with regards to the grid refinement. However, the comparison of the computed stabilized C_D values with the experimental reference included in Table 4.2 shows discrepancies ranging from 12% to 23% and being more important at higher Reynolds. This drag reduction predicted by the simulations is related to the effects of the flow unsteadiness, than could not be captured with a steady solution. Indeed, the flow behavior presented in Figure 4.12 does not account for the *vortex shedding* phenomenon, that will be modeled in Section 4.3.4 by means of harmonic and time marching unsteady computations.

Table 4.2: Mesh dependency study on C_D for steady cylinder computations. Experimental values estimated from Wieselberger (1921)

C_D	Re=75	Re=80	Re=120	Re=150
Vcoarse	1.451	1.426	1.279	1.210
Coarse	1.312	1.288	1.151	1.089
Base	1.312	1.288	1.150	1.089
Fine	1.308	1.284	1.148	1.086
Experimental	1.481	1.459	1.367	1.344

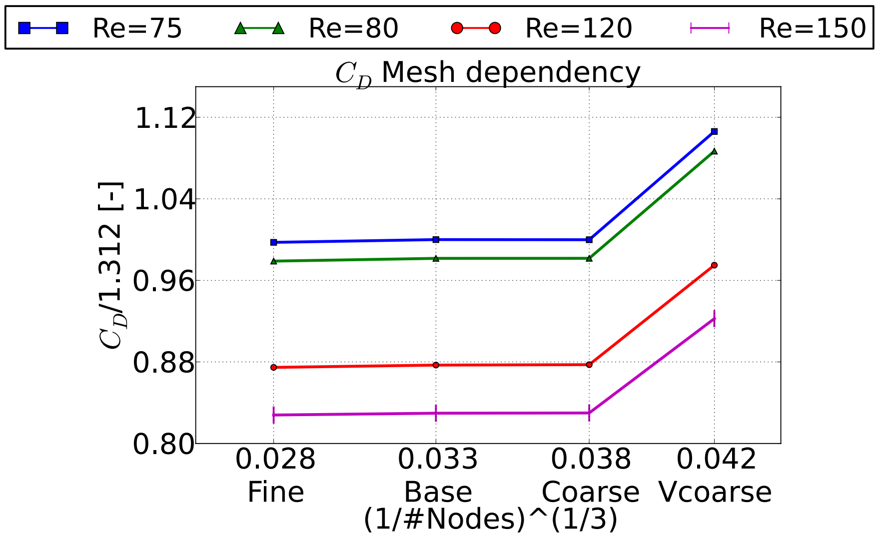

Figure 4.13: Computed C_D for the studied meshes, normalized by the value of the *Base* variant at Re=75

4.3.4 Unsteady computations, fixed cylinder

First unsteady computations assumed a fixed cylinder. Both NLH and *time marching* computations were performed, starting from the already converged steady solutions of Section 4.3.3. Four *Reynolds numbers* in the range [75,150] were studied. For the NLH approach, the impact of the number of harmonics on the computed results was also assessed. Table 4.3 summarizes the performed experiences.

Table 4.3: Fixed cylinder, summary of performed computations (highlighted in grey)

Numerical approach	**Re=75**	**Re=80**	**Re=120**	**Re=150**
NLH 1 harmo	■	■	■	■
NLH 2 harmo		■	■	■
NLH 3 harmo				■
Time marching		■	■	

NLH computations

First NLH computations accounted for a single harmonic. The solved frequency (i.e. the solved *Strouhal number*) was imposed prior to the run of the computation. In opposition to rotating machinery applications, where flow unsteadiness is related to the *blade passing frequency* (BPF), the frequency of the *Von Karman* street could not be directly pre-computed for this test case. In order to solve this issue, an iterative *shedding frequency* identification strategy known as the *phase error method* was used. This technique was initially developed by Spiker et al. (2006) when applying the *Harmonic balance* method to the same test case, and subsequently used for similar purposes in Spiker et al. (2009) and Besem (2015).

Let consider the results of a *Re*=75 simulation with a solved *Strouhal number* of 0.139, obtained based on an *a priori* estimation. An undamped periodic oscillatory behavior of the harmonic lift acting on the cylinder was observed during the NLH solver iterations (see Figure 4.14). Based on the observations of Spiker et al. (2006), this fact reveals that the solved frequency did not correspond to the natural shedding frequency f_{shnat} for these flow conditions.

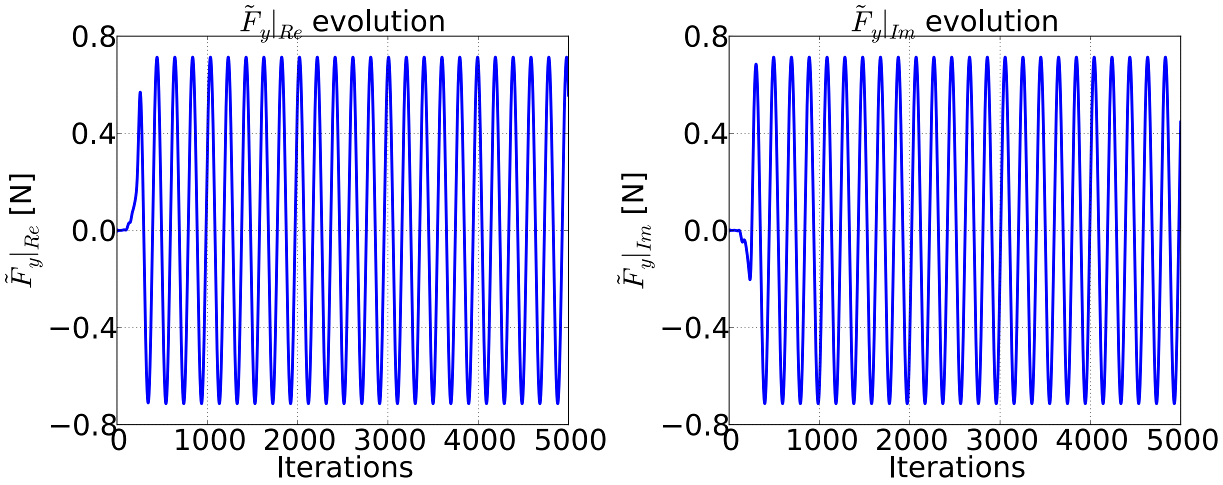

(a) Real part

(b) Imaginary part

Figure 4.14: Fixed cylinder, harmonic lift vs. solver iterations, *Re*=75, solved St=0.139

We can define now the *phase change per iteration* $\Delta\alpha$ of a harmonic quantity $\tilde{Q}$ as the phase difference between two subsequent iterations i and $i-1$:

$$\Delta\alpha(\tilde{Q})|_i = \alpha(\tilde{Q})|_i - \alpha(\tilde{Q})|_{i-1} \,, \tag{4.32}$$

$$\alpha(\tilde{Q}) = \mathrm{atan}\left(\frac{\tilde{Q}|_{Im}}{\tilde{Q}|_{Re}}\right) \,, \tag{4.33}$$

Where *Re* and *Im* refer to the *real* and *imaginary* parts of the harmonic quantity, respectively. The $\Delta\alpha$ related to the harmonic of the cylinder lift force was found to be stable after 300 iterations (see Figure 4.15). As for the *Harmonic balance* approach, converged $\Delta\alpha(\widetilde{F}_y)$ values showed a quasi-linear dependence with respect to the solved St. This allowed to identify the *natural Strouhal number* St_{shnat}, corresponding to f_{shnat}, by an iterative process (see Figure 4.16). The minimization of $|\Delta\alpha(\widetilde{F}_y)|$ was considered as converged when a value lower than 0.1 deg was found. For this particular configuration, a value of $|\Delta\alpha(\widetilde{F}_y)|$ of 0.06 deg was computed after four NLH computations, corresponding to a final St_{shnat}=0.147. For this simulation, the oscillation of the harmonic lift force observed in Figure 4.14 vanished. The numerical stability of this final computation could be equivalently observed during the simulation, since the residuals of the harmonics showed faster decay slopes. This remark is in accordance with the application of the *phase error* methodology on the *Harmonic balance* performed by Besem (2015).

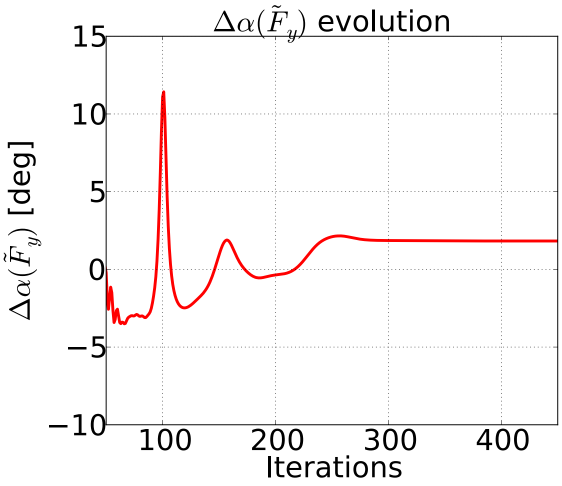

Figure 4.15: Fixed cylinder, $\Delta\alpha(\widetilde{F}_y)$ [deg] vs. solver iterations, Re=75, solved St=0.139

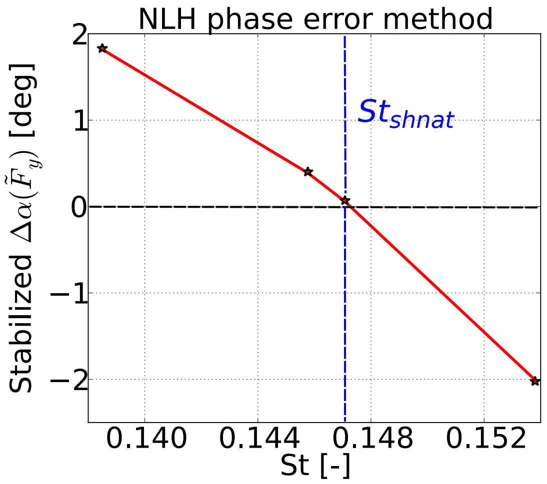

Figure 4.16: Fixed cylinder, stabilized $\Delta\alpha(\widetilde{F}_y)$ for different solved Strouhal numbers, Re=75

The same *phase error* methodology was successfully applied to other *Reynolds numbers* and to multi-harmonic simulations (also accounting for the harmonics of the solved St). The consideration of the interactions between the harmonics of the flow was adopted as a standard for all the multi-harmonic NLH computations presented in this chapter [Debrabandere (2014)]. For all the cases, the $\Delta\alpha(\widetilde{F}_y)$ identification criteria was based on the 1^{st} considered harmonic. Figure 4.17 shows the performance of the *phase error* method for all the analyzed configurations. As also observed by Spiker et al. (2006), a shifting towards higher St_{shnat} values was found when passing from 1 to 2 harmonics. The consideration of a third harmonic did not change the predicted St_{shnat}.

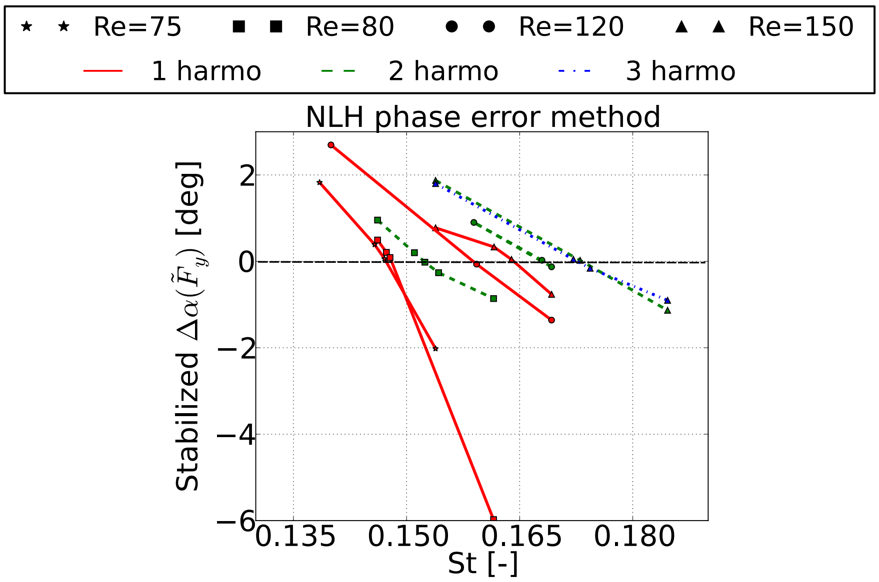

Figure 4.17: Fixed cylinder, stabilized $\Delta\alpha(\widetilde{F}_y)$ for different solved Strouhal and Reynolds numbers

Time marching computations

For the time marching computations, the *physical* time step was chosen in order to be approximately $1/60 f_{shnat}$. This time resolution is equivalent to a 3 harmonics NLH computation, assuming a minimum representation of 20 points per period. In order to allow the flow to develop a total simulation time of $\simeq 40/f_{shnat}$ was used, corresponding to 40 periods of the expected *vortex shedding phenomenon*. Between every time step, 200 inner iterations were performed. Contrary to the NLH method, the f_{shnat} value can be considered as an output of the time marching simulations, and it can be computed *via* the signal processing of the last periods. An uncertainty should be considered for this computation, being proportional to the ratio between the used time step and the signal period.

Prediction of the natural shedding frequency

For the considered Reynolds number range, the identified St_{shnat} are compared against the experiments of Williamson (1996) and Fey et al. (1998) in Figure 4.18. The estimated percentile differences with respect to the latter reference are compiled in Table 4.4. To contextualize the results of this research, Figure 4.18 also includes a set of simulations performed by other authors. For the case of the time marching approach, the uncertainties in the computation of St_{shnat} related to the simulation time step are considered by means of an error range. As a general trend, all the computations included in Figure 4.18 do exhibit an underestimation of the shedding frequency, probably due to the non consideration of three-dimensional flow effects. The St_{shnat} shifting observed in the application of the NLH *phase error* method for multi-harmonic simulations was found to reduce the difference with respect to the experimental references.

Both multi-harmonic NLH and time marching approaches obtained a similar evolution regarding the *Reynolds number*. For both approaches, the differences with respect to the experimental values seemed to increase together with the Reynolds number, with values in the range of [4%,7%] for Re=120 and Re=150. As this behavior was common for both methodologies, it is suspected to be related to the impact of the computational model parameters. A feasible explanation could be the influence of the mesh size of the downstream block, that was not considered in the mesh sensibility study presented in Section 4.3.3. Indeed, the impact of the farfield resolution in the prediction of the Strouhal number was already pointed out in McMullen (2003). Another possible cause could be the influence of the size of the domain, as mentioned in Besem (2015) and Placzek et al. (2009).

Regarding other authors works, the results of McMullen (2003) with the *Non-Linear Frequency Domain* technique showed an almost perfect agreement with the present research results at Re=120 and Re=150. Nevertheless, the *Harmonic balance* method computations of Spiker et al. (2006) were found to be closer to the experimental references, supporting the hypothesis of the influence of the mesh or the computational domain size in the results of this research.

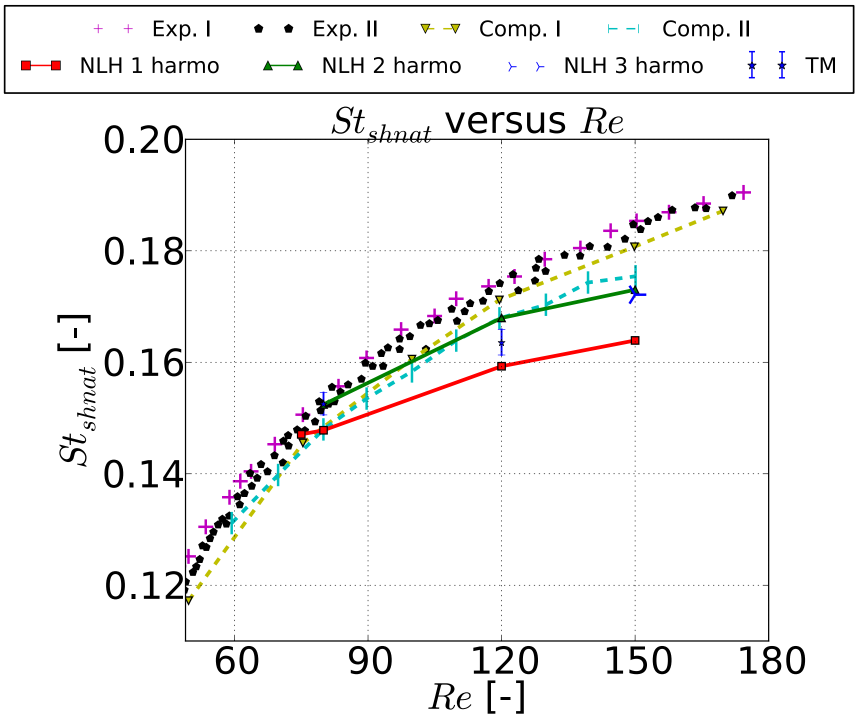

Figure 4.18: Fixed cylinder, comparison of identified St_{shnat}. NLH and TM stand for the Non-Linear Harmonic and time marching computations performed in the present study, respectively. Exp. I refers to the experimental data from Williamson (1996). Exp. II refers to the experiments of Fey et al. (1998). Comp I. refers to the computational results of Spiker et al. (2006) using the *Harmonic balance* method. Comp. II refers to the computational results of McMullen (2003) using the *Non-Linear Frequency Domain*.

Table 4.4: Estimated relative St differences [%] with respect to Williamson (1996)

	Re=75	Re=80	Re=120	Re=150
NLH 1 harmo	-2.38	-3.93	-8.87	-11.66
NLH 2 harmo	-	-0.97	-3.96	-6.66
NLH 3 harmo	-	-	-	-7.16
Time marching	-	[-2.17,0.43]	[-7.45,-4.82]	-

Load coefficients analysis

For unsteady simulations, lift and drag coefficients can be decomposed into a time-averaged value and a fluctuating part. Denoting both components by the superscripts ¯ and ’ respectively and assuming a null time-averaged lift coefficient due to the symmetry of the vortex shedding phenomenon, it can be written:

$$C_D(t) = \bar{C_D} + C'_D(t); \tag{4.34}$$

$$C_L(t) = C'_L(t); \tag{4.35}$$

Figure 4.19 shows the computed C_D and C_L for several NLH and time marching computations, normalized by the maximum observed fluctuation values $C'_{D,max}$ and $C'_{L,max}$. For the drag coefficient, the averaged value $\bar{C_D}$ was also subtracted from the transient signal. As an immediate observation, a different main frequency was observed for both C_D and C_L . Indeed, the analysis of the harmonic content these signals revealed that while the lift force was dominated by the first harmonic, the drag fluctuations were only captured by the second one.

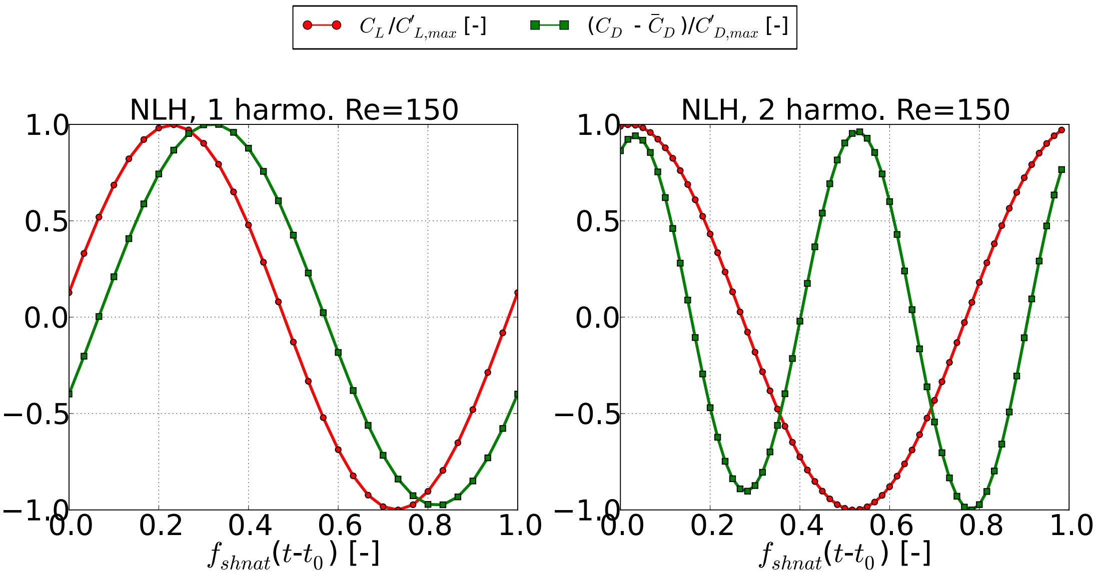

(a) NLH, 1 harmonic

(b) NLH, 2 harmonics

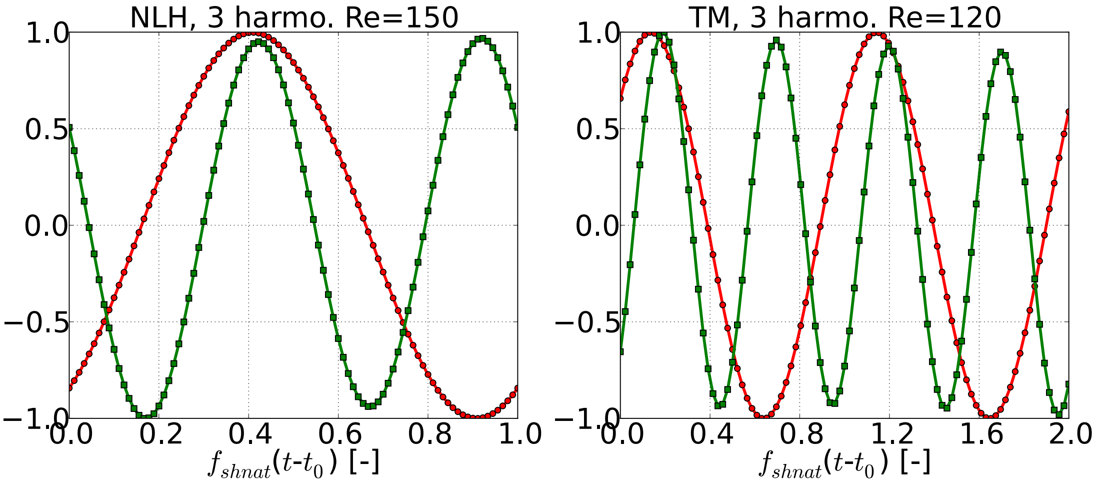

(c) NLH, 3 harmonics

(d) Time marching

Figure 4.19: Fixed cylinder, lift and drag coefficients evolution for several computations. The time-averaged value was removed from C_D. The two last periods are shown for the time marching simulation. Markers do not represent data sampling

This fact is depicted in Figure 4.20 by means of the results of the NLH computations. This frequency decoupling was already described in Placzek et al. (2009) and Ji et al. (2011), and it explains the increase of St_{shnat} prediction accuracy of multi-harmonic NLH simulations. The insignificant contribution of the third harmonic on lift and drag fluctuations could also justify its small impact on the prediction of St_{shnat}. Finally, for both NLH and time marching computations a similar phase shifting was observed between lift and drag loads transients. The same described pattern was repeated in all the performed simulations.

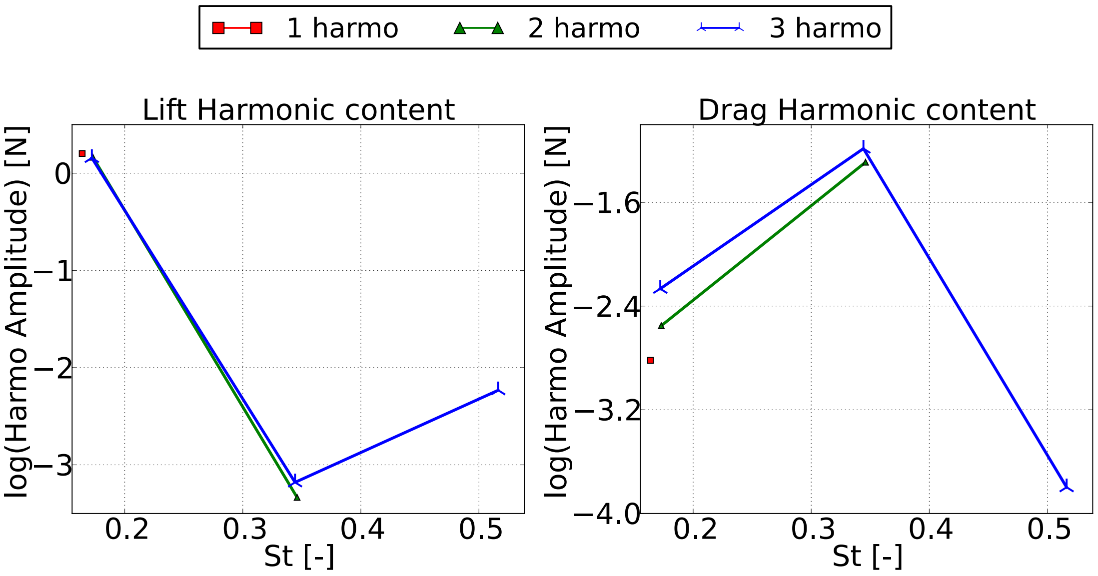

(a) Lift **(b)** Drag

Figure 4.20: Harmonic amplitudes for fixed cylinder loads at Re=150. First point corresponds to St_{shnat}, followed by its harmonics. Ordinates expressed in logarithmic scale

Obtained cylinder loads were compared against experimental references. The *Root Mean Square* (RMS) values of the lift coefficient are shown in Figure 4.21a. An important scatter is observed in the experimental data, related to the complexity of the *shedding* phenomenon. However, it can be concluded that performed computations properly captured the evolution of $RMS\,(C_L)$ with respect to the *Reynolds number*. Considerable discrepancies were observed for the single harmonic NLH computations with respect to the rest of the performed simulations. As pointed out in Figure 4.20, this issue is certainly due to the non consideration of the second harmonic, that also lead to an underestimation of S_{shnat}. A fair agreement was also found when comparing NLH and time marching methodologies with the results of the *Harmonic Balance* method computations of Spiker et al. (2006), with maximum observed differences of around 13%.

Averaged drag coefficients are displayed in Figure 4.21b. The estimated percentile differences with respect to the experiments of Wieselberger (1921) are compiled in Table 4.5. A good agreement between experimental and computational data was found for both time marching and NLH methods, even when considering a single harmonic in the latter approach. Bigger differences were observed at high *Reynolds numbers*, with a maximum of 3% at Re=150. These results revealed the impact of the flow unsteadiness in the mean drag prediction, since the steady computations of Section 4.3.3 showed discrepancies between 13% and 23% with respect to the same experimental references.

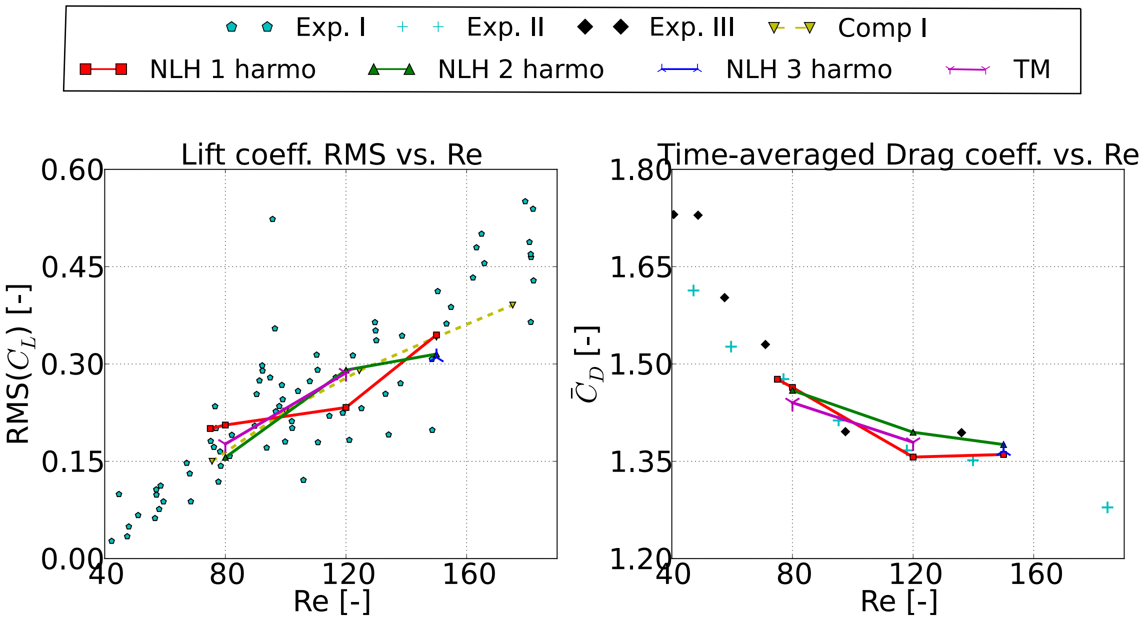

(a) $RMS\,(C_L)$ **(b)** $\overline{C_D}$

Figure 4.21: Fixed cylinder, validation of computed load coefficients with the NLH and time marching methods. Exp. I refers to the experiments collected by Norberg (2001). Exp. II refers to the experiments included in Wieselberger (1921). Exp. III refers to the experiments of Hoerner (1965). Comp. I refers to the numerical simulations of Spiker et al. (2006) with the *Harmonic Balance* method

Table 4.5: Fixed cylinder, estimated $\overline{C_D}$ relative differences [%] with respect to Wieselberger (1921)

	Re=75	Re=80	Re=120	Re=150
NLH 1 harmo	-0.41	-0.17	-0.65	1.90
NLH 2 harmo	-	-0.48	2.15	3.05
NLH 3 harmo	-	-	-	2.31
Time marching	-	-0.88	1.37	-

No data concerning the harmonic drag fluctuation was found in the literature for validation purposes. The results of the performed computations showed C_D fluctuations two order of magnitudes smaller than C_L, being more important at higher *Reynolds numbers*. For future references, the computed values of $C'_{D,max}$ are summarized in Table 4.6, together with the corresponding $\overline{C_D}$ and $C'_{L,max}$ coefficients.

Table 4.6: Summary of load coefficients for fixed cylinder computations

	Re	$\overline{C_D}$	$C'_{D,max}$ 10^{-2}	$C'_{L,max}$
NLH 1 harmo	75	1.476	0.040	0.327
NLH 1 harmo	80	1.464	0.040	0.335
NLH 2 harmo	80	1.459	1.877	0.259
Time marching	80	1.440	0.921	0.250
NLH 1 harmo	120	1.356	0.040	0.372
NLH 2 harmo	120	1.395	1.880	0.463
Time marching	120	1.380	1.807	0.406
NLH 1 harmo	150	1.360	0.052	0.542
NLH 2 harmo	150	1.376	1.835	0.494
NLH 3 harmo	150	1.366	2.431	0.499

Vortex shedding analysis

For both time marching and NLH computations, the shedding pattern was found to be qualitatively the same for the whole studied Re range. To illustrate this fact, Figure 4.22 shows the vorticity contours of the NLH reconstructed solution at Re=120 for different considered phases φ. Corresponding images for the time marching simulation are also included, based on the last computed period. Since flow phase was not uniquely defined in this case, the time marching solution corresponding to φ=0 was chosen by visual comparison with NLH results. For both approaches, vortices were alternately shed from the upper and lower parts of the cylinder every half a period. Shed structures are in accordance with the computations in the laminar regime performed by other authors [Besem (2015); Placzek et al. (2009)]. It is important to remark that the NLH solution (accounting for 2 harmonics) predicted two vorticity peaks per vortex. This issue was found to be related to the inherent limitation of the NLH method in the prediction of stepwise fluctuations. A similar behavior can be found in the works of McMullen (2003) when using a single harmonic with the *Non Linear Frequency Method*. It is interesting to exemplify this concept in the more simplistic scenario of a step function. Figure 4.23 shows how a harmonic signal can approximate such a function depending on the considered number of harmonics. Due to the discontinuity present at t/T=0, an infinite number of harmonics is theoretically needed to reproduce the step function behavior. Harmonic solutions accounting for 2 and 3 harmonics can already estimate the change in the averaged values of t/T<0 and t/T>0. Nevertheless an oscillatory behavior is still observed, where the peaks and valleys of the maximum considered frequency can be identified. Even if the studied vortex shedding phenomenon is less constraining than this ideal case, a similar behavior was observed for the NLH simulations. To illustrate this fact, Figure 4.24 compares the NLH solutions at Re=150 when considering 1,2 and 3 harmonics. It can be observed that the solution of more harmonics lead to the prediction of smoother vorticity structures. For the particular case of the 3 harmonics computation, a single peak per vortex could be identified, and the computed vorticity structures could be directly comparable with the results of the time marching simulations. This difference on the shedding pattern between the 2 and 3 harmonics NLH computations did not seem to have a significant impact on the computed cylinder loads coefficients (see Section 4.24).

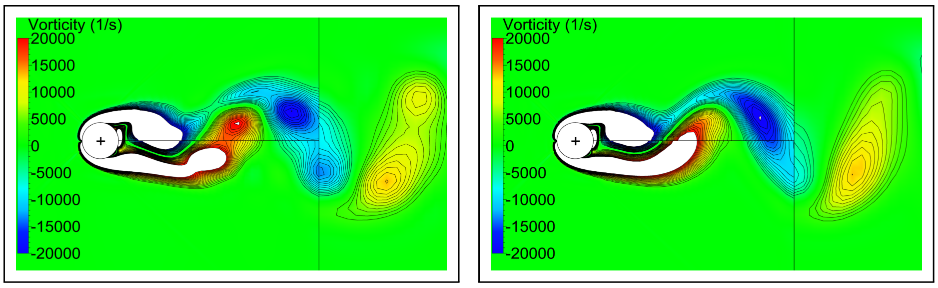

(a) φ=0, NLH **(b)** φ=0, time marching

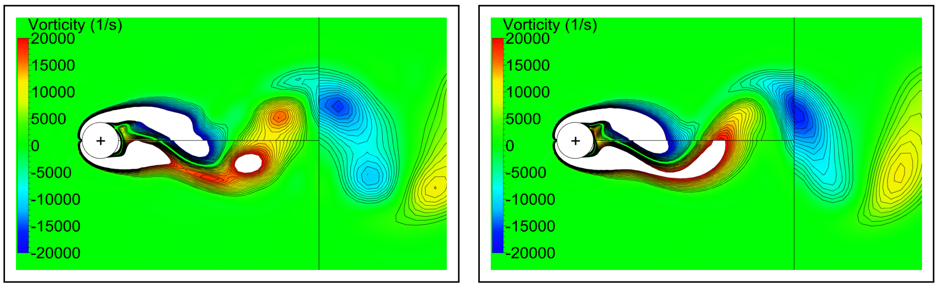

(c) $\varphi=\frac{\pi}{2}$, NLH **(d)** $\varphi=\frac{\pi}{2}$, time marching

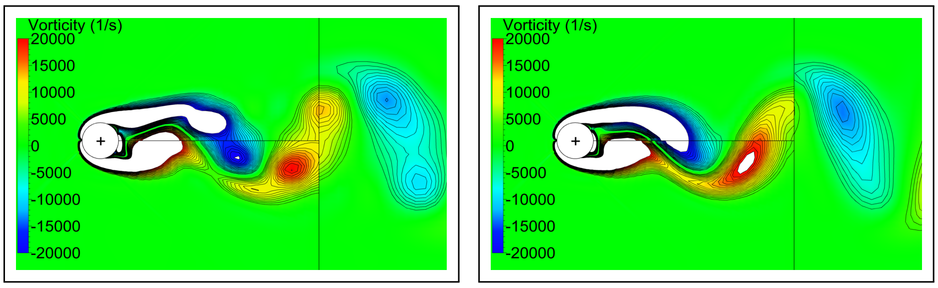

(e) $\varphi=\pi$, NLH **(f)** $\varphi=\pi$, time marching

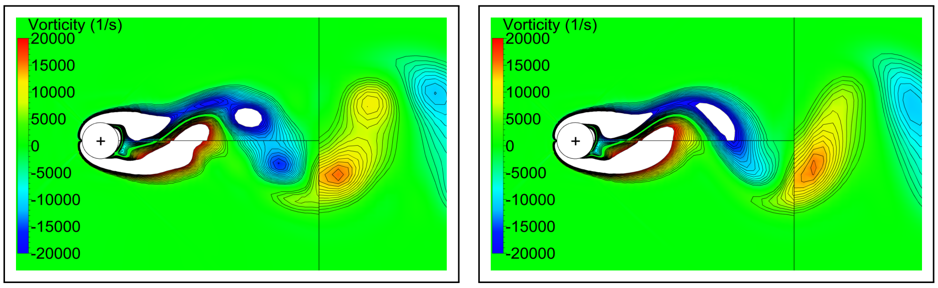

(g) $\varphi=\frac{3\pi}{2}$, NLH **(h)** $\varphi=\frac{3\pi}{2}$, time marching

Figure 4.22: Vorticity contours of fixed cylinder, NLH (2 harmonics) and time marching computations at Re=120. Solutions at similar phases are displayed. Isolines increment corresponds to 1000 s^{-1}. Solid lines represent block lines, and the cross sign is included at the center of the initial cylinder position

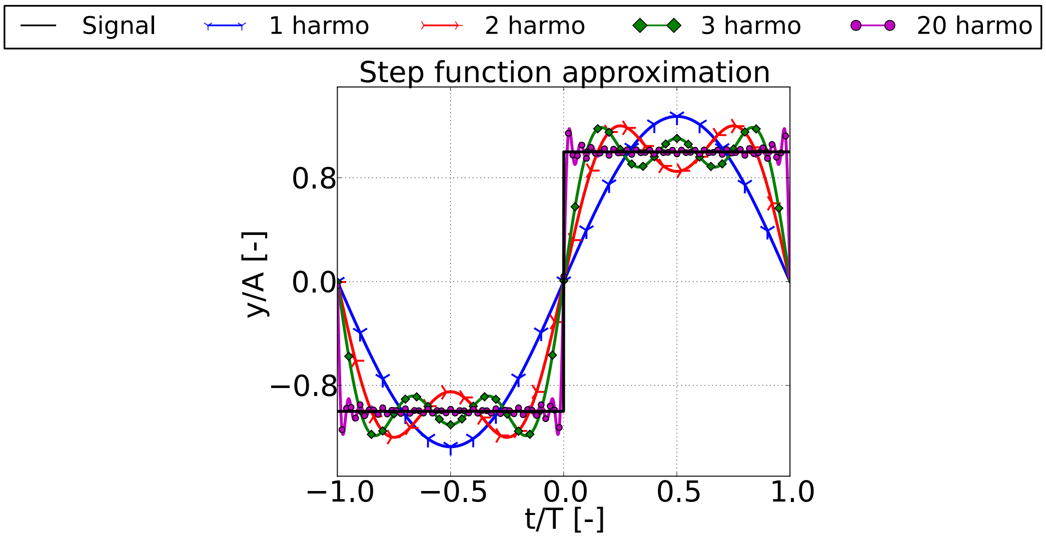

Figure 4.23: Approximation of an step function of height A and width T by means of a harmonic function accounting for different number of harmonics. Markers do not represent data sampling

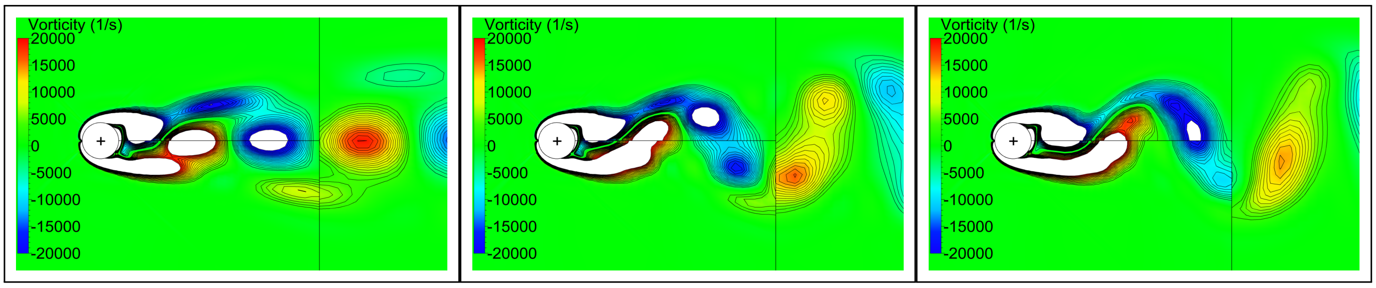

(a) 1 harmonic **(b)** 2 harmonics **(c)** 3 harmonics

Figure 4.24: Vorticity contours of fixed cylinder, NLH computations at Re=150. Solutions at similar phases are displayed. Isolines increment corresponds to 1000 s^{-1}. Solid lines represent block lines, and the cross sign is included at the center of the initial cylinder position

4.3.5 1-way coupling

After the validation of fixed cylinder computations in Section 4.3.4, both NLH and time marching methodologies were assessed in a forced motion context for the particular case of Re=80. Starting from already converged steady simulations, a harmonic cylinder displacement in y direction was imposed. Only real part harmonic content was considered, with an amplitude A and a forced frequency f_F. Hence, the imposed motion D_y could be written as:

$$D_y(t) = D'_y(t) = A\cos(2\pi f_F t) \tag{4.36}$$

Only the study of the so called *lock-in region* was considered in this research. The lock-in regime is characterized by a single fundamental frequency in the flow, which corresponds to the imposed cylinder motion frequency f_F [Besem (2015); Placzek et al. (2009)]. The existence of the lock-in depends on both the imposed amplitude A and the ratio between the forced frequency f_F and the natural shedding frequency f_{shnat}. Four computations were performed in this study, which parameters are compiled in Table 4.7. In order to allow a direct comparison with the experiments of Tanida et al. (1973), the imposed displacement amplitude was fixed to be 14% of the cylinder diameter. In theory all the computations were assumed to be in the lock-in region, as it is illustrated in Figure 4.25 by means of a comparison with the experiments of Koopmann (1967) at Re=100. However, this hypothesis was verified during the simulation for both time marching and NLH methodologies, as it is shown later on in this document.

Table 4.7: Forced cylinder motion, summary of performed computations

Numerical approach	Re	A/D	f_F/f_{shnat}
NLH	80	0.14	0.91
NLH	80	0.14	1.00
NLH	80	0.14	1.06
Time marching	80	0.14	1.00

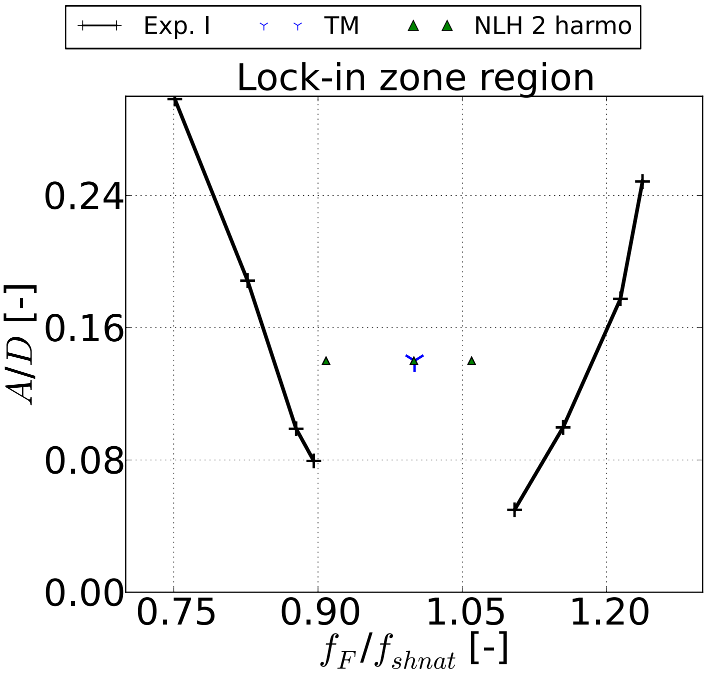

Figure 4.25: Forced cylinder motion, position of performed computations with respect to the lock-in region of Exp. I, issued from the experiments of Koopmann (1967) at Re=100. TM stands for the time marching approach

NLH computations

Based on the results of Section 4.3.4 for the fixed cylinder configuration, only simulations accounting for 2 harmonics were considered. The mesh was deformed *via* the harmonic formulation of the RBF+TFI method (see Section 3.6). For all the performed simulations, very small $\Delta\alpha(\widetilde{F_y})$ converged values were, in the order of 10^{-6} deg, were obtained (see Equation 4.33 for the definition of this parameter). This fact revealed the existence of a lock-in phenomenon with the imposed frequency f_F.

Time marching computation

The same time-step and simulation procedure of the fixed cylinder case described in Section 4.3.4 was used. Mesh was deformed *via* the RBF+TFI method. The signal processing of the lift coefficient transient verified the existence of a lock-in phenomenon with the imposed frequency f_F.

Loads coefficients analysis

Figure 4.26 shows C_D and C_L for the performed NLH and time marching (TM) computations, superposed to the imposed displacement D_y. For the drag coefficient, the averaged value $\bar{C}_D$ was subtracted from the transient signal. All variables were normalized by the maximum observed fluctuation values. As for the fixed cylinder case, the frequency of the computed lift corresponded to f_F and the drag to $2f_F$. At f_F/f_{shnat}=1.00, both NLH and time marching simulations predicted a similar phase shift between the three illustrated signals (being f_{shnat} the shedding frequency in the absence of motion). Important differences between the phases of C_L and D_y could be observed when comparing the other two NLH computations. Indeed, the relative phase of these two variables determines the role that the flow is playing in this aeroelastic phenomenon. To better illustrate this aspect, Figure 4.27 shows the evolution of C_L with respect to D_y, often referred in the literature as the *phase portraits* or *Lissajous curves*. For f_F/f_{shnat}=0.91, maximum cylinder displacements corresponded to negative lift coefficients, and vice-versa. Hence, the force exerted by the fluid was in opposition to the cylinder movement. It is concluded that the fluid was acting as an energy dissipation mechanism or, equivalently, that it exerted a positive aerodynamic damping [Placzek et al. (2009); Tanida et al. (1973)]. The inclination of the phase portrait was reversed when analyzing the f_F/f_{shnat}=1.06 NLH simulation. As a consequence, the fluid was expected to transfer energy into the system by means of a negative aerodynamic damping, leading to an unstable configuration. Both TM and NLH computations showed a similar behavior at f_F/f_{shnat}=1.0, with almost flat phase portraits. Another interesting indicator of the fluid behavior is the imaginary part of the first harmonic of the lift coefficient $\widetilde{C_L}|_{Im,1}$, which is out of phase with respect to the imposed cylinder motion D_y. In Figure 4.28 the results issued from this research are compared against the experimental data from Tanida et al. (1973) and the numerical simulations of Spiker et al. (2006), expressed as a function of the reduced frequency $(f_F D)/U$.

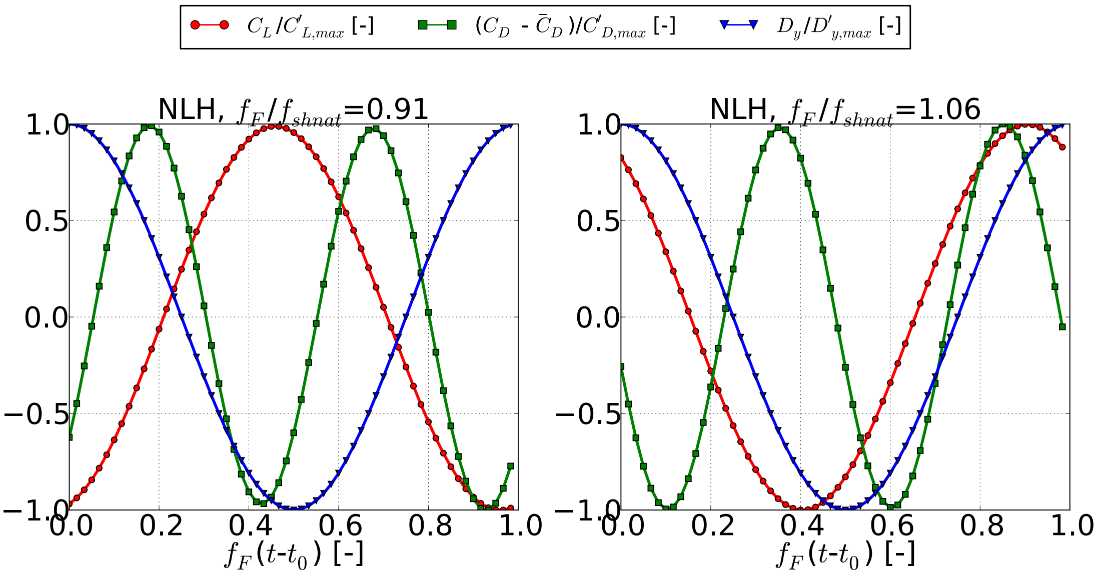

(a) NLH, f_F/f_{shnat}=0.91 **(b)** NLH, f_F/f_{shnat}=1.06

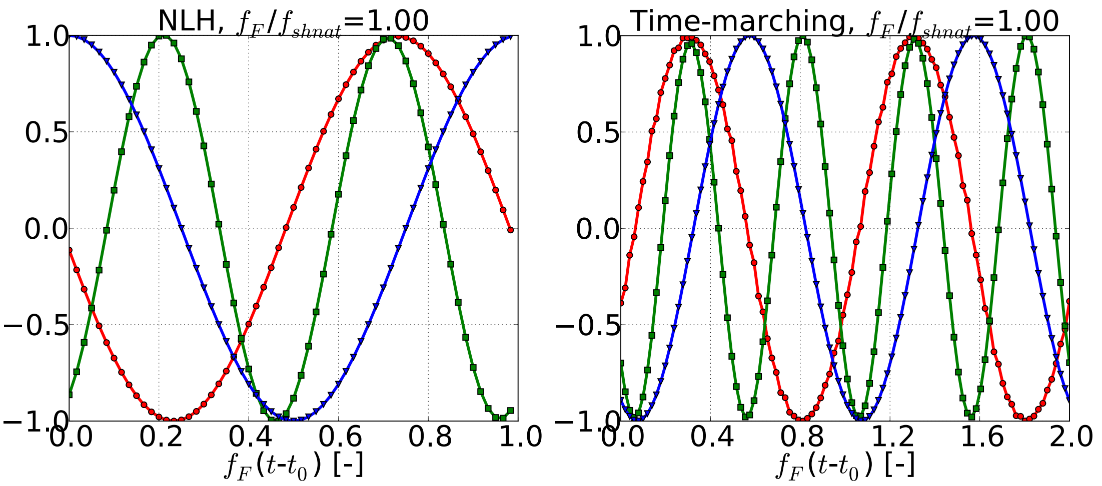

(c) NLH, f_F/f_{shnat}=1.00 **(d)** TM, f_F/f_{shnat}=1.00

Figure 4.26: Forced cylinder motion, lift and drag coefficients evolution superposed to D_y. Curves are normalized by the corresponding maximum oscillation amplitude. The time-averaged value was removed from C_D. The two last periods are shown for the time marching simulation. Markers do not represent data sampling

The NLH computations were able to predict the increase of $\widetilde{C_L}|_{Im,1}$ related to the growth of the energy transfer already observed in the analysis of the phase portraits. In addition, a fair agreement was found with the time marching simulation at f_F/f_{shnat}=1.0, with a relative difference of 7%. However, underestimations of approximately 20% with respect to the experimental reference were found. This could be explained by comparing the natural shedding frequency computed in this research and the one observed in Tanida et al. (1973). Indeed, at Re=80 both NLH and time marching predicted St_{shnat}=0.152, while in the experiments a value of 0.129 was recorded. This discrepancy of 18% could explain the shifting of the obtained results towards lower values of the imaginary lift coefficient. The hypothesis of the influence of S_{shnat} on the obtained results is supported when analyzing the computational re-

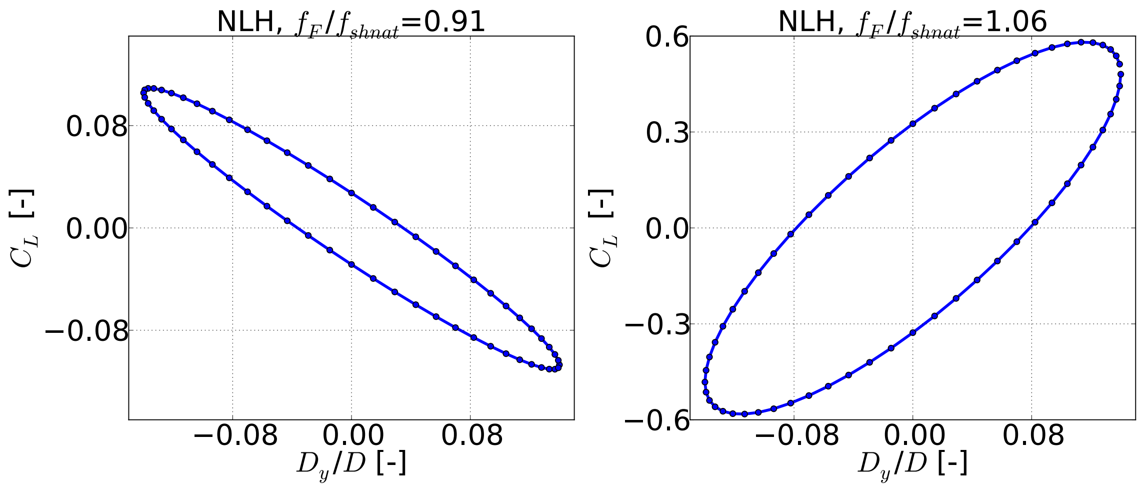

(a) NLH, f_F/f_{shnat}=0.91 **(b)** NLH, f_F/f_{shnat}=1.06

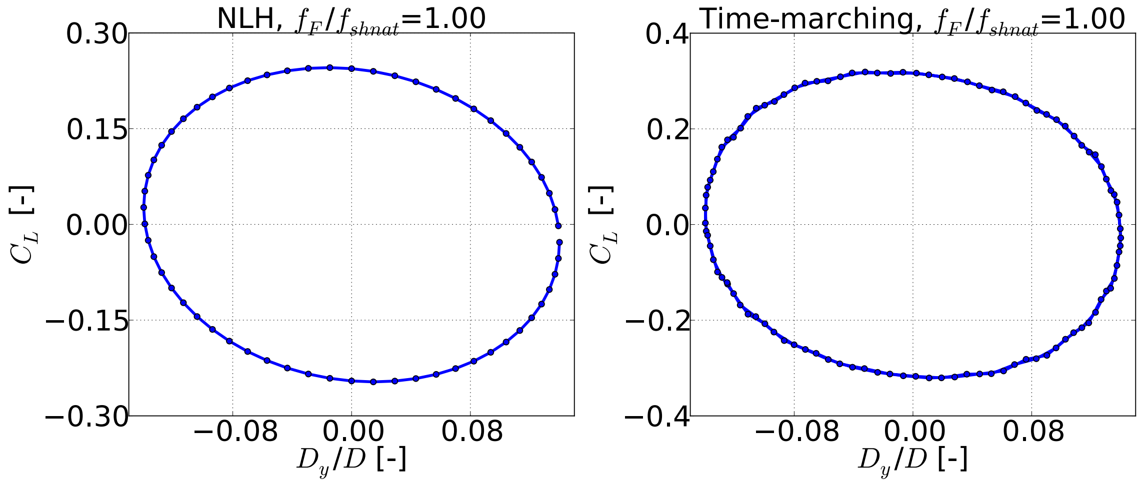

(c) NLH, f_F/f_{shnat}=1.00 **(d)** TM, f_F/f_{shnat}=1.00

Figure 4.27: Forced cylinder motion phase portraits. Markers do not represent data sampling

sults of Spiker et al. (2006), that predicted a natural Strouhal number of approximately 0.149. Additional simulations should be performed in order to compare the performance of the time marching method for f_F/f_{shnat}=0.91 and f_F/f_{shnat}=1.06. Additionally, it could be interesting to evaluate the modeling capabilities of the presented numerical set-up while assessing the drop of $\widetilde{C_L}|_{Im,1}$ near the end of the lock-in region, related to a sudden phase lag as reported in Tanida et al. (1973).

The center of the lock-in region was also characterized by an increase of the computed time averaged and fluctuating drag. The values of these coefficients are compiled in Table 4.8 for future references, together with the computed $C'_{L,max}$.

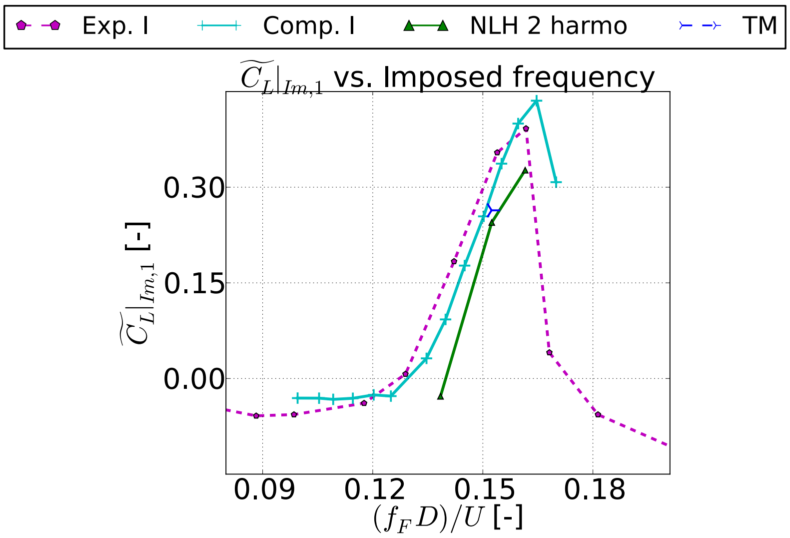

Figure 4.28: Forced cylinder motion, evolution of the imaginary part of first harmonic of C_L with respect to the imposed oscillation frequency f_F at Re=80. Exp. I refers to the experimental data from Tanida et al. (1973). Comp. I refers to the simulations of Spiker et al. (2006) with the *Harmonic Balance*

Table 4.8: Summary of load coefficients for forced motion computations

Cylinder motion	$(f_F D)/U$	$\overline{C_D}$	$C'_{D,max}$	$C'_{L,max}$
NLH, f_F/f_{shnat}=0.91	0.139	1.467	0.016	0.110
NLH, f_F/f_{shnat}=1.00	0.152	1.565	0.049	0.247
TM, f_F/f_{shnat}=1.00	0.152	1.563	0.057	0.321
NLH, f_F/f_{shnat}=1.06	0.161	1.543	0.045	0.582

Vortex shedding analysis

For both time marching and NLH computations, the shedding pattern was found to be qualitatively the same. Upper part vortices were shed during the ascending movement of the cylinder, while the release of lower part vortices took place during the descent. Figure 4.29 shows the vorticity contours of the NLH reconstructed solution for f_F/f_{shnat}=1.00 depending on the imposed cylinder deformation D_y. Equivalent time steps for the time marching simulation are also included. The observed common shedding pattern corresponds to the 2S mode described by Khalak and Williamson (1999) (where two vortex per period are shed). Both NLH and time marching computations showed a very similar wake generation. The two peaks per period captured by the former approach were also found for the fixed cylinder configuration and discussed in Section 4.3.4. This behavior should not be confused with the so called 2P mode (4 vortex per period), that has not been previously observed in the laminar regime [Khalak and Williamson (1999)]. For the NLH computations, the consideration of different f_F/f_{shnat} values did not modify the structure of the shed vortices (see Figure 4.30).

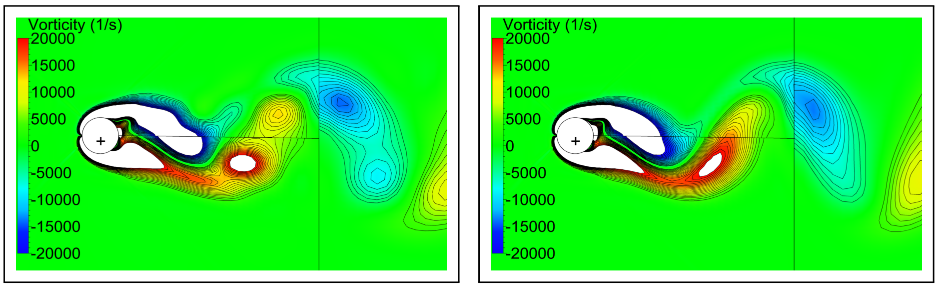

(a) D_y=0.14D, NLH **(b)** D_y=0.14D, time marching

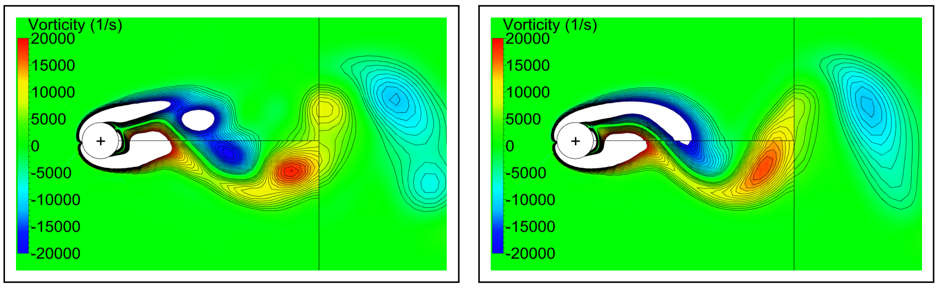

(c) D_y=0 (descending), NLH **(d)** D_y=0 (descending), time marching

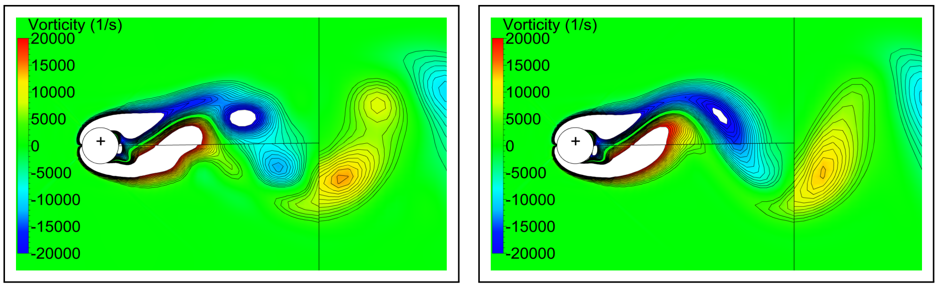

(e) D_y=-0.14D, NLH **(f)** D_y=-0.14D, time marching

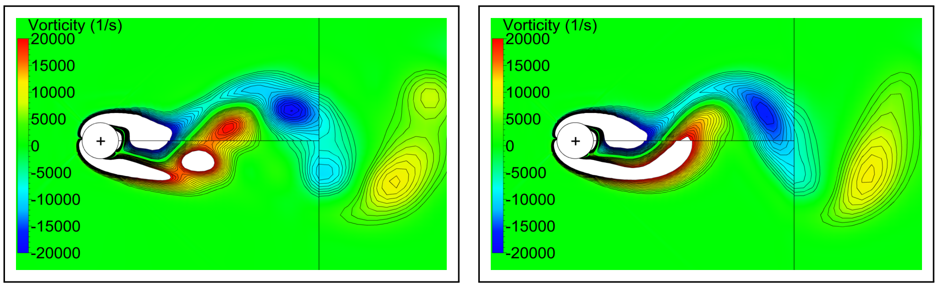

(g) D_y=0 (ascending), NLH **(h)** D_y=0 (ascending), time marching

Figure 4.29: Vorticity contours of forced cylinder motion, NLH (2 harmonics) and time marching computations at Re=80, f_F/f_{shnat}=1.00. Isolines increment corresponds to 1000 s^{-1}. Solid lines represent block lines, and the cross sign is included at the center of the initial cylinder position

4.3.6 2-way coupling

In order to validate the implemented FSI 2-way coupling harmonic module, the single degree of freedom aeroelastic system sketched in Figure 4.31 was analyzed. This problem is referred

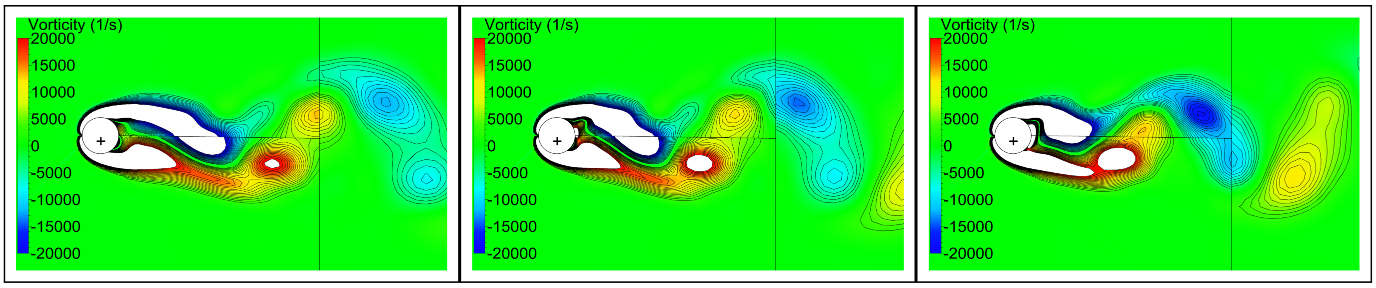

(a) f_F/f_{shnat}=0.91 **(b)** f_F/f_{shnat}=1.00 **(c)** f_F/f_{shnat}=1.06

Figure 4.30: Vorticity contours of forced cylinder motion, NLH computations (2 harmonics) at Re=80 and D_y=0.14D. Isolines increment corresponds to 1000 s^{-1}. Solid lines represent block lines, and the cross sign is included at the center of the initial cylinder position

to in the literature as the *Vortex Induced Vibrations* (VIV) of a cylinder in transversal oscillation [Griffin et al. (1973)]. All the computations were performed at Re=120, using both NLH and time marching approaches and starting from an already converged steady simulation described in Section 4.3.3. The elastic system was characterized by a natural frequency of oscillation f_k and a damping ratio ξ, both understood as an input of the numerical set-up. The same mass m was considered for all the simulations. In order to allow the comparability with other experiments, it is interesting to express this variable in terms of the *reduced mass* m^*, here defined as in Shiels et al. (2001):

$$m^* = \frac{m}{\frac{1}{2}\rho D^2 L} \tag{4.37}$$

with m^* fixed to 7.49 for all the simulations, ρ being the fluid density, D the cylinder diameter and L the span.

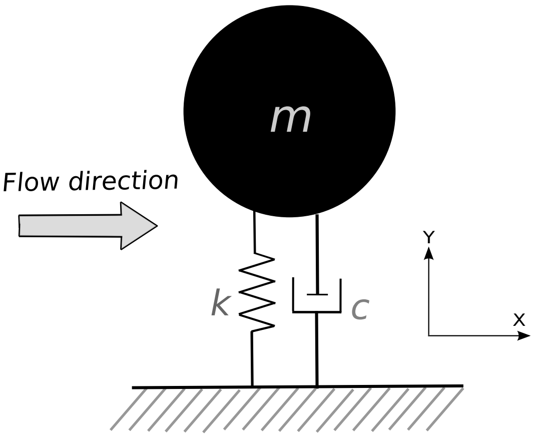

Figure 4.31: Sketch of the elastic system attached to the cylinder in free oscillation

Most part of previous computations concerning the study of this phenomenon in the laminar regime were validated against Anagnostopoulos and Bearman (1992). In these experiments, the mass and the damping ratio of the elastic system were fixed, and the evolution of the computed cylinder displacements and aeroelastic frequencies with the considered *Reynolds number* was analyzed. In this context, we can find the computations of Besem (2015) and Dowell et al. (2008) with the *Harmonic Balance* method. This validation approach was found to be limited for the comparison of the performance of both NLH and time marching methods, due to the differences in the computed St_{shnat} and the impact of the elastic mounting properties on the system behavior. A more insightful analysis regarding all the parameters concerned by the VIV phenomenon and its influence on the cylinder displacements was given in the inspiring numerical studies of Shiels et al. (2001) and Placzek et al. (2009) at Re=100. The milestone of both researches was the relation of the cylinder response to the so called *effective stiffness* k^*_{eff}, that combines the effects of the spring stiffness, the damping and the cylinder mass. Even if k^*_{eff} does not account for the influence of the *Reynolds number*, it was found to be a very useful parameter to reduce the aeroelastic behavior of different VIV systems, even at the limits of zero mass and/or zero damping. In particular, k^*_{eff} is defined as:

$$k^*_{eff} = k^* - 4\pi^2 f^{*2} m^* \tag{4.38}$$

where k^* is the dimensionless rigidity of the cylinder and f^* refers to the non-dimensioning of the observed shedding frequency f_{shed}:

$$k^* = \frac{k}{\frac{1}{2}\rho U_\infty^2 L}; \tag{4.39}$$

$$f^* = \frac{f_{shed} D}{U_\infty}; \tag{4.40}$$

In this research, the impact of three different aspects of the VIV phenomenon were analyzed:

- The numerical methodology: NLH 2-way coupling and time marching 2-way coupling
- The rigidity of the spring: by means of the ratio f_k/f_{shnat}, where f_{shnat} refers to the natural shedding frequencies computed for the fixed cylinder case in Section 4.3.4
- The structural damping ratio of the elastic system ξ

In particular, the test cases matrix presented in Table 4.9 was performed.

Time marching computations

The same numerical set-up used for the forced oscillation simulation of Section 4.3.5 was used for the free oscillation time marching computations. Time marching 2-way coupled simulations were performed based on the modal approach. The modal shapes were normalized based on the cylinder mass. The shedding frequency f_{shed} was computed by signal

Table 4.9: Matrix of free oscillation computations. NLH refers to the configurations studied with the *Non Linear Harmonic* approach. TM refers to time marching method computations

f_k/f_{shnat}	ξ, (structural damping ratio)				
	0	0.0012	0.03	0.1	0.2
0.76			TM		
0.99			TM		
1.00	NLH	NLH	NLH	NLH	
1.01			TM		
1.06	TM	TM	TM,NLH		TM
1.20	TM		TM		
1.22			NLH		

processing of the last periods of the lift transient, which showed a limit cycle oscillation for all the considered cases. As for the fixed cylinder simulations an error should be attached to this estimation, related to the used time step. However and for the sake of simplicity, presented results do not consider this uncertainty. Figure 4.32 shows the obtained f_{shed} as a function of the structural damping, normalized by the considered spring frequency f_k and natural shedding frequency of the fixed cylinder f_{shnat}. It is important to remark that f_{shed} did not necessarily correspond to neither f_k nor f_{shnat}. In addition and in accordance with previous observations of Klamo (2007) and Williamson and Govardhan (2004), the effect of the damping tended to decrease the value of f_{shed}. Both considerations will be evaluated by means of its impact on k^*_{eff} (and consequently on the cylinder response) later on in this document.

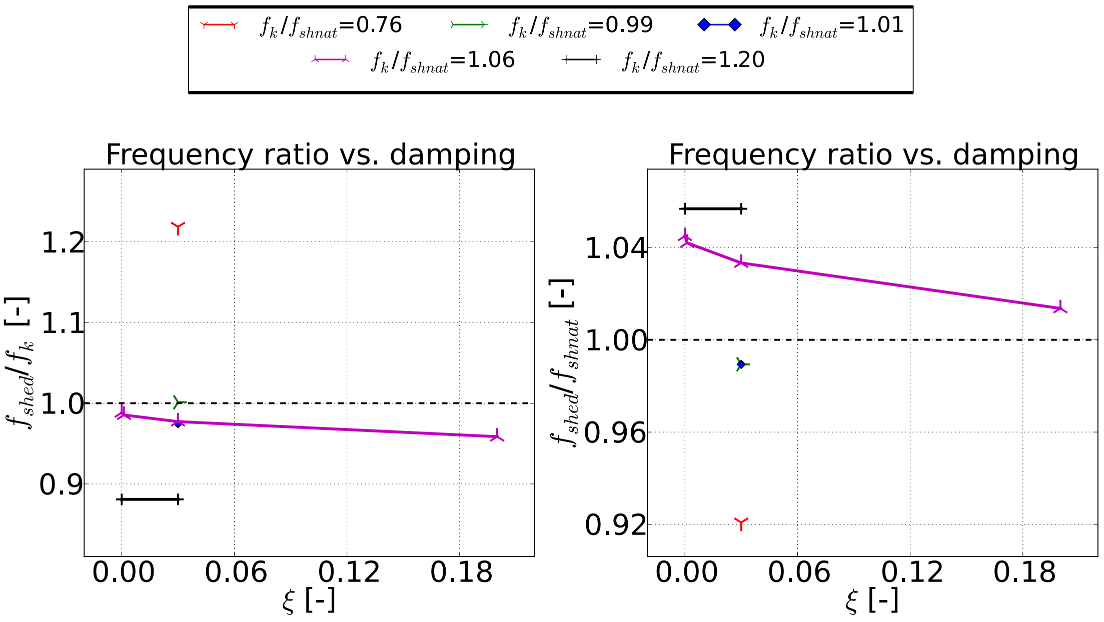

(a) f_{shed}/f_k **(b)** f_{shed}/f_{shnat}

Figure 4.32: Free oscillation cylinder, evolution of the shedding frequency f_{shed} with respect to the damping for time marching computations

NLH computations

Based on the results of Section 4.3.4 for the fixed cylinder configuration, only simulations accounting for 2 harmonics were considered. The new developed 2-way coupled harmonic modal approach was used (see Section 4.2), assuming the same modal shapes as previously performed time marching simulations. As a general practice, 300 iterations of the laminar Navier-Stokes equations were performed between every call to the harmonic structural Equation 4.23 (*ITCPL*=300). The computation of the generalized displacements was under-relaxed with a factor of 0.7 in order to avoid abrupt displacements prior to the convergence of the harmonic loads (γ=0.7). Mesh was deformed *via* the harmonic formulation of the RBF+TFI. As for the fixed cylinder case, the first solved harmonic frequency (corresponding to f_{shed}) was not known *a priori*. On the contrary to the fixed configuration the choice of an inappropriate f_{shed} was not manifested as a considerable value of $|\Delta\alpha(\widetilde{F_y})|$, that used to remain below 0.1 deg. However an oscillatory behavior was found for the first harmonic of the cylinder displacement $\widetilde{D_y}$ for every solution of the harmonic structural equation. The value of the corresponding phase shift $\Delta\alpha(\widetilde{D_y})$ showed a stabilization after a certain number of iterations (see Figure 4.33).

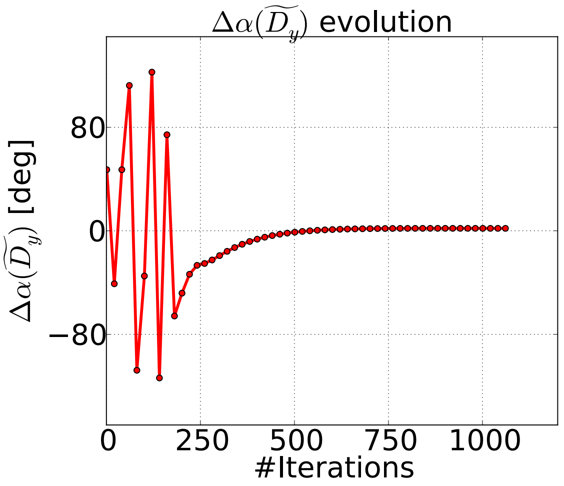

Figure 4.33: Free oscillation cylinder $\Delta\alpha(\widetilde{D_y})$ [deg] vs. solver iterations, corresponding to the NLH computation at f_k/f_{shnat}=1.0 and ξ=0.0012 solved for a frequency $\neq f_{shed}$. Markers correspond to every call to the harmonic structural equation

Inspired in the procedure followed for the identification of f_{shnat}, an iterative methodology was set-up in order to minimize the phase change of the first deformation harmonic between every deformation step, $|\Delta\alpha(\widetilde{D_y})|$. A maximum of 1 deg was chosen as a convergence criteria. This technique was applied to all the NLH computations in order to find the f_{shed} corresponding to every configuration (see Figure 4.34). As for the fixed cylinder case, a quasi linear evolution was observed.

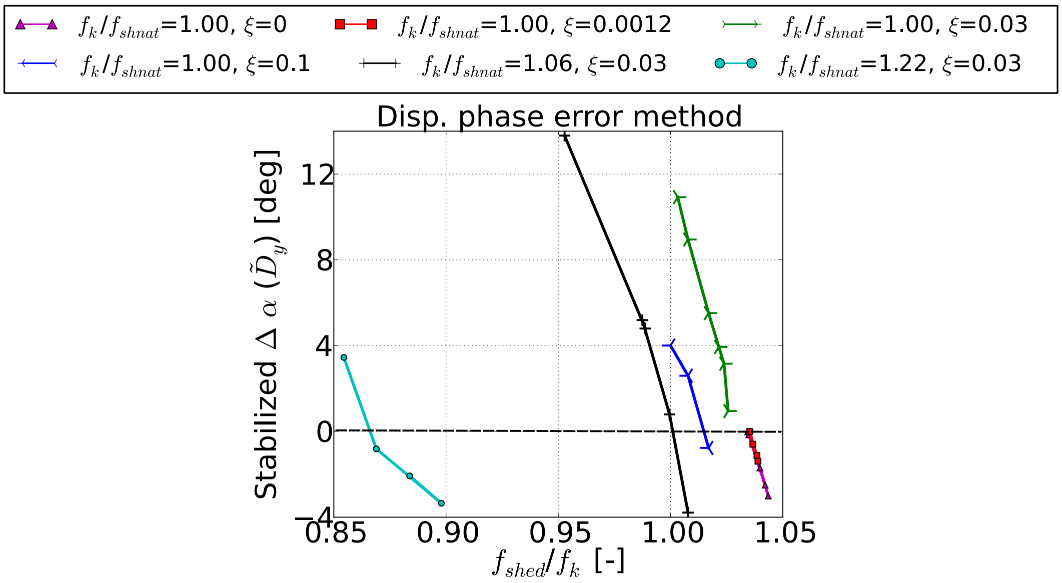

Figure 4.34: Free oscillation cylinder, stabilized $\Delta\alpha(\widetilde{D_y})$ for different NLH (2 harmonics) computations as a function of f_{shed}/f_k

Numerical instabilities were found in the first applications of this shedding frequency identification methodology for the computations with f_{shed}/f_k at the vicinity of 1 (corresponding to the resonance of the structure with the aerodynamic loads). This issue was assumed to be related to the behavior of the harmonic structural equation when assessing $f_{shed} \simeq f_k$ with low damping coefficients. Indeed, Equation 4.23 can be rewritten as:

$$\widetilde{q_k}|_h = \frac{\vec{\phi}_{k,s}^T}{4\pi^2 f_k^2}\,(F1 - IF2)\,\widetilde{\vec{f}_S}|_h \tag{4.41}$$

With:

$$F1 = \frac{1-\Lambda^2}{(1-\Lambda^2)^2 + 4\xi_k^2\Lambda^2}; F2 = \frac{2\xi_k\Lambda}{(1-\Lambda^2)^2 + 4\xi_k^2\Lambda^2}; \Lambda = \frac{f_h}{f_k} \tag{4.42}$$

Equation 4.41 is not defined for the particular case of ξ=0.0 and Λ=1.0. For our application, the latter equality is translated as f_{shed}=f_k when considering the first harmonic. For configurations close to this limit, important amplification factors should be considered between fluid loads and generalized displacements. This fact is illustrated in Figure 4.35, where $F1$ and $F2$ factors are shown as a function of Λ and ξ.

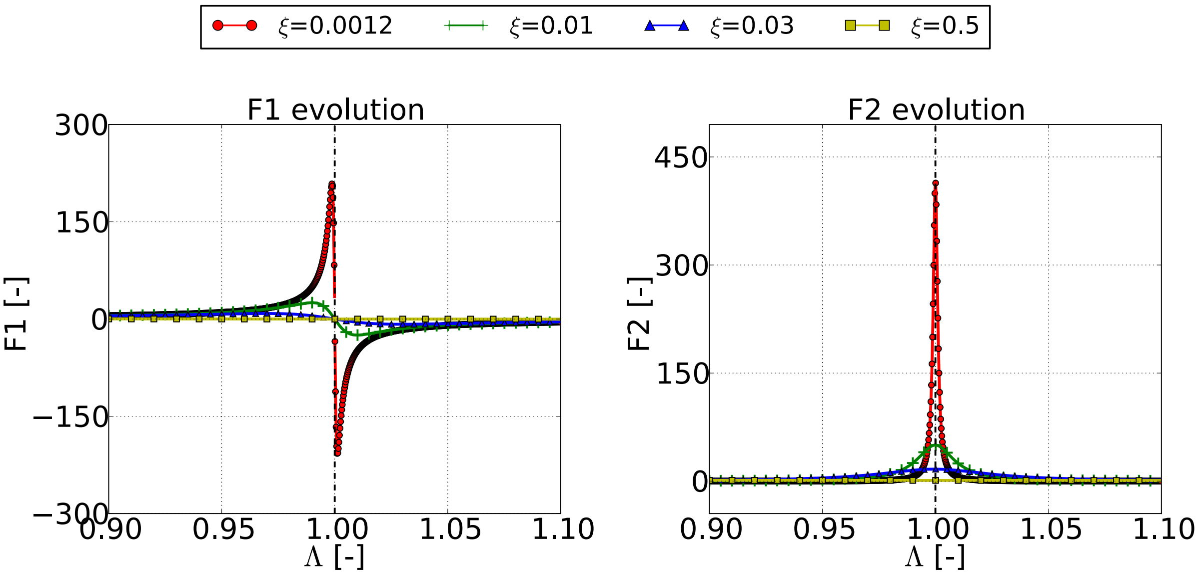

(a) $F1$ **(b)** $F2$

Figure 4.35: Evolution of $F1$ and $F2$ factors as a function of α and the damping ratio

In our case, where Λ reached values up to 1.003 with $\xi \leq 0.1$, even slight fluctuations of the harmonic loads during the development phase of the flow lead to unphysical generalized displacements. This issue could be overcome by the modification of $ITCPL$ and γ parameters for the concerned simulations. In particular, the combination of $ITCPL$=10 and γ=0.1 offered a very good stability. The simulations corresponding to the final identified f_{shed} verified the double criteria defined in this study ($|\Delta\alpha(\widetilde{F_y})|$<0.1 deg and $|\Delta\alpha(\widetilde{D_y})|$<1 deg). The frequency shifting related to ξ already observed for the time marching computations was reproduced (see Figure 4.36).

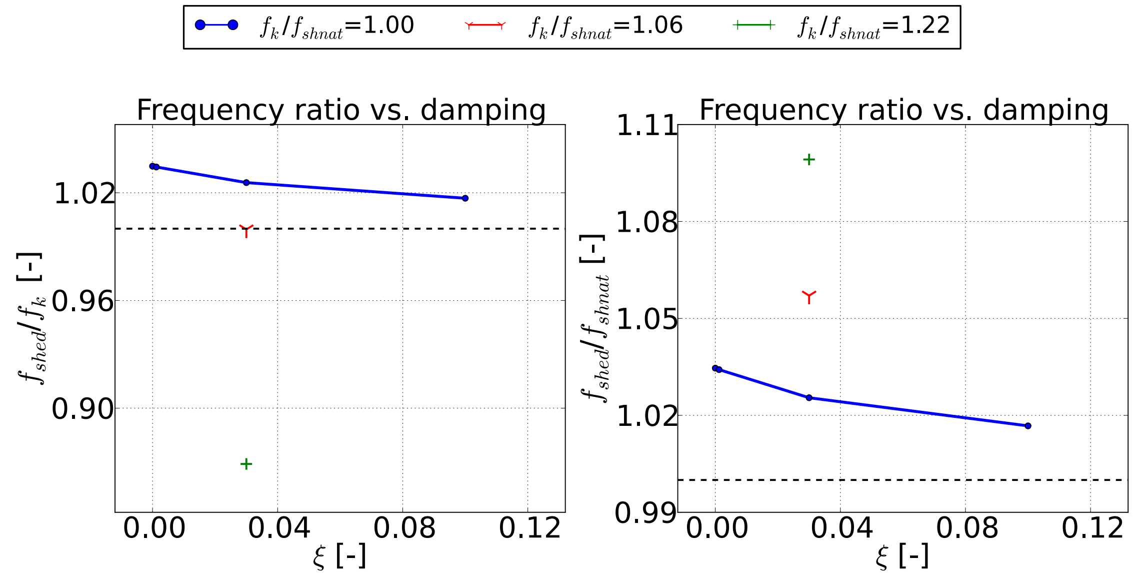

(a) f_{shed}/f_k **(b)** f_{shed}/f_{shnat}

Figure 4.36: Free oscillation cylinder, evolution of the shedding frequency f_{shed} with respect to the damping for NLH computations (2 harmonics)

The influence of k^*_{eff}

In free oscillation conditions, the prediction of the cylinder displacement amplitude showed an important dependence with both the flow conditions and the considered structural damping [Klamo (2007)]. In order to be able to compare both NLH and time marching results the so called *effective stiffness* k^*_{eff} was used in this study, as defined in Shiels et al. (2001) and Placzek et al. (2009). The value of k^*_{eff} is always understood as an output of the simulation, due to its dependence to the shedding frequency f_{shed}. Table 4.10 compiles the computed f_{shed} and k^*_{eff} in the performed simulations, together with the cylinder loads coefficients C_L and C_D and the observed cylinder displacements D_y. Figure 4.37a shows the maximum observed cylinder displacement, expressed as a function of k^*_{eff}. Results are compared with the computations of Shiels et al. (2001) and Placzek et al. (2009) at Re=100. An amplification of the displacement amplitudes can be observed in the range k^*_{eff}=[0,5]. Due to its similarity with the forced oscillations mechanism, this region is often referred as the *lock-in region*. Based on the obtained results in this research, it is convenient to divide this area into three different sub regions: the *pre lock-in region*, the *full lock-in region* and the *post lock-in region*, which are also illustrated in Figure 4.37a. The *pre lock-in region* starts at the vicinity of k^*_{eff}=0, and it corresponds to the beginning of the amplitude amplification. Both NLH and time marching approaches were able to predict this phenomenon, and their results followed the trend established by other authors computations. The *full lock-in region* refers to the area where the highest displacements were computed (i.e. $D'_{y,max}/D$>0.4). Only simulations based on the time marching approach laid in this region. Computed amplitudes were in

Table 4.10: Summary of free oscillation cylinder variables. All quantities are non-dimensional

	Input variables		**Output variables**					
	f_k/f_{shnat}	ξ	$(f_{shed}D)/U_\infty$	$\bar{C_D}$	$C'_{D,max}$	$C'_{L,max}$	$D'_{y,max}/D$	k^*_{eff}
TM	0.76	0.03	0.152	1.37	0.023	-0.219	0.091	-2.24
	0.99	0.03	0.164	1.78	0.364	0.220	0.417	-0.02
	1.01	0.03	0.164	1.81	0.368	0.199	0.427	0.42
	1.06	0	0.173	1.93	0.525	0.149	0.509	0.15
		0.0012	0.172	1.93	0.521	0.154	0.506	0.20
		0.03	0.171	1.85	0.394	0.280	0.429	0.35
		0.2	0.168	1.56	0.110	0.552	0.161	0.67
	1.20	0	0.175	2.00	0.373	0.893	0.500	2.60
		0.03	0.175	1.86	0.371	0.909	0.397	2.61
NLH	1.00	0	0.174	1.59	0.041	0.148	0.256	-0.59
		0.0012	0.174	1.59	0.041	0.147	0.255	-0.58
		0.03	0.172	1.57	0.029	0.167	0.233	-0.43
		0.1	0.171	1.54	0.036	0.305	0.169	-0.29
	1.06	0.03	0.178	1.63	0.074	0.145	0.258	0.01
	1.22	0.03	0.185	1.54	0.088	0.906	0.296	3.27

fair agreement with Shiels et al. (2001) and Placzek et al. (2009). However, two important remarks should be made. On the one hand, the *full lock-in region* computed in this research was found to be narrower than the one predicted by other authors. This fact could be attributed to the uncertainty in the prediction of f_{shed}. As it was observed in Section 4.3.4 regarding the computation of the fixed configuration shedding frequency f_{shnat}, numerical aspects such as the size of the domain or the mesh resolution could influence this estimation. Another feasible explanation to the k^*_{eff} shifting could be the difference in the considered *Reynolds number*, which is not taken into account by the effective stiffness parameter and can have an impact on the width of the *lock-in region*. On the other hand, Shiels et al. (2001) and Placzek et al. (2009) predicted a maximum normalized displacement slightly higher than 0.58, while in this PhD work it seemed to be 0.509. Nevertheless the latter assumption should be confirmed by performing additional time marching simulations laying in the range k^*_{eff}=[1,2.5], where maximum vibrations are expected [Klamo (2007)]. This last comment also concerns the NLH method computations. Finally, the *post lock-in region* is defined as the area where the cylinder amplitudes start to decrease below $D'_{y,max}/D$=0.4. The *post lock-in region* was predicted by both NLH and time marching approaches. Computed amplitudes also support the hypothesis of a narrower lock-in region with respect to the results of Shiels et al. (2001) and Placzek et al. (2009).

Figure 4.37b shows the values of $C'_{L,max}$ as a function of k^*_{eff}. The increase of the lift fluctuations in the *pre lock-in* and *full lock-in* regions predicted by Shiels et al. (2001) and Placzek et al. (2009) was reproduced by both NLH and time marching methodologies. The points laying in the *post lock-in region* were found to be shifted to lower k^*_{eff} with respect to the results of both authors. This issue is probably related to the narrower lock-in region computed by the NLH and time marching simulations.

Figure 4.37c depicts a comparison of the average drag coefficients as a function of k^*_{eff}. As for the harmonic lift, a monotonic increase of $\bar{C}_D$ was obtained by Shiels et al. (2001) and Placzek et al. (2009) in the *pre lock-in* and *full lock-in* regions. This behavior was reproduced by both NLH and time marching computations. Contrary to the lift fluctuation, a fair agreement with respect to the references was also found for the computations performed after the drag crisis. It should be noticed that in Shiels et al. (2001) and Placzek et al. (2009) simulations the drop in $C'_{L,max}$ was delayed with respect to the $\bar{C}_D$ crisis.

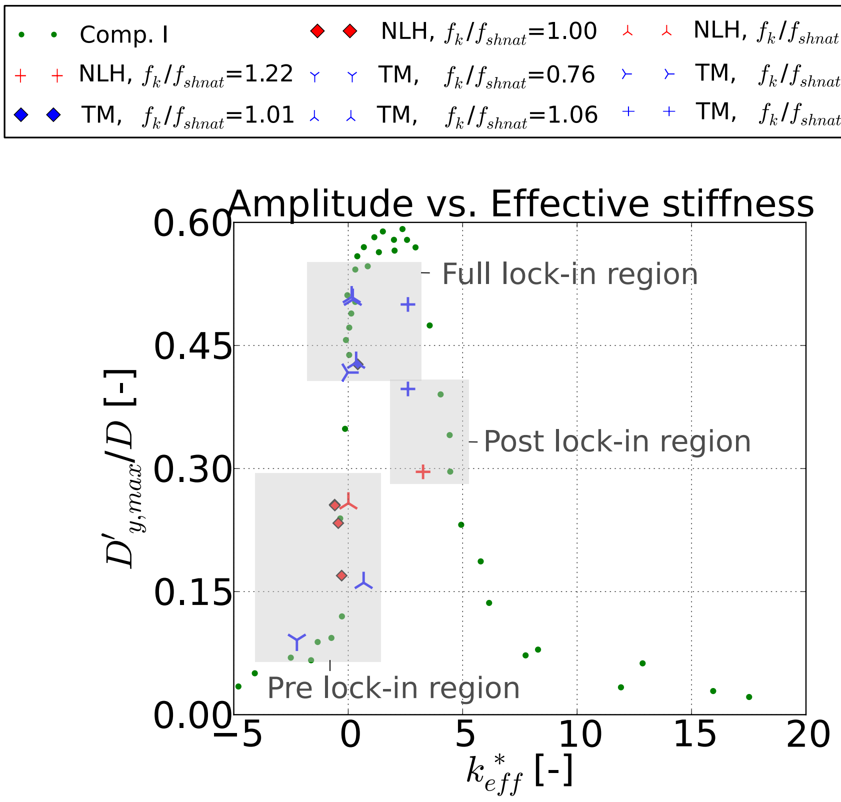

(a) $D'_{y,max}/D$

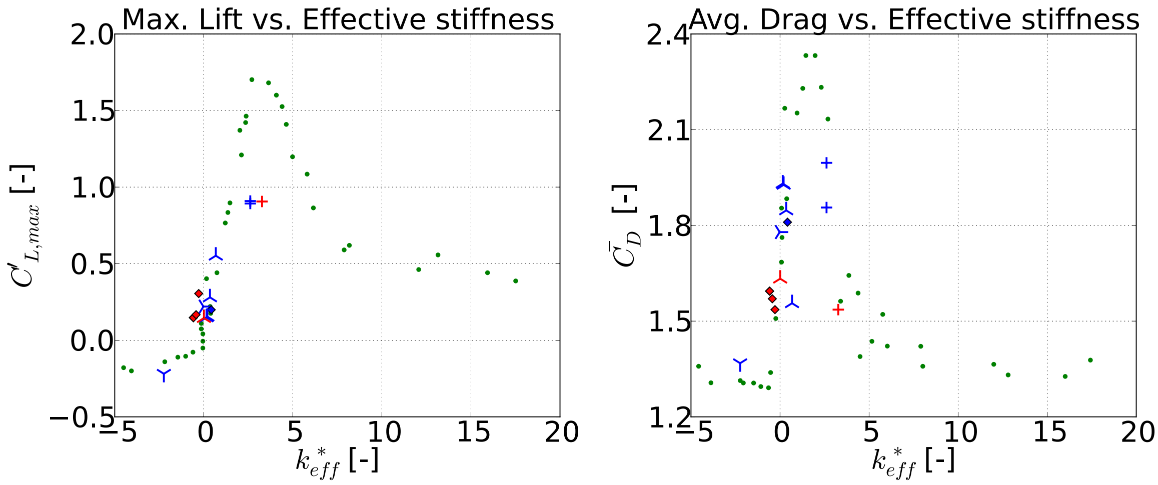

(b) $C'_{L,max}$ **(c)** $\bar{C}_D$

Figure 4.37: Computed variables for free oscillation cylinder as a function of k^*_{eff}. NLH (2 harmonics) and time marching computations (TM) at Re=120. Comp. I combines the computations of Shiels et al. (2001) and Placzek et al. (2009) at Re=100

Flow analysis

The lock-in region was characterized by a shedding frequency f_{shed} very close to the spring frequency f_k (see Figure 4.38a). This observation was already made by Placzek et al. (2009) and Mittal and Kumar (2001), and it is the reason why such a name was suggested. The evolution of f_{shed} normalized by f_{shnat} is illustrated in Figure 4.38b. The values issued from this research are compared against the results of Shiels et al. (2001) and Placzek et al. (2009), showing a very similar trend. Outside of the lock-in, the shedding frequency corresponds to f_{shnat}. The increase of the cylinder displacements observed in the *pre lock-in* and *full lock-in* regions is accompanied by a rise in the f_{shed}/f_{shnat} ratio. Maximum cylinder displacements were predicted for f_{shed}/f_{shnat}=[1.2,1.3] by Shiels et al. (2001) and Placzek et al. (2009). This fact was not captured in our simulations, revealing that additional configurations should be analyzed in order to have a deeper knowledge of the modeling capabilities of the presented methodology in the *full lock-in region*. Finally, a decrease of f_{shed}/f_{shnat} is expected in the *post lock-in region*, till a value of 1.0 is achieved.

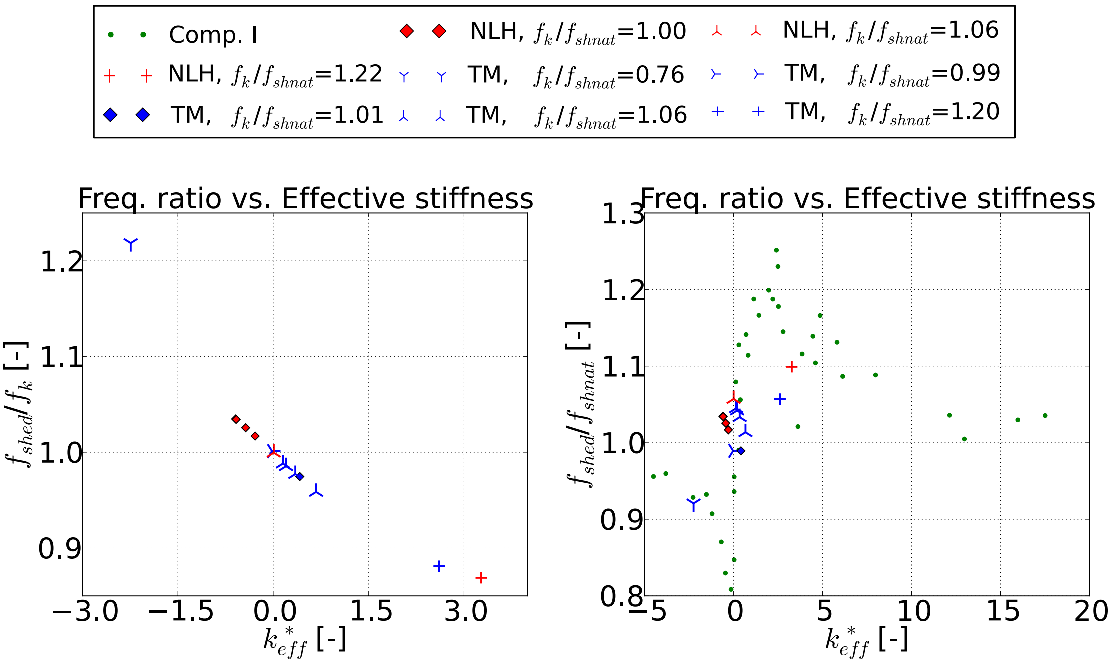

(a) f_{shed}/f_k **(b)** f_{shed}/f_{shnat}

Figure 4.38: Computed frequencies for free vibration cylinder as a function of k^*_{eff}. NLH (2 harmonics) and time marching computations (TM) at Re=120. Comp. I combines the computations of Shiels et al. (2001) and Placzek et al. (2009) at Re=100

Figure 4.39 shows C_D and C_L for several of the performed NLH and time marching computations, superposed to the imposed displacement D_y. As it can be observed, a limit cycle oscillation was predicted for all the computations that used the latter method. The harmonic content of these signals is included in Figure 4.40, and the corresponding phase portraits can be found in Figure 4.41. The transients of Figure 4.39a and Figure 4.39b correspond to time marching and NLH computations laying in the *pre lock-in region*, respectively. For both simulations the frequency of C_L was found to be centered at f_{shed}, while the drag force fluctuations contribution was carried out by $2f_{shed}$. In addition, C_L and D_y were found to be out of phase. As it was already discussed for the forced oscillation configuration described in Section 4.3.5, in this situation the fluid is assumed to act as an aerodynamic damper. This fact can be verified in Figure 4.41a and Figure 4.41b, by means of the orientation of the corresponding phase portraits. The *full lock-in region* was characterized by the re-synchronization of D_y and C_L, together with the appearance of an extra frequency into the latter coefficient (Figure 4.39c, Figure 4.39d and Figure 4.39e). This additional frequency was found to be $3f_{shed}$ (see Figure 4.40), in accordance with the observations of Placzek et al. (2009). The orientation of the phase portraits revealed that the flow was injecting energy into the cylinder oscillation, justifying the important amplification of the computed displacements (Figure 4.41c, Figure 4.41d and Figure 4.41e). Finally, in the *post lock-in region* the contribution of the $3f_{shed}$ component progressively disappeared (Figure 4.39f and Figure 4.39g). The analysis of the phase portraits revealed that the fluid was still exerting a negative damping into the cylinder oscillation for both NLH and time marching methodologies, even if more ovoid shapes were obtained (Figure 4.41f and Figure 4.41g).

For all the performed simulations, the shedding pattern was found to be qualitatively the same and equivalent to the previously observed for the forced oscillations configuration. Upper part vortices were shed during the ascending movement of the cylinder, while the release of lower part vortices took place during the descent. A total of two vortices were shed per period, corresponding to the so-called 2S mode. Figure 4.42 displays the vorticity contours for the simulations included in previous graphs at the instant of maximum cylinder displacement. The increase of k^*_{eff} lead to the stretching of the vortices, in accordance with the observations of Placzek et al. (2009). This is assumed to be related to the attached growth of f_{shed} (see Figure 4.38b), since the velocity of convection of the shed structures was common for all the performed simulations.

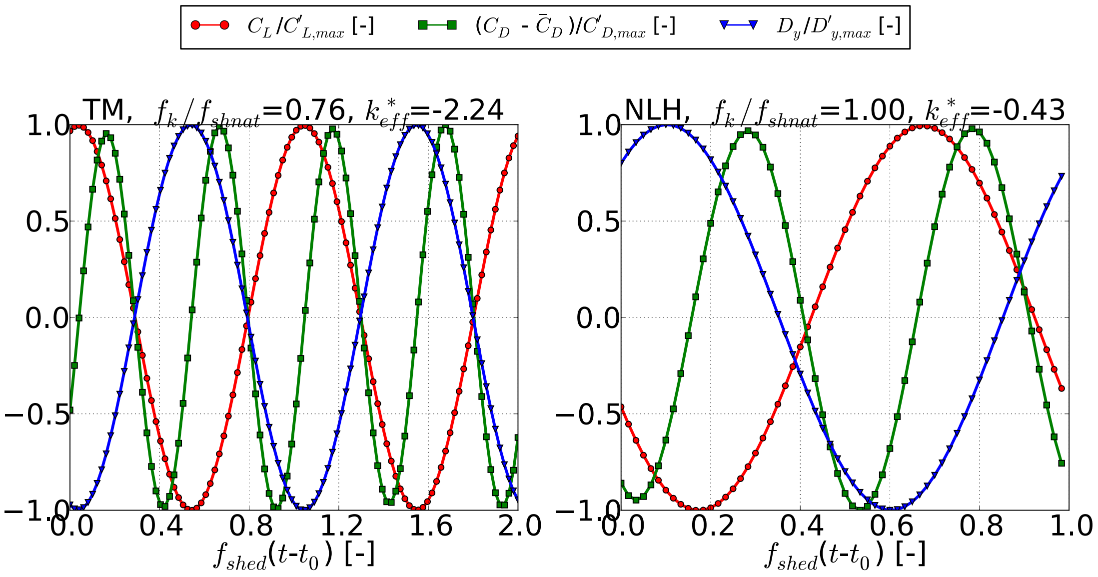

(a) TM, $\frac{f_k}{f_{shnat}}$=0.76, k^*_{eff}=-2.24 **(b)** NLH, $\frac{f_k}{f_{shnat}}$=1.00, k^*_{eff}=-0.43

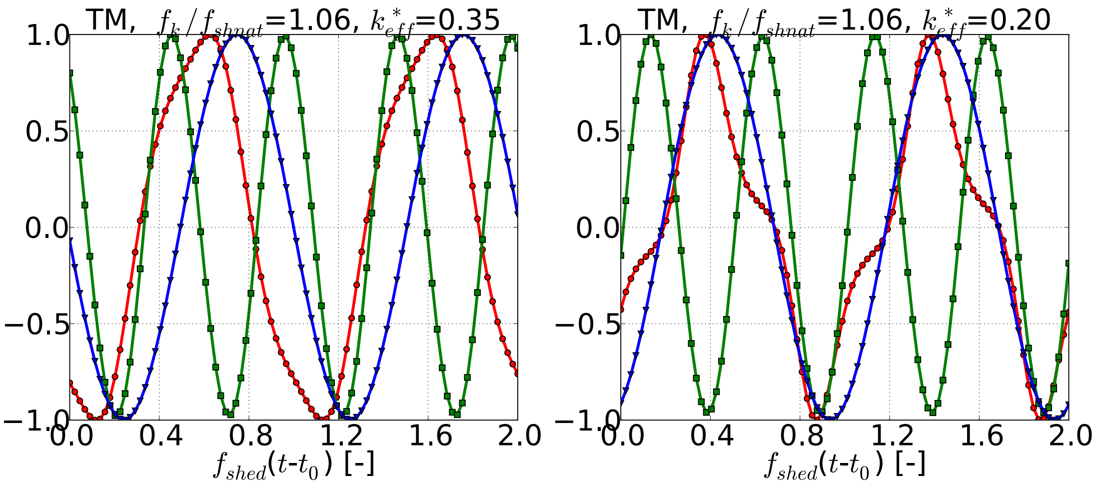

(c) TM, $\frac{f_k}{f_{shnat}}$=1.06, k^*_{eff}=0.35 **(d)** TM, $\frac{f_k}{f_{shnat}}$=1.06, k^*_{eff}=0.20

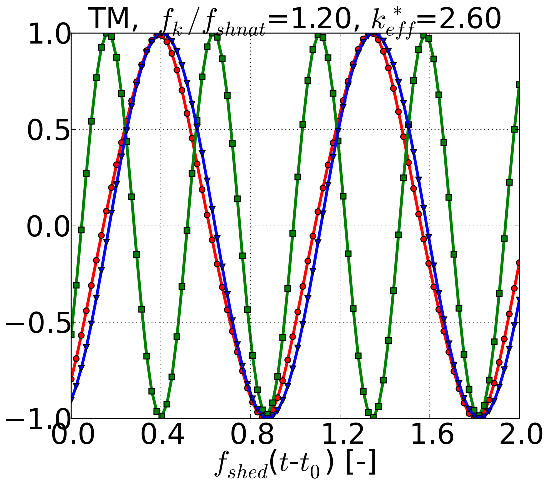

(e) TM, $\frac{f_k}{f_{shnat}}$=1.20, k^*_{eff}=2.60

Figure 4.39: Free oscillation cylinder, lift and drag coefficients evolution superposed to D_y. *Pre lock-in region*: (a), (b) , *Full lock-in region*: (c), (d), (e) , *Post lock-in region*: (f), (g). NLH simulations account for 2 harmonics. Markers do not represent data sampling. Continued on next page. . .

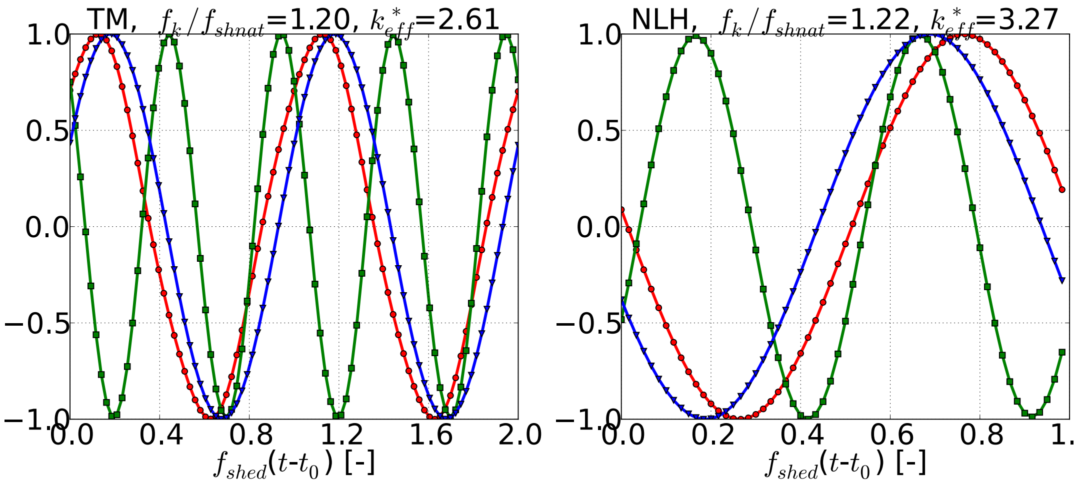

(f) TM, $\frac{f_k}{f_{shnat}}$=1.20, k^*_{eff}=2.61

(g) NLH, $\frac{f_k}{f_{shnat}}$=1.22, k^*_{eff}=3.27

Figure 4.39: Free oscillation cylinder, lift and drag coefficients evolution superposed to D_y. *Pre lock-in region*: (a), (b) , *Full lock-in region*: (c), (d), (e) , *Post lock-in region*: (f), (g). Markers do not represent data sampling. Concluded

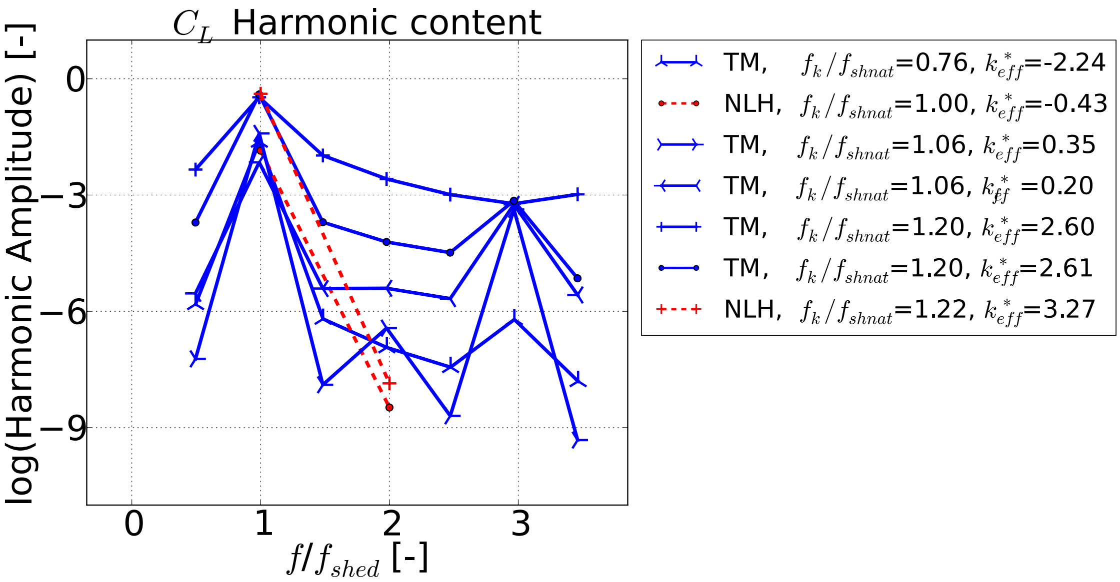

Figure 4.40: Free oscillation cylinder, harmonic content of lift coefficient. NLH simulations account for 2 harmonics

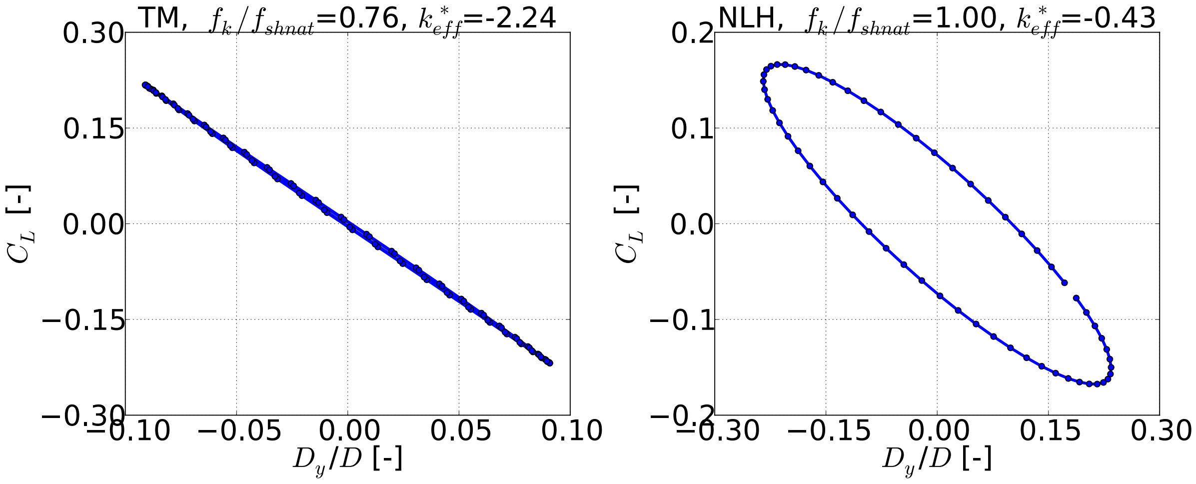

(a) TM, $\frac{f_k}{f_{shnat}}$=0.76, k^*_{eff}=-2.24

(b) NLH, $\frac{f_k}{f_{shnat}}$=1.00, k^*_{eff}=-0.43

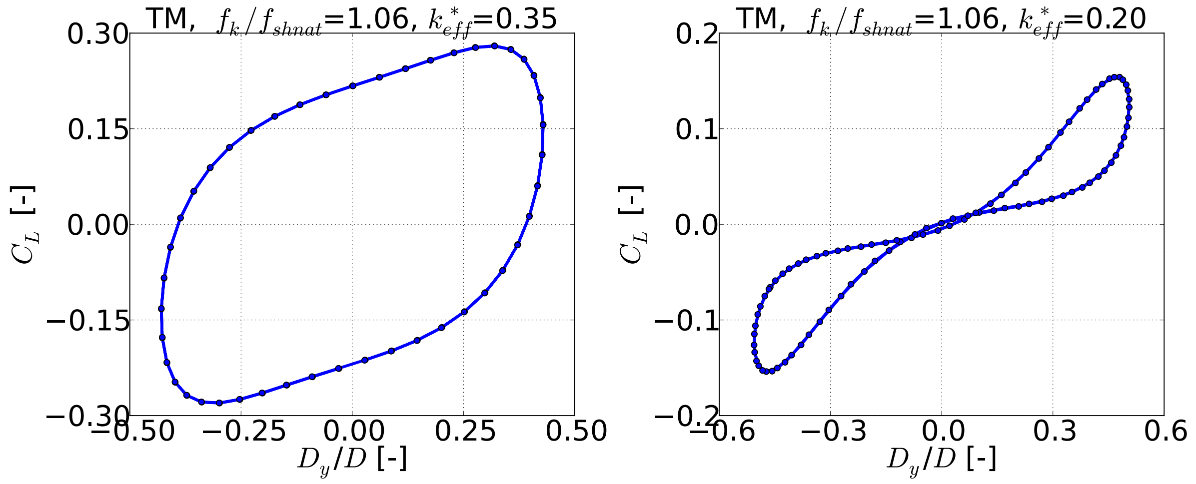

(c) TM, $\frac{f_k}{f_{shnat}}$=1.06, k^*_{eff}=0.35

(d) TM, $\frac{f_k}{f_{shnat}}$=1.06, k^*_{eff}=0.20

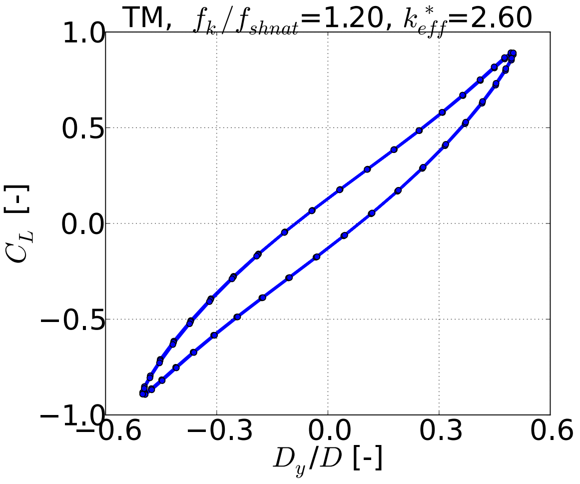

(e) TM, $\frac{f_k}{f_{shnat}}$=1.20, k^*_{eff}=2.60

Figure 4.41: Free oscillation cylinder phase portraits. *Pre lock-in region*: (a), (b) , *Full lock-in region*: (c), (d), (e) , *Post lock-in region*: (f), (g). NLH simulations account for 2 harmonics. Markers do not represent data sampling. Continued on next page. . .

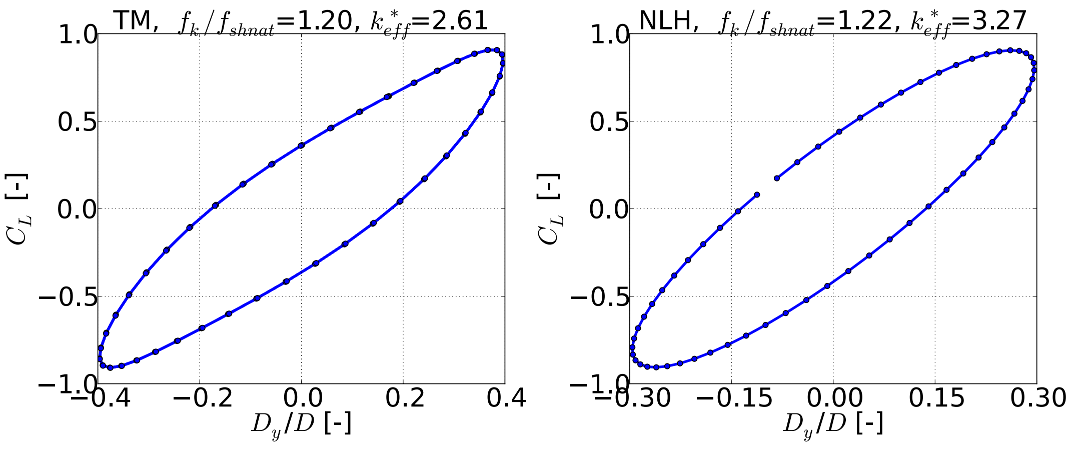

(f) TM, $\frac{f_k}{f_{shnat}}$=1.20, k^*_{eff}=2.61 **(g)** NLH, $\frac{f_k}{f_{shnat}}$=1.22, k^*_{eff}=3.27

Figure 4.41: Free oscillation cylinder phase portraits. *Pre lock-in region*: (a), (b) , *Full lock-in region*: (c), (d), (e) , *Post lock-in region*: (f), (g). Markers do not represent data sampling. Concluded.

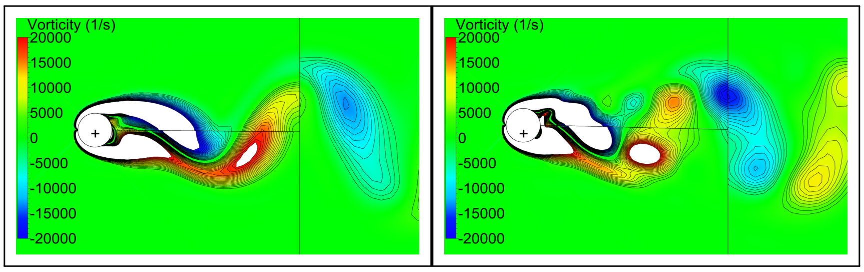

(a) TM, f_k/f_{shnat}=0.76, k^*_{eff}=-2.24 **(b)** NLH,f_k/f_{shnat}=1.00,k^*_{eff}=-0.43

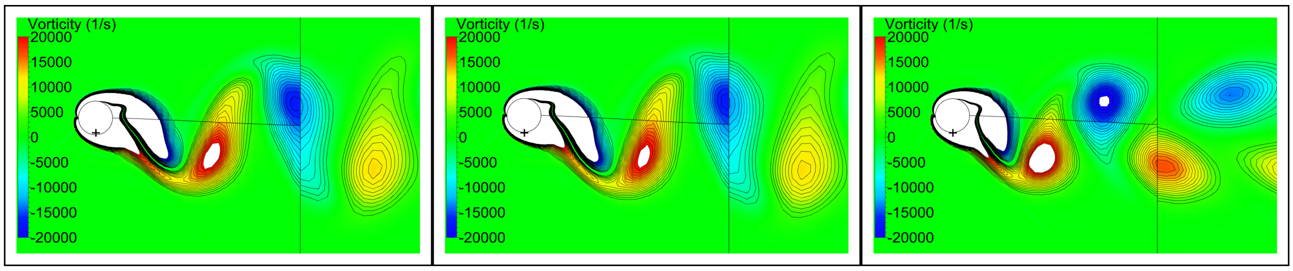

(c) TM, f_k/f_{shnat}=1.06, k^*_{eff}=0.35 **(d)** TM, f_k/f_{shnat}=1.06, k^*_{eff}=0.20 **(e)** TM, f_k/f_{shnat}=1.20, k^*_{eff}=2.60

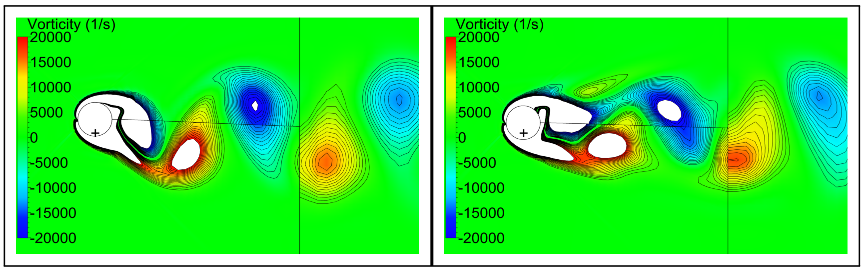

(f) TM, f_k/f_{shnat}=1.20, k^*_{eff}=2.61 **(g)** NLH, f_k/f_{shnat}=1.22, k^*_{eff}=3.27

Figure 4.42: Vorticity contours of free cylinder motion at maximum displacement. *Pre lock-in region*: (a), (b) , *Full lock-in region*: (c), (d), (e) , *Post lock-in region*: (f), (g). Isolines increment corresponds to 1000 s^{-1}. Solid lines represent block lines, and the cross sign is included at the center of the initial cylinder position

4.4 Comments about the computational time

Table 4.11 summarizes typically obtained CPU factors for the fixed cylinder configuration, defined as $\frac{T_h N_p}{N_n}$. With T_h the computational time in hours, N_n the number of mesh points in millions and N_p the number of processors (that was fixed to 1 for all the performed simulations). Similar values were observed for the 1-way and 2-way coupling simulations, since the time required for the update of the cylinder position was found to be negligible with respect to the cost of the solution of the Navier-Stokes equations. The computed ratio between the CPU factor of a time marching solution and a NLH simulation accounting for 2 harmonics is approximately 4.7. This remark directly shows that in the scope of the study of locked-in *forced oscillations* (see Section 4.3.5), the NLH approach was more efficient than the time marching method. Nevertheless, the analysis of both *fixed* and *free oscillation* configurations by means of the NLH method required of an iterative frequency identification process (Section 4.3.4 and Section 4.3.6). Since generally from 3 to 6 NLH computations were involved in this process, this method cannot be seen as an alternative to the time marching simulations from an efficiency point of view. Two clarifications should be made in this context. First, that the developed iterative approach could be eventually automatized in the CFD code, allowing to perform a single computation at the correct shedding frequency. A similar technique was implemented in the *Non-Linear Frequency Domain* method by McMullen et al. (2006), where the shedding frequency was computed by means of a minimization of the unsteady residuals. Secondly, that the conclusions issued from this test case regarding the computational time will certainly change when assessing other VIV problems.

Table 4.11: CPU factor for the cylinder simulations

NLH (1 harmo)	NLH (2 harmo)	NLH (3 harmo)	Time marching
39.51	69.85	91.70	326.3

4.5 Conclusion

In this section, the development of a 2-way FSI coupling method based on a generalized harmonic formulation was presented. Fluid loads were first computed with the NLH technique. A modal representation of the structure allowed then to estimate boundaries deformation, that were diffused into the whole CFD mesh by means of a harmonic version of the RBF+TFI *hybrid mesh deformation* method introduced in Section 3. A complete validation of this new development was conducted by studying the *Vortex Induced Vibrations* (VIV) phenomenon of a two-dimensional cylinder. Only the laminar regime was considered, in order to isolate the uncertainties in the prediction of the turbulence from the observations of the study. During this validation, the modeling capabilities of the proposed numerical method were also compared against a classical time marching approach (based on dual-time stepping). This task was performed in three steps of increasing complexity.

In the first stage of the validation, the cylinder was considered as *fixed*. For that fixed cylinder and in order to identify the natural shedding frequency of the flow for further NLH computations, the phase error method described in Spiker et al. (2006) was used. Similar predictions in terms of cylinder loads and shedding pattern were made by both NLH and time marching approaches. Concerning the *Strouhal number*, both methods showed an under-prediction with respect to available experimental data at high laminar *Re*. This discrepancy reached up to 7% when evaluating *Re*=150, and it is assumed to be related to the numerical model parameters. In particular, both the influence of the size of the domain and the mesh refinement of the downstream block could be assessed in future studies.

For the second step of the validation, a harmonic displacement law with frequency f_F was imposed to the cylinder geometry (1-way coupling). For both NLH and time marching methods, a lock-in of the shedding frequency with respect to f_F was observed. For that forced cylinder oscillation, the NLH approach showed an under-prediction of the harmonic lift of 7% with respect to the time marching solution, probably related to the differences in the estimation of the Strouhal number.

The final step of the validation concerned the *free oscillation* of the cylinder based on the computed fluid loads (2-way coupling). This set-up was achieved by mounting the cylinder on a single degree of freedom elastic system, allowing to move transversally to the incoming flow. In order to identify the frequency of cylinder oscillations in the NLH computations, an adaptation of the phase error method used in the first validation step was proposed. NLH and time marching results were compared against other authors simulations. Special attention was put in the understanding of the mechanisms driving the *vortex induced vibrations* phenomenon, and in particular in the so-called *lock-in zone*. Both NLH and time marching methodologies were able to predict the evolution of the cylinder response and the characteristics of the shed wake. However, small differences were observed with respect to the reference computations, probably related to the effects of the *Reynolds numbers* and to the differences in the prediction of the shedding frequency. Further studies will be needed in order to assess the capabilities of both approaches in the *full lock-in region*. For the particular case of the NLH method, the consideration of 3 harmonics are required based on the results of this research.

Two important contributions can be extracted from the development and the numerical simulations included in this chapter. On the one hand, it constitutes a detailed analysis of the performance of the NLH method when dealing with vortex shedding modeling. It was shown that the uncertainty in the value of the shedding frequency can be bypassed by the application of an iterative simulation process. Even if this approach has several limitations from the industrialization point of view, it opens the door to a potential development concerning the automatic shedding frequency identification. On the other hand, it describes the first 2-way coupling module based on the NLH method. As for the fixed cylinder case, it was shown that the identification of the aeroelastic frequency can be performed by means of an iterative process.

The application of this new technology into a wind energy context can be found later on in this document in Section 6.3. In opposition to the cylinder case, the use of the harmonic 2-way coupling NLH on wind turbines assumes that the main source of unsteadiness is carried out by the *blade passing frequency*. Hence, the application of a frequency identification process is not required. It should be also reminded that wind turbines use to operate at high *Reynolds numbers*, where important turbulent effects are to be expected. Since those are taken into account in the fluid loads computed by the NLH approach, the proposed FSI harmonic methodology is assumed to be applicable for wind turbine analysis without implying any additional limitations.

Chapter 5

DTU 10MW RWT Rotor-only analysis

Due to the continuous upscaling of modern HAWTs, important *aeroelastic effects* are to be expected. Traditional CFD approaches do not consider the flexibility of the rotor. However, blade deflections can have a non negligible impact on the machine performance, and a possible *blade-tower impact* should be considered at the design stage. This requires the consideration of rotor structural models in the CFD computations, as well as FSI effects. Due to the lack of publicly available *industrial* configurations, previous studies concerning wind turbines *aeroelasticity* are based on the so-called *academic* or *reference* designs. In this group we find the works of Corson et al. (2012) for the SNL-100-00 blade and the studies of the NREL 5MW performed by Hsu and Bazilevs (2012) and Yu and Kwon (2014). In all these publications, blade deflections were found to have a direct impact on the final rotor performance.

In this chapter, a complete characterization of the DTU 10MW RWT aeroelasticity in a *rotor-only* context is presented. A brief description of this machine is included in Section 5.1. A *Reynolds Averaged Navier Stokes* (RANS) approach was used in order to perform steady simulations of the relative flow field of this HAWT. The rotor was considered either as *rigid* or *flexible*. For the latter case, the consideration of a blade structure sub-model was necessary. Mesh deformation was carried out by the 3-steps *hybrid method* described in Chapter 3.

First computations included in Section 5.2 were based on the standard DTU 10MW RWT rotor, assuming a *rigid* configuration. *Straight* blades were considered, equipped with the so-called *Gurney flaps* devices at low span range [5%,40%]. Obtained results were compared with 3D CFD simulations performed by other authors. In Section 5.3, *static aeroelasticity* computations were performed by means of a 2-way coupling FSI approach. The behavior of the structure was linearized by means of its natural frequencies and deformed shapes. The same methodology was used in Section 5.4 to compare the performance of this standard blade with a “clean” variant, where *Gurney flaps* were removed. Both *rigid* and *flexible* rotor configurations were studied. In order to analyze the DTU 10MW RWT rotor in a more assembly-oriented configuration, additional simulations accounting for blades *pre-cone* and *pre-bending* were performed and their results are included in Section 5.5.

In all the simulations included in this chapter, turbulence was considered by means of Spalart-Allmaras model [Spalart and Allmaras (1992)]. A brief study of the turbulence modeling sensitivity for the *pre-cone* and *pre-bent* blade configuration is also included is Appendix C, by means of a comparison with the k-ω SST model [Menter (1993)]. The same flow separation regions and blade deformations were observed for both turbulence models. Even if a direct impact on the computed rotor performance was observed, the trends predicted by the Spalart-Allmaras and the k-ω SST models regarding the effects of aeroelasticity and rotor speed were consistent.

5.1 The DTU 10MW RWT

The DTU 10 MW RWT is a variable pitch, variable speed and *upwind* HAWT [Bak et al. (2013)]. It was designed as an upscaling of the NREL 5MW reference wind turbine [Jonkman et al. (2009)]. The blade design was however modified by equipping FFA-W3-xxx airfoil series. The main parameters characterizing the DTU 10MW RWT are summarized in Table 5.1. In Figure 5.1, the 3D view of the DTU 10MW RWT whole assembly included in Bak et al. (2013) is reproduced.

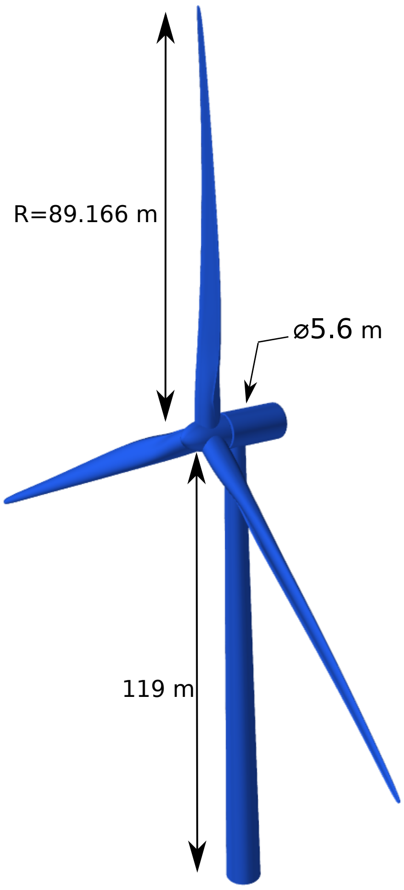

Figure 5.1: 3D view of DTU 10MW RWT

Parameter description	Parameter Value
Cut in wind speed	4 m.s^{-1}
Cut out wind speed	25 m.s^{-1}
Rated wind speed	11.4 m.s^{-1}
Rated power	10 MW
Number of blades	3
Rotor total radius (R)	89.166 m
Min. rotor speed	6 RPM
Max. rotor speed	9.6 RPM
Hub diameter	5.6 m
Hub height	119 m
Rotor mass	227.962 kg
Nacelle mass	446.036 kg
Tower mass	982.765 kg
Tower diameter top	5.5 m
Tower diameter base	8.3 m
Tower clearance	18.26 m

Table 5.1: DTU 10MW RWT main parameters

The DTU 10MW RWT tower is made from steel. The blades structure is based on glass fiber reinforced composites and balsa wood. The radial evolution of the blade geometrical properties is depicted in Figure 5.2. The low span range accounted for thicker airfoils. A maximum chord of 6.2 m was designed for r=25 m. In order to adapt the incidence of the blade to the tangential velocity, a twist law was also defined. The blade root cross section was assumed to be perfectly cylindrical, followed by a transition towards the FFA-W3=xxx airfoil series. At low span ranges [5%,40%], *Gurney flaps* were installed in order to increase the aerodynamic performance of the blade. These devices consisted in smooth wedge shapes located at the blade trailing edge, as it is depicted in Figure 5.3. A representation of the cross section shapes evolution of the DTU 10MW RWT blade is shown in Figure 5.4. The *Gurney flap* device can be identified for the section at r=23.528 m.

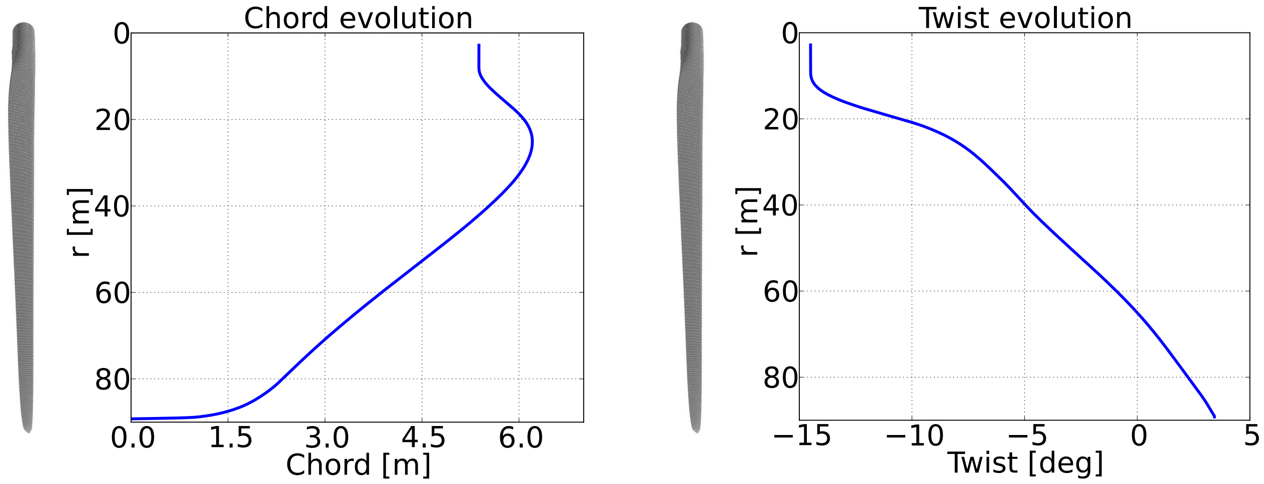

(a) Chord **(b)** Twist

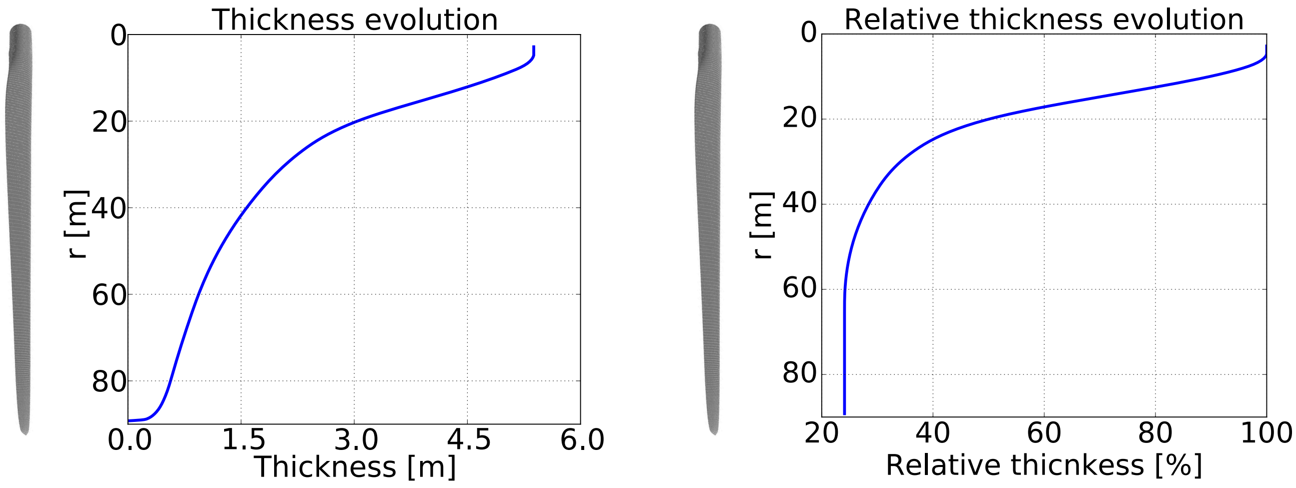

(c) Thickness **(d)** Relative thickness

Figure 5.2: Radial evolution of the DTU 10MW RWT blade geometrical parameters. A blade sketch is included at every plot for clarity purposes

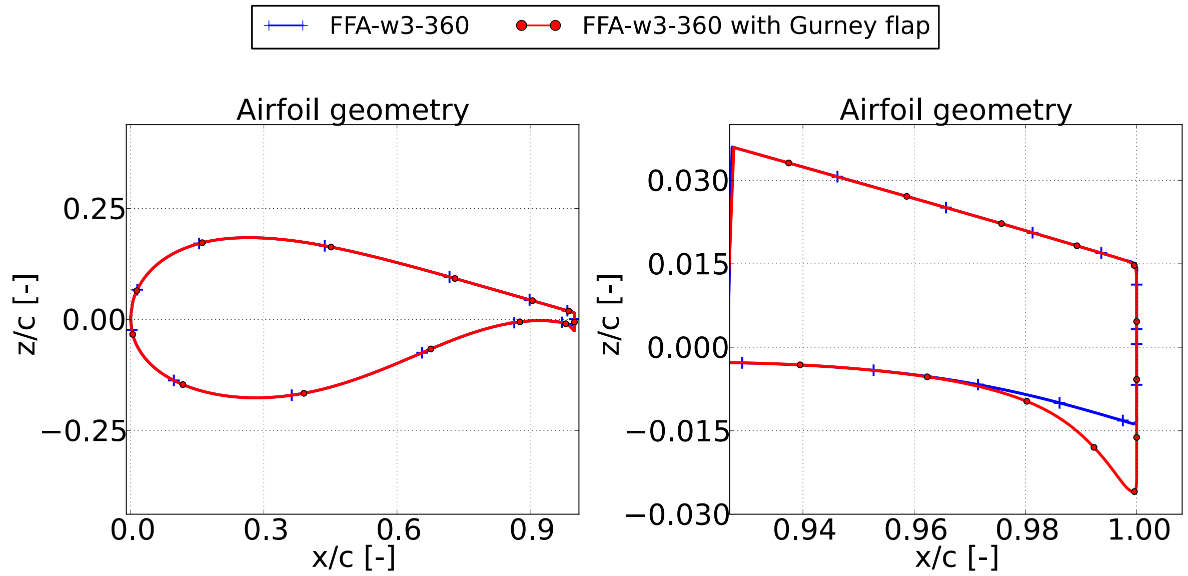

(a) Global view **(b)** Trailing edge zoom

Figure 5.3: FFA-w3-360 airfoil, equipped by the DTU 10MW RWT at low span. Comparison of the original shape and its modification after the introduction of the *Gurney flaps*. Coordinates are normalized by the chord c. Markers do not represent data sampling

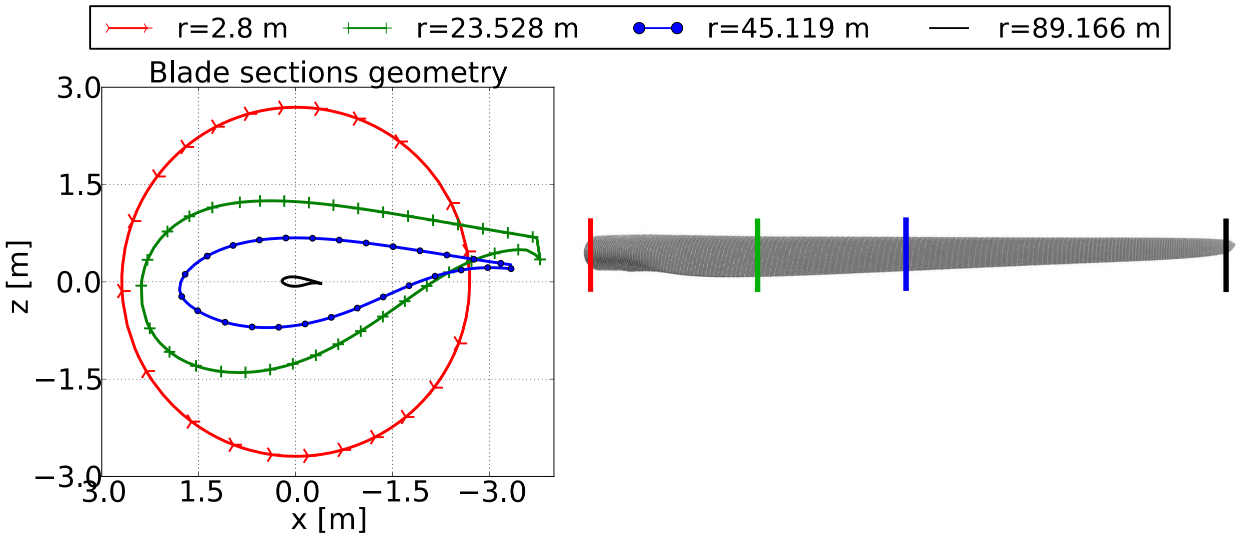

Figure 5.4: Cross sections of DTU 10MW RWT blade for different radii. Markers do not represent data sampling. A sketch of the cross sections location on the blade span was added for clarity purposes

Two blade variants of the DTU 10MW RWT blade geometry were defined in Bak et al. (2013), considering a *straight* and a *pre-bent* axis. As it will be discussed in Section 5.5, the latter geometry constitutes a more realistic scenario when dealing with *flexible* blades. The *pre-bending* law is illustrated in Figure 5.5. A complete FEM model of the *straight* blade structure was also described in Bak et al. (2013), and it is publicly available for direct download. The commercial package Abaqus was used for this task [Simulia (2008)]. External and internal geometries of the blade and composite layup were modeled by means of 8-node layered shell elements. The adhesive connecting the suction side shell and the pressure side

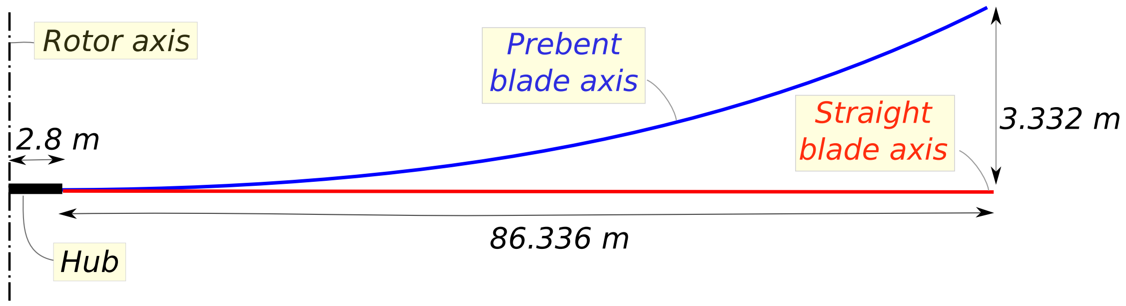

Figure 5.5: DTU 10MW RWT blade axis prebending

shell was modeled by means of hexahedral elements. The whole FEM model accounted for a total of 35.000 elements and 104.000 nodes. In order to properly define the composite layup, the blade was split into 11 circumferential regions and 100 radial regions. A 3D view of the whole FEM model is depicted in Figure 5.6.

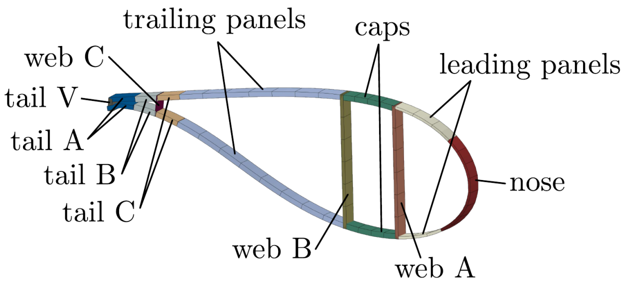

(a) Radial segment

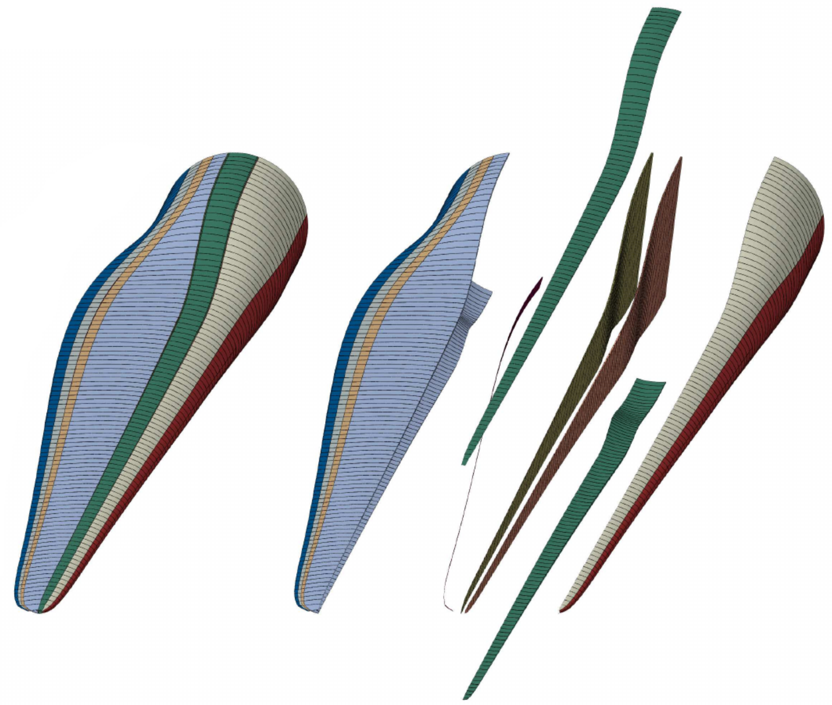

(b) Whole assembly

Figure 5.6: DTU 10MW RWT *straight* blade FEM model. Reproduced from Bak et al. (2013). (a): Detail of every radial segment, accounting for 11 circumferential regions. (b): Global view of the assembly, including the 100 radial segments

5.2 Steady aerodynamics, original geometry

The first set of performed CFD computations was based on the *straight* variant of the DTU 10MW RWT rotor, assuming the blades as *rigid*. The original blade geometry defined in Bak et al. (2013) was considered, accounting for the *Gurney flaps* at low span range. This *rotor-only* configuration was also studied with other 3D RANS solvers. The results of Ellypsis3D can be found in the DTU 10MW RWT definition document [Bak et al. (2013)], and the simulations of the HMB2 solver were compiled in the MAREWINT project deliverable D5.4 [Leble et al. (2015)]. In order to assess the sensitivity of the developed model, the results issued from this research were compared against both references. The whole 0 deg pitch operating range of the DTU 10MW RWT was considered for this code to code comparison.

5.2.1 Methodology

The considered rotor geometry accounted for the DTU 10MW RWT *straight* blade at 0 deg pitch. Both the nacelle and the hub were also taken into account, based on their original definition. Figure 5.7c shows a 3D view of the complete rotor. Autogrid5™ structured grids generator was used in order to perform a 3D mesh [NUMECA International (2013a)]. Only one blade passage was meshed, assuming rotational periodicity boundary conditions for the radial surfaces. The rest of boundary conditions, referred in this document as *externals*, relied in the subsonic far-field formulation described in Hirsch (1990). Figure 5.7a shows a 3D view of the computational domain, including the blocking topology of the generated mesh (solid lines). Flow inlet and outlet were located at 2.2 and 3.1 blade radius from the nacelle respectively. In order to avoid the alignment of the fluid speed and the external boundary conditions, those accounted for an expansion angle in the longitudinal direction. A scaled sketch of the computational domain is included in Figure 5.7b.

The generated mesh accounted for a total of 7.2×10^6 nodes and 24 blocks. A first cell height of 10^{-4} m was imposed at the boundary layer of the blade, in order to target y+ values of less than 10 at the first inner cell as suggested in NUMECA International (2013b). This height value corresponds to approximately 1.1×10^{-6} R. Figure 5.8 shows a global overview of the mesh. For clarity purposes the three blades are displayed, and 1 out of 2 grid lines are skipped. In Figure 5.9a, the cross-section mesh at mid-span is illustrated. The geometry of *Gurney flaps* at 20% of span together with the surrounding cross-section mesh is shown in Figure 5.9b.

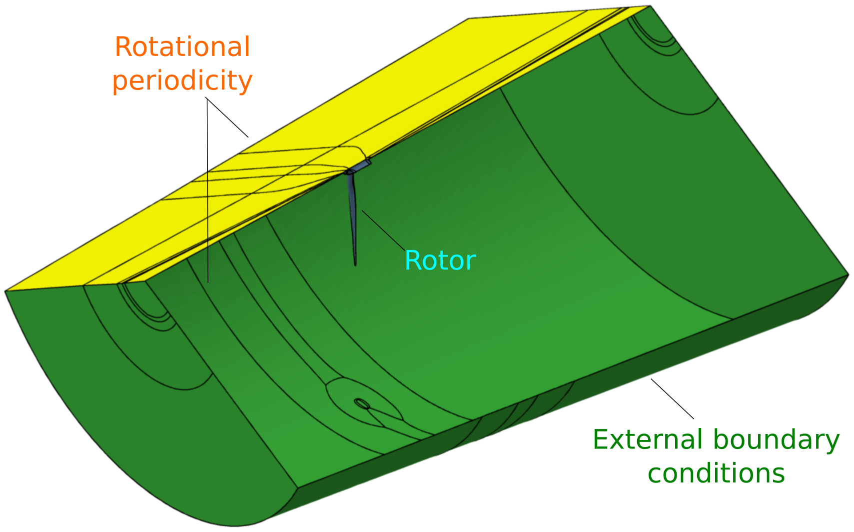

(a) Computational domain, 3D view

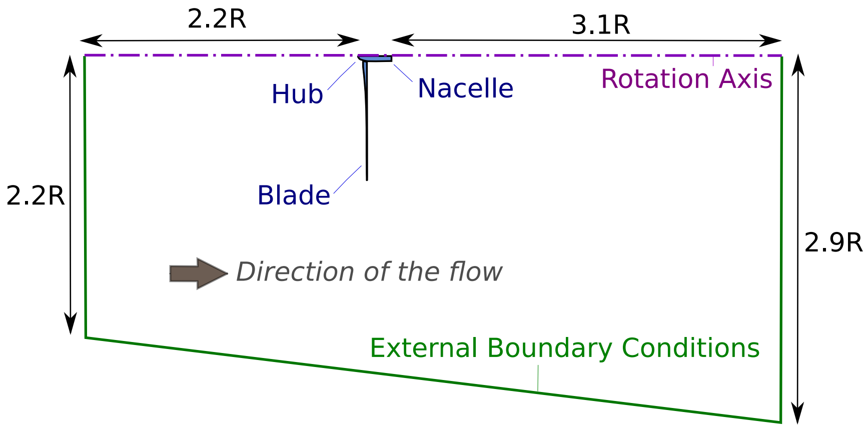

(b) Computational domain, scaled sketch

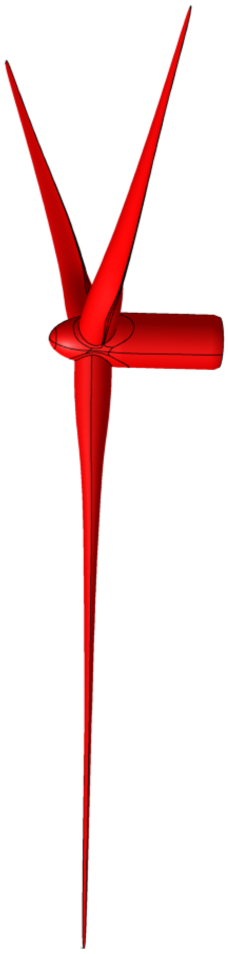

(c) Geometry

Figure 5.7: Geometry and computational domain for the *straight* blade *rotor-only* simulations. In (a), one of the periodic boundary conditions was removed to allow the visualization of the interior.

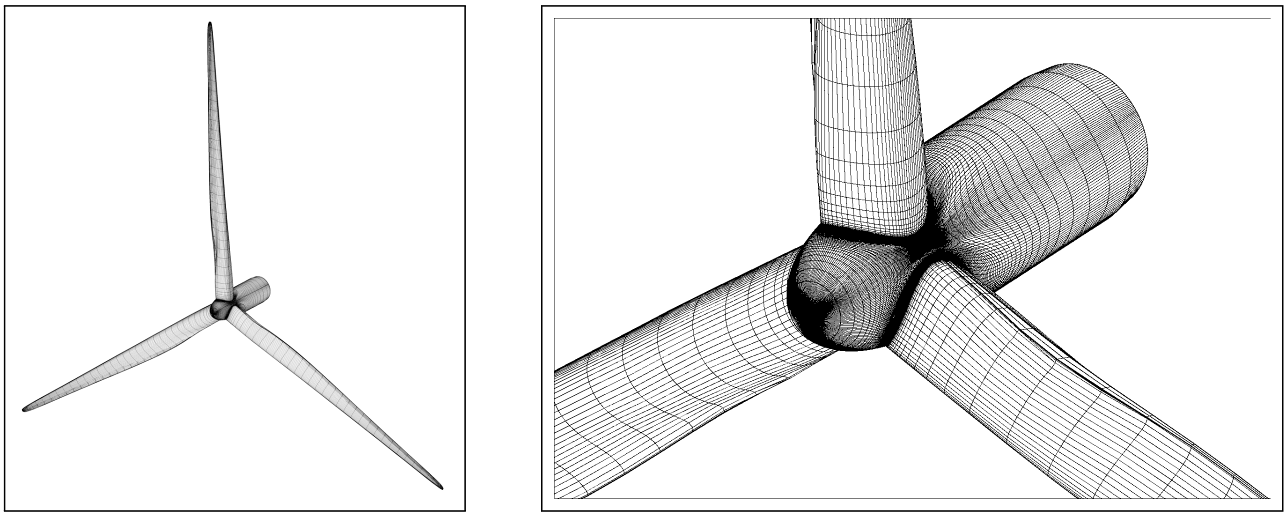

(a) Global view **(b)** Detail of nacelle and low blade span range

Figure 5.8: DTU 10MW RWT surface mesh overview (displayed 1 every 2 grid lines)

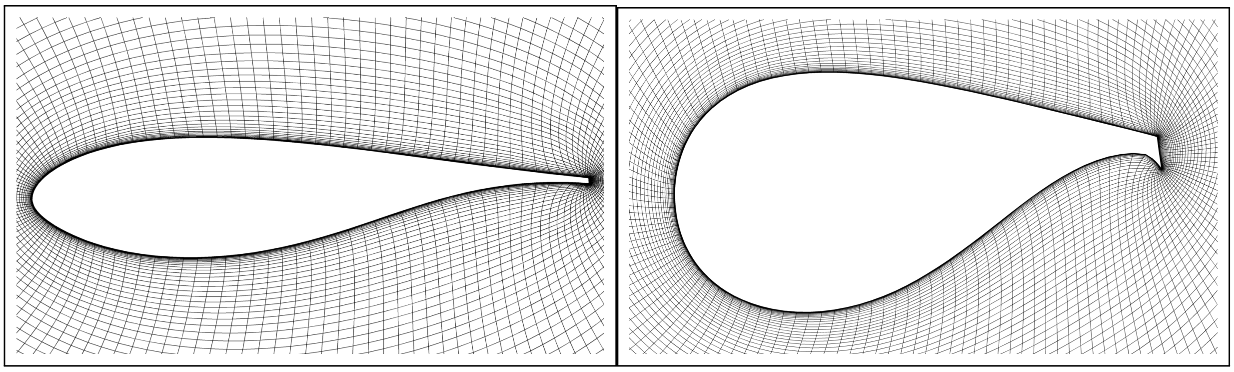
(a) 50% span **(b)** 20% span

Figure 5.9: DTU 10MW RWT cross-section meshes, 20% and 50% span

The fluid was modeled as a perfect gas. The Spalart-Allmaras turbulence model [Spalart and Allmaras (1992)] was used for the RANS simulations, enhanced by Merkle preconditioner [Merkle et al. (1998)]. A multigrid approach was followed in order to speed-up the computations. Different operating points of the DTU 10MW RWT wind turbine at 0 deg pitch were analyzed, as defined in Bak et al. (2013). These points are listed in Table 5.2. To contextualize the expected flow behavior, the radial evolution of the *Reynolds number* and *Mach number* at 11 ms^{-1} are illustrated in Figure 5.10. Those coefficients were computed based on the relative flow velocity and axial chord. A maximum value of Re=1.28×10^7 is observed at the loads production region of the blade (r/R=0.58). The blade tip Mach number corresponded to 0.24. Hence, no compressibility effects were expected.

Table 5.2: DTU 10MW RWT aerodynamic load cases definition

DLC Identifier	Wind speed [ms^{-1}]	RPM
FT_WSP07	7	6.000
FT_WSP08	8	6.426
FT_WSP09	9	7.229
FT_WSP10	10	8.032
FT_WSP11	11	8.836

5.2.2 Flow visualization at 11 ms^{-1}

The imposed first cell hight along the blade was considered as sufficiently small with regards to the requirements of the Spalart-Allmaras turbulence model, since the y+<10 criterion was satisfied for all the performed computations. A number of nodes ranging from 30 to 40 laid in the boundary layer for the blade sections at the vicinity of the blade tip. Figure 5.11 displays y+ around different blade sections, normalized by the corresponding axial chord *c*. A maximum value of 6.3 is observed for r/R=0.9. Flow separation was observed at the low

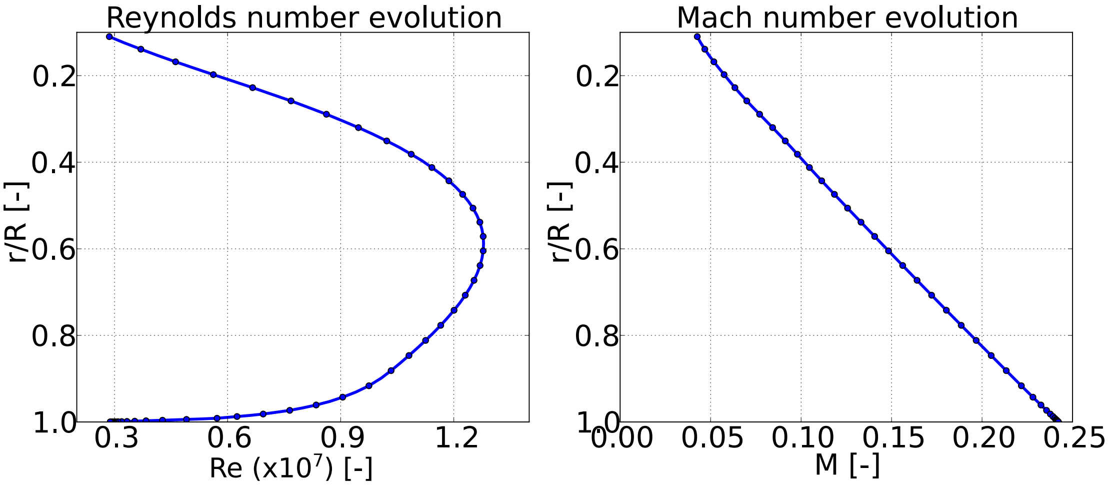

(a) Reynolds number (Re) **(b)** Mach number (M)

Figure 5.10: DTU 10MW RWT, relative *Mach* and *Reynolds* numbers radial evolution at nominal operating point

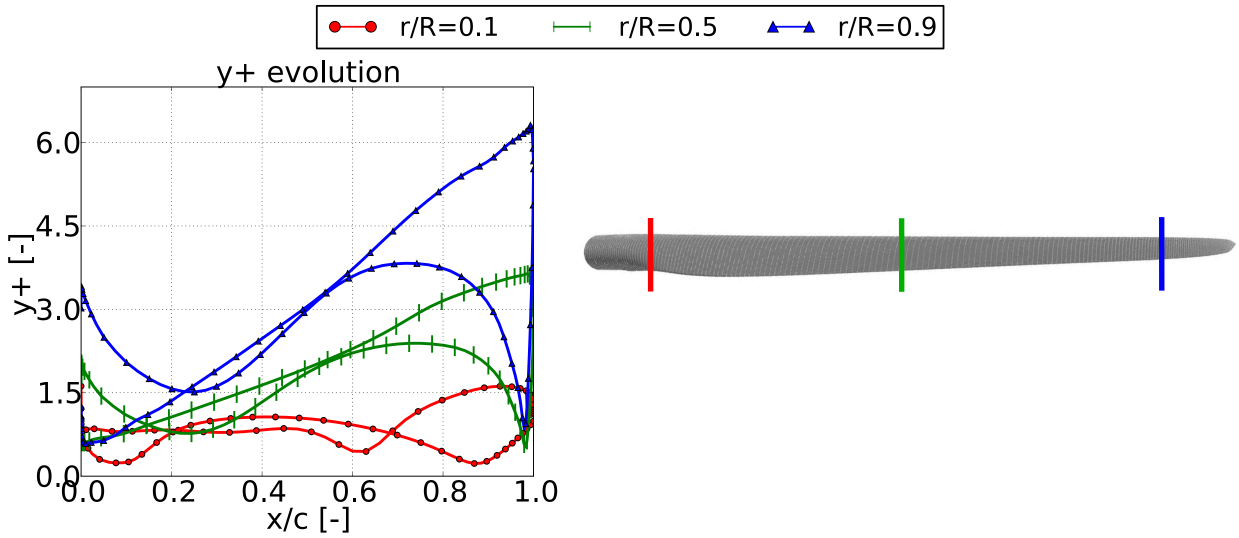

Figure 5.11: Computed y+ values at different cross sections of the DTU 10MW RWT blade. A sketch of the cross sections location on the blade span was added for clarity purposes

blade span range. Figure 5.12 shows the surface restricted streamlines for different cross sections. At r/R=0.2, two trailing edge recirculation bubbles can be observed. The flow separation can be better understood by means of the friction streamlines of the blade surfaces (see Figure 5.13). Both pressure surface and suction surface separation bubbles were identified. While the former ranged from r=14.9 m to r=20.3 m (r/R=[0.17,0.23]), the latter spread from the blade hub up to r=39.7 m (r/R=0.45). This last remark is in-line with the EllipSys3D computations performed by Zahle et al. (2014), where the suction surface separation was found up to an approximate radius of 30 m (r/R=0.34). It is important to remark that the computed pressure surface separation bubble was highly three-dimensional. Indeed the recirculation was dragged in the radial direction toward the blade tip, due to the centrifugal

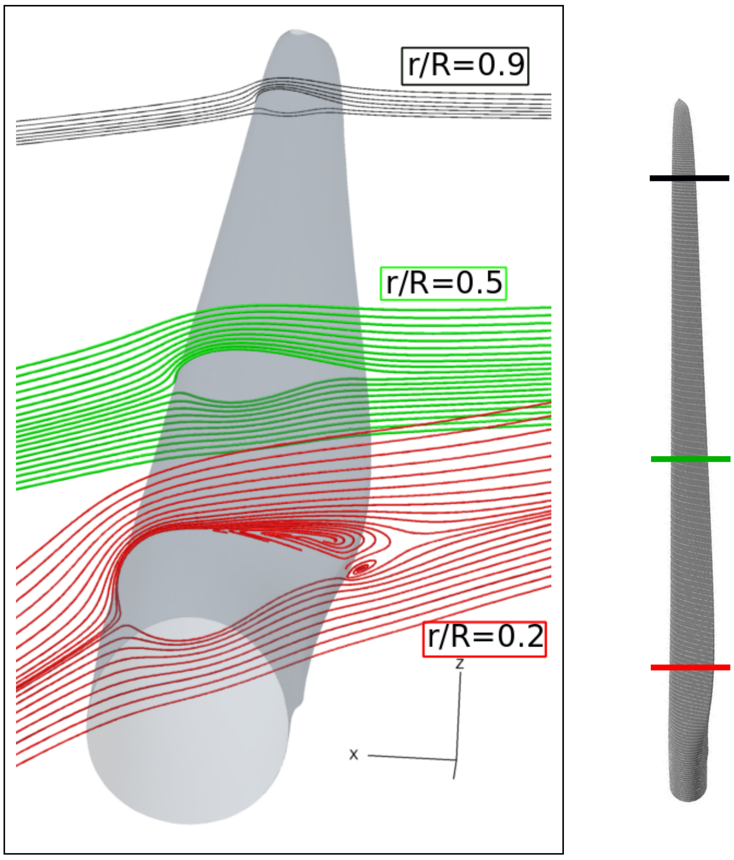

Figure 5.12: DTU 10MW RWT, surface restricted relative velocity streamlines for blade sections at r/R=0.1 (red), r/R=0.2 (green) and r/R=0.9 (black). A sketch of the cross sections location on the blade span was added for clarity purposes

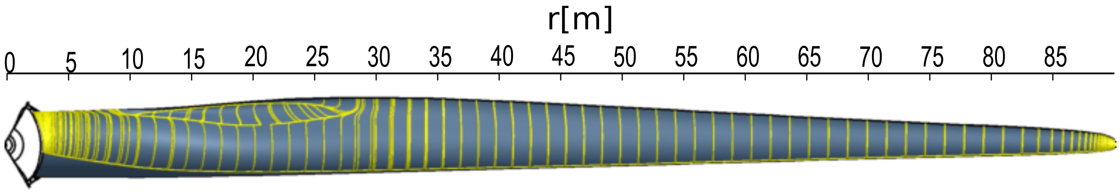

(a) Pressure surface

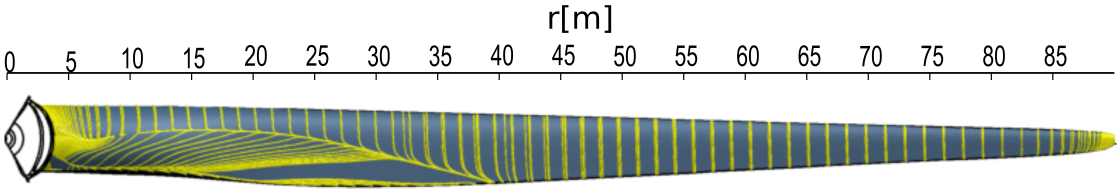

(b) Suction surface

Figure 5.13: Blade friction streamlines at 11 ms^{-1} along blade surfaces, showing flow separation regions for both the pressure side and the suction side

effects. This effect is graphically put in evidence in Figure 5.14, *via* the streamlines of the incoming flow at ∼r/R=0.1. This 3D behavior of the flow could be hardly modeled with pure 2D approaches, such as the BEM method, justifying the use of CFD for this analysis. Finally, Figure 5.15 displays the streamlines of the incoming flow at the blade tip. The tip vortex can be clearly identified, as well as the expansion of the wake due to the capture of kinetic energy performed by the rotor (as illustrated by means of the actuator disc model in Section 2.1.1).

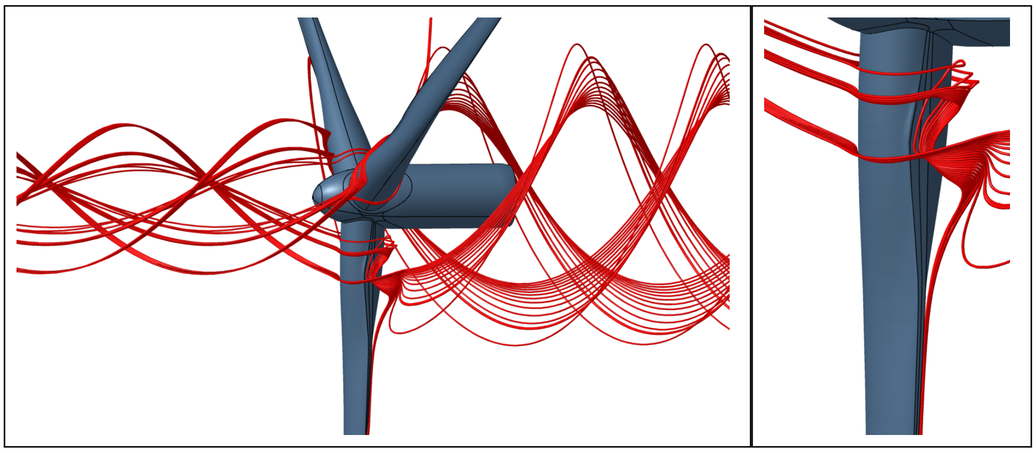

(a) Global view **(b)** Blade zoom

Figure 5.14: DTU 10MW RWT, relative velocity streamlines at low span

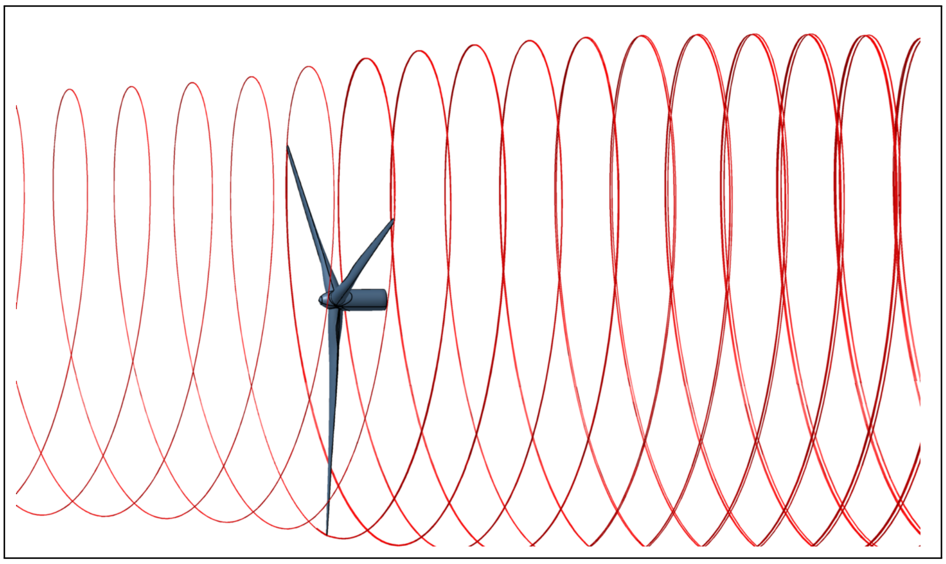

(a) Global view

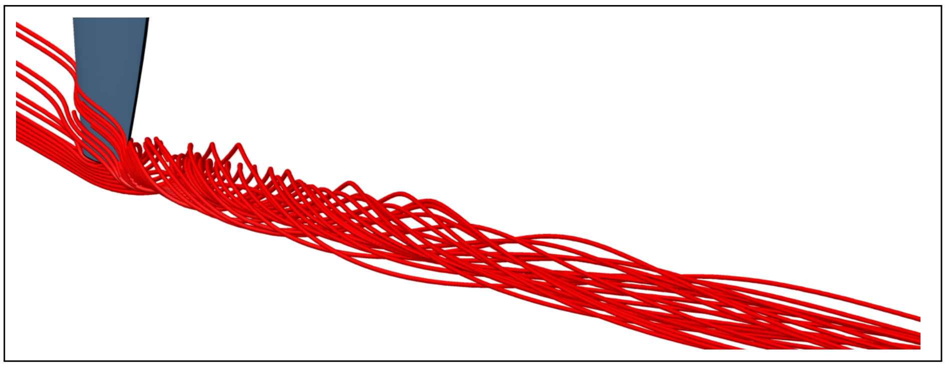

(b) Blade zoom

Figure 5.15: DTU 10MW RWT, relative velocity streamlines at the vicinity of blade tip

5.2.3 Rotor performance

Figure 5.16 shows the computed rotor loads for all the considered operating points, compared with RANS simulations performed by other authors. The different solutions captured a similar monotonic increase of both thrust and power for the considered operating range. The HMB2 solution seemed to systematically over predict both quantities when compared to the results of Ellypsis3D and the values obtained with FINE™/Turbo in this research. The differences between the last two solvers is quantified in Table 5.3. For all the considered wind speeds, the maximum percentile difference was smaller than 1.5%. Hence, it can be concluded that both methodologies do predict a similar flow solution. Due to the lack of experimental data of the DTU 10MW RWT, no further conclusions can be made regarding their accuracy. Since different operating points are considered in this section, it is interest-

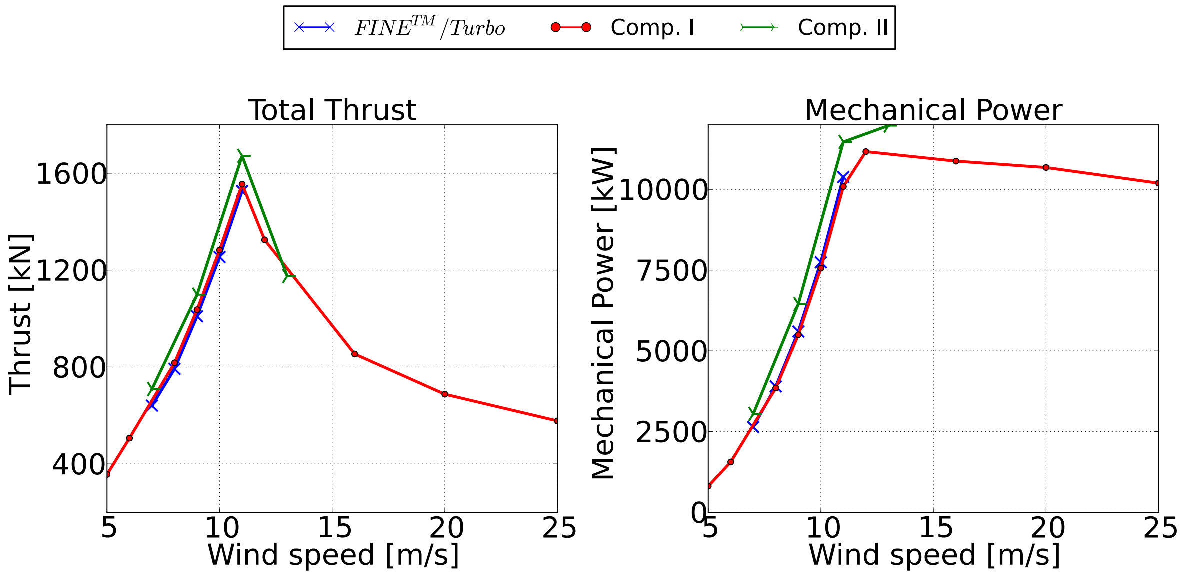

(a) Total thrust **(b)** Mechanical power

Figure 5.16: DTU 10MW RWT total rotor loads versus wind speed, original *straight* blade with *Gurney flaps*. Comp. I refers to the Ellypsis3D computations included in Bak et al. (2013). Comp. II refers to the HMB2 results included in Leble et al. (2015)

Table 5.3: Computed DTU 10MW RWT rotor loads compared with Bak et al. (2013) simulations, original *straight* blade with *Gurney flaps*

Operating point	**Thrust [kN]**			**Power [MW]**		
	Current research	Bak et al. (2013)	**Diff [%]**	Current research	Bak et al. (2013)	**Diff [%]**
FT_WSP08	804.6	817.0	1.5	3.886	3.848	-1.0
FT_WSP09	1022.9	1036.6	1.3	5.562	5.497	-1.2
FT_WSP10	1266.4	1282.6	1.3	7.660	7.561	-1.3
FT_WSP11	1539.6	1555.0	1.0	10.024	10.088	0.63

ing to express the rotor thrust and mechanical power in terms of the *global thrust coefficient* $C_t|_{global}$ and *global mechanical power coefficient* $C_p|_{global}$:

$$C_t|_{global} = \frac{BT}{0.5\rho U_\infty^2 \pi R^2}, C_p|_{global} = \frac{B\tau\Omega}{0.5\rho U_\infty^3 \pi R^2} \tag{5.1}$$

where T stands for the thrust force generated per blade, τ is the torque per blade, B stands for the number of blades, U_∞ is the incoming fluid speed, ρ is the fluid density, R is the total blade span and Ω is the rotating speed.

$C_t|_{global}$ and $C_p|_{global}$ are depicted in Figure 5.17. Due to the adaptation of the rotor speed for the considered operating points, an almost constant evolution of both coefficients is expected. This corresponds to the power production range of the machine. Due to the normalization of the rotor loads, the gap between the different numerical solutions is emphasized. This is especially true for the value of $C_p|_{global}$. In order to analyze the local differences between the presented methodologies, the local evolution of thrust and mechanical power coefficients is shown in Figure 5.2. The expressions of $C_t|_{local}$ and $C_p|_{local}$ used in Johansen et al. (2007) were adopted. For every considered blade segment s centered at a radius r and with a length of Δr, they can be written as:

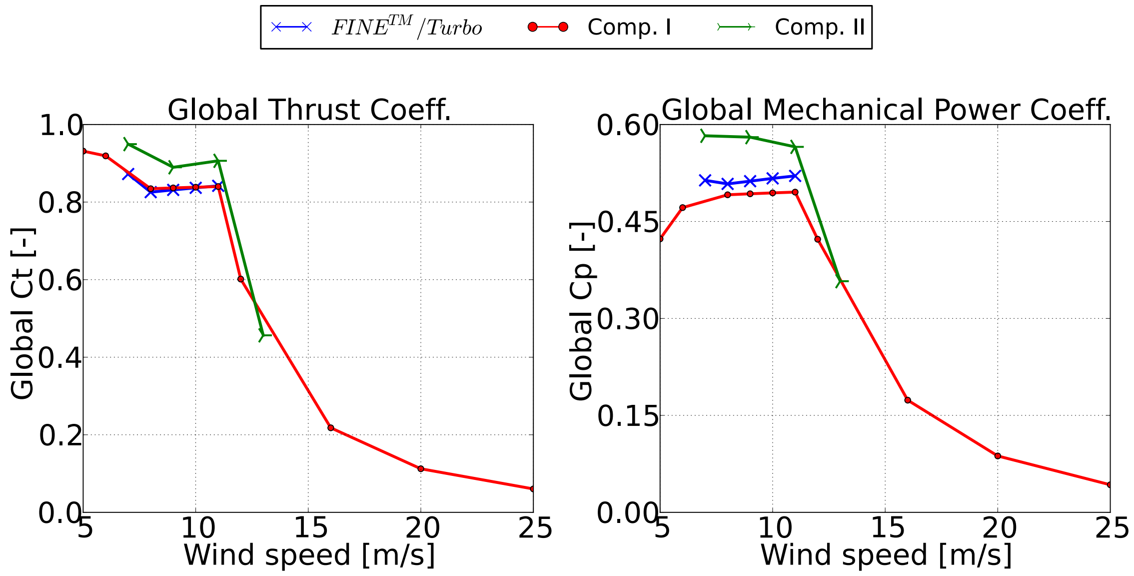

(a) Global thrust coefficient **(b)** Global power coefficient

Figure 5.17: DTU 10MW RWT global coefficients versus wind speed, original *straight* blade with *Gurney flaps*. Comp. I refers to the Ellypsis3D computations included in Bak et al. (2013). Comp. II refers to the HMB2 results included in Leble et al. (2015)

$$C_t|_{local} = \frac{BT_s}{0.5\rho U_\infty^2 2\pi r\Delta r}, C_p|_{local} = \frac{rB\tau_s\Omega}{0.5\rho U_\infty^3 2\pi r\Delta r} \tag{5.2}$$

where T_s and τ_s are the the thrust and mechanical power generated by the segment s.

The *loads production range* of the DTU 10MW RWT was identified to be approximately between 40% and 80% of the span. In this region, the performed computations showed an overestimation with respect to the results of Ellypsis3D. This gap was found to be less pronounced for $C_t|_{local}$. Between r/R=0.3 and r/R=0.4, the three compared CFD simulations showed an overshoot of the thrust, even it was less important for the case of FINE™/Turbo. This is related to the presence of the *Gurney flaps*, as it is discussed later on in this document in Section 5.4. HMB2 and FINE™/Turbo predicted an increase of both local coefficients at span values lower than 30%. This fact could be related to the influence of the hub and nacelle geometries, that were not present in the EllipSys3D rotor geometry.

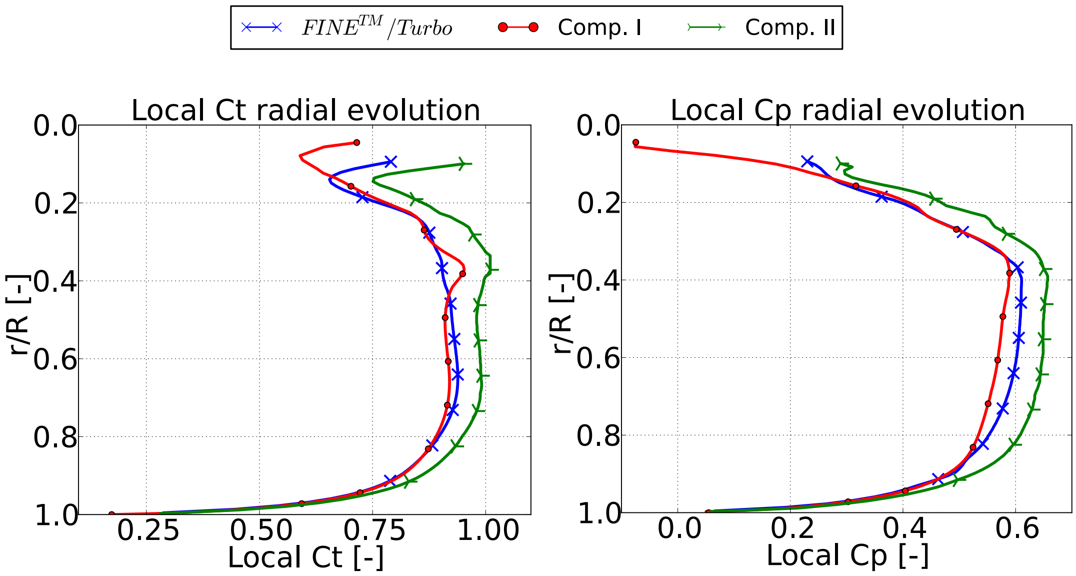

(a) Local thrust coefficient **(b)** Local power coefficient

Figure 5.18: DTU 10MW RWT local load coefficients at 11 ms^{-1}, original *straight* blade with *Gurney flaps*. Comp. I refers to the Ellypsis3D computations included in Bak et al. (2013). Comp. II refers to the HMB2 results included in Leble et al. (2015). Markers do not represent data sampling

5.2.4 Influence of the mesh

In order to verify results mesh independence, presented rotor loads have been compared against the ones computed in a coarser mesh. This new spatial discretization has been created by merging every 8 cell volumes of the base (*fine*) mesh. The total number of the generated *coarse* mesh was 9.5×10^5 nodes (approximately 1/8 th of the base mesh). As shown in Table. 5.4, observed rotor loads difference was below 5% for all the studied operational range, concluding that the *fine* mesh provides accurate enough results for the type of analysis to perform. Higher discrepancies were found for low wind speed range.

Table 5.4: Computed loads for fine and coarse meshes in function of the operating point

Operating point	**Thrust [kN]**			**Power [MW]**		
	Coarse	**Fine**	**Diff [%]**	**Coarse**	**Fine**	**Diff [%]**
FT_WSP07	636.9	651.7	2.3	2.519	2.635	4.6
FT_WSP08	788.7	804.6	2.0	3.742	3.886	3.8
FT_WSP09	1009.5	1022.9	1.3	5.416	5.562	2.7
FT_WSP10	1259.4	1266.4	0.6	7.535	7.660	1.7
FT_WSP11	1543.2	1521.8	-1.4	10.169	10.036	-1.3

5.3 Static aeroelasticity, original geometry

In Section 5.2, *rotor-only* simulations of the *straight* DTU 10MW RWT rotor geometry were presented. The assumption of *rigid blades* was made. Results showed a fair agreement when compared to other CFD computations, both from the global and local loads perspectives. During the operation of the DTU 10MW RWT, important rotor deflections are expected due to the size and the slenderness of the blade. These deformations may have an impact on the rotor performance. This is the reason why another set of simulations of the *straight* variant of the DTU 10MW RWT original blade was performed, also accounting for its *flexibility*. This set-up corresponds to the analysis of the *static aeroelasticity* of the DTU 10MW RWT, since the flow was considered as steady.

5.3.1 Methodology

The same mesh and fluid computational settings described in Section 5.2.1 were kept for the *static aeroelasticity* simulations of the original *straight* blade. The behavior of the structure was linearized by means of its natural frequencies and deformed shapes. To reduce the computational cost attached to FSI simulations, only the first six frequencies of the obtained modal basis were used to model blade flexibility. An iterative procedure *fluid simulation/structure deformation* allowed to find the final static deformed blade and flow behavior after several steps. The details of this 2-way coupling approach were described in Section 4.1.1. The *hybrid mesh deformation* method developed within this PhD thesis was used in order to re-adapt the grid to the deflected blade geometry (see Section 3.6). As for the *rigid* configurations, all the operating points listed in Table 5.2 were studied.

Blade structural model

To obtain a set of modal shapes and natural frequencies of the blade structure, different modal analysis of the FEM model provided by Bak et al. (2013) were performed. The commercial package Abaqus was used for this task [Simulia (2008)]. First computation assumed a clamped root and a non-rotating blade. Obtained natural frequencies are compared in Table 5.5 with the results of HAWC2 [Larsen and Hansen (2007)], a third party software based on *Blade Element Momentum* (BEM) theory. The details of the HAWC2 model of the DTU 10MW RWT together with the predicted structure frequencies are also included in the report of Bak et al. (2013).

Table 5.5: DTU 10MW RWT blade modes, comparison in the absence of rotation

Natural Frequency [Hz]		Isolated blade modes	
Abaqus	HAWC2	Identifier	Description
0.61	0.61	1	1st flap
0.96	0.93	2	1st edge
1.75	1.74	3	2nd flap
2.88	2.76	4	2nd edge
3.58	3.57	5	3rd flap
5.71	5.69	6	1st torsion
5.75	-	7	Mixed flap/torsion
6.16	6.11	8	4th flap
-	6.66	9	3rd edge

A mixed mode was found between 1st torsion and 4th flap. No pure 3rd edge mode was identified within the considered frequency range. These differences could be explained by the complexity of the structural models used for natural frequencies extraction. As it will be shown later on in this document, the high order modes did not have a significant impact on blade deformation for the considered operating points.

Additional simulations were performed by considering the blade rotation of each operating point in the modal analysis. This allowed to include the *centrifugal effects* in the computed modal basis, in order to take them into account in the FSI simulations. A slight structural frequencies shift was observed due to the consideration of the centrifugal stiffening. This effect is illustrated in Figure 5.19, where the variations of blade frequencies against non-rotating frequency are plotted at every RPM. Even if this frequency shifting is not as important as in other rotatory applications including large blade deformations (such as helicopters), a non-negligible value is observed for the first modes. As an example a difference up to 6.12% was found for the first mode at 9.6 RPM.

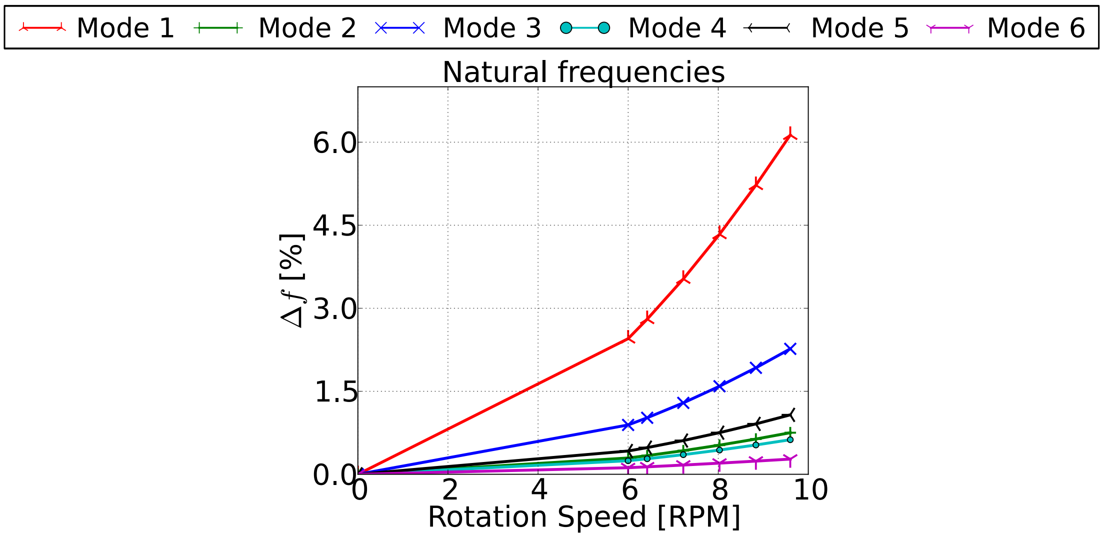

Figure 5.19: Evolution of DTU 10MW RWT blade frequencies in function of rotational speed (first six modes plotted)

5.3.2 Blade deformation at 11 ms^{-1}

Figure 5.20 shows the computed blade deflection at 11 ms^{-1}, superposed to the original (i.e. undeformed) geometry. The resulting blade deformation was mainly dominated by first flapping mode. The measured blade tip deflection normal to the rotor axis d_n was 0.9%R, while the deformation parallel to the rotor axis d_p was found to be 8.73%R (7.78 m). The latter value is considerably high due to the dimensions of the DTU 10MW RWT. For example, the equivalent deformation computed by Carrión (2014) for the NREL Phase VI was 0.59%R (29.7 mm). For the particular case of 11 ms^{-1}, both RBF+TFI and RBF+TFI+ELA *hybrid mesh deformation* methods were evaluated (see Section 3.6). Table 5.6 illustrates the performance of both approaches. An estimation of the computational cost of a classical *Radial Basis Function* (RBF) based deformation is included for comparison purposes. As already pointed out in in Chapter 3, the CPU cost attached to the RBF when dealing with multi-million meshes was found to be prohibitive.

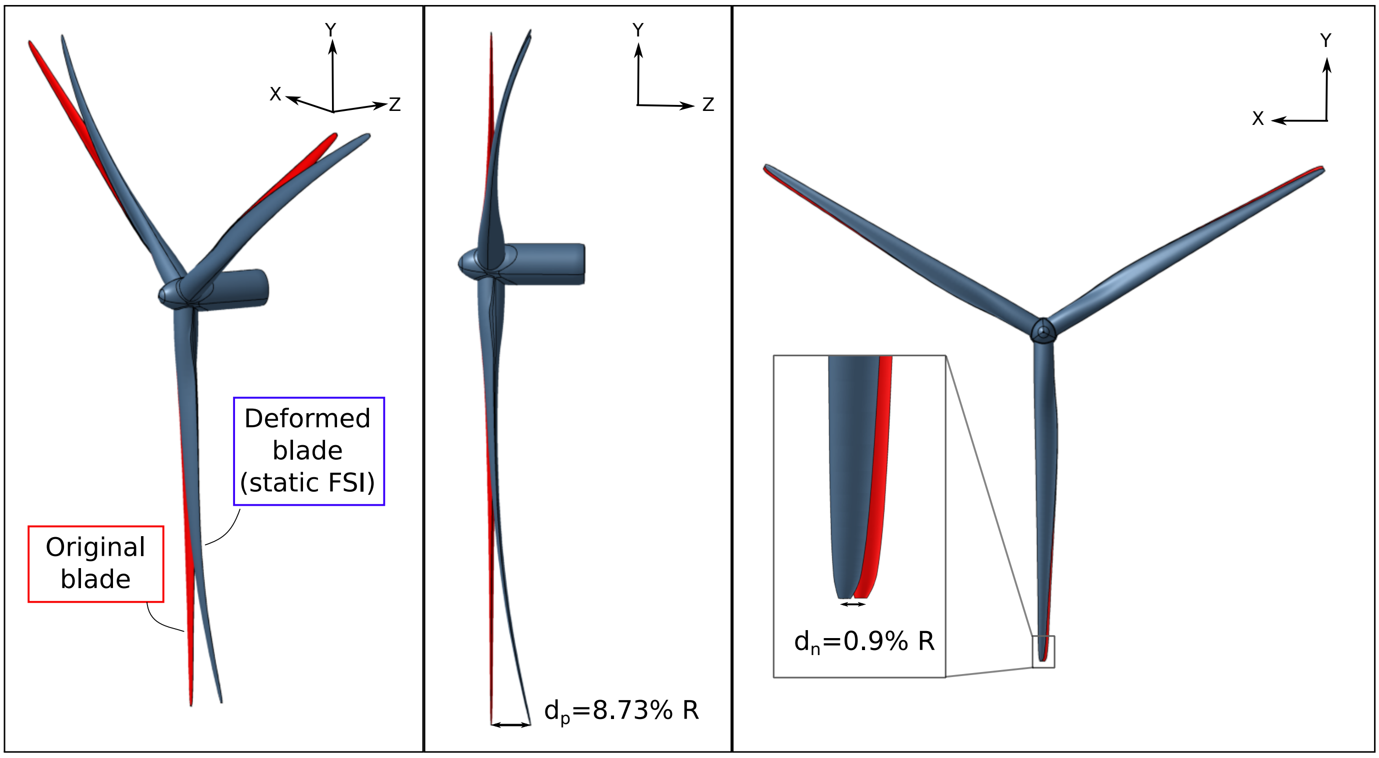

(a) 3D view **(b)** Side view **(c)** Front view

Figure 5.20: Static blade deflection of the DTU 10MW RWT at 11 ms^{-1}

Table 5.6: Mesh quality of original and deformed DTU 10MW blade mesh

Def. method	OR	AR	ER	Computational Data		
	Min.	Max.	Max.	#Proc	t_{def}/t_{sim}	Mem.
Original	15.2	41700	1.66	-	-	-
RBF	-	-	-	-	∼400.0	∼15630
RBF+TFI	15.2	47200	1.66	9	0.003	1385
RBF+TFI+ELA	15.2	47200	1.66	9	0.39	3706

OR: Orthogonality [deg], *AR*: Aspect Ratio, *ER*: Expansion Ratio

t_{def}/t_{sim}: Ratio between total mesh deformation and fluid simulation times

Mem.: Max. memory allocated [MB], divided by number of processors *#Proc*

The grid computed by the RBF+TFI method already kept the original overall mesh quality parameters. Regarding the the blade sections mesh, both RBF+TFI and RBF+TFI+ELA approaches computed very similar deformed grids (Figure 5.21, 5.22). This fact is related to the absence of a significant twist deflection. The additional computational effort of the *Elastic Analogy* (ELA) step could be justified by looking at the local mesh quality around the blade. Near-wall orthogonality was improved by the introduction of the *Elastic Analogy* in spanwise direction (Figure 5.23). Even if this slight improvement did not change the results of the aeroelastic computations for the studied operating points, its was decided to use the RBF+TFI+ELA mesh deformation method as a standard for all the FSI analysis presented in this chapter

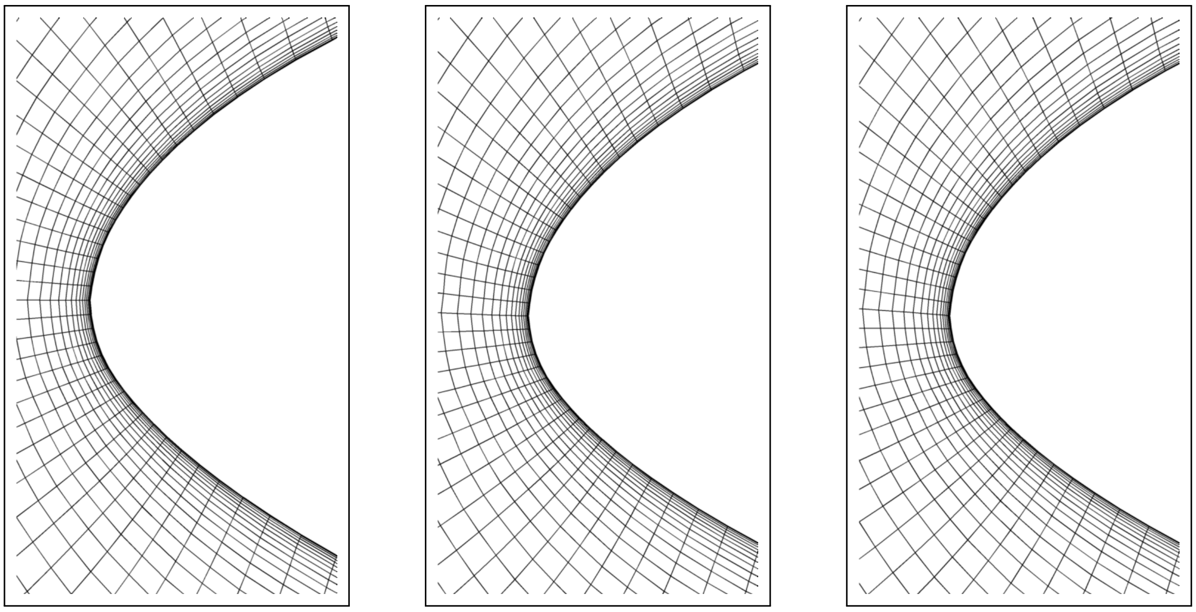

(a) Original mesh **(b)** Def. RBF+TFI **(c)** Def. RBF+TFI+ELA

Figure 5.21: DTU 10MW RWT leading edge at 90% span, original and deformed meshes

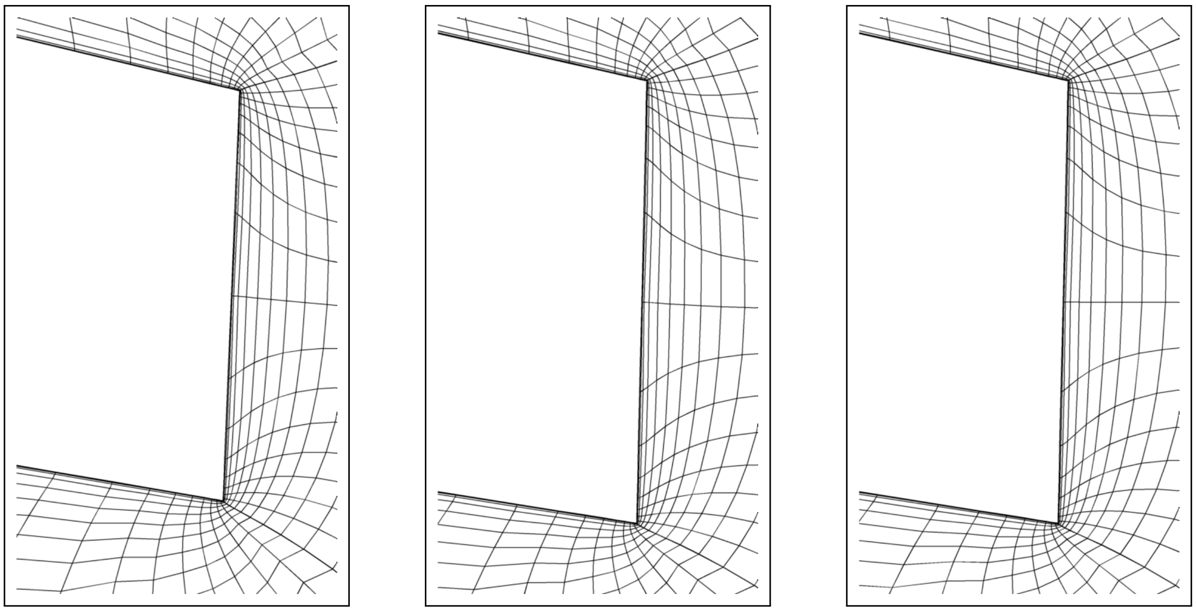

(a) Original mesh **(b)** Def. RBF+TFI **(c)** Def. RBF+TFI+ELA

Figure 5.22: DTU 10MW RWT trailing edge at 90% span, original and deformed meshes

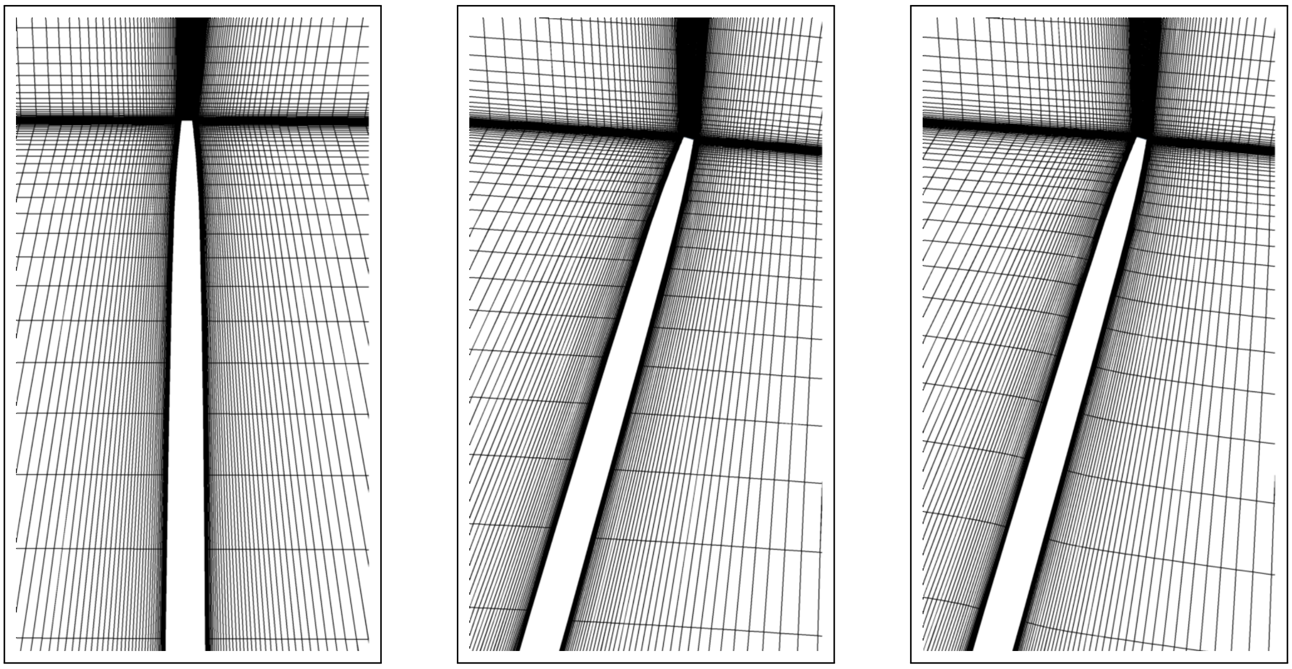

(**a**) Original mesh (**b**) Def. RBF+TFI (**c**) Def. RBF+TFI+ELA

Figure 5.23: DTU 10MW RWT spanwise cut near tip region, original and deformed meshes

5.3.3 Rotor performance

Figure 5.24 shows the evolution of the computed total rotor loads by means of the presented 2-way coupling FSI approach, referred to as *flexible*. The results of the steady computations presented in Section 5.2.3 are reproduced and labeled as *rigid*. The computed loads by HMB2 are also included for both *rigid* and *flexible* blade configurations. For both HMB2 and FINE™/Turbo solvers, the consideration of the blade flexibility lead to a decrease of the computed rotor load coefficients. For the latter solver, the difference seemed to increase with regards to the wind speed. For the particular case of 11 ms^{-1}, FINE™/Turbo predicted a reduction of 1.34% of $C_p|_{global}$ and 2.25% of $C_t|_{global}$. This difference was magnified for the HMB2 solver, probably due to the fact that the *elastic* configuration did not account for the first 35% of the blade span.

The local evolution of thrust and power coefficients at 11 ms^{-1} is depicted in Figure 5.25. Both HMB2 and FINE™/Turbo predicted a slight increase of the loads at the vicinity of r/R=0.5. However, this gain of $C_p|_{global}$ and $C_t|_{global}$ was not able to counteract the decrease observed for high span ranges (r/R>0.6).

The drop of the loads at the high span was related to the important deformation experienced by the blades at this region (see Figure 5.26). The proportionality of the blade deflection with the considered wind speed also explained the higher difference in the computed loads for the *rigid* and *flexible* configurations. At 11 ms^{-1}, both FINE™/Turbo and HMB2 predicted a similar radial evolution of the blade deflection. The increase of the deformation magnitude predicted by HMB2 was certainly related to the systematic overprediction of the rotor thrust, even when considering the blades as *rigid*.

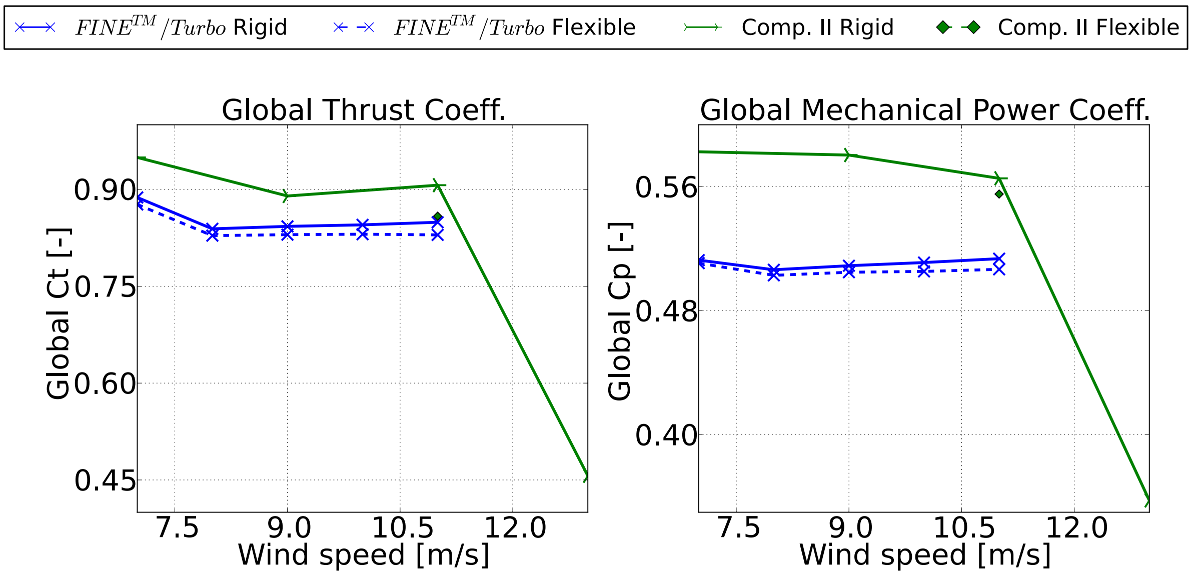

(a) Global Thrust coefficient **(b)** Global Mechanical Power coefficient

Figure 5.24: DTU 10MW RWT global coefficients versus wind speed, *rigid* and *flexible* configurations of the original blade. Comp. II refers to the HMB2 results included in Leble et al. (2015)

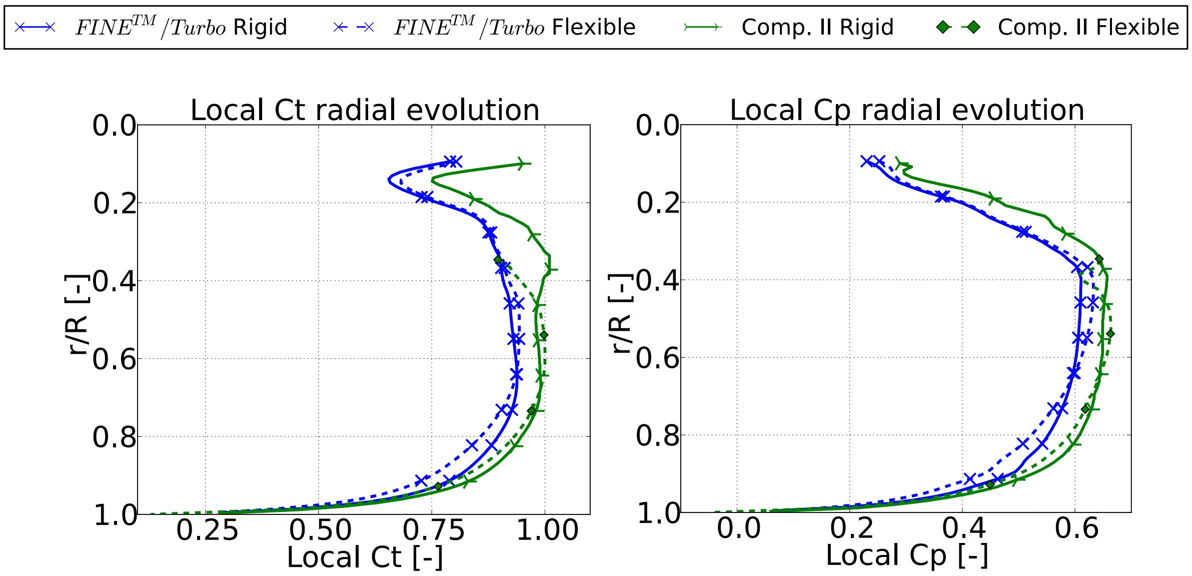

(a) Local thrust coefficient **(b)** Local power coefficient

Figure 5.25: DTU 10MW RWT local loads coefficients at 11 ms^{-1} for *flexible* and *rigid* configurations. Comp. II refers to the HMB2 results included in Leble et al. (2015). Markers do not represent data sampling

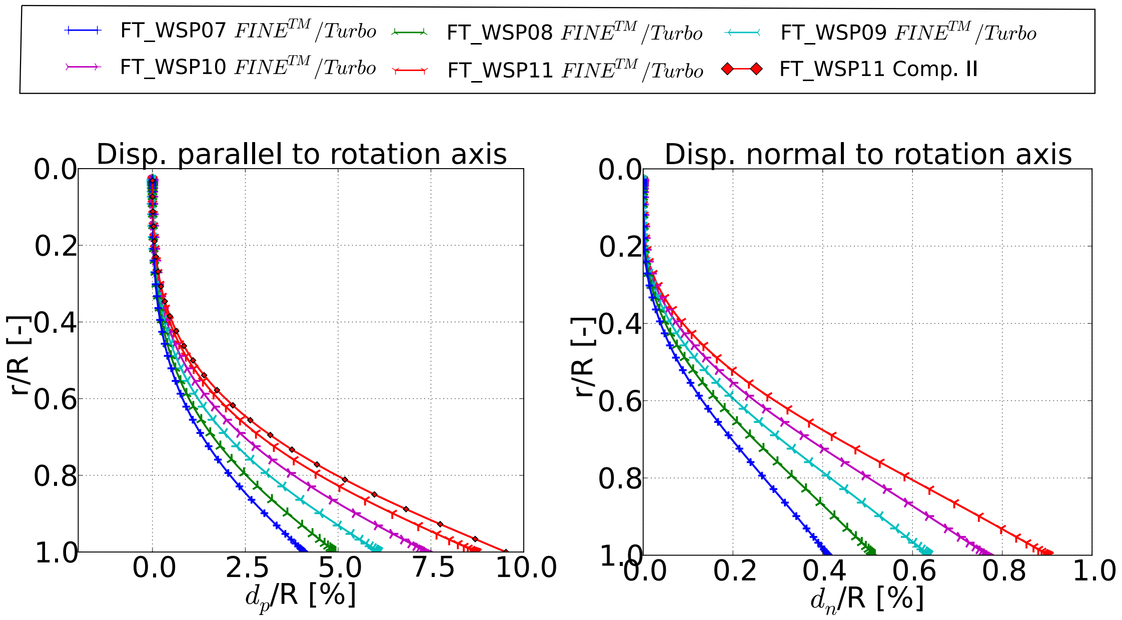

(a) Blade axis displacement parallel to rotor axis

(b) Blade axis displacement normal to rotor axis

Figure 5.26: DTU 10MW RWT blade axis deformation in function of normalized radius for the original *straight* blade. Comp. II refers to the HMB2 results included in Leble et al. (2015)

5.4 Impact of Gurney flaps

Original DTU 10MW RWT blade geometry is equipped with the so-called *Gurney flaps*. This device, originally developed for race car applications, consists on a small plate located at the trailing edge. It is used to increase the lift produced by the airfoil when operating in separated flow conditions. A low drag penalty is also expected. First studies characterizing the performance of this passive device were performed by Liebeck (1978). Figure 5.27 reproduces the conclusions of this work. The beneficial effects of the *Gurney flaps* installation were explained by the re-attachment of the suction side flow close to the trailing edge. The performance improvement related to the presence of the *Gurney flap* was verified by several subsequent experimental studies based on relatively thin airfoils and accounting for sharp trailing edges. To this group belong the work of Jeffrey et al. (2000) [relative thickness of 12.5%], the study of Troolin et al. (2006) [15%] and the research performed by Storms and Jang (1994) [12%]. Cole et al. (2011) performed an exhaustive experimental comparison of different *Gurney flap* geometries installed for several airfoils, which maximum relative thickness ranged from 8% to 10.9%. It was concluded that under the existence of massive upstream separation (covering between 20% to 30% of the airfoil surface), the effectiveness of the *Gurney flaps* was reduced. This led, in some cases, to the reduction of the maximum lift coefficient when compared to the corresponding *clean* geometries. In Prospathopoulos et al. (2014), a numerical investigation was conducted in order to study the performance of large HAWT blades at low span, where thick airfoils are equipped. Unsteady 2D CFD URANS simulations based on the k-ω SST turbulence model were carried out, assuming fully turbulent conditions. The increase of the thickness was found to reduce the generated lift and drag in the post-stall region. Additionally, thick airfoils separation happened at lower angles of attack. For the FFA-w3-360 airfoil, that accounts for a maximum relative thickness of 36%, the effect of the *Gurney flap* was also studied. An increase in the slope of the lift coefficient over the linear range was predicted when compared to the original airfoil geometry, together with a higher maximum lift.

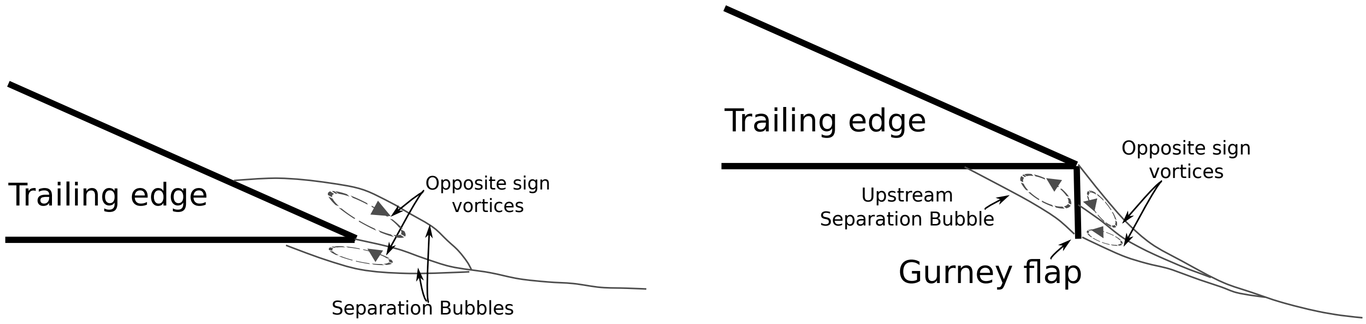

(a) Clean trailing edge **(b)** Trailing edge accounting for a *Gurney flap*

Figure 5.27: Expected effects on trailing edge flow due to *Gurney flaps* installation

In the original DTU 10MW RWT blade geometry, *Gurney flaps* are equipped at low blade span [5%,40%] in order to improve the performance of this region. Due to the thickness of blade profiles and incoming flow properties, important separation effects are expected at the power production operating range. The wedge shaped variant used for the DTU 10MW RWT *Gurney flap* is also known in the literature as *trailing edge wedge* or *divergent trailing edge*. The behavior of this type of flow control device was previously analyzed by several authors by studying non-rotating airfoils. In Timmer and van Rooij (2003), several wind tunnel experiments were performed aiming to understand the effect of different *Gurney flap* shapes on the generated lift and drag loads. The DU 93-W-210 airfoil was used, which maximum relative thickness is 21% (see Figure 5.28a). The tests showed an increase of the maximum generated lift with an attached reduction of the maximum lift-to-drag ratio, regardless the considered *Gurney flap* shape. The experiments also revealed that there was no difference between the performance of the airfoil equipped with a traditional *Gurney flap* and the wedge shape variant based on an isosceles triangle. This was explained by the fact that the wedge was filling the place otherwise taken by the upstream separation bubble. The study of the rest of wedge shapes of Figure 5.28a showed that increasing the upstream wedge length tended to attenuate the benefits of the *Gurney flap*, by decreasing the maximum lift and increasing the maximum lift-to-drag ratio with respect to the traditional geometry. Analogous observations regarding the almost equivalent behavior between wedge shaped and traditional *Gurney flap* geometries were stated in Salcedo et al. (2006) (see Figure 5.28b). In this work 2D CFD

RANS computations using k-ω SST model and accounting for transition were performed, in order to study several airfoils with maximum relative thickness ranging from 8% to 24%. Similar CFD simulations were performed by Mohammadi and Doosttalab (2012) for the 25% thick DU 91-W2-250 airfoil equipped with the wedge shaped *Gurney flap* depicted in Figure 5.28c. These computational results also verified the expected *Gurney flaps* behavior, with an increase of the lift coefficients for all the studied angles of attack and a reduction of the maximum lift-to-drag ratio.

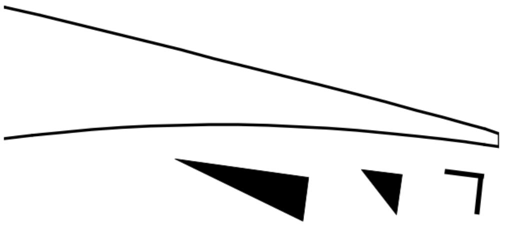

(a) Experiments of Timmer and van Rooij (2003)

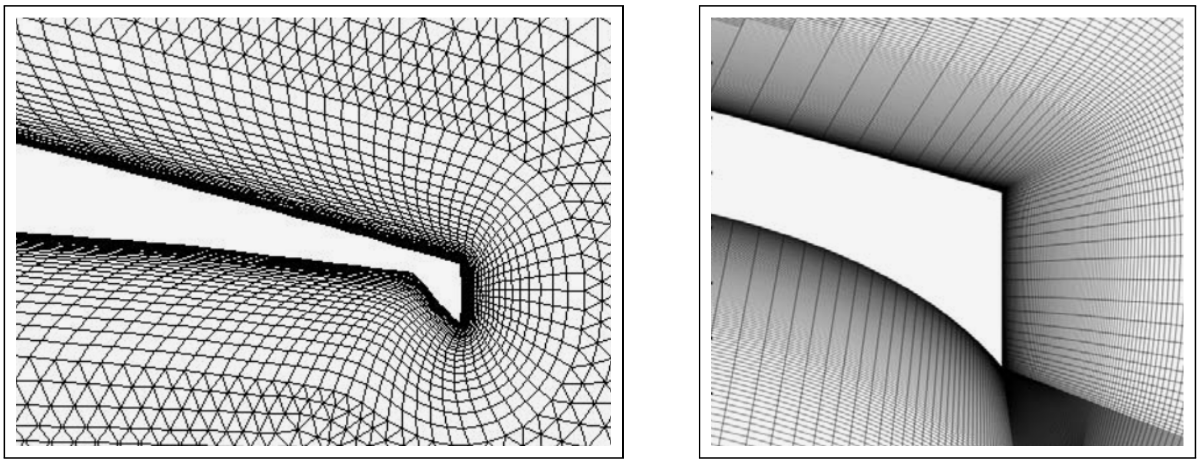

(b) CFD computations of Salcedo et al. (2006)

(c) CFD computations of Mohammadi and Doosttalab (2012)

Figure 5.28: Examples of wedge shaped *Gurney flaps* studied by other authors

The global impact of the installation of the wedge shaped *Gurney flaps* for the DTU 10MW RWT is claimed to be an increase of 1.2% of the total mechanical power at the design operating point [Zahle et al. (2013)]. This section aims to evaluate this result by a 3D computational study, since no prior experiences were found in the literature supporting this statement.

5.4.1 Methodology

In order to evaluate the impact of the *Gurney flaps* installation, the load cases of Table 5.2 were studied again in a geometry with *clean trailing edges*. Both *rigid* and *flexible* blades were considered in the new computations. For the latter configuration, the first 6 modes of the ROM described in Section 5.3.1 were used in order to account for blade flexibility. A new mesh was generated with the same characteristics as the one described in Section 5.2.1, but based on a variant geometry of the DTU 10MW RWT, where the *Gurney flaps* were replaced by the unmodified blade profiles definition. This new mesh will be referred in this document as as *no-Gurney* or as *NG*. For clarity purposes, the one initially created in Section 5.2.1 based on the original geometry of the DTU 10MW RWT is referred to as *Gurney* or *G*. In order to illustrate the differences between *G* and *NG* configurations, Figure 5.29 displays a cross section of the mesh corresponding to a 25% of blade span.

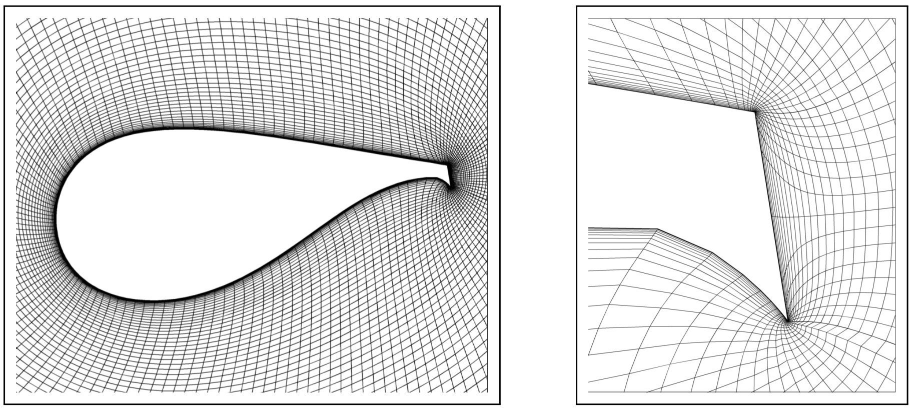

(a) *G* cross section mesh **(b)** *G* trailing edge

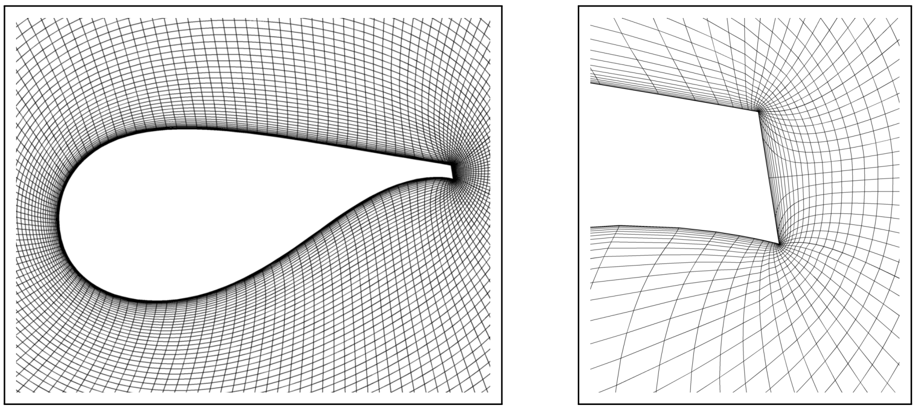

(c) *NG* cross section mesh **(d)** *NG* trailing edge

Figure 5.29: Cross-section meshes at 25% span for *G* (*Gurney*) and *NG* (*no-Gurney*) configurations

5.4.2 Flow visualization at 11 ms^{-1}

In order to check if the *Gurney flaps* flow control mechanism illustrated in Figure 5.27 was reproduced in the DTU 10MW RWT geometry, a detailed analysis of the *rigid* configuration at 11 ms^{-1} was performed. Figure 5.30 shows a comparison of the cross-section streamlines at a radius of 22.3 m (r/R=0.25). The generation of the pressure surface separation bubble was visible for the *G* configuration. A detailed view of this phenomenon is included in Figure 5.30b. The suppression of the suction surface recirculation, expected after the installation of the *Gurney flaps*, was not observed. This behavior was found for the whole low span range, as it can be deduced from the comparison of blade surface streamlines of Figure 5.31a. and Figure 5.31b. Indeed, the removal of the *Gurney flaps* led to a slight decrease of the maximum radius of the suction surface separation (passing from 39.7 m for *G* to 38.1 m for *NG*). In addition, the flow around the pressure surface of *NG* remained attached for the whole blade span, except for a small recirculation bubble located at r=[14.9,20.3] m (see Figure 5.31d). A similar flow pattern was observed for all the operating points of Table 5.2.

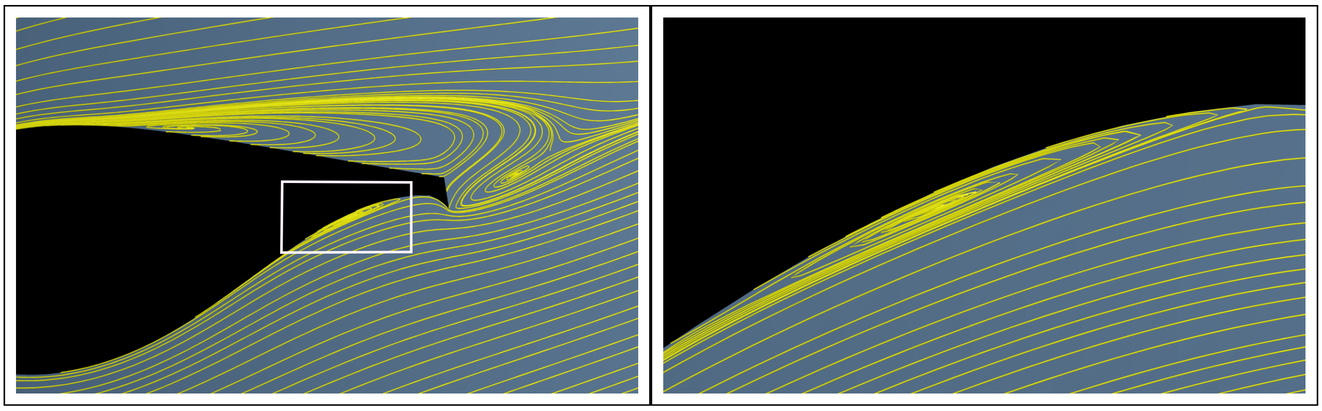

(a) *G* (*Gurney*), global view

(b) *G* (*Gurney*), pressure side zoom

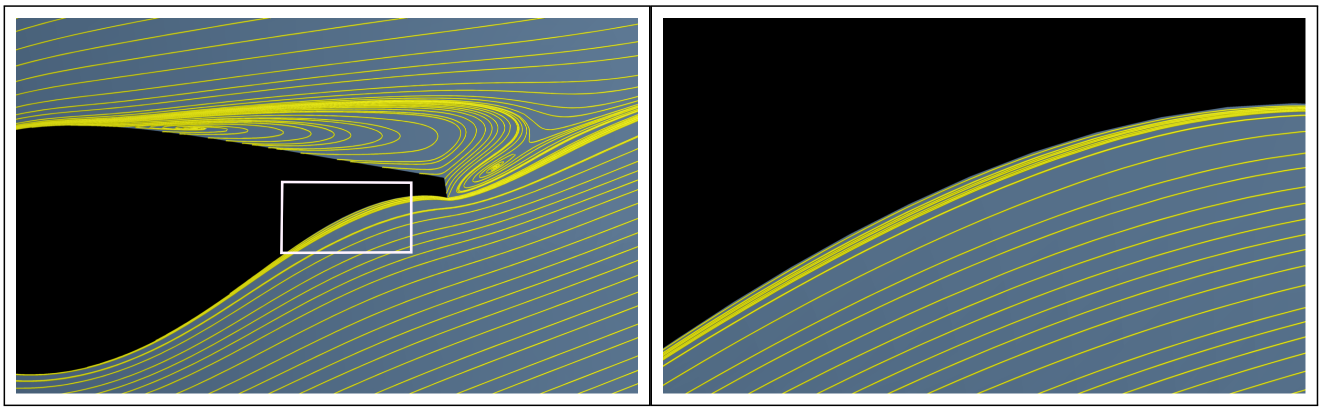

(c) *NG* (*no-Gurney*), global view

(d) *NG* (*no-Gurney*), pressure side zoom

Figure 5.30: Cross-section streamlines at 11 ms^{-1} for r=22.3 m (r/R=0.25). *Rigid* simulations of *G* (*Gurney*) and *NG* (*no-Gurney*) configurations

5.4.3 Rotor performance

The benefits of the *no-Gurney NG* configuration on flow behavior had a direct impact on global rotor performance. Figure 5.32 shows the global thrust and mechanical power coefficients computed for both *G* and *NG* configurations. The results for *rigid* and *flexible* blade models are included. The installation of the *Gurney flaps* resulted in a decrease of the mechanical power and an increase of the thrust for both *rigid* and *flexible* configurations. At

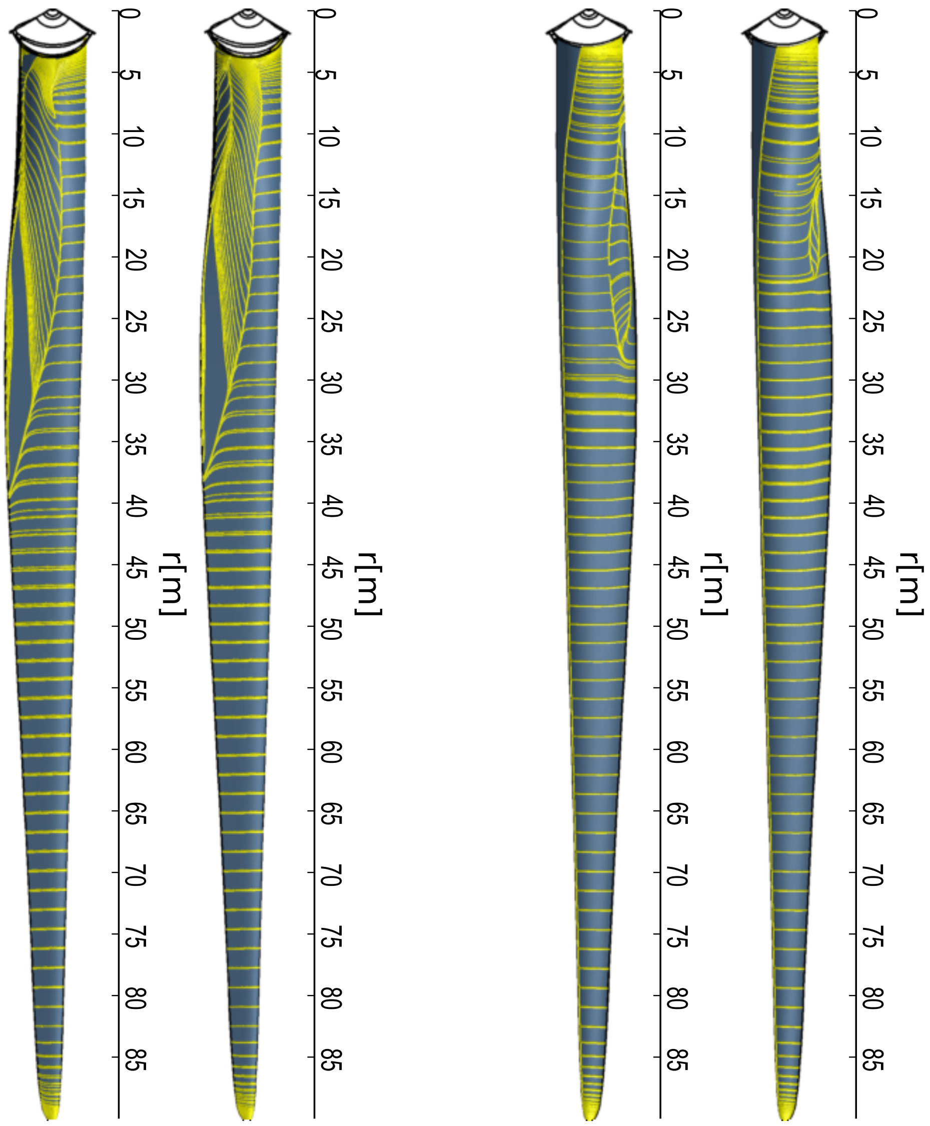

(a) *SS-G* **(b)** *SS-NG* **(c)** *PS-G* **(d)** *PS-NG*

Figure 5.31: Friction streamlines at 11 ms^{-1} for suction and pressure surfaces (referred as *SS* and *PS* respectively). *Rigid* simulations of *G* (*Gurney*) and *NG* (*no-Gurney*) configurations. Flow separation regions can be observed on both the pressure side and the suction side for both configurations

11 ms^{-1} and for the *rigid* blade model, $C_p|_{global}$ was reduced in 1.4% while an increase of 0.8% was observed for $C_t|_{global}$. As for the original blade geometry, the consideration of the blade flexibility lead to a decrease of the rotor loads computed for the *NG* variant. In percentage terms, these reductions were found to be very similar. This fact could be explained by analyzing the computed blade deflections, since no significant differences between both configurations were found (see Figure 5.33).

Based on the presented results, a decrease of the performance of the DTU 10MW RWT rotor is expected after the integration of the *Gurney flaps*. This issue can be explained by the massive separation observed at the suction side of the airfoil (even for the *clean* airfoil geometry), as pointed out by Cole et al. (2011). The important region covered by the suction side bubble is at the same time related to the significant thickness of the DTU 10MW RWT blade,

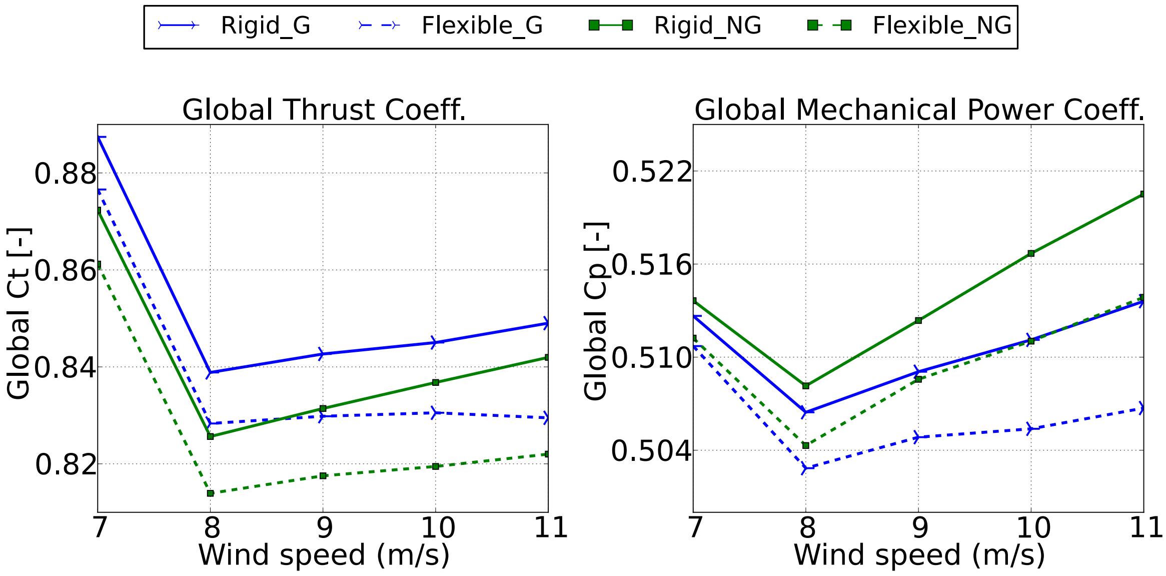

(a) Global Thrust coefficient **(b)** Global Mechanical Power coefficient

Figure 5.32: Global load coefficients in function of wind speed for *G* (*Gurney*) and *NG* (*no-Gurney*) configurations

as suggested by Prospathopoulos et al. (2014). Indeed the airfoils located in the recirculation areas are related to a relative thickness ranging from 30% to 99% (see Figure 5.2d), and they also account for considerably wide blunt trailing edges. To the best of author's knowledge, no previous experiments or simulations supporting the use of *Gurney flap* for this type of geometries were carried out. Another plausible cause for the inefficiency of the *Gurney flaps* could be the role played by the axial flow, that was neglected in all the experiments described in Section 5.4 (since they assumed a non-rotating framework). Other alternatives in order to avoid the observed flow separation can be found in the literature. In Gaunaa et al. (2013), the use of leading edge slats at low span regions $r/R = [0.8, 0.32]$ was studied. Troldborg et al. (2015) considered the installation of *vortex generators* in order to control flow separation.

5.5 Impact of prebending and precone

The distance between the blade tip and the tower is often referred in the wind energy context as the *tower clearance*. In order to increase this gap (especially when dealing with big rotors), wind turbine designers use to introduce three geometrical considerations on the assembly:

- **Tilt angle**: Angle between rotor axis and tower
- **Precone angle**: Angle between blade axis and rotor axis
- **Prebending**: Blade deflection towards the incoming wind direction imposed during the blade design stage

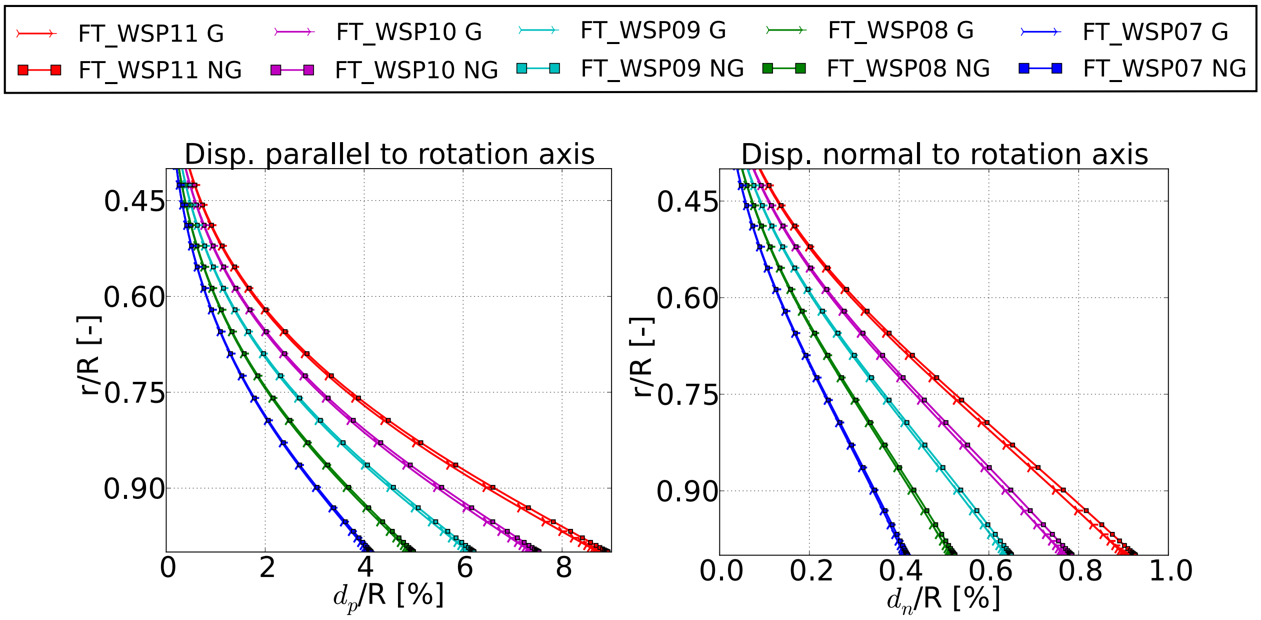

(a) Blade axis displacement parallel to rotor axis

(b) Blade axis displacement normal to rotor axis

Figure 5.33: DTU 10MW RWT blade deformation in function of normalized radius. *G* (*Gurney*) and *NG* (*no-Gurney*) configurations. For clarity purposes, only the second half of the blade is shown

The DTU 10MW RWT accounts for all of them, as shown in Figure 5.34a, where a sketch from the definition document of Bak et al. (2013) is reproduced. The geometrical effects of *prebending*, *tilt* and *preconing* are highlighted. In an operating wind turbine, the combination of all these modifications will try to align the deformed blade with the tower, as shown in Figure 5.34b. The aim of this section is to analyze how these geometrical considerations will impact rotor performance. The results of the already studied *straight* configuration were compared against a new and more *realistic* variant, accounting for *tower clearance* increase devices.

5.5.1 Methodology

Based on the conclusions of Section 5.4, new simulations were based on a blade geometry without *Gurney flaps*. The study was carried out in a *rotor-only* context, as a starting point for full machine computations. In order to explore the whole 0 deg operating range of the machine, the load cases from Table 5.2 were analyzed again and compared with the *straight-NG* configuration results. Both *rigid* and *flexible* blades were analyzed. For the latter configuration, mesh deformation relied in the *hybrid method* summarized in Section 3.6

A new mesh was generated with the same characteristics as the one described in Section 5.2.1. Since the introduction of the tilt angle was not compatible with the angular periodicity hypothesis for steady state flow simulations, only the *prebending* and the *preconing* were considered. Based on the design specifications from Bak et al. (2013), the new consid-

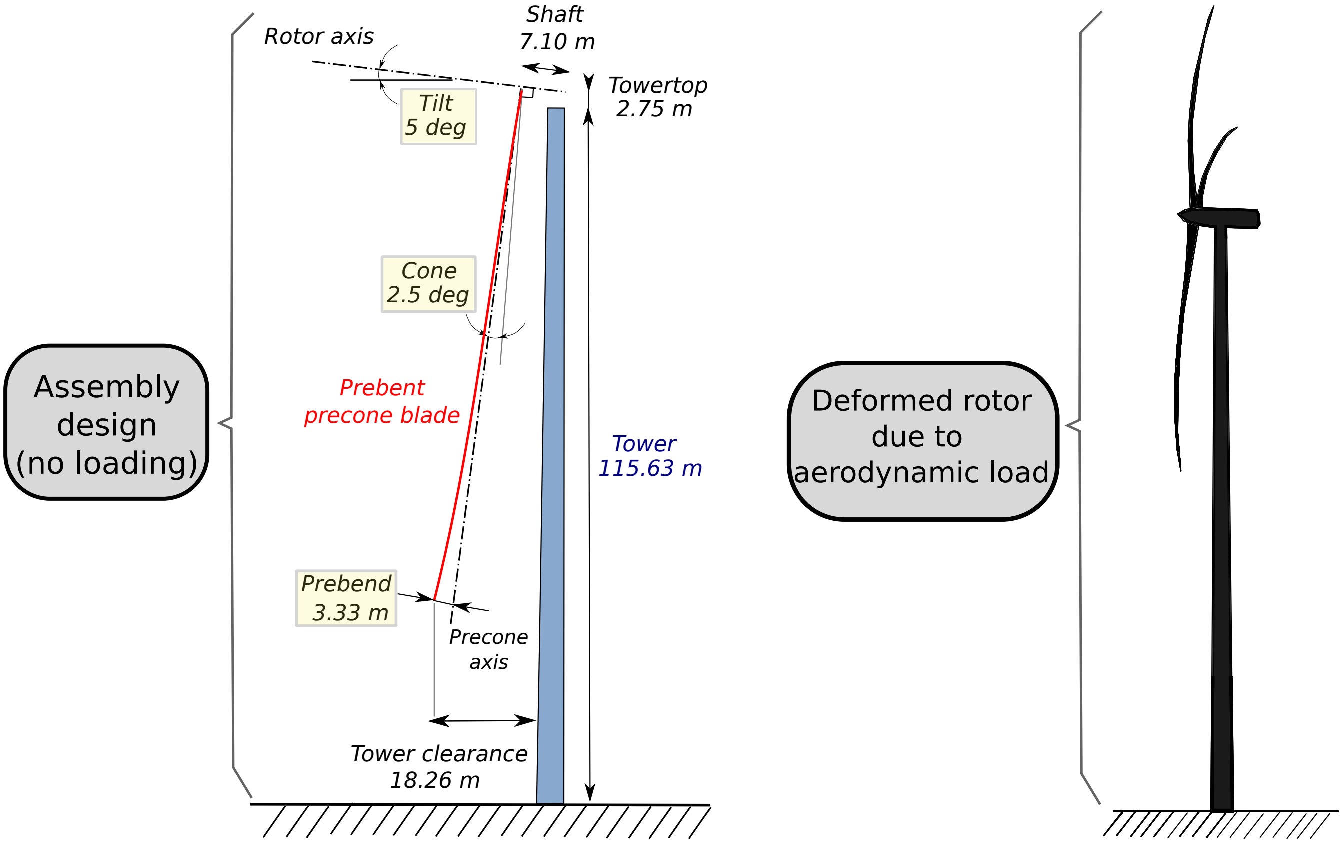

(a) Design assembly **(b)** Expected deformation during operation

Figure 5.34: Sketch of the DTU 10MW RWT whole assembly

ered geometry was generated by the application of the following geometrical operators on the standard DTU 10MW RWT configuration:

1. Application of the prebending law definition on the straight blade (see Figure 5.5)
2. Application of the 2.5 deg precone angle to the already prebent blade

Figure 5.35 illustrates both *straight* and *prebent-precone* variants of the DTU 10MW RWT rotor, as considered in FINE™/Turbo.

Blade structural model

Due to the significant geometrical modifications performed on the new *prebent-precone* blade, a new set of natural structural frequencies and mode shapes was required. The methodology described in Section 5.4 was used in order to perform modal analysis for each one of the considered RPM. The same blade modes identified for the *straight* blade were observed for the new geometry. As previously shown in Figure 5.19 for the *straight* configuration, a small RPM dependency was observed. In Figure 5.36, the relative variations of natural frequencies corresponding to both configurations are compared. They are normalized by the frequency of the non-rotating *straight* blade. The evolutions of the frequencies with the rotation speed

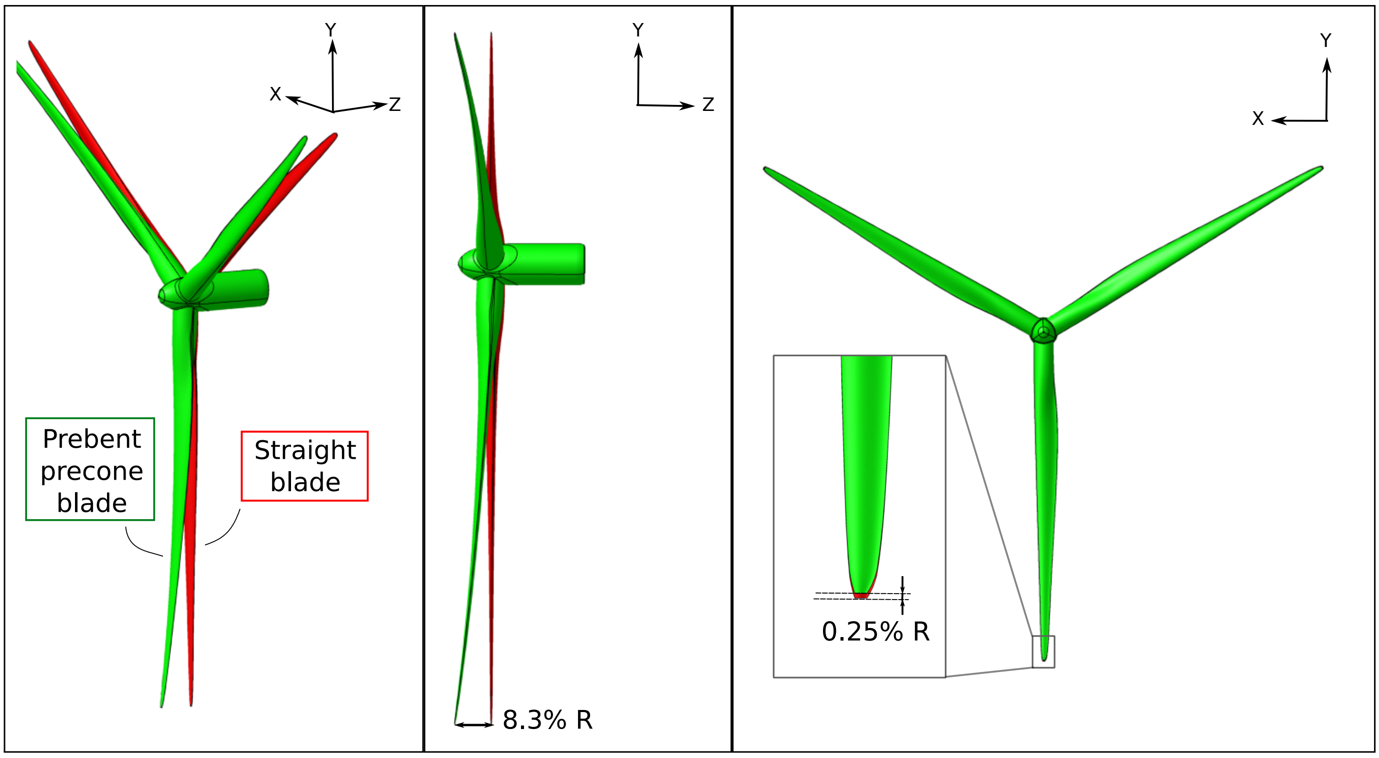

(a) 3D view **(b)** Side view **(c)** Front view

Figure 5.35: Comparison of *straight* and *prebent-precone* configurations, DTU 10MW RWT rotor

were very similar. Only a constant shift between *straight* and *prebent-precone* configuration was observed. This shift tended to increase with the mode number. As for the computations of the *straight blade*, only the first 6 frequencies of the computed modal basis were used to model the rotor flexibility in the FSI simulations.

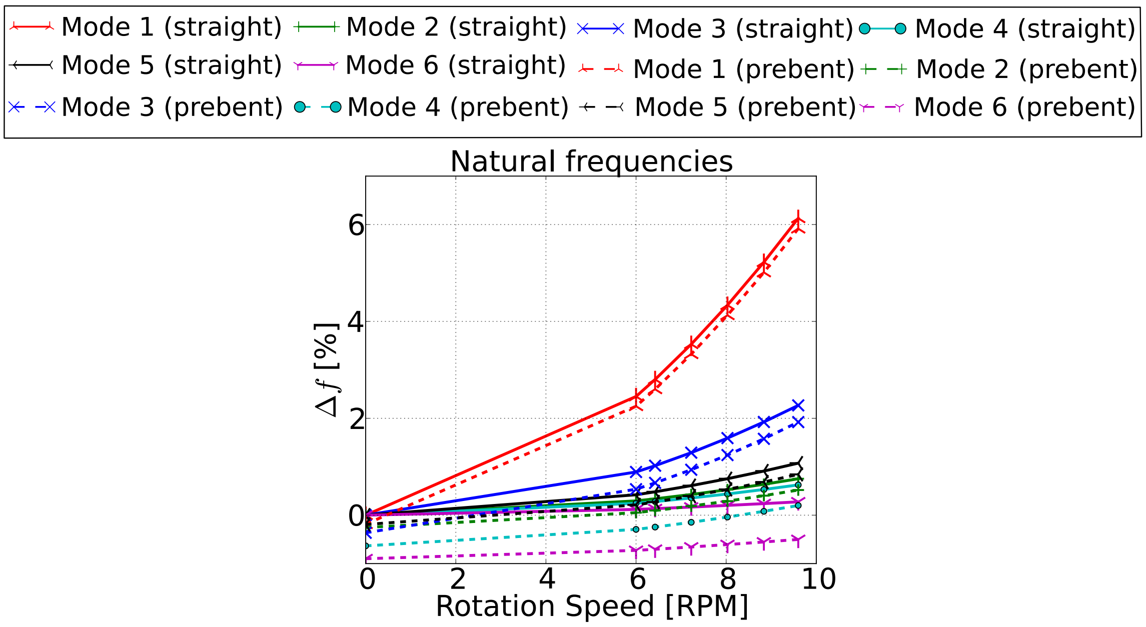

Figure 5.36: Evolution of DTU 10MW RWT blade frequencies in function of rotational speed, *straight* and *prebent-precone* blades (first six modes plotted)

5.5.2 Rotor performance

Figure 5.37 shows the blade deformations for the *flexible* simulations of the *prebent-precone* rotor. Computed deformations were slightly higher than the ones corresponding to the *straight* rotor and previously displayed in Figure 5.33. However, higher deformed blade tip/tower distances were observed for the *prebent-precone* configuration, due to its more conservative initial *tower clearance*. In order to illustrate this fact, Figure 5.38 shows the reference (i.e. undeformed) and deformed blade axis coordinates for each of the presented aeroelastic computations. A global view is provided as well as a close zoom in order to properly contextualize the magnitude of the deformations. For the *prebent-precone* configuration, a blade tip/blade root alignment was observed for for the 10 m.s^{-1} simulation. This operating point is indeed very close to the *rated speed* of the machine (11.4 ms^{-1}), verifying the prebending law defined at the design stage. Computed global mechanical power coefficients of *straight* and *prebent-precone* configurations are shown in Figure 5.39, together with a diagram superposing reference and deformed rotor geometries at 11 ms^{-1}. When considering the blades as *rigid*, a decrease in power was observed when introducing blade *prebending* and *preconing*. At 11 ms^{-1}, this reduction corresponded to 1.24%. As previously discussed in Section 5.4.3, the consideration of the blade *flexibility* led to a decrease of the computed *straight* blade power. This trend was reversed for the *prebent-precone* configuration, since the effect of flexibility tended to deform the blade towards a more orthogonal geometry with respect to the incoming flow (Figure 5.39b). The power produced by the *rigid straight* blade showed an overprediction with respect to the *flexible prebent-precone* configuration for the whole studied operating

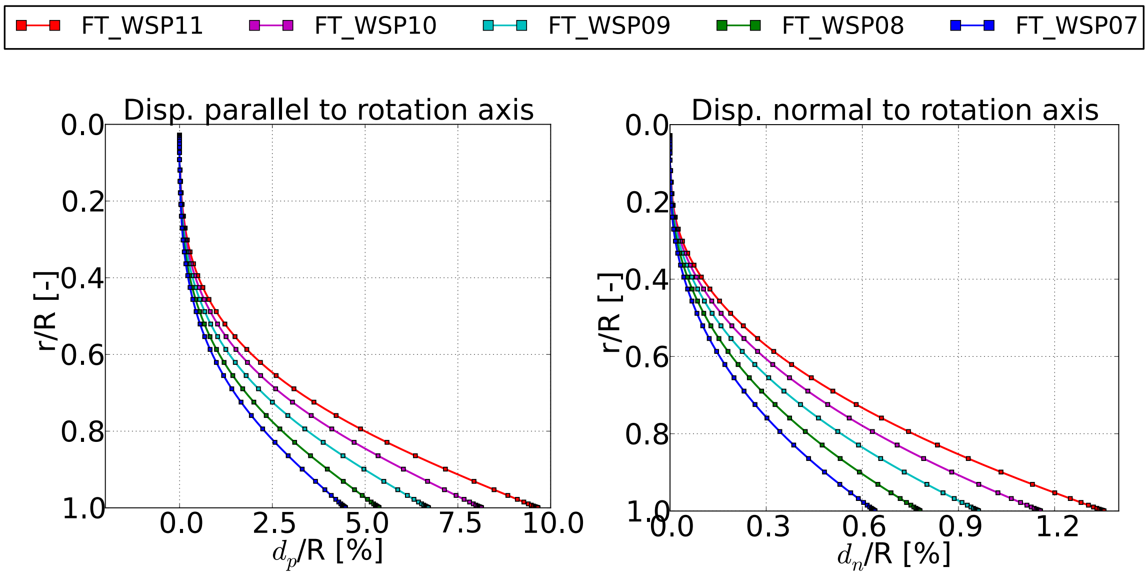

(a) Blade axis displacement parallel to rotor axis **(b)** Blade axis displacement normal to rotor axis

Figure 5.37: DTU 10MW RWT blade deformation in function of normalized radius for the *prebent-precone* configuration

range. A maximum relative difference of 0.7 % was observed for 8 ms^{-1}. An analogous plot regarding rotor global thrust coefficient is included in Figure 5.40. Lower thrust values were computed for the *prebent-precone* configuration with respect to the *straight* rotor. At 11 ms^{-1}, a relative reduction of 2.1% was observed. No significant differences between *flexible* and *rigid* simulations were observed for the *prebent-precone* configuration.

As a global conclusion, presented results show that aeroelastic analysis of DTU 10MW RWT cannot be performed without considering the *prebending* and the *preconing* of the blades. Indeed, even if it does not largely affect the natural frequencies of the blade, its shape modification significantly influences the performance of the wind turbine. In addition the *straight rigid* blade (that use to be taken as a basis for the design stage), lead to a systematic overprediction of the power with respect to the more realistic *prebent-precone flexible* configuration.

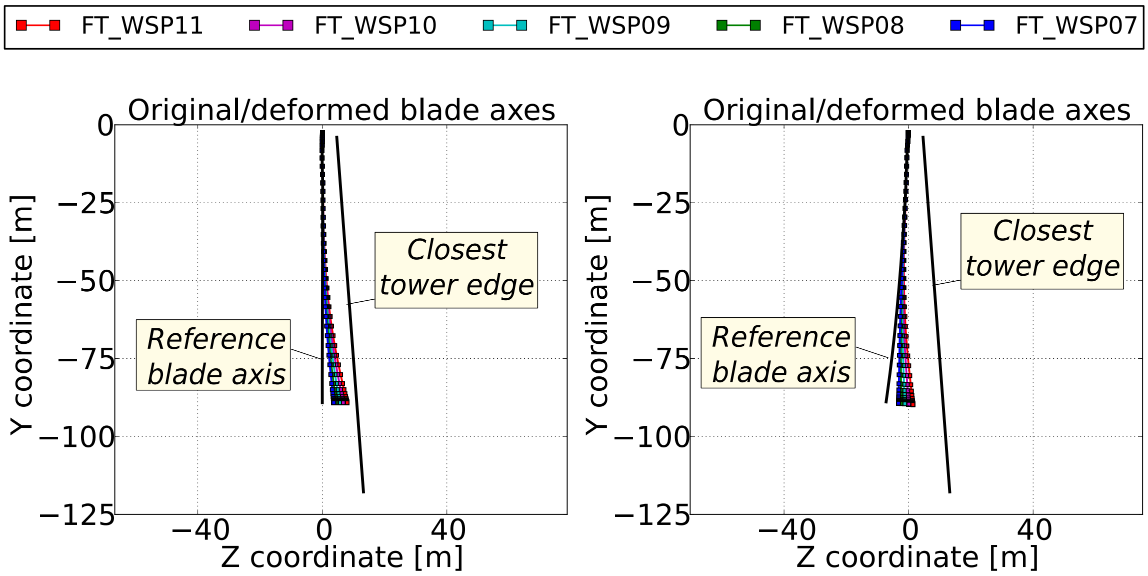

(a) *Straight* rotor (global view) **(b)** *Prebent-precone* rotor (global view)

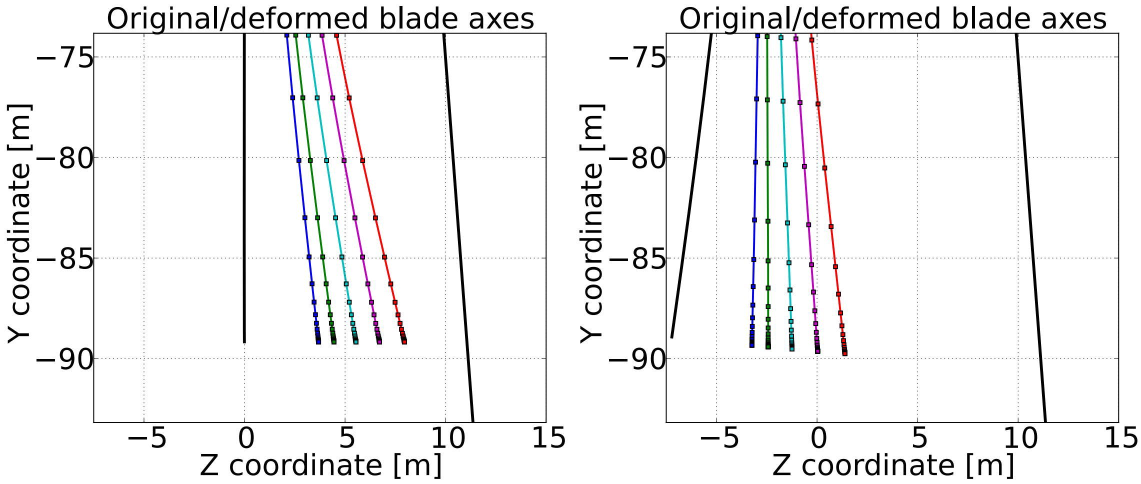

(c) *Straight* rotor (zoom) **(d)** *Prebent-precone* rotor (zoom)

Figure 5.38: Reference and deformed DTU 10MW RWT blade axis coordinates with respect to closest tower edge

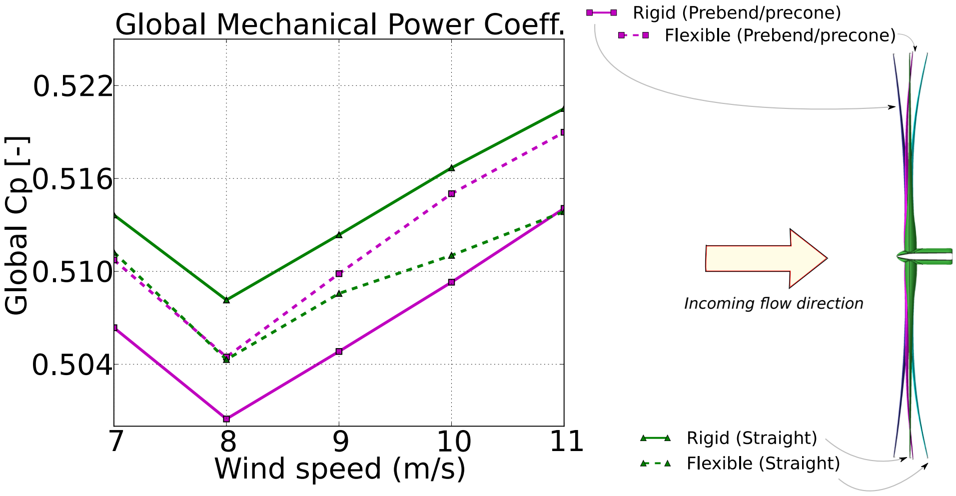

(a) Global mechanical power coefficient **(b)** View of deformed blades at 11 ms^{-1}

Figure 5.39: Global mechanical power coefficient of the DTU 10MW RWT rotor, effects of *prebending-preconing* and flexibility

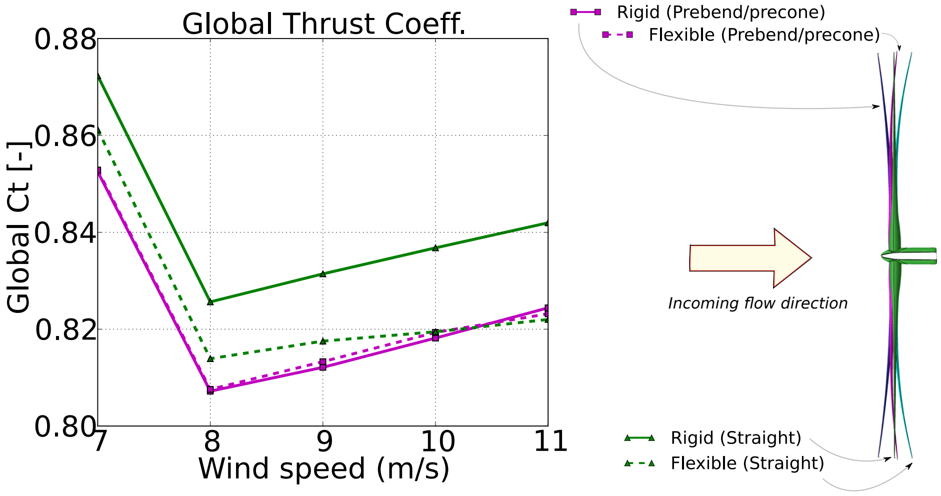

(a) Global Thrust coefficient **(b)** View of deformed blades at 11 ms^{-1}

Figure 5.40: Global thrust coefficient of the DTU 10MW RWT rotor, effects of *prebending-preconing* and flexibility

5.6 Computational cost

Table 5.7 summarizes the computational time required to perform the simulations included in this chapter. A complete characterization of an operating point, including both *rigid* and both *flexible* evaluations, could be performed in 24 hours on a modern computer. It should be reminded that all the performed simulations used a single blade passage of the rotor, thanks to the spatial periodicity of rotation.

Table 5.7: Total computational resources per analysis,*rigid* and *flexible* approaches

	Rigid	*Flexible*
Millions of nodes (N_n)	7	7
#Processors (N_p)	8	8
CPU hours (T_h)	8	16
CPU factor ($\frac{T_h N_p}{N_n}$)	9	18

5.7 Conclusions and future work

A numerical model for the study of DTU 10MW RWT rotor aerodynamics was set-up, allowing the analysis of local flow effects in a completely three-dimensional environment. In a first step, the hypothesis of *rigid* blades was made. Obtained results at 0 deg pitch operating points were successfully compared with simulations performed by other authors. In particular, maximum discrepancies in terms of rotor loads of 1.5% were observed with respect to the results of Bak et al. (2013) with EllipSys3D. The initial set-up was extended by including a structural model of the rotor in order to account for FSI effects. The blade was represented by its natural frequencies and deformed mode shapes. 2-way coupling simulations were performed in oder to assess the *static aeroelasticity* of the rotor. In order to accommodate the important observed blade deflection, the *hybrid mesh deformation* RBF+TFI+ELA method presented in Section 3.6 was successfully used. The maximum computed blade tip deformation in the rotor axis direction was observed at 11 ms^{-1} and corresponded to 8.73% of the rotor radius. This significant blade deflection had a direct impact on the loads computed at the high span range of the blade. At 11 ms^{-1}, a total reduction of the mechanical power coefficient of 1.34% was found, while the thrust coefficient was decreased by 2.25%.

The same developed numerical model was used for the study of two different aspects related to the rotor design:

- The impact of *Gurney flaps* installation on the blade was discussed. No re-attachment of the suction surface separation bubble was observed after the introduction of these devices, and a wider pressure surface recirculation zone was identified. The evaluation of the total mechanical power and thrust showed that *Gurney flaps* reduced the global performance of the DTU 10MW RWT rotor for all the considered operating points. This remark could be made for both *rigid* and *flexible* configurations. At 11 ms^{-1}, the installation of the *Gurney flaps* lead to a reduction of the power coefficient $C_p|_{global}$ of 1.4%, while the thrust coefficient $C_t|_{global}$ was increased by 0.8%. It was concluded that a decrease of the performance of the DTU 10MW RWT rotor is expected after the integration of the *Gurney flaps*.

- The results of a *prebent-precone* rotor were also compared with the standard *straight* configuration. When considering the blades as *rigid*, the combination of both geometrical modifications led to a decrease of the computed rotor loads. At 11 ms^{-1}, reductions of 1.24% of $C_p|_{global}$ and 0.7% of $C_t|_{global}$ were observed. When analyzing the corresponding *flexible* blade configurations, the effect of aeroelasticity on rotor performance was reversed. Indeed, while a reduction in the generated power was observed for the deformed *straight* rotor, an increase was found for the *prebent-precone* configuration. This inversion was explained by the deformed rotor geometries, since for the *prebent-precone* simulations the blade flexibility tended to recover the orthogonality with respect to the incoming flow. It was also shown that the consideration of a *straight rigid* blade lead to an overprediction of the $C_p|_{global}$ when compared to the more realistic *prebent-precone* configuration. A maximum relative difference of 0.7 % was observed for 8 ms^{-1}. It was concluded that the aeroelastic analysis of DTU 10MW RWT cannot be performed without considering the *prebending* and the *preconing* of the blades.

As a future work a systematic investigation in the whole operating range of velocities could be performed, including lower and higher wind speeds, in order to evaluate the performance of the presented methodology when considering other angles of attack and pitch angles. Additionally, the sensitivity of the developed model to different parameters such as the size of the CFD domain could be assessed.

Chapter 6

DTU 10MW RWT Full Machine analysis

The aim of this chapter is to analyze the unsteady effects introduced by the presence of the tower in the DTU 10MW RWT assembly. These works can be seen as a continuation of the complete aeroelastic characterization of the rotor flow already presented in Section 5. Due to the proximity of the HAWT rotor with respect to the tower, the generation of complex unsteady flow phenomena interacting with the mast is expected. This mechanism is often referred as *rotor-tower interaction*, and it is driven by the so-called *Blade Passing Frequency* (BPF) (i.e. the rotor frequency multiplied by the number of blades of the HAWT).

Regarding unsteady flow simulations, industry has relied on a straightforward variant of RANS methodology, often referred as *Unsteady Reynolds-Averaged Navier Stokes* (URANS). The required computational time in order to perform a URANS simulation of a complex geometry is however difficult to fit in an industrial work-flow. An alternative methodology was explored in this chapter. The *Non-linear Harmonic* (NLH) approach presented by Vilmin et al. (2006) allows to drastically reduce the required computational time of turbulent unsteady simulations. In the NLH method, unsteady flow perturbations are Fourier decomposed. Navier-Stokes equations are then cast in the frequency domain, leading to the extraction of a set of transport equations for each harmonic. The number of calculated harmonics is an input for the method, and drives the accuracy of the results in time and space. For the application of the NLH approach, only a single *blade passage* mesh is required. Therefore an additional CPU time and memory reduction is introduced when compared to a classical URANS approach, that requires a full rotor meshing. To the best of the authors' knowledge, no prior research concerning the flow analysis of complete HAWTs by means of high fidelity frequency domain approaches has been published. However, some publications based on the application of the *Harmonic balance* technique to representative wind turbine airfoils can be found in the literature [Campobasso et al. (2014a,b); Howison and Ekici (2014)].

6.1 Methodology

In this chapter, three different numerical approaches were used in a complementary manner:

- **RANS:** Preliminary analysis of the flow and assessment of mesh dependency
- **NLH:** Characterization of DTU 10MW RWT flow unsteadiness
- **URANS:** Comparison of the accuracy and computational effort of this technology against the NLH method

All the performed simulations were based on a rotor configuration representing an optimal DTU 10MW RWT operating point. This point is characterized by an incoming wind speed of 10.5 m.s^{-1}, a rotor speed of 8.836 RPM and a 0 deg pitch. Spalart-Allmaras turbulence model was used [Spalart and Allmaras (1992)]. As a first approach and in order to keep the rotational periodicity of the problem, the incoming wind is assumed to be aligned with rotor axis. In terms of structural model, two different configurations were analyzed:

- **Rigid blades**: Initial NLH and URANS computations were devoted to characterize unsteady aerodynamics of a *rigid* rotor. This works are described in Section 6.2.2 and Section 6.2.3 respectively.
- **Flexible blades**: The dynamic aeroelasticity problem is assessed in Section 6.3.2 by considering a modal representation of the rotor structure in both NLH and URANS approaches. For both methods, blade deflection was estimated based on computed fluid loads (2-way coupling approach).

Due to the lack of available experimental data, the study focuses in the phenomenological description of the observed global and local flow phenomena. Results are also discussed from a qualitative point of view, and compared against previous numerical experiences in other wind turbine models.

6.1.1 Considered geometry

Figure 6.1 illustrates the main geometrical properties of the studied DTU 10MW RWT assembly, based on its definition from Bak et al. (2013). The rotor axis was co-linear with the Z axis. A *tilt angle* of 5 deg was considered between rotor and tower axes. Blades accounted for a *pre-cone* angle of 2.5 deg, as well as a distributed *pre-bending*. Based on the disadvantageous effects on rotor performance found in the previous study of Section 5.4, *Gurney flaps* were removed from the blade geometry.

In order to present the unsteady results of this chapter, the normalized time t/T was used. In this context, t is defined as the already lapsed time in the current revolution and T refers to the period of rotation. The DTU 10MW RWT operates in clockwise rotation, and it was assumed that at t/T=0 one of the blades was aligned in its down position with the tower axis. This particular blade, displayed in red in Figure 6.1, is referred in this document as the *observed blade*.

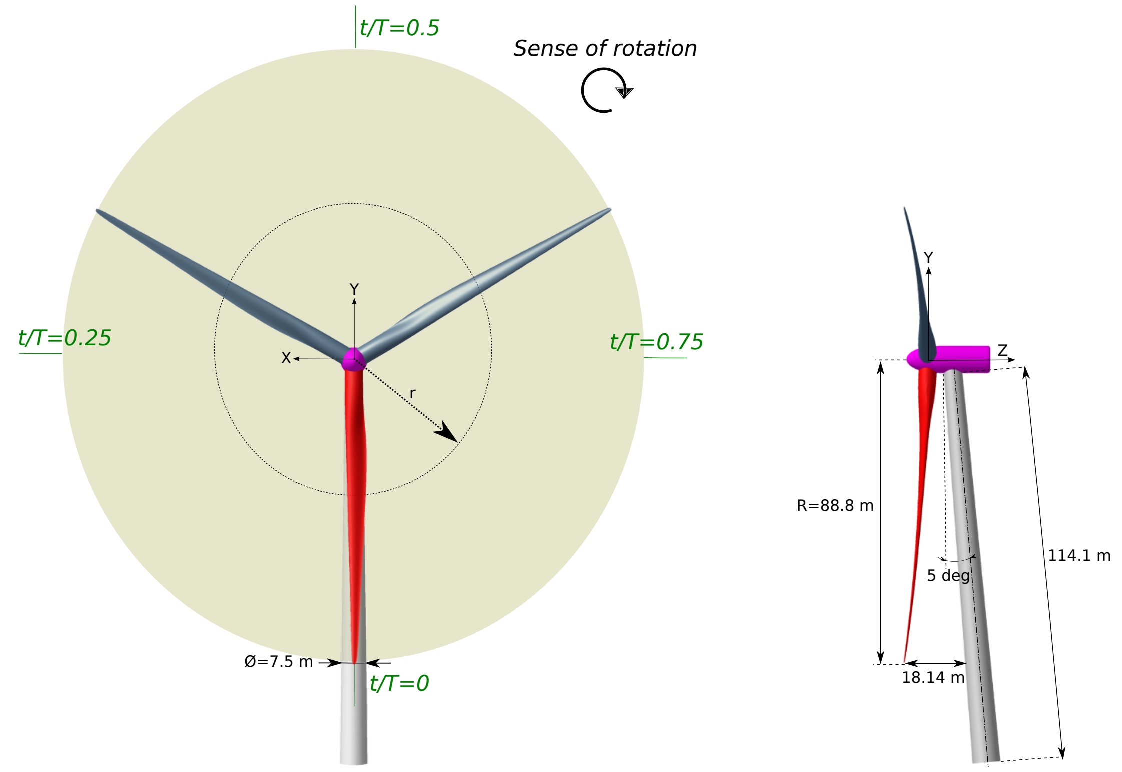

(a) Front view **(b)** Side view

Figure 6.1: Sketch of the DTU 10MW RWT assembly

6.1.2 Considered meshes and computational domains

The structure grid generator Autogrid5™ [NUMECA International (2013a)] was used in order to create three different meshes:

- **1B**: Devoted to *rotor-only* analysis, this mesh accounted for a single *blade passage* of the DTU 10MW RWT, including original nacelle and hub geometries. A first cell height of 10^{-4} m was imposed at the boundary layer of the blade, in order to target y+ values of less than 10 at the first inner cell [NUMECA International (2013b)]. This height value corresponds to approximately 1.1×10^{-6} R.
- **1B-1T**: This mesh can be seen as an adaptation of the $1B$ grid to perform NLH method simulations of the whole DTU 10MW RWT assembly. A radial *rotor/stator interface* crossing the nacelle was defined in order to allow the introduction of the tower mesh. The same blade grid topology of $1B$ was used, and a single *blade passage* was meshed

for the rotor. A 360 deg grid was generated for the tower side, also accounting for a first cell height of 10^{-4} m.

- **3B-1T**: The final goal of this mesh was the study of the whole DTU 10MW RWT assembly by means of the URANS method. It was created by repeating the rotor *blade passage* of 1*B*-1*T* thrice, keeping the same tower side mesh. It led to a 360 deg mesh at both sides of the *rotor/stator interface*, as it is required for the application of the URANS approach.

For all the considered meshes, the same computational domain size was considered (see Figure 6.2). Flow inlet and outlet were respectively located at 2.2 and 3.2 blade radius from the origin of coordinates. Non-periodic boundary conditions, referred to as *externals*, relied in the subsonic far-field formulation described in Hirsch (1990). A contraction angle was considered in the longitudinal direction of the domain. This angle was assumed to be the *tilt* angle, in order to achieve an orthogonal intersection with the tower axis. In order to explore the impact of the spatial discretization on our results, a *coarse* version of each mesh was also considered. *Coarse* variants were created by merging each 8 volume cells of the base/*fine* mesh into 1 (2 in each direction). Table 6.1 summarizes the main parameters characterizing all the described configurations.

Figure 6.3 shows the surface meshes for every configuration. Figure 6.4 displays the cross-section meshes corresponding to the grid line closest to r/R=0.5 (i.e. half of blade span). For clarity purposes, the *coarse* mesh variants are displayed in both figures.

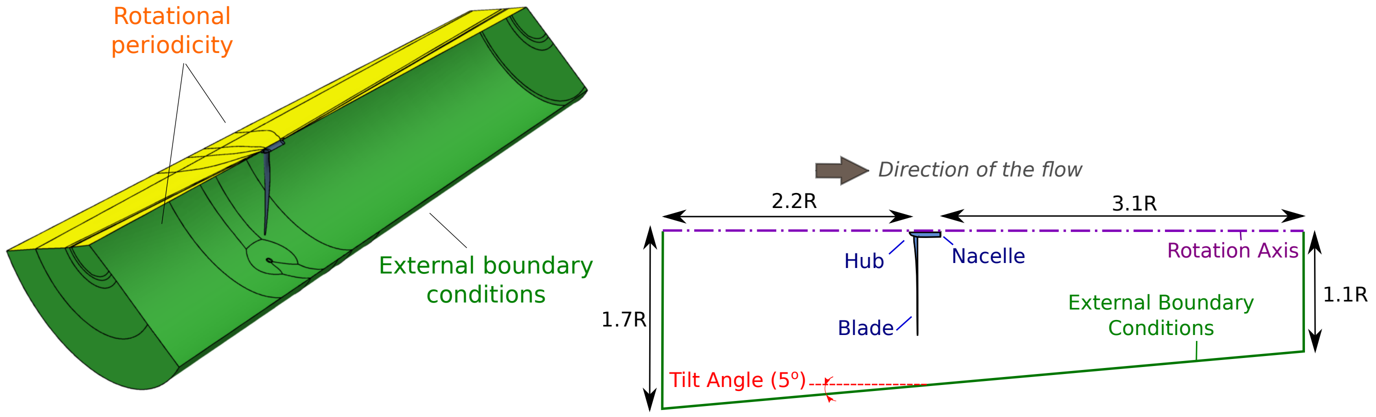

(a) 1B, 3D view **(b) 1B**, scaled sketch

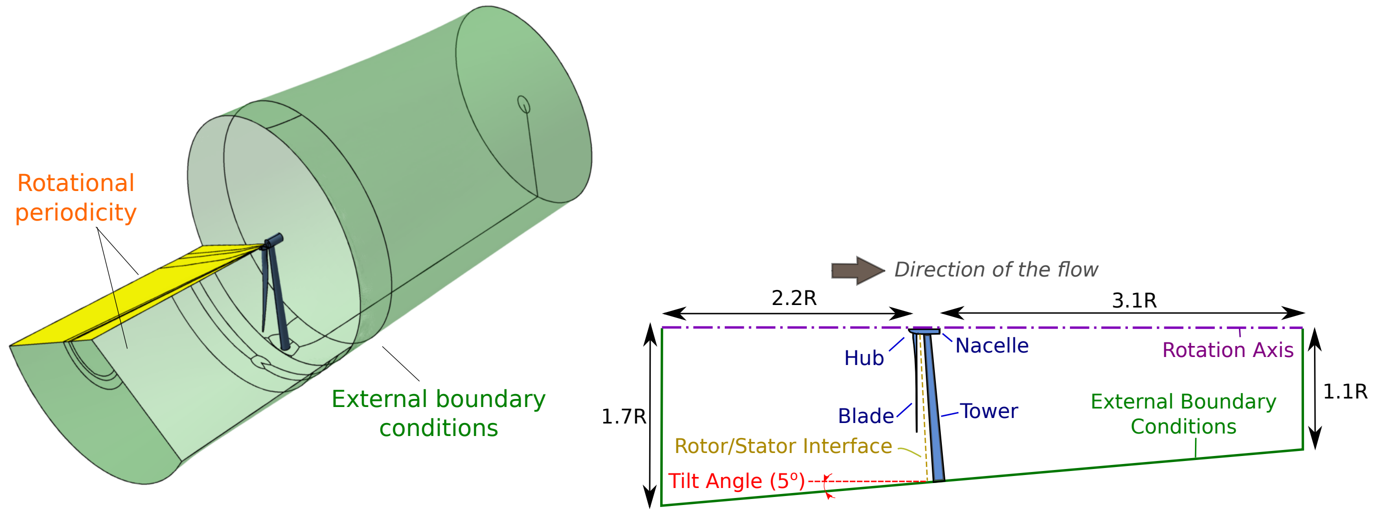

(c) 1B-1T, 3D view **(d) 1B-1T**, scaled sketch

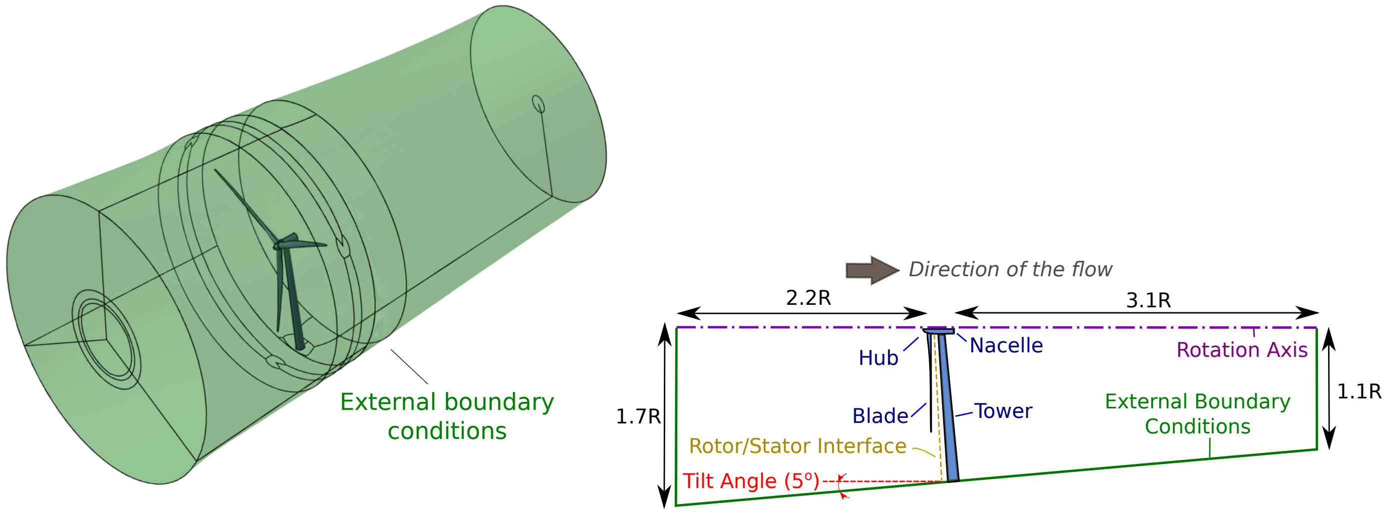

(e) 3B-1T, 3D view **(f) 1B-1T**, scaled sketch

Figure 6.2: Description of the computational domains for **1B**, **1B-1T** and **3B-1T** meshes. Solid lines represent mesh blocking. In (a) and (c), one of the periodic boundary conditions was removed to allow the visualization of the interior of the domain. In (c) and (e), the domain of the tower side was set to translucent to get a clearer visualization

Table 6.1: Description of the different DTU 10MW RWT meshes

	$1B$	$1B$-$1T$	$3B$-$1T$
Meshed sector [deg], rotor side	120	120	360
Meshed sector [deg], tower side	-	360	360
Millions of nodes, *Fine* variant	7	13	25
Millions of nodes, *Coarse* variant	0.95	1.8	3.3

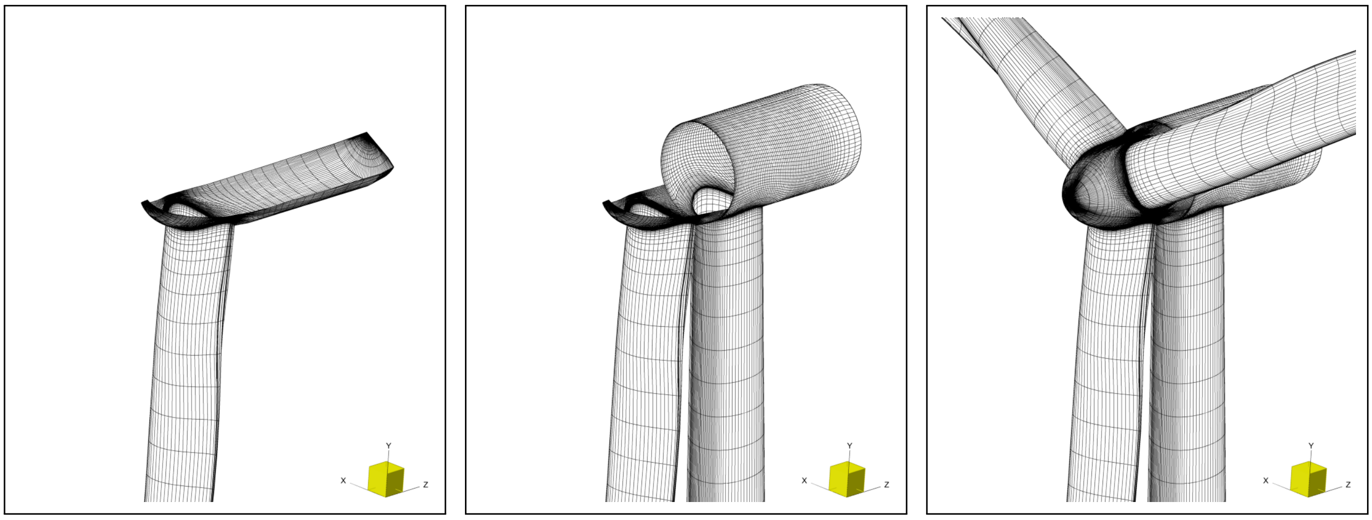

(a) $1B$ mesh **(b)** $1B$-$1T$ mesh **(c)** $3B$-$1T$ mesh

Figure 6.3: Detail of the DTU 10MW RWT surface meshes. *Coarse* variants

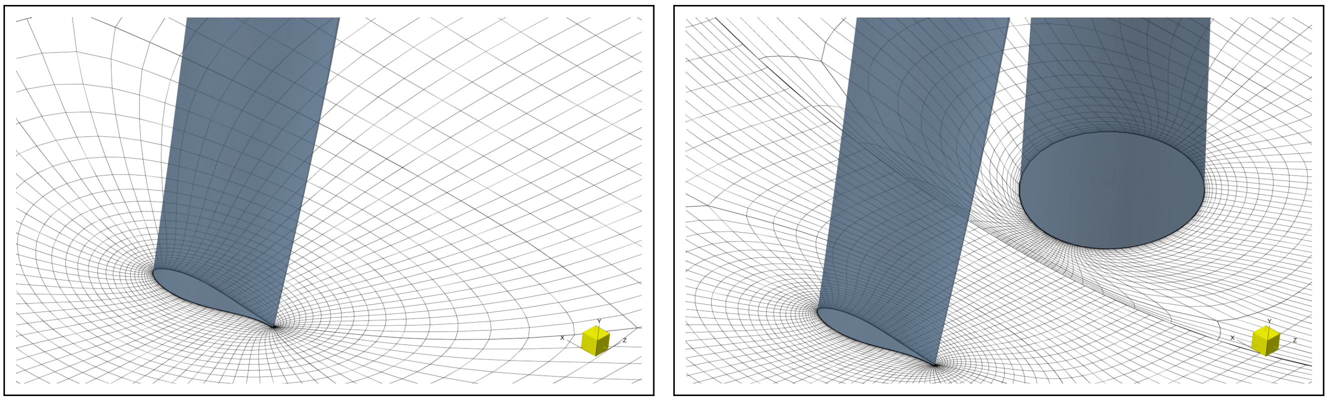

(a) $1B$ mesh **(b)** $1B$-$1T$ and $3B$-$1T$ meshes

Figure 6.4: DTU 10MW RWT cross-section meshes, grid line closest to r/R=0.5. *Coarse* variants

6.2 Unsteady aerodynamics of rigid rotor

In this section, the unsteady aerodynamics of the DTU 10MW RWT is studied. The rotor was assumed to be *rigid*. Preliminary steady RANS computations are included in Section 6.2.1. Those simulations aimed to compute the rotor loads in a *rotor-only* configuration and to evaluate the sensitivity of the mesh. In Section 6.2.2, the unsteady results computed with the NLH method are discussed. A especial attention was put in the analysis of the influence of the number of harmonics. Finally, Section 6.2.3 includes a comparison of the modeling capabilities observed for the NLH and URANS methodologies.

6.2.1 Steady RANS results

Steady RANS simulations were performed based on the three meshes described in Section 6.1.2 and their corresponding *fine* and *coarse* variants. The rotor was assumed to be *rigid*. When considering both $1B$-$1T$ and $3B$-$1T$ meshes, the *rotor/stator interface* relied on a mixing plane formulation, enabling steady RANS computations. For all simulations, a flow separation was identified at the low span region of the blade suction surface (up to an approximate radius of 40 m, r/R=0.45). A pressure surface recirculation bubble was also observed for the range r=[14,22] m (r/R=[0.16,0.25]). To illustrate this issue, Figure 6.5 shows the surface streamlines around the blade for the *fine* variant of the $1B$ mesh. This flow pattern was found to be in a good agreement with the results for a *straight* blade configuration of Zahle et al. (2014), where the suction surface separation extended to up to r=32.3 m (r/R=0.36).

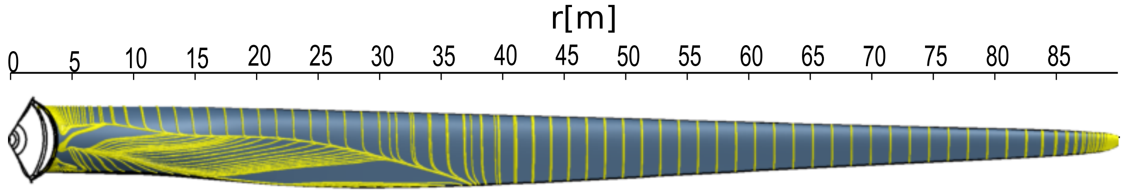

(a) Suction surface

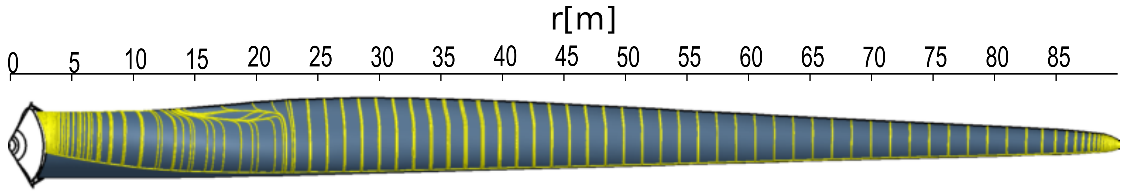

(b) Pressure surface

Figure 6.5: DTU 10MW RWT surface streamlines corresponding to $1B$ mesh and *fine* variant RANS computation

Table 6.2 lists the rotor loads for every considered mesh, computed *via* the static pressure integration around the three blades. For both $1B$-$1T$ and $3B$-$1T$ meshes, a loads decay that can be attributed to the introduction of the tower is observed. For the *fine* mesh variant, this decrease corresponded to approximately 5% of the *rotor-only* thrust and 6% of the power. Regarding the effect of mesh refinement, computed loads for the *fine* mesh showed reductions lower than 3.3% when compared to the corresponding *coarse* variant results.

Table 6.2: Computed steady rotor loads for every considered mesh and their corresponding variants

Mesh	**Thrust [kN]**			**Power [kW]**		
	coarse	**fine**	**diff. [%]†**	**coarse**	**fine**	**diff. [%]†**
$1B$	1478.8	1440.4	-2.6	9664.5	9570.0	-1.0
$1B$-$1T$	1404.3	1362.7	-3.0	9130.6	8996.3	-1.5
$3B$-$1T$	1406.8	1360.5	-3.3	9155.1	8979.6	-1.9

†: diff. refers to the observed load variation when passing from *coarse* to *fine* mesh variants

6.2.2 Unsteady NLH results

To study the unsteady flow behavior, the NLH method was applied on the $1B$-$1T$ whole assembly mesh described in Section 6.1.2. The *fine* discretization level was adopted, assuming a *rigid* rotor. A full non-matching non-reflecting approach was used for the modeling of the unsteady behavior of the *rotor/stator interface* [Vilmin et al. (2006)]. First solved rotor harmonic was located at 0.15 Hz, corresponding to the considered rotational speed. Since the DTU 10MW RWT has a 3-bladed rotor, a frequency of 0.45 Hz was observed for the first tower harmonic.

As it can be observed in Figure 6.1, the *blade-tower alignment* is a very specific event both in time and space. This fact increases the total number of harmonics needed for an NLH computation for a good modeling, since this parameter drives the spatial and frequency resolution of the method. To evaluate the dependency of the total number of harmonics several computations were run, accounting for 1, 3, 6 and 9 harmonics respectively. They will be referred in this document as *1 h*, *3 h*, *6 h* and *9 h* simulations. Even if flow variables are solved in the frequency domain, NLH results can be easily reconstructed in time in order to perform a more comprehensive post-processing of the unsteady periodic flow. This process is referred in this document as the *time solution reconstruction*.

Flow characterization

The complexity of this unsteady problem could be already pointed out with the visualization of the flow at a given time. Figure 6.6 illustrates the iso-surfaces of Q-criterion for a value of 0.5 of the time reconstructed solution at t/T=0.5 (corresponding to a half rotation). The Q-criterion Q_c [Jeong and Hussain (1995)] is defined as:

$$Q_c = \frac{1}{2}\left[||\boldsymbol{\Omega}||^2 - ||\boldsymbol{S}||^2\right] \; , \tag{6.1}$$

with $\boldsymbol{\Omega}$ and $\boldsymbol{S}$ being the antisymmetric and symmetric parts of the velocity gradient tensor $\nabla\vec{v}$:

$$\begin{aligned} \boldsymbol{\Omega} &= \frac{1}{2}\left[\nabla\vec{v} - (\nabla\vec{v})^T\right] \; , \\ \boldsymbol{S} &= \frac{1}{2}\left[\nabla\vec{v} + (\nabla\vec{v})^T\right] \; , \end{aligned} \tag{6.2}$$

Important vortical structures could be observed downstream of the tower. These were present all along the tower height, becoming more important while increasing the total number of harmonics of the computation. For *6 h* and *9 h* simulations, high vorticity regions were identified at low blade span range (where the DTU 10MW RWT is equipped with thicker airfoils). The generation of blade tip vortex was clearly observed for all the simulations. It should be mentioned that due to the nature of the numerical approach, those were rapidly dissipated downstream. However, the influence of the wake development on the predicted loads is assumed to be negligible, as observed by Carrión (2014) for the MEXICO wind turbine rotor. The interaction of the blade tip vortex with the tower led to an important increase of downstream vorticity, due to the instability generated after its break.

The observed vorticity for the *6 h* and *9 h* simulations at low blade span can be attributed to the shedding phenomenon. Figure 6.7 shows the streamlines around the *observed blade* for a r=20 m cross-section and different time reconstructed solutions (r/R=0.22). The low span suction side recirculation already identified in the *rotor-only* RANS computations of 1*B* (see Figure 6.5), was shed from the blade for *6 h* and *9 h* simulations. This effect was especially visible when the blade approached the tower (i.e. for t/T=0.00 and t/T=0.76). As a consequence, important pressure fluctuations along the suction surface and at the vicinity of the trailing edge were observed for *6 h* and *9 h*. Figure 6.8 shows the reconstruction of this flow variable at t/T=0.00, where the effect of *blade shedding* led to a local increase of around 100 Pa. A decrease of the airfoil lift is then expected for *6 h* and *9 h*, having a direct impact on the generated rotor power. A similar vortex shedding phenomenon was identified downstream of the tower all along its height.

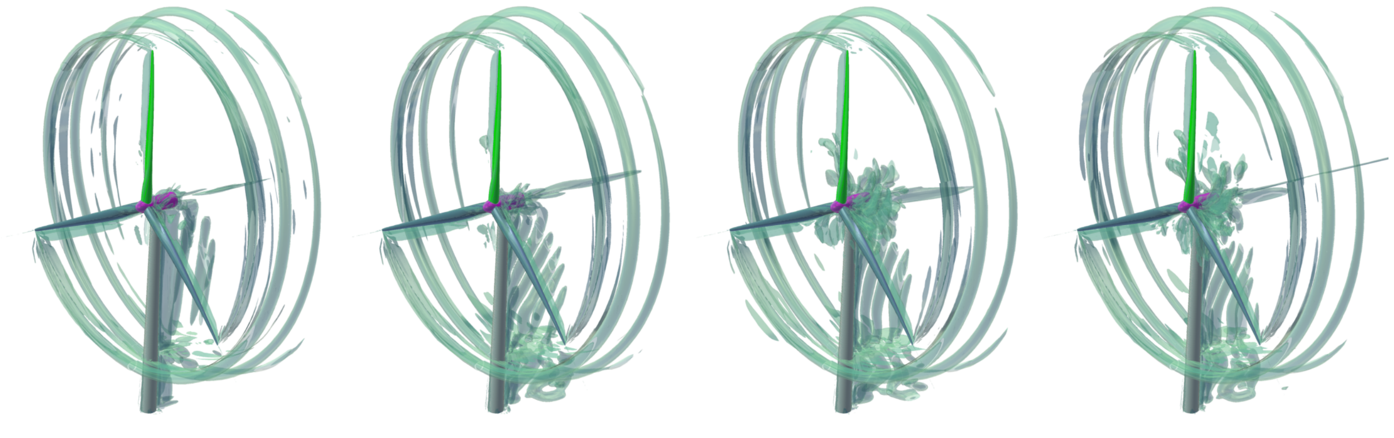

(a) *1 h* **(b)** *3 h* **(c)** *6 h* **(d)** *9 h*

Figure 6.6: Iso-surface of 0.5 Q-criterion for the time reconstructed solutions at t/T=0.50

(a) *1 h*, t/T=0.00 **(b)** *1 h*, t/T=0.24 **(c)** *1 h*, t/T=0.50 **(d)** *1 h*, t/T=0.76

(e) *3 h*, t/T=0.00 **(f)** *3 h*, t/T=0.24 **(g)** *3 h*, t/T=0.50 **(h)** *3 h*, t/T=0.76

(i) *6 h*, t/T=0.00 **(j)** *6 h*, t/T=0.24 **(k)** *6 h*, t/T=0.50 **(l)** *6 h*, t/T=0.76

(m) *9 h*, t/T=0.00 **(n)** *9 h*, t/T=0.24 **(o)** *9 h*, t/T=0.50 **(p)** *9 h*, t/T=0.76

Figure 6.7: Relative velocity streamlines around the *observed blade* for a r/R=0.22 cross-section and different time reconstructed solutions

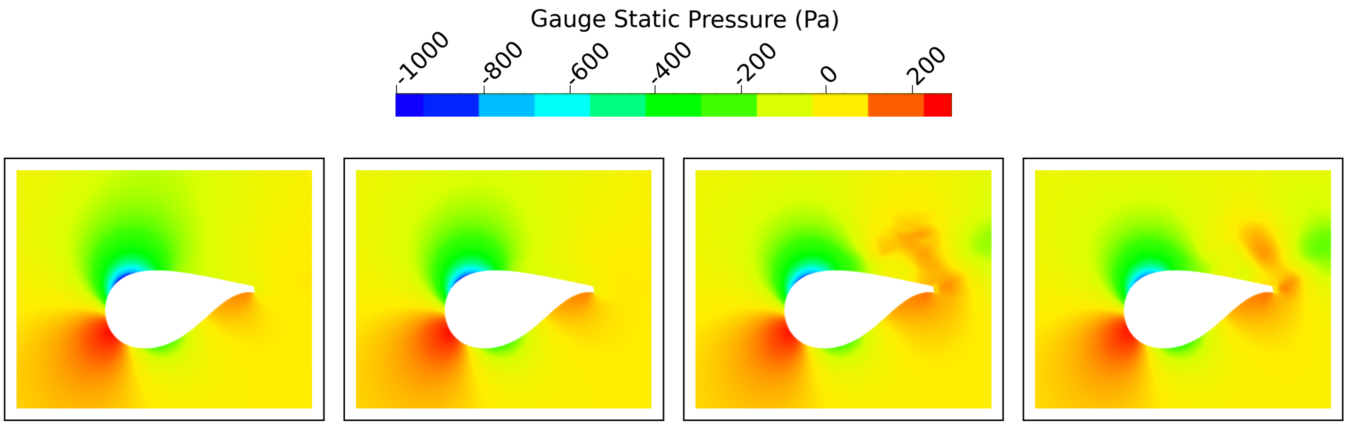

(a) *1 h* **(b)** *3 h* **(c)** *6 h* **(d)** *9 h*

Figure 6.8: Static pressure around the *observed blade* for a r/R=0.22 cross-section, t/T=0.00. Values centered at 101.300 Pa

The observed unsteady flow phenomena had a direct impact on the pressure around the HAWT structure. This implication could be already identified in the results of the *1 h* simulation. Figure 6.9 displays the amplitude of the first pressure harmonic on the DTU 10MW RWT assembly for this computation. Low span pressure fluctuations were identified on both tower and blade surfaces. For the latter case, a maximum value of 136 Pa was computed. At high r, important harmonic content was also found on the blade suction side. Additionally, the impact of the blade tip vortex on the tower also led to an increase of pressure fluctuations.

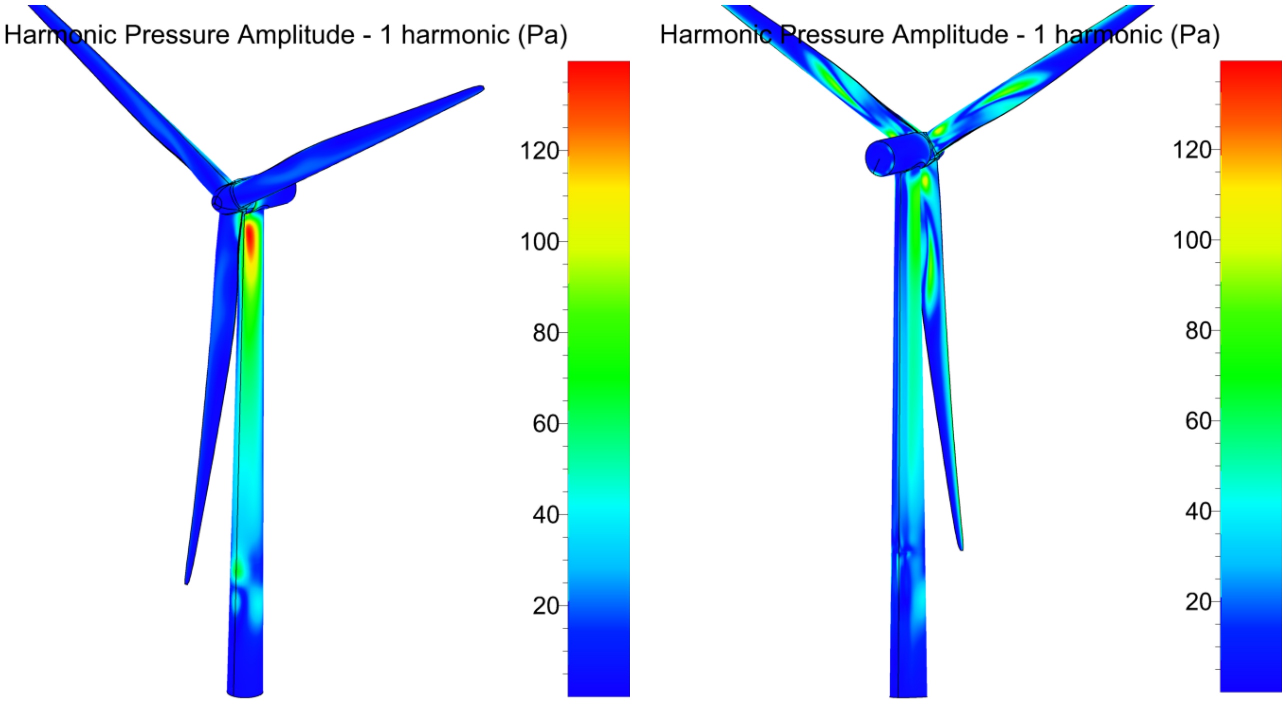

(a) Front view **(b)** Rear view

Figure 6.9: Amplitude of first pressure harmonic on DTU 10MW RWT surface, *1 h* simulation

Blade and rotor loads

In order to assess the impact of the total number of harmonics on the *blade shedding* modeling, the radial evolution of blade loads harmonic amplitudes is displayed in Figure 6.10 and Figure 6.11. This unsteady phenomenon could be identified for *6 h* and *9 h* simulations, where an important high frequency contribution was found for r/R<0.34. Peak amplitudes up to 0.55 kN/m of blade thrust and 4 kW/m of power were computed, being located around the 6th harmonic for *6 h* and at the 5th harmonic for *9 h*. Figure 6.12 shows the *Strouhal numbers* (St) of the corresponding frequencies, computed based on the relative flow velocity and axial chord. In order to contextualize the presented results, values related to cylindrical shapes and estimated based on the works of Lienhard (1966) are also included. A good agreement was observed between this reference and the central span of the *shedding* region observed for *9 h* (where St=0.25). This remark is in line with the observations made by Le Pape and Lecanu (2004) for the NREL Phase VI wind turbine, where it was concluded that the main frequency of torque oscillations was comparable to the frequency of the separations behind a cylinder. At the center of the *shedding* region of *6 h*, a *Strouhal number* of 0.37 was observed. This value was found to be particularly high, pointing towards a potential influence of the truncation effects for this simulation. *Blade shedding* also led to a decrease in the time-averaged power produced by the blade. This fact is illustrated in Figure 6.13b, where at r/R=0.22 *6h* and *9 h* show an approximate reduction of 36% with respect to the NLH simulations accounting for less harmonics. Regarding the time-averaged thrust (Figure 6.13a), only the *9 h* computation showed a considerable thrust reduction related to this phenomenon. A maximum decease of around 20% when compared to the other NLH computations was observed at r/R=0.29. For both plots, the results of the *rotor-only* RANS simulation of the 1*B fine* mesh variant are included. The potential effect related to the existence of the tower could be observed all along the blade span, leading to smaller thrust and power values.

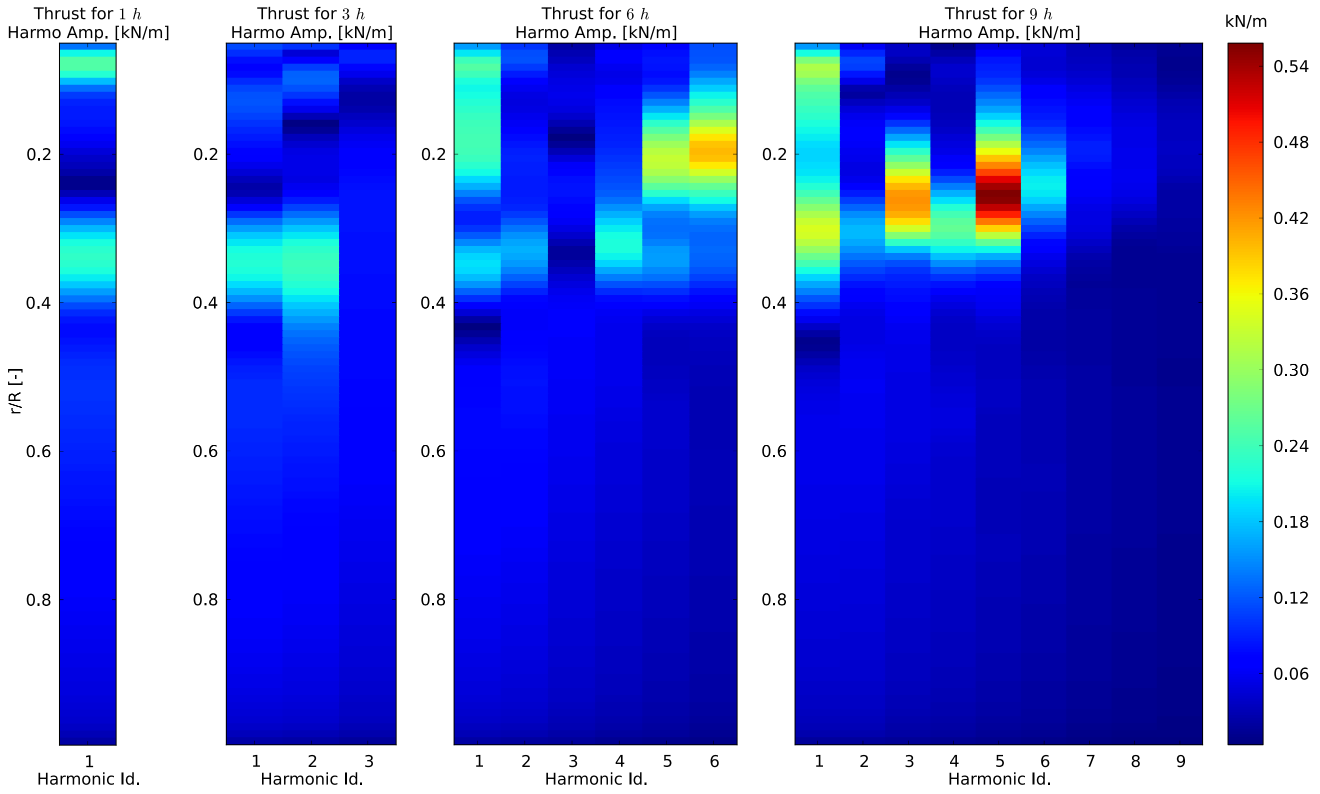

(a) *1 h* **(b)** *3 h* **(c)** *6 h* **(d)** *9 h*

Figure 6.10: Amplitude of blade thrust harmonics [kN/m] as a function of blade radius r/R [-]

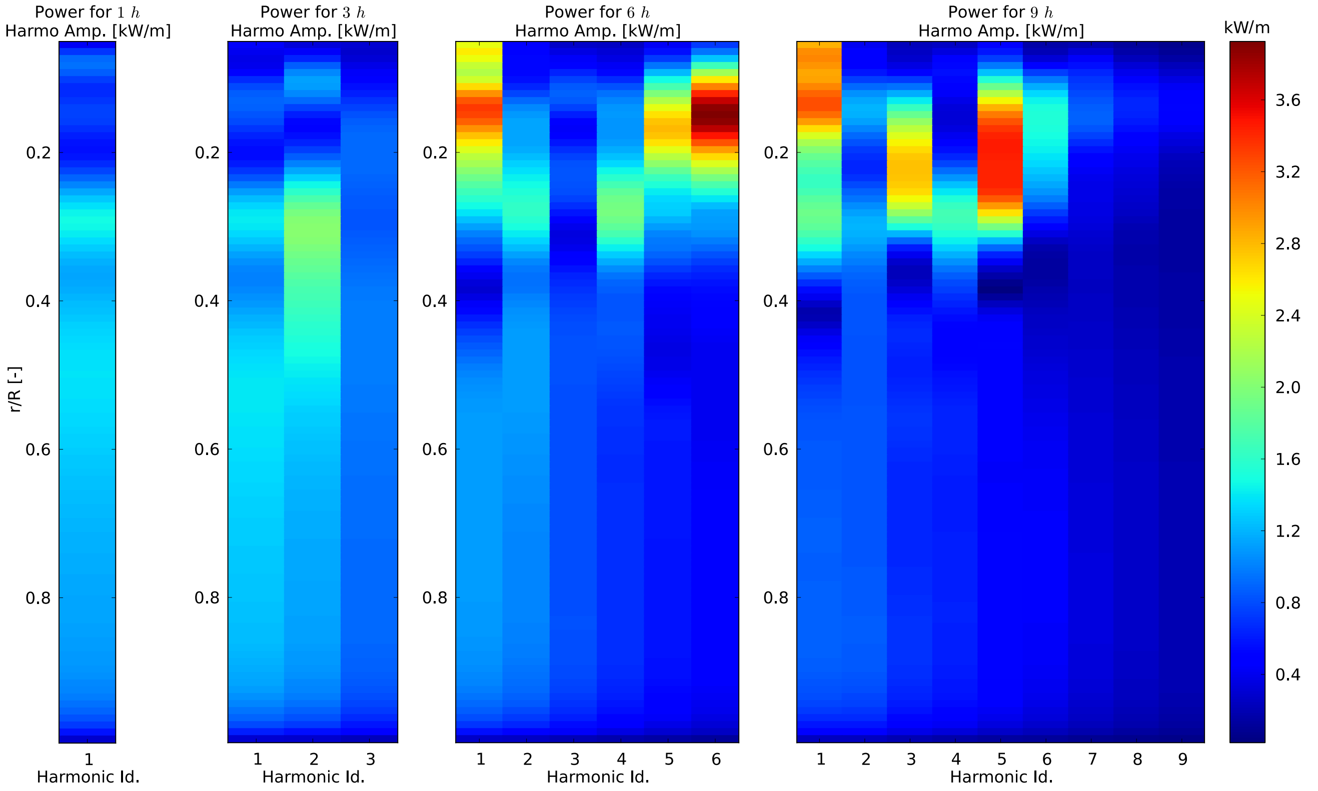

(a) *1 h* **(b)** *3 h* **(c)** *6 h* **(d)** *9 h*

Figure 6.11: Amplitude of blade power harmonics [kW/m] as a function of blade radius r/R [-]

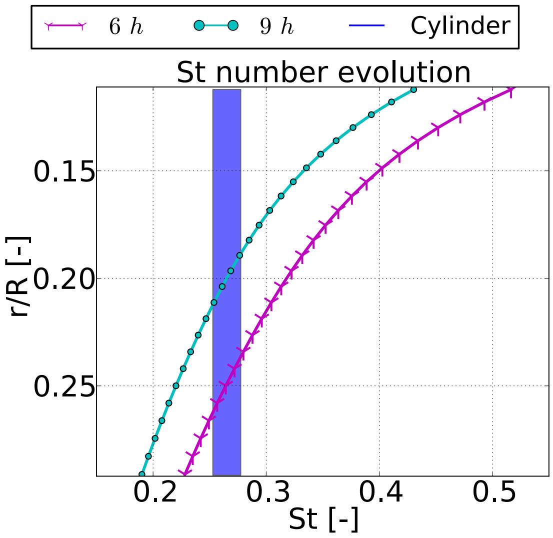

Figure 6.12: St as a function of radius within the range of observed *shedding*. Rectangle represents reference values for a cylindrical shape, estimated based on Lienhard (1966) results for the considered Re

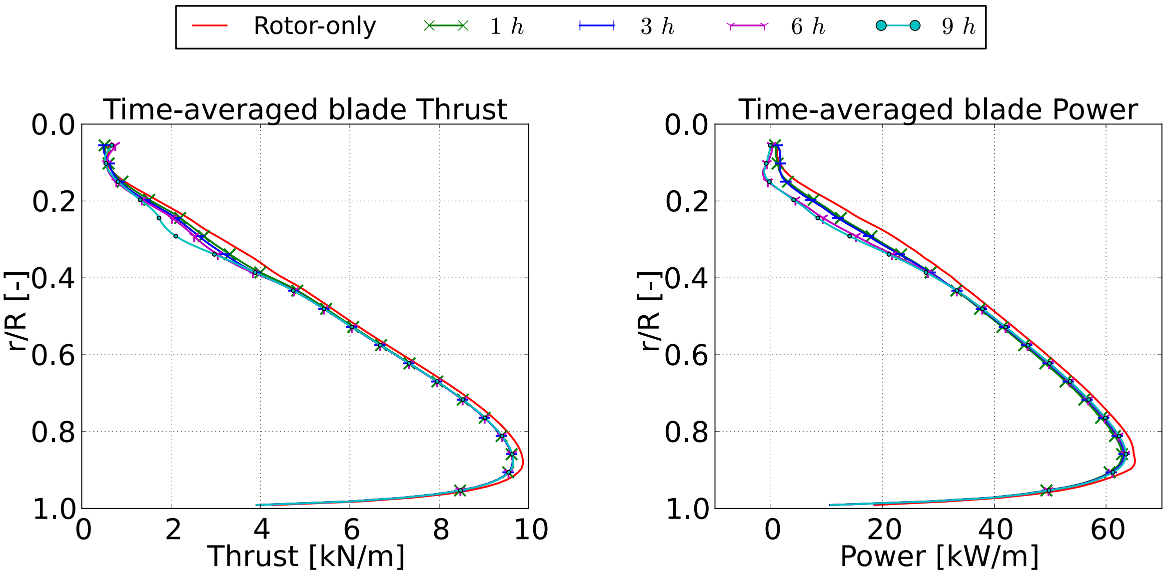

(a) Thrust **(b)** Power

Figure 6.13: Radial evolution of time-averaged blade loads. Markers do not correspond to data sampling

To evaluate the combined effect of all the blades on the DTU 10MW RWT performance, rotor loads were reconstructed in time (Figure 6.14 and Figure 6.15). These transients were computed by integrating time-averaged and harmonic blade loads for different span ranges. The contribution of the harmonic content of the three blades was taken into account by the application of a time shifting in the reconstruction. Indeed, the rotor load F for a lapsed time t can be obtained by means of blade load harmonics $\tilde{f}$ and time-averaged value $\bar{f}$ as:

$$\begin{aligned}F = 3\bar{f} + 2\sum_{h=1}^{N_h}\left[\tilde{f}^h_{Re}cos\left(h\omega t\right) - \tilde{f}^h_{Im}sin\left(h\omega t\right)\right]\\ +2\sum_{h=1}^{N_h}\left[\tilde{f}^h_{Re}cos\left(h\omega\left(t-\frac{2\pi}{3\omega}\right)\right) - \tilde{f}^h_{Im}sin\left(h\omega\left(t-\frac{2\pi}{3\omega}\right)\right)\right]\\ +2\sum_{h=1}^{N_h}\left[\tilde{f}^h_{Re}cos\left(h\omega\left(t+\frac{2\pi}{3\omega}\right)\right) - \tilde{f}^h_{Im}sin\left(h\omega\left(t+\frac{2\pi}{3\omega}\right)\right)\right] ,\end{aligned} \tag{6.3}$$

Where $\tilde{f}^h_{Re}$ and $\tilde{f}^h_{Im}$ are the real and imaginary parts of the h^{th} blade load harmonic, $\bar{f}$ refers to its time-averaged value, N_h is the total number of harmonics and ω the rotor angular velocity. By applying simple trigonometric identities, Equation 6.3 can be rewritten as:

$$F = 3\left(\bar{f} + 2\sum_{h=1}^{N_h} A^h\right) , \tag{6.4}$$

With:

$$A^h = \frac{2}{3}\left[\tilde{f}^h_{Re}cos\left(h\omega t\right) - \tilde{f}^h_{Im}sin\left(h\omega t\right)\right]\left[\frac{1}{2} + cos\left(h\frac{2\pi}{3}\right)\right] , \tag{6.5}$$

By evaluating $cos\left(h\frac{2\pi}{3}\right)$, A^h can be expressed as a function of the harmonic order h as:

$$A^h = \begin{cases} \tilde{f}^h_{Re}cos\left(h\omega t\right) - \tilde{f}^h_{Im}sin\left(h\omega t\right) & \text{if } h \bmod 3 = 0 \\ 0 & \text{if } h \bmod 3 \neq 0 \end{cases} \tag{6.6}$$

From Equation 6.6 it can be concluded that only the harmonics which order is a multiple of the number of blades do contribute to rotor loads fluctuation. For those frequencies, the influence of blade fluctuation on the rotor is indeed multiplied by the number of blades. In order to analyze the impact of *blade shedding* in an isolated manner, three different post-processing are presented:

- **0<r<0.5R**: Integration of the *inner* half of the rotor, where *blade shedding* was observed
- **0.5R<r<R**: Integration of the *outer* half of the rotor, responsible of the most part of the generated loads. In this region, flow unsteadiness was mainly dominated by the first harmonic (i.e. the *blade-tower alignment* event)
- **Whole rotor**: Considers the complete rotor (*inner* and *outer* halves)

For all the plots, the corresponding result for the *rotor-only* RANS simulation based on the 1*B fine* mesh variant is included. All the performed NLH computations showed a decrease in the computed time-averaged loads with respect to this reference. These reductions are summarized in Table 6.3. At the *inner* half of the rotor the *blade shedding* phenomenon

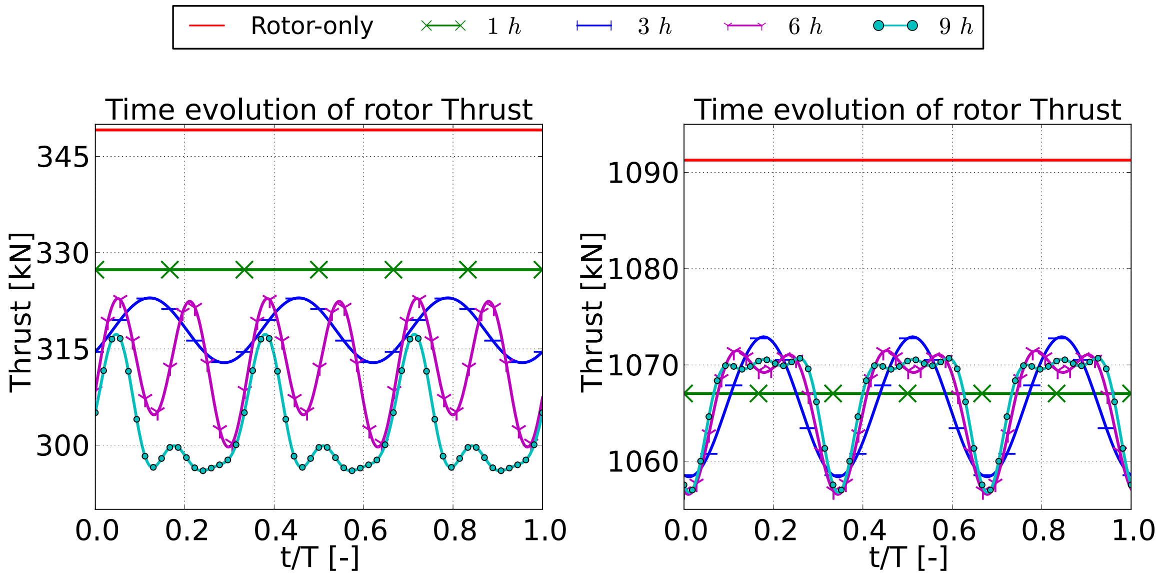

(a) 0<r<0.5R **(b)** 0.5<r<R

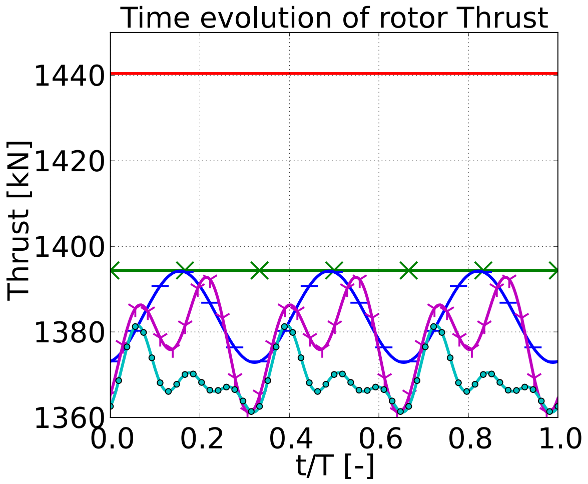

(c) Whole rotor

Figure 6.14: Rotor thrust [kN] time evolution. Markers do not correspond to data sampling

Table 6.3: Time-averaged rotor loads reduction due to the consideration of the tower

	Thrust decrease [%]			**Power decrease [%]**		
	0<r<0.5R	**0.5R<r<R**	**Whole rotor**	**0<r<0.5R**	**0.5R<r<R**	**Whole rotor**
1 h	6.24	2.22	3.20	11.5	4.21	6.13
3 h	8.94	2.35	3.95	12.5	3.51	5.75
6 h	10.5	2.28	4.28	20.8	3.15	7.54
9 h	13.4	2.23	4.95	22.6	2.99	7.85

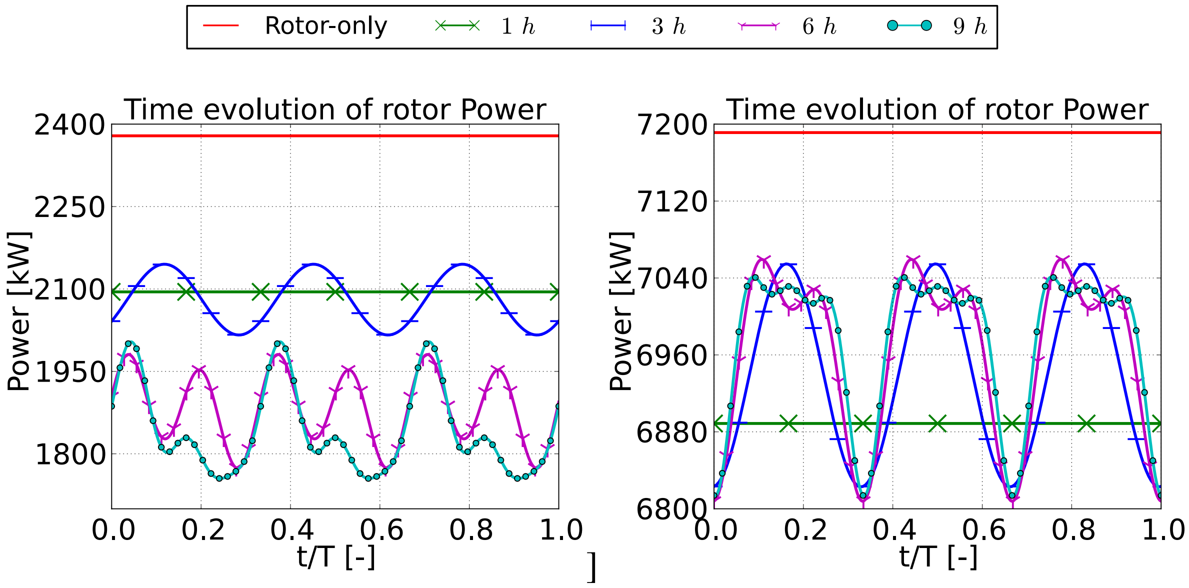

]

(a) 0<r<0.5R

(b) 0.5<r<R

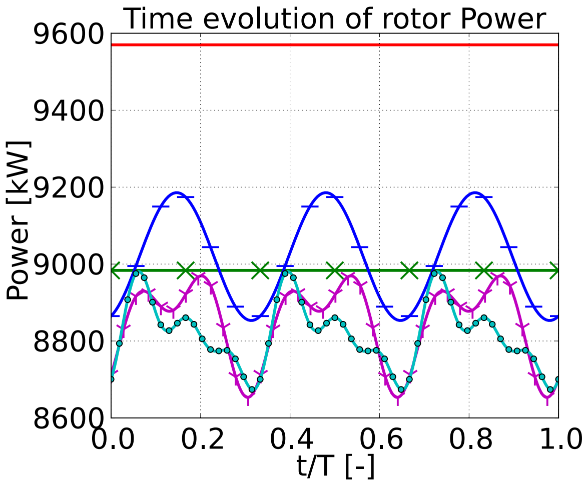

(c) Whole rotor

Figure 6.15: Rotor power [kW] time evolution. Markers do not correspond to data sampling

induced considerable load fluctuations for *3 h*, *6 h* and *9 h* computations, which were triggered every *blade-tower alignment* event (t/T=0, $\frac{1}{3}$, $\frac{2}{3}$). For the particular case of *9 h*, a relative amplitude of 3.5% was observed for the thrust oscillation, while a 6.7% was computed for the power. As deduced from Equation 6.6 a flat evolution was found for the case of *1 h*, since a single harmonic was solved. An important time-averaged rotor power decrease was also attached to the *blade shedding*, reaching up to 22.6% with respect to the corresponding *rotor-only* values. For the *outer* half of the blade, where no *blade shedding* occurred, the consideration of more harmonics led to an improvement in the modeling of the loads decay related to the *blade-tower alignment*. Even if this effect is very specific in time and space, NLH computations showed a good agreement in terms of load oscillations and time-averaged values when using 3,6 and 9 harmonics. Relative amplitudes of approximately 0.7% and 1.7% were obtained for thrust and power fluctuations, respectively. In the time reconstruction of the *whole rotor* loads, the observed effects for the *inner* and *outer* rotor halves were combined. Although different transient patterns were computed for *6 h* and *9 h* simulations due to the *blade shedding* modeling, a reasonable agreement in terms of relative fluctuation amplitudes was found (around 1% for rotor thrust and 2% for the power). Regarding time-averaged loads, the capture of the *blade shedding* for the *6 h* and *9 h* computations introduced an additional decay with respect to the other simulations. For the particular case of *9 h*, total decreases of 4.95% in rotor thrust and 7.85% in power were computed.

Computational cost

Table 6.4 compiles the computational time of the presented simulations. For contextualizing purposes, an estimation of the time needed to perform a URANS simulation based on the *fine* mesh variant of $3B$-$1T$ is also included. The most computationally expensive of the performed NLH simulations, *9 h*, was carried out in 5 days with the use of 128 processors. This represents only 9.6% of the computational time required for a URANS simulation.

Table 6.4: Total computational resources per analysis for the *fine* mesh

	1 h	*3 h*	*6 h*	*9 h*	URANS (Estimated)
Millions of nodes (N_n)	13	13	13	13	25
#Processors (N_p)	64	64	64	128	128
Comp. time, hours (T_h)	24	48	96	120	∼1250
Comp. factor ($\frac{T_h N_p}{N_n}$)	118	236	473	1118	∼6400

6.2.3 Comparison with URANS unsteady results

The URANS method was evaluated in order to compare its performance with the already presented NLH technology in Section 6.2.2. Due to the considerable computational effort required for the application of URANS on the *fine* mesh, the *coarse* variant of $3B$-$1T$ was used instead. In order to assess the impact of mesh refinement on the obtained solution, URANS results were compared against NLH computations based on both *fine* and *coarse* discretization. NLH simulations accounted for a total of 6 harmonics, and they are designated in this section as *6h fine* and *6h coarse* respectively. Note that *6h fine* corresponds to the simulation labeled as *6 h* in Section 6.2.2.

For the *URANS coarse* simulation, the domain-scaling approach was used in order to model the *rotor/stator interface*. A time-step of 0.01 s was chosen, equivalent to an increase in the rotor position of 0.5 deg for the considered period of revolution. Assuming a minimum of 20 points per period, this time resolution can properly model up to 36 rotor harmonics. 1000 inner iterations per time-step were performed. To completely develop the flow solution, 6 preliminary revolutions were computed before analyzing the results of the revolution presented in this chapter. This is illustrated in Figure 6.16 by means of the evolution of the rotor loads during the complete time marching simulation, where a stabilization of both thrust and power was observed from the 5th revolution. A decrease of the rotor loads is also observed with regards to the initial solution, that corresponded to a fully converged steady RANS computation. This fact is discussed and quantified further on in this chapter.

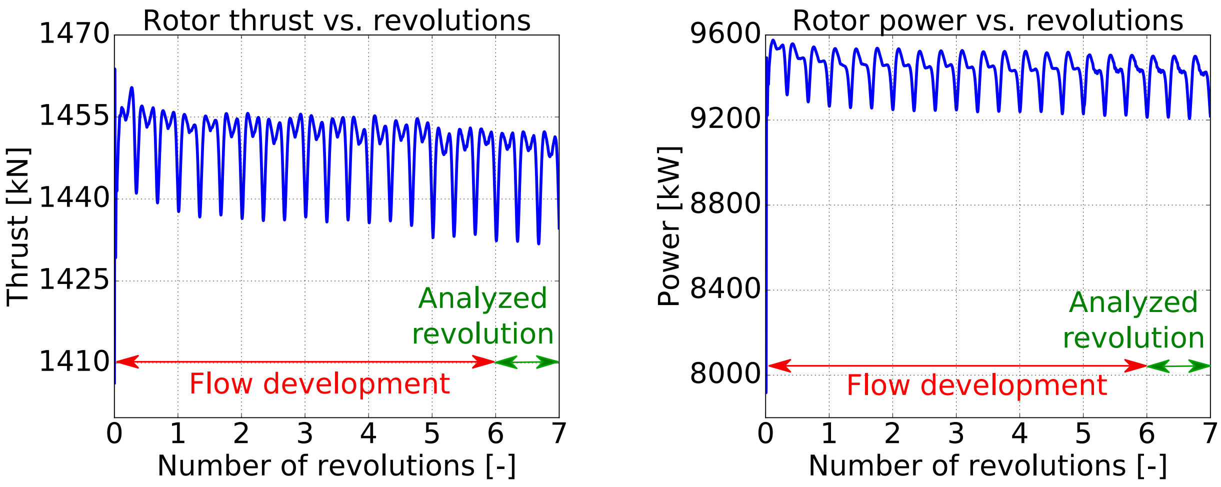

(a) Rotor thrust **(b)** Rotor power

Figure 6.16: *URANS coarse*, rotor loads as a function of the performed revolutions

Flow characterization

Figure 6.17 illustrates the iso-surfaces of Q-criterion for a value of 0.5 at t/T=0.50. Dissipative effects related to the mesh resolution were clearly observed when comparing *6h fine* with *6h coarse*/*URANS coarse* results. Nevertheless, the same vortical structures could be identified for every simulation, regardless their mesh refinement level. It should be remarked that for the *coarse* grid variant, the NLH harmonic solution showed a clearer representation of the tip vortex when compared to *URANS coarse*. This could be related to the total simulation time that was considered for the time marching computation. Indeed, even if the loads for *URANS coarse* were rated to be stabilized (as shown in Figure 6.16), the proper study of the wake vortical structures could require the increase of the number of the revolutions devoted to the development of the flow. This is in line with the remark made for the Q-criterion visualizations of the NLH simulations of Figure 6.6, stating that the influence of the wake development on the loads is assumed to be very small.

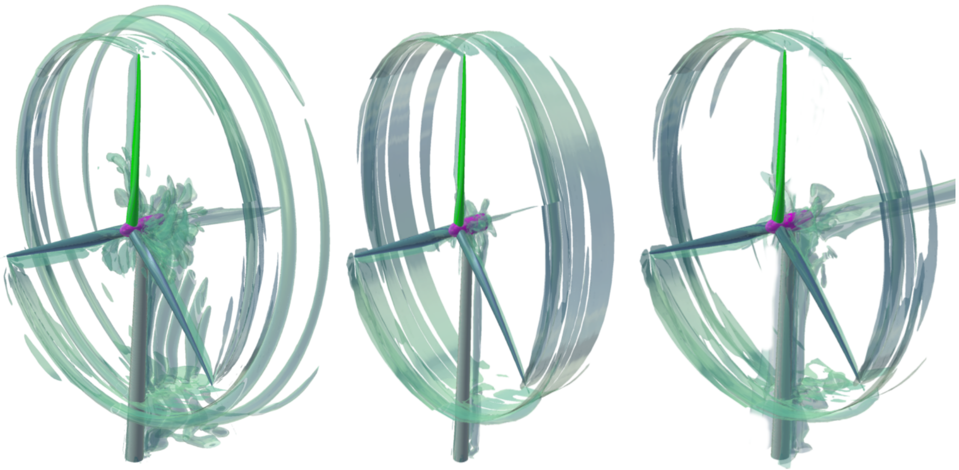

(a) *6h fine* **(b)** *6h coarse* **(c)** *URANS coarse*

Figure 6.17: Iso-surface of 0.5 Q-criterion at t/T=0.50 [including *URANS coarse*]

Blade and rotor loads

Figure 6.18 and Figure 6.19 show the radial evolution of blade loads harmonic amplitudes for *6h coarse* and *URANS coarse*. For the latter simulation, the harmonic content was computed *via* the *Fourier Transform* of the corresponding transient solutions. For clarity purposes only the results of this *Fourier Transform* up to the 9th harmonic are shown, since no significant blade loading content was found for higher frequencies. Low span *blade shedding* was observed for both methodologies. For *6h coarse*, peak amplitudes attached to this phenomenon corresponded to the 5th harmonic (as observed for *6h fine* in Section 6.2.2). The *URANS coarse* solution revealed a *blade shedding* located at the 6th harmonic (as previously seen for *9 h*). *6h coarse* showed a considerable overall load fluctuations overestimation with respect to the *URANS coarse* computation. At the vicinity of the *blade shedding* phenomenon, an approximate multiplication factor of 2 was observed. A better agreement was found in terms of time-averaged blade loads, which are displayed in Figure 6.20. The results of *6h fine* are also included in order to illustrate the effect of mesh refinement, which are especially important at low span due to the existence of *blade shedding*.

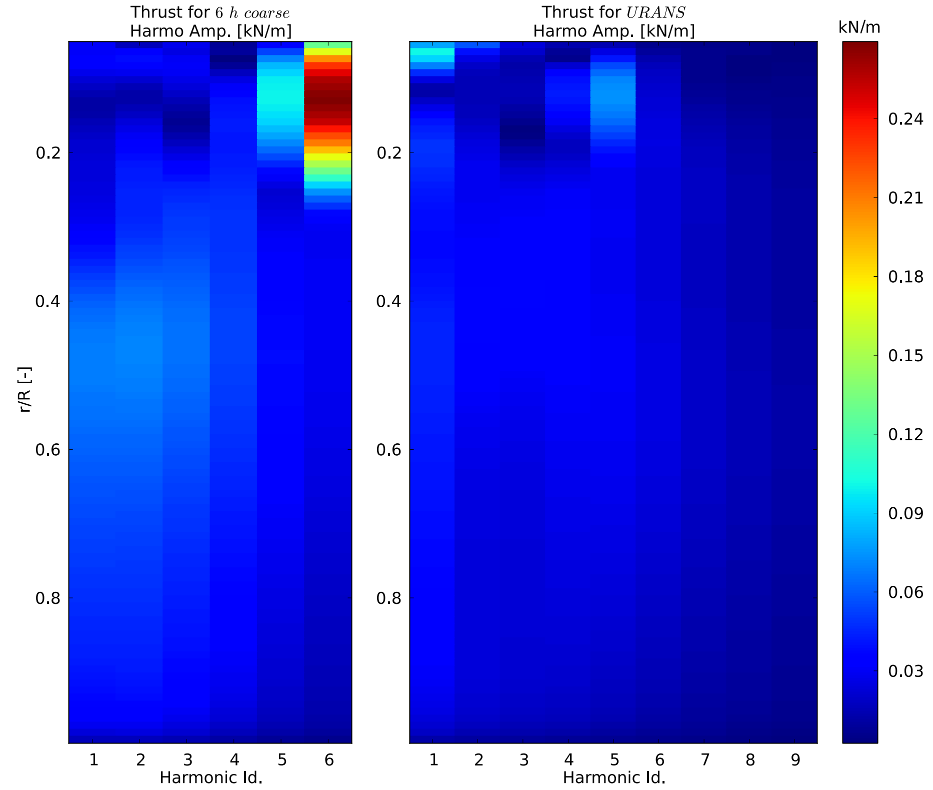

(a) *6h coarse* **(b)** *URANS coarse*

Figure 6.18: Amplitude of blade thrust harmonics [kN/m] as a function of r/R [-], with *URANS coarse*

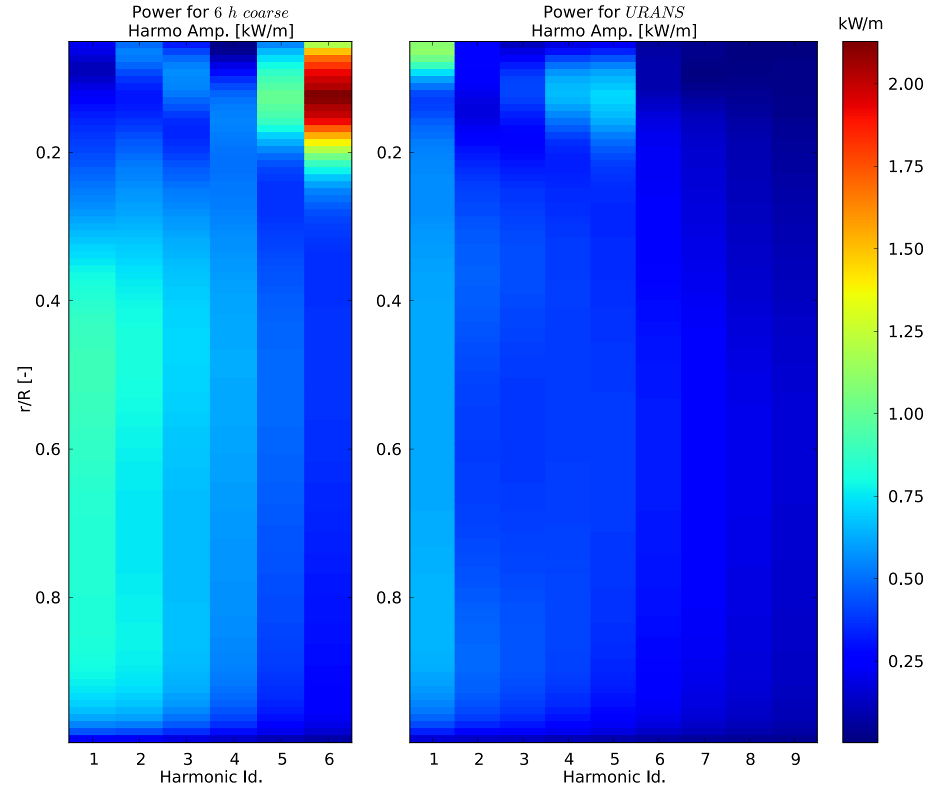

(a) *6h coarse* **(b)** *URANS coarse*

Figure 6.19: Amplitude of blade power harmonics [kW/m] as a function of r/R [-], with *URANS coarse*

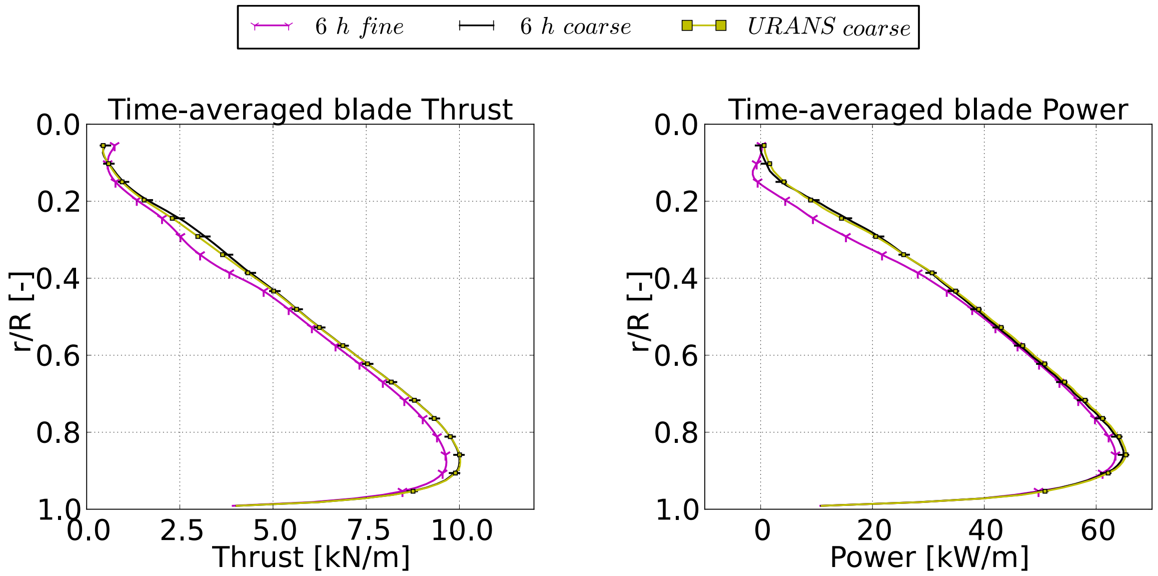

(a) Thrust **(b)** Power

Figure 6.20: Radial evolution of time-averaged blade loads, including *URANS coarse*. Markers do not correspond to data sampling

As performed in Section 6.2.2, Figure 6.21 and Figure 6.22 illustrate thrust and power time evolutions for different rotor segments. The corresponding result for the *rotor-only* RANS simulation based on the 1*B coarse* mesh variant is also displayed. Time-averaged loads reductions experienced by *6h coarse* and *URANS coarse* with respect to this reference are summarized in Table 6.5.

At the *inner* half of the blade (0<r<0.5R), considerably higher load oscillations were observed for *6h coarse*. Multiplication factors of 3.0 and 1.9 were found for thrust and power fluctuations, respectively. In addition, the predicted time-averaged rotor thrust decay due to the introduction of the tower was found to be very dissimilar (3.39% for *6h coarse* and 6.02% for *URANS coarse*). These important discrepancies should be analyzed in detail in future studies. Regarding the NLH computation, the role that the deterministic stresses play in the time-mean equations should be analyzed in deep, together with the impact of the harmonics interaction in the computation of the *shedding*. Regarding the time marching computation, it could be also interesting to evaluate the influence of the total simulation time on the modeling of local aspects of the flow related to the *shedding*. A better agreement was found when considering the *outer* half of the blade (0.5R<r<R), where this unsteady phenomenon did not occur. Even if the *6h coarse* low span load fluctuations overestimation was still observed when analyzing the *whole rotor*, a fair agreement with *URANS coarse* results was found.

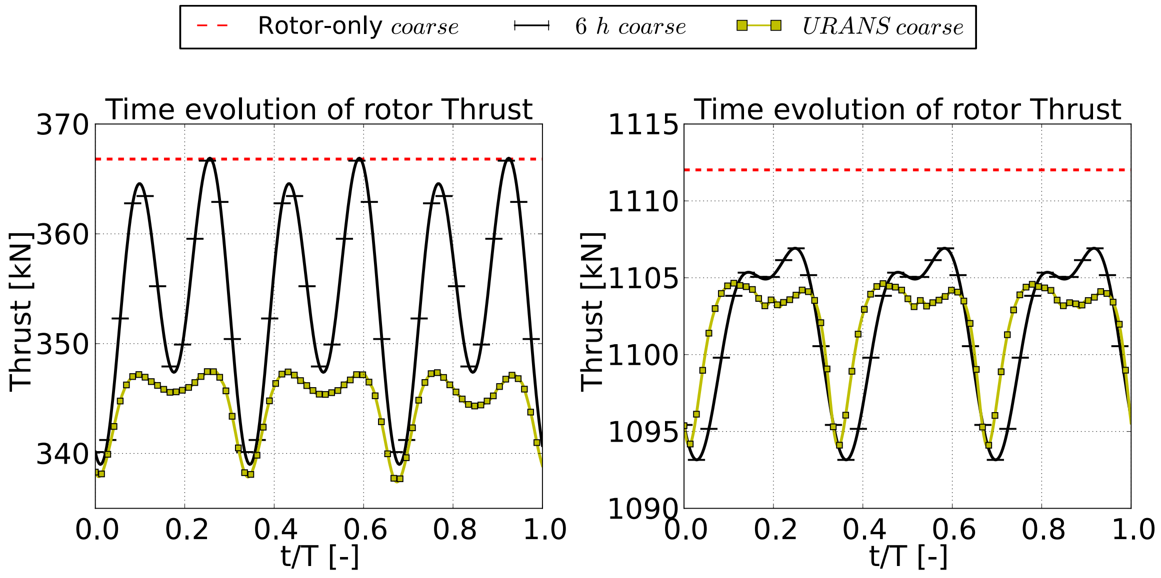

(a) 0<r<0.5R **(b)** 0.5R<r<R

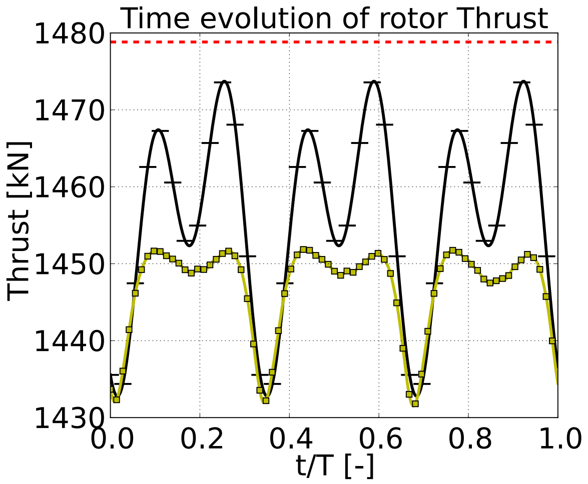

(c) Whole rotor

Figure 6.21: Rotor thrust [kN] time evolution, including *URANS coarse*. Markers do not correspond to data sampling

Table 6.5: Time-averaged rotor loads reduction due to the consideration of the tower, including *URANS coarse*

	Thrust decrease [%]			**Power decrease [%]**		
	0<r<0.5R	**0.5R<r<R**	**Whole rotor**	**0<r<0.5R**	**0.5R<r<R**	**Whole rotor**
6h coarse	3.39	0.92	1.53	8.28	1.78	3.45
URANS coarse	6.02	0.89	2.16	7.99	0.96	2.77

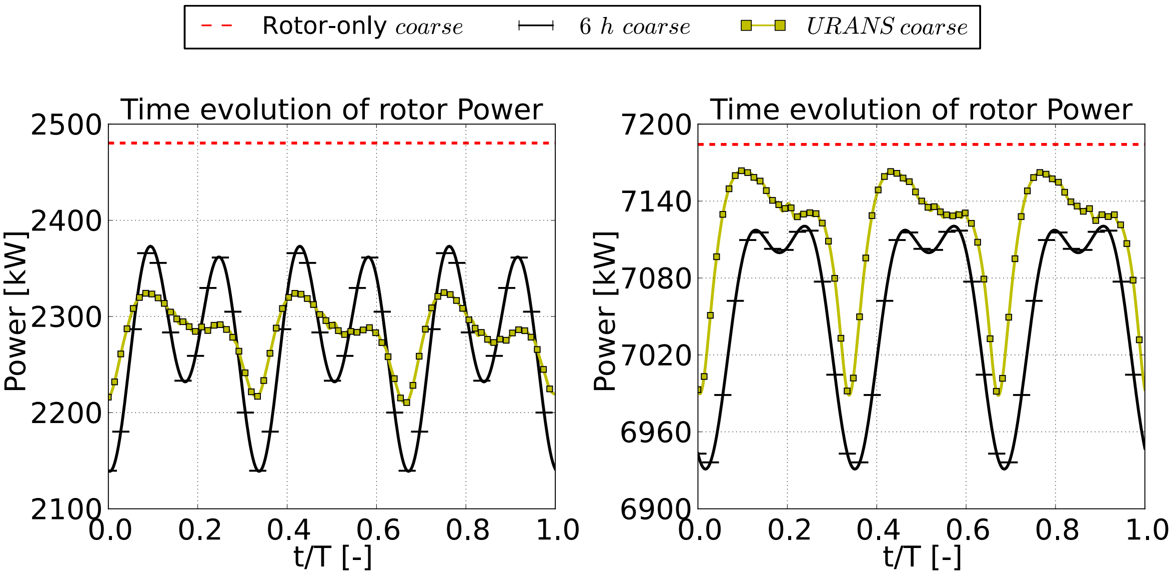

(a) 0<r<0.5R **(b)** 0.5R<r<R

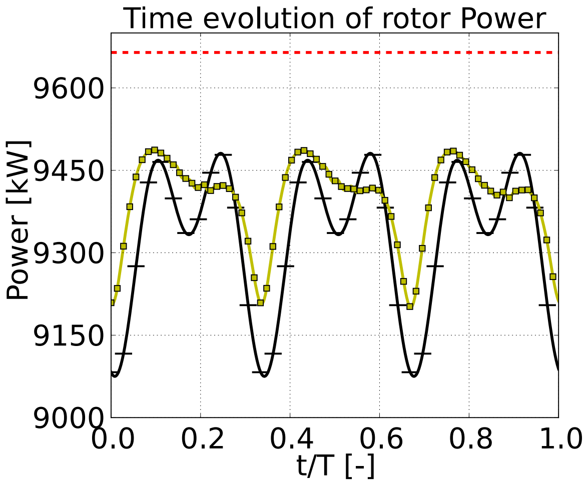

(c) Whole rotor

Figure 6.22: Rotor power [kW] time evolution, including *URANS coarse*. Markers do not correspond to data sampling

Computational cost

Table 6.6 compiles the simulations that are discussed in this section, together with the information of their required computational effort. The estimation of the *URANS fine* computation, already shown in Section 6.2.2, was reproduced for reference. The computational time employed for *6h coarse* only represented 7.7% of the resources needed to perform *URANS coarse* simulation. It should be reminded that the simulation time specified for *URANS coarse* accounts for 6 preliminary revolutions devoted to the development of the flow. As suggested in Section 6.2.3, additional initial revolutions should be considered in order to achieve a similar representation of the wake vortical structures predicted by *6h coarse*. This will imply a computational overhead for the time marching simulation, making the NLH approach even more attractive from this point of view.

Table 6.6: Total computational resources per analysis [including URANS]

	6h fine	*URANS fine*	*6h coarse*	*URANS coarse*
Computational method	NLH	URANS	NLH	URANS
Mesh	$1B$-$1T$	$3B$-$1T$	$1B$-$1T$	$3B$-$1T$
Mesh variant	*fine*	*fine*	*coarse*	*coarse*
Millions of nodes (N_n)	13	25	1.8	3.3
#Processors (N_p)	64	128	64	128
Comp. time, hours (T_h)	96	~1250	27	350
Comp. factor ($\frac{T_h N_p}{N_n}$)	473	~6400	960	13576

6.3 Dynamic aeroelasticity

In Section 6.2.2 and Section 6.2.3, unsteady computations of the DTU 10MW RWT whole machine were presented. All simulations relied in the hypothesis of *rigid* blades. In this section, the dynamic periodic deformation of the blades due to the rotor flexibility was introduced. The structure was linearized by means of its modal shapes and natural frequencies. Both NLH and URANS computations were performed, starting from already converged RANS solutions. The aeroelastic model was based in a 2-way coupling approach. This comparison has a double objective. On the one hand, to estimate the importance of blade flexibility on rotor loads prediction. On the other hand, to assess the capabilities of the developed FSI 2-way coupling harmonic module in the context of a HAWT application (see Section 4). Due to the time constraints of this research, the study was based on *Very coarse* variants of the $1B$-$1T$ and $1B$-$3T$ meshes presented in Section 6.1.2. Those were created by merging each 8 volume cells of the *Coarse* configuration into 1. The same operating point as the simulations previously presented in this chapter was studied. Prior to the evaluation of rotor flexibility, *rigid* computations based on the *Very coarse* mesh variants were performed and they are presented in Section 6.3.1.

6.3.1 Rigid simulations

First computations assumed a *rigid* blade. Concerning the URANS method, 60 angular positions per revolution were computed. Between each time step, 100 inner flow iterations were performed. In order to allow the development of flow unsteadiness, four complete rotations were simulated before analyzing the solution. Only one harmonic was considered for the NLH simulation, corresponding to the *Blade Passing Frequency* (BPF) for the considered operating point.

Figure 6.23 shows time-averaged loads computed for the *observed blade* by both approaches. As previously observed for the *Coarse* mesh results in Section 6.2.3, the NLH method predicts a lower mechanical power and a higher thrust. When integrating the loads evolution all along the span, relative differences of -3.8 % and 0.5 % were respectively observed. Due to the consideration of a single harmonic, an azimuth independent rotor power and thrust were computed (see Equation 6.6). This is the reason why the *observed blade* transients were analyzed instead (see Figure 6.24). Similar peak-to-valley load variations were computed by both NLH and URANS methodologies. These fluctuations represented approximately 3% of the generated blade thrust and 8% of the mechanical power. A shifting in the computation of the minimum and maximum loads azimuthal position of around 0.15 t/T was also observed for the NLH simulation.

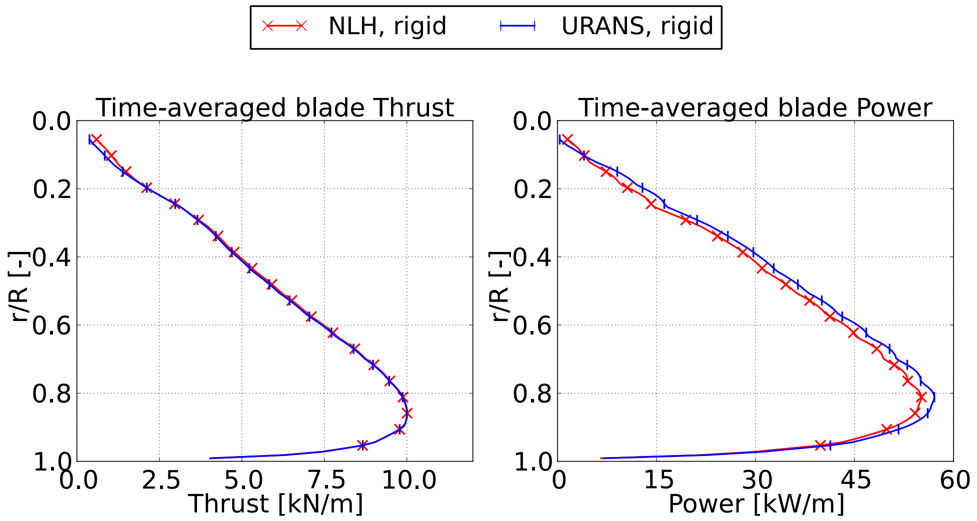

(a) Thrust $[kN/m]$ **(b)** Power $[kW/m]$

Figure 6.23: DTU 10MW RWT, radial evolution of time-averaged blade loads for *rigid* configuration.

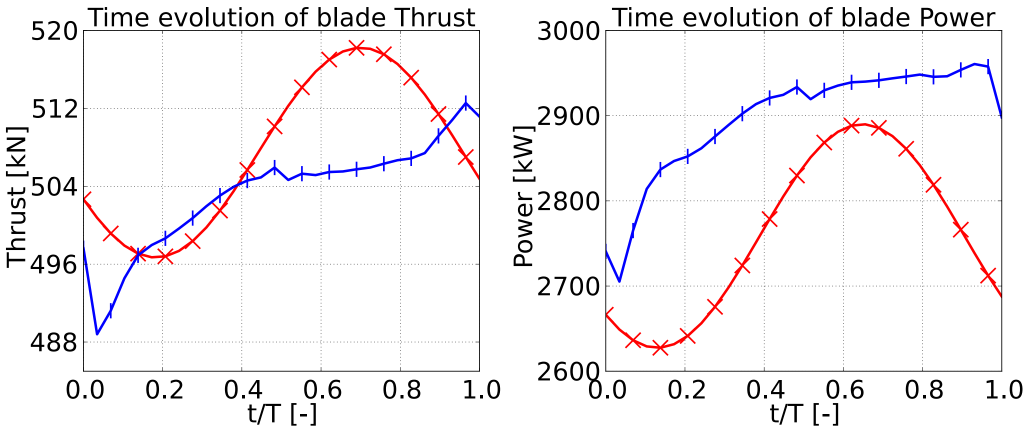

(a) Thrust $[kN]$ **(b)** Power $[kW]$

Figure 6.24: DTU 10MW RWT, *observed blade* loads for *rigid* configuration.

6.3.2 Flexible simulations

For the *flexible* simulations, 2-way coupling computations were performed for both NLH and URANS methods. A simplified version of the blade structural model presented in Section 5.5.1 was used, accounting for a single mode (i.e. the 1st flap). No structural damping was considered, and the mesh deformation was carried out by means of the RBF+TFI approach developed with the scope of this PhD thesis.

Figure 6.25 shows the computed deflections of the *observed blade* axis, both at half span and at the blade tip. A good agreement between URANS and NLH approaches was found in terms of the predicted averaged displacements, with relative differences of around 5% for all the cases. The increase in the averaged deflection predicted by the NLH method is coherent with the *rigid loads* comparison previously shown in Figure 6.24, since the 1st flapping mode is mainly excited by the thrust force. Both methods also predicted similar deformation fluctuations, with relative amplitudes of around 2%. The impact of blade deflection on

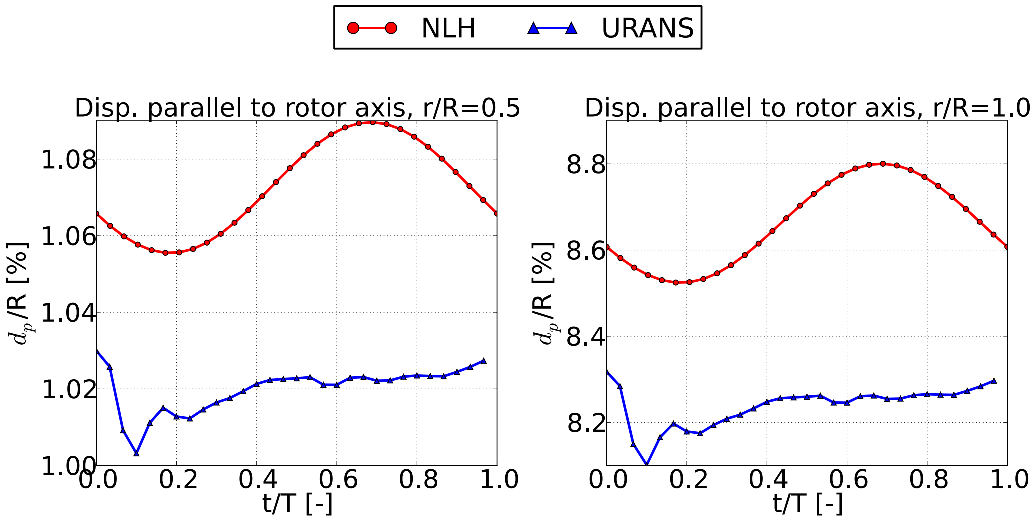

(a) Parallel to rotor axis, r/R=0.5 **(b)** Parallel to rotor axis, r/R=1.0

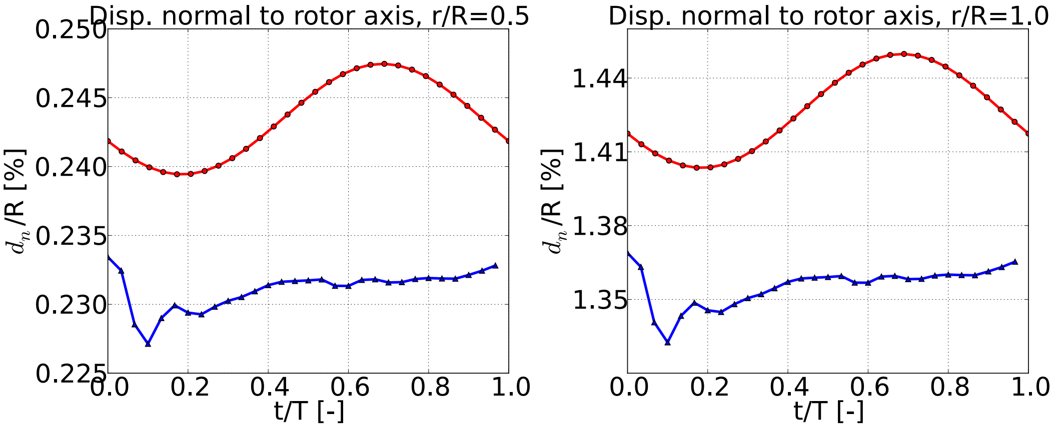

(c) Normal to rotor axis, r/R=0.5 **(d)** Normal to rotor axis, r/R=1.0

Figure 6.25: DTU 10MW RWT, leading edge deformation transients at half span (left) and at blade tip (right). Markers do not represent data sampling

rotor performance is illustrated in Figure 6.26, were *observed blade* loads for both *rigid* and *flexible* approaches are compared. For both NLH and URANS methods, the consideration of blade flexibility results in a decrease in blade averaged mechanical power of around 16%. The decrease on averaged thrust is observed for both methodologies, even if it was found to be more important for the URANS simulation. For this method an approximate relative decrease of 10 % was found, while the NLH approach predicted 5%. For both methodologies, the consideration of blade flexibility also lead into an attenuation of computed load fluctuation amplitudes. However, this effect seemed to be magnified for the harmonic simulation.

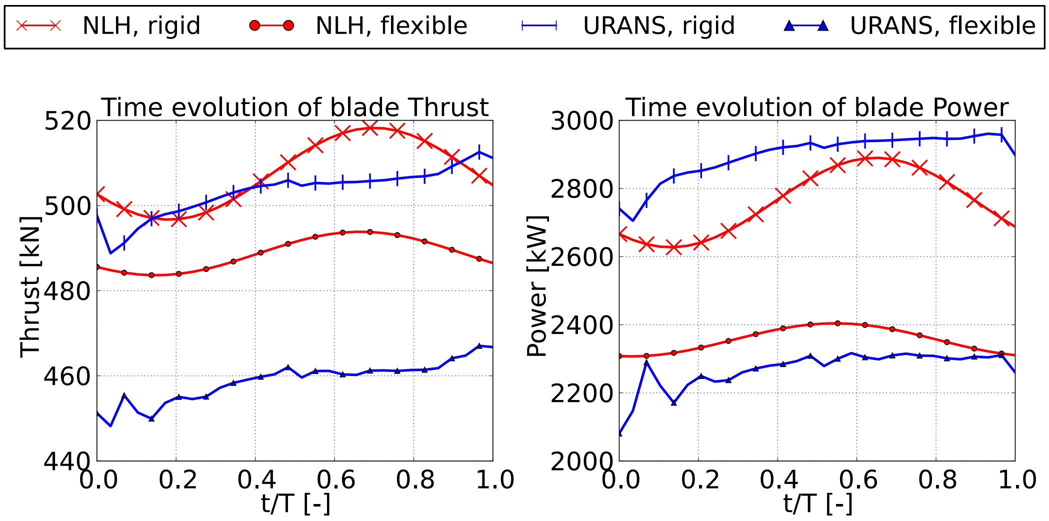

(a) Thrust $[kN]$ **(b)** Power $[kW]$

Figure 6.26: DTU 10MW RWT, *observed blade* loads for *rigid* and *flexible* configurations. Markers do not represent data sampling

6.3.3 Influence of number of modes and harmonics

In order to assess the impact of the considered number of structural modes and harmonics on the NLH FSI 2-way coupling approach, two additional computations were performed. The first one, referred as *2 harmos 1 mode*, accounted for a total number of two harmonics and a structural mode (i.e. the 1^{st} flap). The second one, referred here as *2 harmos 2 modes*, accounted for two harmonics and two structural modes (i.e. the 1^{st} flap and the the 1^{st} edge). Figure 6.27 shows the azimuthal evolution of blade axis deflections at half span and blade tip positions. It can be observed that the consideration of a second harmonic led to a fluctuation pattern closer to the one found by the URANS approach and previously illustrated in Figure 6.25. The position of the predicted displacement peaks and valleys seemed to be improved as well. As expected, the consideration of the 1^{st} edgewise mode had an important impact on the displacement normal to rotor axis. In particular, a relative decrease of 18% was found for the blade tip position, while a 30% was observed at half span. In Figure 6.28, the *observed blade* loads evolution of the performed computations are depicted. While the consideration of an additional harmonic had an impact on the predicted time-averaged loads, the introduction of the edgewise mode did not significantly modified the blade loading.

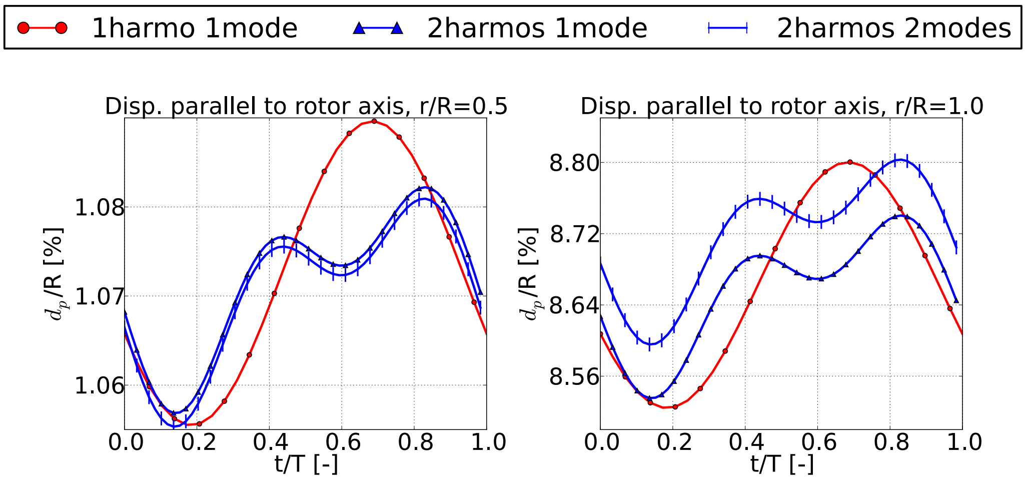

(a) Parallel to rotor axis, r/R=0.5 **(b)** Parallel to rotor axis, r/R=1.0

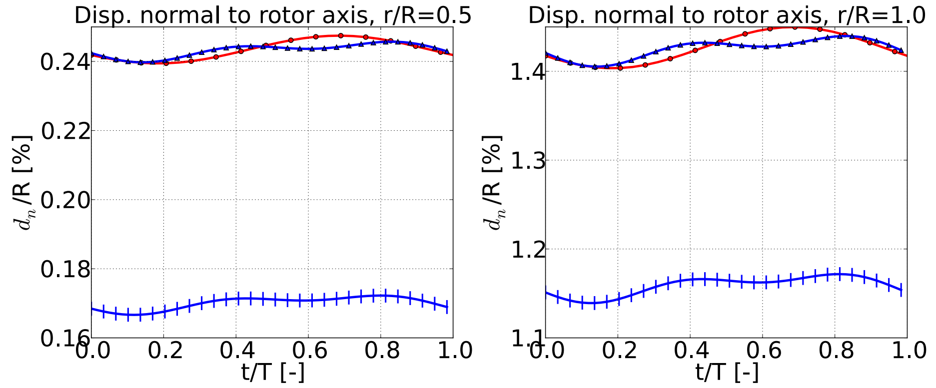

(c) Normal to rotor axis, r/R=0.5 **(d)** Normal to rotor axis, r/R=1.0

Figure 6.27: DTU 10MW RWT, leading edge deformation transients at half span (left) and at blade tip (right) for different NLH method parameters

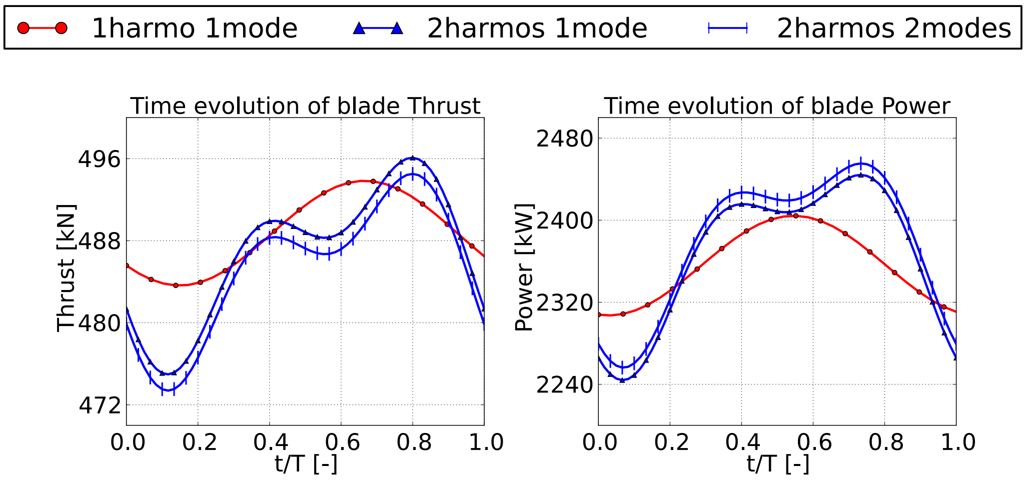

(a) Thrust $[kN]$ **(b)** Power $[kW]$

Figure 6.28: DTU 10MW RWT, *observed blade* loads for different NLH method parameters

6.4 Conclusions and future work

In this chapter, the first complete computational study of a whole HAWT assembly by means of the NLH method was presented. This approach was able to capture the complex unsteady aerodynamics related to the *rotor-tower interactions* of the DTU 10MW RWT reference wind turbine.

First computations assuming a *rigid* rotor were performed. From a global point of view the presence of the tower had a direct impact on rotor performance, justifying the numerical analysis of the *full machine*. Decreases of around 5% for the time-averaged rotor thrust and 8% for the time-averaged power were computed. These reductions are in line with previous studies based on other HAWTs [Carrión (2014); Hsu et al. (2014); Hsu and Bazilevs (2012); Li (2014)]. Local unsteady flow patterns around the whole DTU 10MW RWT assembly were also characterized, including the rotor, the hub, the nacelle and the tower. In particular, both blade and tower *shedding* phenomena were identified. Additionally, the interaction of the blade tip vortex with the tower led to an increase of pressure fluctuations. The results obtained with the NLH method were also compared against the widely used URANS approach. Due to the high computational resources required for the latter method, the benchmark was performed for a coarser grid level. Even if the effect of the mesh discretization did have an impact on the accuracy of the computed results, the comparison showed a fair agreement in the effects captured by both technologies. In terms of computational cost, the NLH method was found to be around 10 times faster than the URANS approach on a coarse mesh. A similar time saving is to be expected when evaluating finer meshes.

From a numerical perspective, two different aspects were found to be particularly constraining for the application of the NLH method. On the one hand, the time and space specificity of the *blade-tower alignment* event is theoretically requiring the use of a high number of harmonics. On the other hand, the modeling of the high frequency *blade shedding* phenomenon observed at low span is needed. In order to independently study both effects and their combined impact on the DTU 10MW RWT performance, three different total loads post-processing were presented (corresponding to the analysis of the *inner* and *outer* halves of the rotor and its whole geometry). Regarding the *blade-tower alignment* event, the study of the *outer* half of the rotor showed similar loads for the computations accounting for 3, 6 and 9 harmonics. A good agreement was also found when comparing the NLH results of this part of the rotor against the URANS methodology. The modeling of the *blade shedding* by means of the NLH method was found to be more challenging. Indeed, only the simulations accounting for a total number of 6 and 9 harmonics were able to capture this high frequency phenomenon. For the former case the main contribution to load fluctuations was performed by the 6th harmonic (0.88 Hz), while for the latter it corresponded to the 5th (0.74 Hz). As an initial explanation for this discrepancy, the truncation effects of the 6 harmonics computation (due to the proximity of the *blade shedding* and cut-off frequencies) were pointed out. This hypothesis was supported by the frequency analysis of the URANS solution, that also located this effect at 0.74 Hz. Moreover, the *Strouhal numbers* related to this harmonic order were found to be in a good agreement the expected value for a cylindrical shape, as previously observed by Le Pape and Lecanu (2004). An important impact on time-averaged loads was also attributed to this unsteady effect, since power reductions up to 22.6% were obtained for the *inner* half of the rotor. The combined effect of *blade-tower alignment* and *blade shedding* could be observed in the time evolution of the *whole rotor* loads. For the simulations accounting for a high number of harmonics, relative fluctuation amplitudes of 1% for the thrust and 2% for the power were computed. This unsteadiness, that can not be captured with isolated rotor simulations, considerably affects final rotor performance. Future work concerning the unsteady aerodynamics of the rigid rotor could assess the influence of the size of the domain in the presented results. In particular, it could be of interest to use a non cylindrical mesh accounting for the geometry of the ground and the atmospheric boundary layer.

Finally, to account for the periodic FSI, the dynamic aeroelasticity of the rotor was assessed by performing preliminary computations on a very coarse mesh. The NLH 2-way coupling approach proposed in Section 4 was successfully compared against *flexible* URANS computations. For both approaches, mean blade deflection was found to have an important impact on computed rotor thrust and mechanical power. Additionally, the consideration of blade flexibility decreased rotor loads fluctuations related to the *blade-tower alignment* event. Future work could be devoted to analyze the generality of these preliminary conclusions by performing dynamic aeroelastic computations on the *fine* grid configuration, and accounting for a complete structural sub-model.

Chapter 7

General conclusions

The presented PhD work focused in the numerical analysis of large rotor *Horizontal Axis Wind Turbine* (HAWT) rotor flows. An initial literature review of the state of the art of numerical methods used in the wind energy sector allowed to identify two important and challenging fields for this research. On the one hand, the low weight and the slenderness of modern wind turbine blades leads to very important blade deflections due to the aerodynamic loading. This requires the consideration of the so-called *Fluid Solid Interactions* (FSI) in the used numerical method. On the other hand, accounting for *rotor-tower interactions* also demands the modeling of flow unsteadiness.

This thesis developed an innovative methodology by extending the capabilities of the *Computational Fluid Dynamics* (CFD) package FINE™/Turbo, edited by NUMECA International. Two new developments were implemented in this solver, aiming to tackle wind turbine rotor analysis problems. On the one hand, a new *mesh deformation* method was developed in order to accommodate wind turbine blades deflection in aeroelastic simulations. On the other hand, a *2-way coupling* FSI methodology to be applied in the study of HAWTs rotors dynamic aeroelasticity was implemented. This development aimed to take into account the combination of both flow unsteadiness and blade flexibility at an affordable computational time.

The development of the new *mesh deformation* methodology was motivated by two particularities inherent to the targeted application. First, the expected blade deflections for large HAWT rotors is significantly more important than the blade deformations observed for turbomachinery applications. Secondly, the size of the CFD mesh of a HAWT rotor use to account for several millions of nodes. While the former issue forced the mesh deformation method to be *robust*, the latter required of an *efficient* approach in order to be computationally affordable. An innovative combination of consolidated technologies allowed to achieve a good trade-off between deformed mesh quality, scalability and computational cost. The developed *hybrid mesh deformation* method for multi-block structured meshes consisted of a first application of the *Radial Basis Function* (RBF), using only the block corners in the interpolation. This allowed to considerably reduce the computational cost attached to the matrix inversion involved in this mesh deformation method when being applied to the whole mesh. The new corner positions were used as an input for the *Transfinite Interpolation* (TFI) in order to generate a deformed mesh of the whole multi-block structured mesh of the CFD domain. The quality of this first deformed mesh could be optionally improved by the application of the *Elastic analogy* (ELA). This last step was only necessary when dealing with large displacements and/or large rotations. The performance of the developed approach was illustrated in Chapter 3 by means of several mesh deformation scenarios, ranging from academic 2D cases to a 3D mesh around the complete AGARD 445.6 wing. For the latter case the computational cost of the traditional RBF approach in the whole mesh was rated as prohibitive, since the inversion of the coefficients matrix required about 25 days. The developed *hybrid deformation* methodology for multi-block structured meshes was found to be a very good alternative for this constraining case. A high quality deformed mesh could be computed in less than 10 minutes, even when dealing with large deflections.

The development of an innovative *2-way coupling* FSI approach in the framework of the *Non-Linear Harmonic* (NLH) method was presented in Chapter 4. A general formulation of the harmonic aeroelastic coupling between the *fluid* and the *structure* physics was proposed. This allowed to reduce the needed computational time with respect to traditional time marching solutions. The mesh deformation was carried out by a harmonic adaptation of the *hybrid mesh deformation* methodology also developed within the scope of this thesis. A complete validation of this new implementation was conducted by studying the *Vortex Induced Vibrations* (VIV) phenomenon of a two-dimensional cylinder in the laminar regime. The cylinder was mounted on a single degree of freedom elastic system, allowing to move transversally to the incoming flow due to the generation of the *vortex shedding*. During this validation, the modeling capabilities of the proposed numerical method were also compared against time marching simulations performed within this PhD work and by other authors. The VIV phenomenon was influenced by both the properties of the flow (the *Reynolds number* and the *Strouhal number*) and the elastic properties of the elastic mounting (the mass, the spring stiffness and the damping ratio). All these factors were interrelated and drove the resulting amplitude of oscillations and the *aeroelastic frequency* (corresponding both to the frequency of oscillation and to the observed flow frequency). Since the *aeroelastic frequency* was not known *prior* to performing the NLH computations, it was identified by means of an iterative *phase error* method. Both *2-way coupling* NLH and time marching methodologies were able to predict the evolution of the cylinder response and the characteristics of the shed wake in the so-called *lock-in zone*. However, small differences were observed with respect to the reference computations, probably related to the effects of the *Reynolds numbers* and to the differences in the prediction of the shedding frequency.

To explore the capabilities of the performed developments in a wind energy context, a comprehensive analysis of the DTU 10MW RWT was carried out. The permutation of structural flexibility and flow unsteadiness modeling lead to four different numerical analyses: *steady aerodynamics*, *static aeroelasticity*, *unsteady aerodynamics* and *dynamic aeroelasticity*. The first two types of simulations were carried out in a *rotor-only* framework, while for the rest the *full machine* was considered (also accounting for the tower geometry).

Steady aerodynamics computations already revealed the complexity of the rotor flow. Important three-dimensional flow patterns were observed around blades and hub geometries. Computed rotor loads were successfully compared against the results from other authors simulations. When performing *static aeroelasticity* computations, the blade structure was linearized by means of its modal shapes and natural frequencies. The *hybrid mesh deformation* method implemented within this PhD work was successfully used in order to deform the whole CFD grid. Blade tip displacements up to 7.78 m were computed, corresponding to 8.73% of the total blade radius. This significant blade deflection had a direct impact on the loads computed at the high span range of the blade. At the maximum studied wind speed, a total reduction of the mechanical power coefficient of 1.34% was found, while the thrust coefficient was decreased by 2.25%. These modifications of the aerodynamic performance induced by the aeroelastic interactions highlight the benefit and the importance of being able to perform efficient simulations accounting for FSI. The same methodology was used in order to study two particular design related problems: the influence of the *Gurney flaps* devices on the rotor performance and the impact of the rotor *pre-bending* and *pre-cone*.

Unsteady aerodynamics computations relied on the *Non-Linear Harmonic* (NLH) approach. This PhD work constituted the first application of such a method in a large rotor HAWT context. The NLH was able to capture the complex unsteady aerodynamics related to the *rotor-tower interactions*. A study of the number of harmonics was performed in order to highlight its influence on the NLH results. From a global point of view, the presence of the tower had a direct impact on rotor performance, justifying the numerical analysis of the *full machine*. Decreases of around 5% of the time-averaged rotor thrust and 8% of the time-averaged rotor power were computed. Local unsteady flow patterns around the whole DTU 10MW RWT assembly were also characterized. In particular, both blade and tower shedding phenomena were identified. The results of the NLH method were also compared against the widely used URANS approach. The comparison showed a fair agreement in the effects captured by both technologies. In terms of computational cost the NLH method was found to be around 10 times faster than the URANS approach, making the NLH simulations affordable to the present industry requirements. Two different aspects were found to be particularly constraining for the application of the NLH method, requiring the use of a considerable number of harmonics. On the one hand, the time and space specificity of the *blade-tower alignment* event. On the other hand, the modeling of the high frequency *blade shedding* phenomenon observed at low span. While the rotor loads decay related to the former issue was already properly estimated with the consideration of 3 harmonics, the modeling of the *blade shedding* effects required 9 harmonics. The combined effect of *blade-tower alignment* and *blade shedding* introduced an important azimuthal dependency on the rotor loads. For the simulations accounting for a high number of harmonics, relative fluctuation amplitudes of 1% for the thrust and 2% for the power were computed. This unsteadiness, that can not be captured with isolated rotor simulations, considerably affects the final rotor performance. Finally, the *2-way coupling* NLH module developed in the scope of this PhD work allowed to perform *dynamic aeroelastic* computations based on a coarse mesh, where the combined effect of flow unsteadiness and blade flexibility was assessed. In the performed preliminary computations, the mean blade deflection was found to have an important impact on the computed rotor thrust and mechanical power (as previously observed in static conditions). Additionally, the consideration of blade flexibility decreased rotor loads fluctuations related to the *blade-tower alignment* event.

This PhD has shown overall a whole computational framework for the design of large rotor HAWTs within the FINE™/Turbo software. It is mainly addressed to wind turbine manufacturers aiming to improve their blades design or to extract detailed aerodynamic information for *extreme* and *fatigue* loads analysis. The developed platform allows to perform both *rotor-only* and *full machine* computations accounting for either *flexible* or *rigid* rotor blades. The reduced computational cost attached to the developed methodology makes it affordable for an industrial use and enables its direct introduction into the wind energy market. This is in line with the aims of the MAREWINT project, that funded this research through a *Marie Skłodowska-Curie* scholarship. Indeed, the use of sophisticated but computationally affordable modeling techniques during the wind turbine design stage can not only reduce the costs associated to its construction, but also improve its reliability. In particular, the study of a given operating point in isolated rotor conditions could be performed in 24 hours with the use of 8 modern processors. Even if the full machine simulations were considerably more costly (5 days on 120 processors), they were found to be one order of magnitude more efficient than traditional time marching CFD approaches. This time saving of the NLH methodology can be attributed to the introduction of a harmonic based solution of both the unsteady flow and the aeroelastic coupling. This PhD work constituted the first experience in the implementation of such an approach for the study of a complete HAWT assembly. Future work could be devoted to extend the presented *dynamic aeroelastic* analysis of the DTU 10MW RWT and to systematically explore the performance of the developed methodology on other wind turbine models. In addition, it could be interesting to include the structural model of the tower in order to analyze a complete flexible assembly.

References

Abedi, H., Davidson, L., and Voutsinas, S. (2013). Vortex method application for aerodynamic loads on rotor blades. In *EWEA 2013*, number February, pages 4–7, Vienna.

Abgrall, R., Dobzrynski, C., and Froehly, A. (2012). A method for computing curved 2D and 3D meshes via the linear elasticity analogy: preliminary results. Technical report, Inria.

Acikgoz, N. and Bottasso, C. L. (2007). A unified approach to the deformation of simplicial and non-simplicial meshes in two and three dimensions with guaranteed validity. *Computers & Structures*, 85(11):944–954.

Acosta, S. and Acosta, P. (2015). Numerical wave scattering taking account of energy dissipation and media stiffness as modeled by the telegraph equation. *Journal on Applied Algebra and Geometry*, 1(2):100–119.

ACUSIM (2009). AcuSolve, General Purpose CFD Software Package.

Adhikari, S. (2000). *Damping models for structural vibration.* PhD thesis, Cambridge University.

Agoes Moelyadi, M. (2006). *Stage Separation Aerodynamics of Future Space Transport Systems*. PhD thesis, Technische Universität München.

Allen, C. B. (2007). Parallel universal approach to mesh motion and application to rotors in forward flight. *International Journal for Numerical Methods in Engineering*, 69:2126–2149.

Amirante, D., Hills, N. J., and Barnes, C. J. (2012). A moving mesh algorithm for aero-thermo-mechanical modelling in turbomachinery. *International Journal for Numerical Methods in Fluids*, 70(9):1118–1138.

Anagnostopoulos, P. and Bearman, P. (1992). Response characteristics of a vortex-excited cylinder at low reynolds numbers. *Journal of Fluids and Structures*, 6(1):39–50.

Arabi, S., Camarero, R., and Guibault, F. (2012). Unstructured Mesh Motion Using Sliding Cells and Mapping Domains. In *20th Annual Conference of the CFD Society of Canada.*

Aranake, A. C. (2013). Computational Analysis of Shrouded Wind Turbine Configurations. In *51st AIAA Aerospace Sciences meeting including the New Horizons Forum and Aerospace Exposition*, Grapevine.

Augarde, C., Ramage, A., and Staudacher, J. (2006). An element-based displacement preconditioner for linear elasticity problems. *Computers & Structures*, 84(31-32):2306–2315.

Azad, A. K., Rasul, M. G., Alam, M. M., Ameer Uddin, S. M., and Mondal, S. K. (2014). Analysis of wind energy conversion system using Weibull distribution. *Procedia Engineering*, 90:725–732.

Backaert, S., Chatelain, P., Wincklemans, G., and DE Visscher, I. (2014). Vortex Particle-Mesh Simulations of Atmospheric Turbulence Effects on Wind Turbine Blade Loading and Wake Dynamics. In Holling, M., Pinke, J., and Ivanell, S., editors, *Wind Energy-Impact of Turbulence*, pages 134–139. Springer, Oldenburg, Germany.

Bak, C., Zahle, F., Bitsche, R., Kim, T., Yde, A., Henriksen, L. C., Natajaran, A., and Hansen, M. H. (2013). Description of the DTU 10 MW Reference Wind Turbine. Technical report, Technical University of Denmark Wind Energy, Roskilde, Denmark.

Baker, T. J. and Carvallo, P. A. (1999). Dynamic adaptation of deforming tetrahedral meshes. In *14th Computational Fluid Dynamics conference*. American Institute of Aeronautics and Astronautics.

Baldwin, B. and Lomax, H. (1978). Thin-layer approximation and algebraic model for separated turbulentflows. In *16th Aerospace Sciences Meeting*, Aerospace Sciences Meetings. American Institute of Aeronautics and Astronautics.

Bar-Yoseph, P. Z., Mereu, S., Chippada, S., and Kalro, V. J. (2001). Automatic monitoring of element shape quality in 2-D and 3-D computational mesh dynamics. *Computational Mechanics*, 27(5):378–395.

Barakos, G., Steijl, R., Badcock, K. J., and Brocklehurst, A. (2005). Development of CFD capability for full helicopter engineering analysis. In *31st European Rotorcraft Forum*.

Barral, N., Luke, E., and Alauzet, F. (2014). Two mesh deformation methods coupled with a changing-connectivity moving mesh method for CFD applications. In *23rd International Meshing Roundatble (IMR)*, volume 00, London, United Kingdom. Elseiver.

Bartels, R. E. (1999). An elasticity-based mesh scheme applied to the computation of unsteady three-dimensional spoiler and aeroelastic problems. In *14th Computational Fluid Dynamics conference AIAA Computational Fluid Dynamics Conference*, Norfolk, USA.

Bartels, R. E. (2005). Finite Macro-Element Mesh Deformation in a Structured Multi-Block Navier-Stokes Code. *NASA Technical Memorandum*, 213789(July).

Batina, J. T. (1989). Unsteady Euler Airfoil Solutions Using Unstructured Dynamic Meshes. In *27th Aerospace Sciences Meeting*, Reno, Nevada. American Institute of Aeronautics and Astronautics.

Bazilevs, Y., Calo, V., Cottrell, J., Hughes, T., Reali, A., and Scovazzi, G. (2007). Variational multiscale residual-based turbulence modeling for large eddy simulation of incompressible flows. *Computer Methods in Applied Mechanics and Engineering*, 197(1-4):173–201.

Bender, J. and Deul, C. (2013). Adaptive cloth simulation using corotational finite elements. *Computers & Graphics*, 37(7):820–829.

Benek, J., Buning, P., and Steger, J. (1985). A 3-D chimera grid embedding technique. In *7th Computational Physics Conference*, Meeting Paper Archive. American Institute of Aeronautics and Astronautics.

Besem, F. M. (2015). *Aeroelastic Instabilities due to Unsteady Aerodynamics*. PhD thesis, Duke University.

Betz, A. (1920). Maximum der theoretisch moglichen Ausnutzung des Windes durch Windmotoren. *Zeitschrift fur das gesamte Turbinenwesen*, 26:307–309.

Biedron, R. and Thomas, J. (2009). Recent Enhancements to the FUN3D Flow Solver for Moving-Mesh Applications. In *47th Aerospace Sciences Meeting including The New Horizons Forum and Aerospace Exposition*, Reston, Virigina. American Institute of Aeronautics and Astronautics.

Bir, G. and Jonkman, J. (2007). Aeroelastic Instabilities of Large Offshore and Onshore Wind Turbines. Technical Report August.

Bishop, R. E. D. and Hassan, A. Y. (1964). The Lift and Drag Forces on a Circular Cylinder Oscillating in a Flowing Fluid. *Proceedings of the Royal Society of London A: Mathematical, Physical and Engineering Sciences*, 277(1368):51–75.

Bisplinghoff, R. L., Ashley, H., and Halfman, R. L. (1995). *Aeroelasticity*. Dover Publication, Inc., Mineola, New York.

Biswas, R. (2005). NASA's Science and Engineering Applications in the Future. In *ZettaFLOPS Forum: Frontiers of Extreme Computing*, Santa Cruz, CA.

Blanc, F., Roux, F.-X., and Jouhaud, J.-C. (2010). Harmonic-Balance-Based Code-Coupling Algorithm for Aeroelastic Systems Subjected to Forced Excitation. *AIAA Journal*, 48(11):2472–2481.

Blom, F. J. (2000). Considerations on the spring analogy. *International Journal for Numerical Methods in Fluids*, 32(6):647–668.

Bos, F. M., van Oudheusden, B. W., and Bijl, H. (2013). Radial basis function based mesh deformation applied to simulation of flow around flapping wings. *Computers & Fluids*, 79:167–177.

Bottasso, C. L. (2011). Short Course on Wind Energy - Introduction to Wind Turbine Aerodynamics. Technical Report November, Politecnico di Milano.

Brandt, A. (1982). Guide to multigrid development. In Hackbusch, W. and Trottenberg, U., editors, *Lecture notes in mathematics*, pages 220–312. Springer, Berlin, Heidelberg.

Burton, T., Sharpe, D., Jenkins, N., and Bossanyi, E. (2001). *WInd energy handbook*. John Wiley & Sons, Ltd, West Sussex, England.

Calaf, M., Meneveau, C., and Meyers, J. (2010). Large eddy simulation study of fully developed wind-turbine array boundary layers. *Physics of Fluids*, 22(1):015110.

Cambier, L. and Gazaix, M. (2002). elsA : An efficient object-oriented solution to CFD complexity. In *40th AIAA Aerospace Sciences Meeting Exhibit*, Aerospace Sciences Meetings, Reno, Nevada. American Institute of Aeronautics and Astronautics.

Campobasso, S., Gigante, F., and Drofelnik, J. (2014a). Turbulent unsteady flow analysis of horizontal axis wind turbine airfoil aerodynamics based on the harmonic balance Reynolds-Averaged Navier-Stokes equations. In *ASME Turbo Expo 2014: turbine technical conference and exposition*, Düsseldrof, Germany. The American Society of Mechanical Engineers.

Campobasso, S., Yan, M., Drofelnik, J., Piskopakis, A., and Caboni, M. (2014b). Compressible Reynolds-Averaged Navier-Stokes analysis of wind turbine turbulent flows using a Fully-Coupled Low-Speed preconditioned multigrid solver. In *ASME Turbo Expo 2014*, Düsseldrof, Germany. The American Society of Mechanical Engineers.

Carrica, P. M., Wilson, R. V., and Stern, F. (2007). An unsteady single-phase level set method for viscous free surface flows. *International Journal for Numerical Methods in Fluids*, 53(2):229–256.

Carrión, M. (2014). *Low Mach Number CFD for Wind Turbine Analysis*. PhD thesis, University of Liverpool.

Carvallo, P. A., Hosangadi, A., Lee, R. A., and Dash, S. M. (1997). Dynamic unstructured grid methodology with application to aero/propulsive flowfields. In *15th Applied aerodynamics conference*. American Institute of Aeronautics and Astronautics.

Chatelain, P., Backaert, S., Winckelmans, G., and Kern, S. (2013). Large eddy simulation of wind turbine wakes. *Flow, Turbulence and Combustion*, 91(3):587–605.

Chiandussi, G., Bugeda, G., and Onate, E. (2000). A simple method for automatic update of finite element meshes. *Communications in Numerical Methods in Engineering*, 16(1):1–19.

Churchfield, M., Lee, S., Moriarty, P., Martinez, L. A., Leonardi, S., Vijayakumarm, G., and Brasseur, J. G. (2012). A Large-Eddy Simulation of Wind-Plant Aerodynamics. In *50th AIAA Aerospace Sciences meeting including the New Horizons Forum and Aerospace Exposition*, number January, pages 1–19, Nashville, Tenessee. American Institute of Aeronautics and Astronautics.

Cole, J. a., Vieira, B. a. O., Coder, J. G., Premi, A., and Maughmer, M. D. (2011). Experimental Investigation into the Effect of Gurney Flaps on Various Airfoils. In *49th AIAA Aerospace Sciences Meeting including the New Horizons Forum and Aerospace Exposition*, pages 1–9, Orlando, USA. American Institute of Aeronautics and Astronautics.

Collar, A. R. (1946). The expanding domain of aeroelasticity. *Journal of the Royal Aeronautical Society*, L(August):613–636.

Corson, D., Griffith, D. T., Ashwill, T., and Shakib, F. (2012). Investigating Aeroelastic Performance of Multi-Mega Watt Wind Turbine Rotors Using CFD. In *53rd AIAA/ASME/ASCE/AHS/ASC Structures, Structural Dynamics and Materials Conference*, Structures, Structural Dynamics, and Materials and Co-located Conferences. American Institute of Aeronautics and Astronautics.

Crosh, E. A., Haldeman, C. W., Dunn, M. G., Holmes, D. G., and Mitchell, B. E. (2009). Investigation of Turbine Shroud Distortions on the Aerodynamics of a One and One-Half Stage High-Pressure Turbine. *ASME Conference Proceedings*, 2009(48883):1–15.

Crosh, E. A., Haldeman, C. W., Dunn, M. G., Holmes, D. G., and Mitchell, B. E. (2011). Investigation of Turbine Shroud Distortions on the Aerodynamics of a One and One-Half Stage High-Pressure Turbine. *Journal of Turbomachinery*, 133(3):031002.

De Boer, A., Van der Schoot, M., and Bijl, H. (2007). Mesh deformation based on radial basis function interpolation. *Computers & Structures*, 85(11-14):784–795.

Debrabandere, F. (2014). *Computational methods for industrial Fluid-Structure Interactions*. PhD thesis, Université de Mons (UMONS).

Debrabandere, F., Tartinville, B., Hirsch, C., and Coussement, G. (2011). Fluid-Structure Interaction Using a Modal Approach. In *ASME 2011 Turbo Expo: Turbine Technical Conference and Exposition*, pages 1263–1269, Vancouver, Canada. American Society of Mechanical Engineers (ASME).

Degand, C. and Farhat, C. (2002). A three-dimensional torsional spring analogy method for unstructured dynamic meshes. *Computers & Structures*, 80(3):305–316.

Ding, L., Lu, Z., and Guo, T. (2014). An Efficient Dynamic Mesh Generation Method for Complex Multi-Block Structured Grid. *Advances in Applied Mathematics and Mechanics*, 6(1):120–134.

Diznabi, B. (2009). Investigation of the flow relation to nacelle anemometry. Technical report, Technical University of Denmark.

Dowell, E. H., Hall, K. C., Thomas, J. P., Kielb, R. E., Spiker, M. A., and Denegri Jr., C. M. (2008). A New Solution Method for Unsteady Flows Around Oscillating Bluff Bodies. In *IUTAM Symposium on Fluid-Structure Interaction in Ocean Engineering*, pages 37–44. Springer.

Dubuc, L., Cantariti, F., Woodgate, M., Gribben, B., Badcock, K. J., and Richards, B. E. (2000). A grid deformation technique for unsteady flow computations. *International journal for numerical methods in fluids*, 32(3):285–311.

Durbin, P. A. (1995). Separated flow computations with the k-epsilon-v-squared model. *AIAA Journal*, 33(4):659–664.

Eça, L. (1999). Orthogonal Generating Systems. In Nigel P . Weatherill, Soni, B. K. ., and Thompson, J. F. ., editors, *Handbook of Grid Generation*. CRC Press.

Elfarra, M. A., Sezer-Uzol, N., and Akmandor, I. S. (2014). NREL VI rotor blade: numerical investigation and winglet design and optimization using CFD. *Wind Energy*, 17(4):605–626.

Fan, Z. and Kang, S. (2009). Numerical simulation of the aerodynamic performance of HAWT. In *EWEC 2009*, pages 1–7, Marseille, France. European Wind Energy Association.

Farhat, C., Degand, C., Koobus, C., and Lesoinne, M. (1998). Torsional springs for two-dimensional dynamic unstructured fluid meshes. *Computer Methods in Applied Mechanics and Engineering*, 163(1):231–245.

Felippa, C. (2016). Introduction to Aerospace Structures (online notes of the Department of Aerospace Engineering Sciences of the University of Colorado at Boulder): http://www.colorado.edu/engineering/CAS/courses.d/Structures.d/.

Felippa, C. A., Park, K. C., and Runtz, J. A. (1977). Stabilization of staggered solution procedures for uid-structure interaction analysis. *Computational methods for uid-structure interaction problems*, pages 95–124.

Fenwick, C. L. and Allen, C. B. (2007). Flutter Analysis of the BACT Wing with Consideration of Control Surface Representation. In *25^{th} AIAA Applied Aerodynamics Conference*.

Fey, U., König, M., and Eckelmann, H. (1998). A new Strouhal-Reynolds-number relationship for the circular cylinder in the range $47 < Re < 2x10^5$. *Physics of Fluids*, 10(7):1547.

Fransson, T. H., Jöcker, M., Bölcs, A., and Ott, P. (1999). Viscous and inviscid linear/nonlinear calculations versus quasi 3D experimental cascade data for a new aeroelastic turbine standard configuration. *Journal of Turbomachinery*, 4(12):717–725.

Fraunhofer Institute for ALgorithms and Scientific Computing (SCAI) (2012). MpCCI User Manual v4.2.1.

Froude, R. E. (1889). On the part played in propulsion by differences of fluid pressure. *Transactions of the Institute of Naval Achitects*, 30:390.

Gao, X.-w., Chen, P.-c., and Tang, L. (2002). Deforming mesh for computational aeroelasticity using a nonlinear elastic boundary element method. *Aerospace Science and Technology journal*, 40(8):1512–1517.

Gaunaa, M., Zahle, F., Sørensen, N. N., Bak, C., and Réthoré, P.-e. (2013). Rotor Performance enhancement using slats on the Inner part of a 10MW rotor. In *EWEA 2013*, Vienna.

Georgii, J. and Westermann, R. (2008). Corotated finite elements made fast and stable. In Faure, F. and Teschner, M., editors, *Workshop in Virtual Reality Interactions and Physical Simulation VRIPHYS*, Grenoble, France.

Gerhold, T. and Neumann, J. (2008). The parallel mesh deformation of the DLR TAU-Code. In *New Results in Numerical and Experimental Fluid Mechanics VI*, pages 162–169. Springer.

Glauert, H. (1935). Aerodynamic Theory: A General Review of Progress Under a Grant of the Guggenheim Fund for the Promotion of Aeronautics. chapter Airplane P, pages 196–360. Springer Berlin Heidelberg, Berlin, Heidelberg.

Gopalakrishnan, P. and Tafti, D. K. (2009). A parallel boundary fitted dynamic mesh solver for applications to flapping flight. *Computers & Fluids*, 38(8):1592–1607.

Gordon, W. J. and Hall, C. A. (1973). Construction of curvilinear co-ordinate systems and applications to mesh generation. *International Journal for Numerical Methods in Engineering*, 7(4):461–477.

Green, B. R., Mathison, R. M., and Dunn, M. G. (2012). Comparison of Harmonic and Time-Marching Unsteady CFD Solutions with measurements for a single stage high-pressure Turbine. In *ASME Turbo Expo 2012*, pages 1–15, Copenhagen. American Society of Mechanical Engineers (ASME).

Griffin, D. a. and Zuteck, M. D. (2001). Scaling of Composite Wind Turbine Blades for Rotors of 80 to 120 Meter Diameter. *Journal of Solar Energy Engineering*, 123(4):310.

Griffin, O., Skop, R., and Koopmann, G. (1973). The vortex-excited resonant vibrations of circular cylinders. *Journal of Sound and Vibration*, 31(2):235–249.

Griffith, D. T. and Ashwill, T. D. (2011). The Sandia 100-meter All-glass Baseline Wind Turbine Blade : SNL100-00. Technical Report SAND2011-3779, Sandia National Laboratories.

Gritskevich, M., Garbaruk, A., Sch ütze, J., and Menter, F. (2012). Development of DDES and IDDES Formulations for the k-ω Shear Stress Transport Model. *Flow, Turbulence and Combustion*, 88(3):431–449.

Guidotti, E. and Turner, M. G. (2009). Analysis of the Unsteady Flow in an Aspirated Counter-Rotating Compressor Using the Nonlinear Harmonic Method. *ASME Conference Proceedings*, pages 685–698.

Hakimi, N. (1997). *Preconditioning methods for time dependent Navier-Stokes equations. Application to Environmental and Low Speed Flows*. PhD thesis, Vrije Universiteit Brussel.

Hall, K. C., Thomas, J. P., and Clark, W. S. (2002). Computation of Unsteady Nonlinear Flows in Cascades Using a Harmonic Balance Technique. *AIAA Journal*, 40(5):879–886.

Hand, M. M., Simms, D. A., Fingersh, L. J., Jager, D. W., Cotrell, J. R., Schreck, S., and Larwood, S. M. (2001). Unsteady Aerodynamics Experiment Phase VI : Wind Tunnel Test Configurations and Available Data Campaigns. Technical Report NREL/TP-500-29955, National Renewable Energy Laboratory (NREL), Golden, CO.

Hansen, M. O. L. (2008). *Aerodynamics of wind turbines*. Earthscan, London, 2edition.

Hansen, M. O. L., Sørensen, J. N., Voutsinas, S., Sørensen, N. N., and Madsen, H. A. (2006). State of the art in wind turbine aerodynamics and aeroelasticity. *Progress in Aerospace Sciences*, 42(4):285–330.

Hau, E. (2006). *Wind Turbines. Fundamentals, Technologies, Application, Economics*. 2edition.

Hauth, M. and Strasser, W. (2004). Corotational Simulation of Deformable Solids. In *The 12th International Conference in Central Europe on Computer Graphics, Visualization and Computer Vision*, pages 2–9.

He, J. and Fu, Z.-F. (2001). *Modal Analysis*. Butterworth Heinemann, Woburn, MA.

He, L. and Ning, W. (1998). Efficient Approach for Analysis of Unsteady Viscous Flows in Turbomachines. *AIAA Journal*, 36(11):2005–2012.

Heege, A., Gaull, A., Horcas, S. G., Bonnet, P., and Defourny, M. (2013). Experiences in controller adaptations of floating wind turbines through advanced numerical simulation. In *AWEA Wind Power Conference*, pages 1–8, Chicago.

Heege, A., Hemmelmann, J., Omiciuolo, M., and Sanchez, J. L. (2011). Comparison of wind turbine component damage computed by linear and fully non-linear fatigue methodologies. In *EWEC 2011*.

Helenbrook, B. T. (2003). Mesh deformation using the biharmonic operator. *International Journal for Numerical Methods in Engineering*, 56(7):1007–1021.

Hembera, M., Loos, A., and Kau, H. (2009). Comparing a 40 Mio Gridpoints Full-Annulus Computation with a 7 Mio Gridpoints Nonlinear Harmonic Computation. In *47th Aerospace Sciences Meeting*, number January, pages 1–14, Orlando, Florida. American Institute of Aeronautics and Astronautics.

Hermansson, J. and Hansbo, P. (2003). A variable diffusion method for mesh smoothing. *Communications in Numerical Methods in Engineering*, 19(11):897–908.

Hess, J. L. (1975). Review of integral-equation techniques for solving potential-flow problems with emphasis on the surface-source method. *Computer Methods in Applied Mechanics and Engineering*, 5(2):145–196.

Hirsch, C. (1990). *Numerical computation of internal and external flows, Volume 2, Computational Methods for inviscid and Viscous flows*. John Wiley & Sons, Ltd, 1edition.

Hirsch, C. (2007). *Numerical computation of internal and external flows, Volume 1: Fundamentals of Computational Fluid Dynamics*. Elseiver, 2edition.

Hoerner, S. F. (1965). *Fluid-Dynamic Drag, Practical information on aerodynamic drag and hydrodynamic resistance*. Hoerner fluid dynamics, Washington D.C.

Horcas, S. G., Debrabandere, F., Tartinville, B., Hirsch, C., and Coussement, G. (2014). Mesh deformation tool for Offshore Wind Turbines fluid-structure interaction. In E. Onate, J. Oliver, and A. Huerta, editors, *11th World Congress on Computational Mechanics*, pages 1–12, Barcelona.

Horcas, S. G., Debrabandere, F., Tartinville, B., Hirsch, C., and Coussement, G. (2015a). A new, high fidelity offshore wind turbines aeroelasticity prediction method with significant CPU time reduction. In *EWEA Offshore 2015*, pages 1–10, Copenhagen. European Wind Energy Association.

Horcas, S. G., Debrabandere, F., Tartinville, B., Hirsch, C., and Coussement, G. (2015b). Hybrid Mesh Deformation Tool for Offshore Wind Turbines Aeroelasticity Prediction. In Ferrer, E. and Montlaur, A., editors, *CFD for Wind and Tidal Offshore Turbines*, Springer Tracts in Mechanical Engineering, chapter 8, pages 83–94. Springer International Publishing.

Horcas, S. G., Debrabandere, F., Tartinville, B., Hirsch, C., and Coussement, G. (2016a). CFD Study of DTU 10MW RWT Aeroelasticity and Rotor-Tower Interactions. In Ostachowicz, W., McGugan, M., Schröder-Hinrichs, J.-U., and Luczac, M., editors, *MARE-WINT, New Materials and Reliability in Offshore WInd Turbine Technology*, chapter 18, pages 309–334. Springer International Publishing, 1 edition.

Horcas, S. G., Debrabandere, F., Tartinville, B., Hirsch, C., and Coussement, G. (2016b). Rotor-tower interactions of DTU 10MW reference wind turbine with a non-linear harmonic method. *Wind Energy*, 20(4):619–636.

Howison, J. and Ekici, K. (2014). Dynamic stall analysis using harmonic balance and correlation-based $\gamma - \overline{Re_{\theta t}}$ transition models for wind turbine. *Wind Energy*.

Hron, J. and Turek, S. (2006). A Monolithic FEM/Multigrid Solver for an ALE Formulation of Fluid-Structure Interaction with Applications in Biomechanics. *Lecture Notes in Computational Science and Engineering*, 53:146–170.

Hsu, M.-C., Akkerman, I., and Bazilevs, Y. (2014). Finite element simulation of wind turbine aerodynamics: validation study using NREL Phase VI experiment. *Wind Energy*, 17:461–481.

Hsu, M.-C. and Bazilevs, Y. (2012). Fluid-structure interaction modeling of wind turbines: simulating the full machine. *Computational Mechanics*, 50(6):821–833.

Hsu, S.-y. and Chang, C.-l. (2007). Mesh deformation based on fully stressed design: the method and 2-D examples. *International Journal for Numerical Methods in Engineering*, 72(5):606–629.

Hsu, S.-Y., Chang, C.-L., and Samareh, J. (2004). A Simplified Mesh Deformation Method Using Commercial Structural Analysis Software. In *10th AIAA/ISMO Multidisciplinary Analaysis and Optimization Conference*, Albany, USA. American Institute of Aeronautics and Astronautics.

Hübner, B., Walhorn, E., and Dinkler, D. (2004). A monolithic approach to fluid-structure interaction using space-time finite elements. *Computer Methods in Applied Mechanics and Engineering*, 193(23-26):2087–2104.

Hughes, T. J., Liu, W. K., and Zimmermann, T. K. (1981). Lagrangian-Eulerian finite element formulation for incompressible viscous flows. *Computer Methods in Applied Mechanics and Engineering*, 29(3):329–349.

Jameson, A. (1991). Time dependent calculations using multigrid, with applications to unsteady flows past airfoils and wings. In *10thComputational Fluid Dynamics Conference*, Fluid Dynamics and Co-located Conferences, pages 1–13. American Institute of Aeronautics and Astronautics, Honolulu, Hi.

Jameson, A., Schmidt, W., and Turkel, E. (1981). Numerical solutions of the Euler equations by finite volume methods using Runge-Kutta time-stepping schemes. *AIAA paper*, pages 1–19.

Jasak, H. and Weller, H. G. (2000). Application of the Finite Volume Method and Unstructured Meshes to Linear Elasticity. *International Journal for Numerical Methods in Engineering*, 48:267–287.

Jeffrey, D., Zhang, X., and Hurst, D. W. (2000). Aerodynamics of Gurney Flaps on a Single-Element High-Lift Wing. *Journal of Aircraft*, 37(2):295–301.

Jeong, J. and Hussain, F. (1995). On the identification of a vortex. *Journal of Fluid Mechanics*, 285:69–94.

Ji, C., Xiao, Z., Wang, Y., and Wang, H. (2011). Numerical investigation on vortex-induced vibration of an elastically mounted circular cylinder at low Reynolds number using the fictitious domain method. *International Journal of Computational Fluid Dynamics*, 25(4):207–221.

Johann, E. and Swoboda, M. (2007). Laminar to turubulent transitional behaviour of the boundary layer obtained from high speed rig test results and 3D-Navier Stokes calculation with transition model. In *ISABE, International Symposium on Air Breathing Engines*, Reston. American Institute of Aeronautics and Astronautics.

Johansen, J., Madsen, H. A., Sørensen, N. N., and Bak, C. (2007). Numerical Investigation of a Wind Turbine Rotor with an aerodynamically redesigned hub-region. Technical report, Risø National Laboratory, Roskilde, Denmark.

Johnson, A. and Tezduyar, T. (1994). Mesh update strategies in parallel finite element computations of flow problems with moving boundaries and interfaces. *Computer methods in applied mechanics and engineering*, 119(1):73–94.

Johnson, M. P. (2003). *Exploiting Quaternions to Support Expressive Interactive Character Motion*. PhD thesis, Massachusetts Institute of Technology.

Jonkman, J. (2010). Definition of the Floating System for Phase IV of OC3. Technical Report NREL/TP-500-47535, National Renewable Energy Laboratory (NREL), Golden, CO.

Jonkman, J., Butterfield, S., Musial, W., and Scott, G. (2009). Definition of a 5-MW reference wind turbine for offshore system development. Technical Report NREL/TP-500-38060, National Renewable Energy Laboratory (NREL), Golden, CO.

Jonkman, J. and Musial, W. (2010). Offshore Code Comparison Collaboration (OC3) for IEA Task 23 Offshore Wind Technology and Deployment. Technical Report NREL/TP-5000-48191, National Renewable Energy Laboratory (NREL).

Jonkman, J., Robertson, A., Popko, W., Vorpahl, F., Zuga, A., Kohlmeier, M., Larsen, T., Yde, A., Saetertro, K., Osktad, K. M., Nichols, J., Nygaard, T. A., Gao, Z., Manolas, D., KIm, K., Yu, Q., Shi, W., Park, H., Vasquez-Rojas, A., Dubois, J., Kaufer, D., Thomassen, P., de Ruiter, M. J., Peeringa, J. M., Zhiwen, H., and von Waaden, H. (2012). Offshore Code Comparison Collaboration Continuation (OC4), Phase I - Results of Coupled Simulations of an Offshore Wind Turbine with Jacket Support Structure. Technical Report NREL/CP-5000-54124, National Renewable Energy Laboratory (NREL).

Jonkman, J. M. and Buhl Jr., M. L. (2007). Development and Verification of a Fully Coupled Simulator for Offshore Wind Turbines. In *NREL/CP-500-40979*, Golden, CO. National Renewable Energy Laboratoty.

Karman Jr., S. L. (2010). Virtual Control Volumes for Two-Dimensional Unstructured Elliptic Smoothing. In *19th International Meshing Roundatble (IMR)*, volume m, pages 121–142.

Kavan, L., Collins, S., Sullivan, C. O., and Zara, J. (2006). Dual Quaternions for Rigid Transformation Blending. Technical report, Trinity College Dublin.

Khalak, A. and Williamson, C. (1999). Motions, forces and mode transitions in vortex-induced vibrations at low mass-damping. *Journal of Fluids and Structures*, 13(7-8):813–851.

Kholodar, D. B., Morton, S. A., and Cummings, R. M. (2005). Deformation of unstructured viscous grids. In *43rd Aerospace Sciences Meeting and Exhibit*. American Institute of Aeronautics and Astronautics.

Klamo, J. T. (2007). *Effects of Damping and Reynolds Number on Vortex-Induced Vibrations*. PhD thesis, California Insititute of Technology.

Ko, J. H., Kim, J. W., Park, S. H., and Byun, D. (2010). Aerodynamic analysis of flapping foils using volume grid deformation code. *Journal of Mechanical Science and Technology*, 23(6):1727–1735.

Koopmann, G. H. (1967). The vortex wakes of vibrating cylinders at low Reynolds numbers. *Journal of Fluid Mechanics*, 28(3):501–512.

Kowollik, D. S. C., Haupt, M. C., and Horst, P. (2013). Mesh deformation with exact surface reconstruction using a reduced radial basis function approach. In Idelsohn, S., Papadrakakis, M., and Schrefler, B., editors, *V International Conference on Computational Methods for Coupled Problems in Science and Engineering*, Ibiza, Spain. Institute of Aircraft Design and Lightweight Structures (IFL).

Kunzelmann, M., Urban, R., Mailach, R., and Vogeler, K. (2011). Active flow control at a 1.5-stage low-speed research compressor with varying rotor tip clearance. *Proceedings of the Institution of Mechanical Engineers, Part A: Journal of Power and Energy*, 225(7):886–896.

Lai, K.-L., Tsai, H.-M., and Liu, F. (2003). Application of Spline Matrix for Mesh Deformation with Dynamic Multi-Block Grids. *21st AIAA Applied Aerodynamics Conference*.

Larsen, T. and Hansen, A. (2007). How to HAWC2, the user's manual.

Larsen, T. J., Hansen, a. M., and Buhl, T. (2004). Aeroelastic effects of large blade deflections for wind turbines. In *The science of making torque from wind*, pages 238–246, Delft.

Launder, B. and Sharma, B. (1974). Application of the energy-dissipation model of turbulence to the calculation of flow near a spinning disc. *Letters in Heat and Mass Transfer*, 1(2):131–137.

Le Pape, A. and Lecanu, J. (2004). 3D Navier-Stokes computations of a stall-regulated wind turbine. *Wind Energy*, 7(4):309–324.

Leble, V., Horcas, S. G., Stäblein, A., and Suarez, J. M. (2015). MARE-WINT D5.4 Assessment report on Fluid-Structure Interaction. Technical report, European Comission, Brussels.

Lefrançois, E. (2008). A simple mesh deformation technique for fluid – structure interaction based on a submesh approach. *International Journal for Numerical Methods in Engineering*, 75(9):1085–1101.

Li, Y. (2014). *Coupled computational fluid dynamics/multibody dynamics method with application to wind turbine simulations*. PhD thesis, University of Iowa.

Liebeck, R. H. (1978). Design of Subsonic Airfoils for High Lift. *Journal of Aircraft*, 15(9):547–561.

Lienhard, J. H. (1966). Synopsis of lift, drag, and vortex frequency data for rigid circular cylinders. Technical report, Washignton State University, Pullman, WA.

Liu, L., Dowell, E. H., and Thomas, J. (2005). Higher Order Harmonic Balance Analysis for Limit Cycle Oscillations in an Airfoil with Cubic Restoring Forces. *46th AIAA/ASME/ASCE/AHS/ASC Structures, Structural Dynamics and Materials Conference*, (April):1–10.

Liu, X., Qin, N., and Xia, H. (2006). Fast dynamic grid deformation based on Delaunay graph mapping. *Journal of Computational Physics*, 211(2):405–423.

Löhner, R., Baum, J. D., Mestreau, E., Sharov, D., Charman, C., and Pelessone, D. (2004). Adaptive embedded unstructured grid methods. *International Journal for Numerical Methods in Engineering*, 60(3):641–660.

Löhner, R. and Yang, C. (1996). Improved ale mesh velocities for moving bodies. *Communications in Numerical Methods in Engineering*, 12:599–608.

Lund, E., Moller, H., and Jakobsen, L. A. (2001). Shape design optimization of steady fluid-structure interaction problems with large displacements. In *19th AIAA Applied Aerodynamics Conference*. American Institute of Aeronautics and Astronautics.

Lynch, C. E. (2011). *Advanced CFD Methods for Wind Turbine Analysis*. PhD thesis, Georgia Institue of Technology.

Lynch, D. R. and O'Neill, K. (1980). Elastic grid deformation for moving boundary problems in two space dimensions. *Finite elements in water resources*, 2.

Markou, G. a., Mouroutis, Z. S., Charmpis, D. C., and Papadrakakis, M. (2007). The ortho-semi-torsional (OST) spring analogy method for 3D mesh moving boundary problems. *Computer Methods in Applied Mechanics and Engineering*, 196(4-6):747–765.

Martineau, D. G. and Georgala, J. M. (2004). A mesh movement algorithm for high quality generalised meshes. In *42nd Aerospace Sciences Meeting and Exhibit*, volume 614, Reno, Nevada. American Institute of Aeronautics and Astronautics.

Maruyama, M., Nakahashi, K., and Matsushima, K. (2002). Unstructured dynamic mesh for large movement and deformation. In *40th Aerospace Sciences Meeting*, Reno, USA. American Institute of Aeronautics and Astronautics.

Masters, J. S. (2011). 2D Mesh Manipulation. Technical Report November, Arnold Engineering Development Center.

Masud, A., Bhanabhagvanwala, M., and Khurram, R. a. (2007). An adaptive mesh rezoning scheme for moving boundary flows and fluid–structure interaction. *Computers & Fluids*, 36(1):77–91.

Matthias, M., Dorsey, J., Mcmillan, L., Jagnow, R., and Cutler, B. (2002). Stable Real-Time Deformations. In *ACM SIGGRAPH/Eurographics symposium on Computer animation*, San Antonio, USA.

McMullen, M., Jameson, A., and Alonso, J. (2006). Demonstration of Nonlinear Frequency Domain Methods. *AIAA Journal*, 44(7):1428–1435.

McMullen, M. S. (2003). *The application of non-linear frequency domain methods to the Euler and Navier-Stokes equations*. PhD thesis, Standford University.

Mehta, D., van Zuijlen, A. H., Koren, B., Holierhoek, J. G., and Bijl, H. (2014). Large Eddy Simulation of wind farm aerodynamics: A review. *Journal of Wind Engineering and Industrial Aerodynamics*, 133:1–17.

Menter, F. (1993). Zonal Two Equation k-w Turbulence Models For Aerodynamic Flows. In *23rd Fluid Dynamics, Plasmadynamics, and Lasers Conference*, Fluid Dynamics and Co-located Conferences. American Institute of Aeronautics and Astronautics.

Menter, F. R. and Kuntz, M. (2004). Adaptation of Eddy-Viscosity Turbulence Models to Unsteady Separated Flow Behind Vehicles. In McCallen, R., Browand, F., and Ross, J., editors, *The Aerodynamics of Heavy Vehicles: Trucks, Buses, and Trains*, pages 339–352. Springer Berlin Heidelberg.

Menter, F. R., Kuntz, M., and Langtry, R. (2003). Ten Years of Industrial Experience with the SST Turbulence Model. *Turbulence Heat and Mass Transfer 4*, 4:625–632.

Merkle, C. L., Sullivan, J. Y., O. Buelow, P. E., and Venkateswaran, S. (1998). Computation of Flows with Arbitrary Equations of State. *AIAA Journal*, 36(4):515–521.

Meyers, J. and Meneveau, C. (2010). Large Eddy Simulations of Large Wind-Turbine Arrays in the Atmospheric Boundary Layer. In *48^{th} Aerospace Sciences Meeting Including the New Horizons Forum and Aerospace Exposition*, pages 1–10, Orlando, Florida. American Institute of Aeronautics and Astronautics.

Mittal, S. and Kumar, V. (2001). Flow-Induced Vibrations of a Light Circular Cylinder At Reynolds Numbers 10^3 to 10^4. *Journal of Sound and Vibration*, 245(5):923–946.

Mohammadi, M. and Doosttalab, A. (2012). The effect of various gurney flap shapes on the performance of wind turbine airfoils. In *ASME Early Career Technical Conference*, volume 11, pages 244–250, Atlanta, Georgia USA. American Society of Mechanical Engineers (ASME).

Morton, S. A. and McDaniel, D. R. (2009). Efficient mesh deformation for computational stability and control analyses on unstructured viscous meshes. In *47^{th} Aerospace Sciences Meeting including the New Horizons Forum and Aerospace Exposition*, Orlando, Florida. American Institute of Aeronautics and Astronautics.

NASA, L. (2015). FUN3D.

Nielsen, E. J. and Anderson, W. K. (2002). Recent improvements in aerodynamic design optimization on unstructured meshes. *American Institute of Aeronautics and Astronautics Journal*, 40(6):1155–1163.

Norberg, C. (2001). Flow around a circular cylinder: Aspects of fluctuating lift. *Journal of Fluids and Structures*, 4(15):459–469.

Nordwall, G., Leduc, M., and Demeulenaere, A. (2008). Unsteady Blade and Disk Resonant Stress Analysis Due to Supersonic Inlet Guide Vane Wakes. In *Volume 5: Structures and Dynamics, Parts A and B*, pages 801–810. American Society of Mechanical Engineers (ASME).

Norris, S. E., Storey, R. C., Stol, K., and Cater, J. E. (2012). Modeling Gusts Moving Through WInd Farms. In *50^{th} AIAA Aerospace Sciences meeting including the New Horizons Forum and Aerospace Exposition*, pages 1–12, Nashville, Tenessee. American Institute of Aeronautics and Astronautics.

NUMECA International (2013a). Autogrid5™ v9.0 User Manual.

NUMECA International (2013b). FINE$^{\text{TM}}$/Turbo v9.0 User Manual.

Orszag, S. A. (1970). Analytical theories of turbulence. *Journal of Fluid Mechanics*, 41(02):363–386.

Paterson, E. G., Wilson, R. V., and Stern, F. (2003). General-purpose parallel unsteady RANS ship hydrodynamics code: CFDSHip-Iowa. Technical report, IIHR, Hydrosience and ENgineering College of Engineering.

Placzek, A., Sigrist, J. F., and Hamdouni, A. (2009). Numerical simulation of an oscillating cylinder in a cross-flow at low Reynolds number: Forced and free oscillations. *Computers and Fluids*, 38(1):80–100.

Potsdam, M. A. and Mavriplis, D. J. (2009). Unstructured Mesh CFD Aerodynamic Analysis of the NREL Phase VI Rotor. In *47th AIAA Aerospace Sciences Meeting Including The New Horizons Forum and Aerospace Exposition*. American Institute of Aeronautics and Astronautics.

Prospathopoulos, J., Politis, E., Chaviaropoulos, P., and Rados, K. (2009). Enhanced CFD modeling of wind turbine wakes. In *Euromech 508 Colloquium on Wind Turbine Wake*, Madrid, Spain.

Prospathopoulos, J. M., Papadakis, G., Sieros, G., Voutsinas, S. G., Chaviaropoulos, T. K., and Diakakis, K. (2014). Assessment of the aerodynamic characteristics of thick airfoils in high Reynolds and moderate Ma numbers using CFD modeling. In *The science of making torque from wind*, Copenhagen, Denmark.

Quaranta, G., Guardone, A., and Muffo, D. (2008). Compressible fluid-flow ALE formulation on changing topology meshes for aeroelastic simulations. In *26th International congress of the aeronautical sciences*, Alaska, USA.

Rankine, W. (1865). On the mechanical principles of the action propellers. *Transactions of the Institute of Naval Achitects*, 6:13.

Rayleigh, L. (1877). *The theory of sound*. Macmilliand and CO, London, United Kingdom.

Resor, B. R. (2013). Definition of a 5MW/61.5m Wind Turbine Blade Reference Model. Technical Report SAND2013-2569, Sandia National Laboratories, Albuquerque, New Mexico.

Robertson, A., Jonkman, J., Musial, W., Vorpahl, F., and Popko, W. (2013). Offshore Code Comparison Collaboration, Continuation : Phase II results of a floating semisubmersible wind system. Technical Report NREL/CP-5000-60600, National Renewable Energy Laboratory (NREL).

Robertson, A., Wendt, F., Jonkman, J., Popko, W., Vorpahl, F., Trygve, C., Bachynski, E. E., Bayati, I., Beyer, F., Vaal, J. B. D., Harries, R., Yamaguchi, A., Kim, B., Zee, T. V. D., Bozonnet, P., Aguilo, B., Bergua, R., Qvist, J., Qijun, W., Chen, X., Guerinel, M., Tu, Y., Yutong, H., Li, R., and Bouy, L. (2015). OC5 Project Phase I : Validation of Hydrodynamic Loading on a Fixed Cylinder. Technical Report NREL/CP-5000-63567, National Renewable Energy Laboratory (NREL).

Sagaut, P. and Deck, S. (2009). Large eddy simulation for aerodynamics: status and perspectives. *Philosophical transactions. Series A, Mathematical, physical, and engineering sciences*, 367(1899):2849–2860.

Sagaut, P., Deck, S., and Terracol, M. (2006). *Multiscale And Multiresolution Approaches in Turbulence*. Imperial College Press, London.

Salcedo, S., Monge, F., Palacios, F., Gandia, F., Rodriguez, A., and Barcala, M. (2006). Gurney flaps and trailing edge devices for wind turbines. In *EWEC 2006*, pages 1–7, Athens, Greece. The European Wind Energy Association (EWEA).

Samareh, J. A. (2002). Application of Quaternions for mesh deformation. In *8th International Conference on Numerical Grid Generation in Computational Field Simulations*, Honolulu, Hawaii.

Sanchez-Rocha, M., Kirtas, M., and Menon, S. (2006). Zonal Hybrid RANS-LES Method for Static and Oscillating Airfoils and Wings. In *44th AIAA Aerospace Sciences Meeting and Exhibit*, Aerospace Sciences Meetings. American Institute of Aeronautics and Astronautics.

Sanderse, B., van der Pijl, S. P., and Koren, B. (2011). Review of computational fluid dynamics for wind turbine wake aerodynamics. *Wind Energy*, 14:799–819.

Sayma, A., Vahdati, M., and Imregun, M. (2000). An integrated nonlinear approach for turbomachinery forced response prediction. Part I: Formulation. *Journal of Fluids and Structures*, 14(1):87–101.

Schepers, J. G., Boorsma, K., Cho, T., Gomez-iradi, S., Schaffarczyk, P., Jeromin, A., Shen, W. Z., Lutz, T., Meister, K., Stoevesandt, B., Schreck, S., Micallef, D., Pereira, R., Sant, T., Madsen, H. a., and Sørensen, N. N. (2012). Final report of IEA Task 29, Mexnext (Phase 1): Analysis of Mexico wind tunnel measurements. Technical report, Energy Research Centre of the Netherlands (ECN).

Schepers, J. G. and Snel, H. (2007). Model Experiments in Controlled Conditions, Final Report. Technical report, Energy research Centre of the Netherlands (ECN).

Schubel, P. J. and Crossley, R. J. (2012). Wind turbine blade design. *Energies*, 5(9):3425–3449.

Shen, W. Z., Sørensen, J. N., and Zhang, J. (2007). Actuator surface model for wind turbine flow computations. In *EWEC*, Milan, Italy. European Wind Energy Association.

Shepard, D. (1968). A two-dimensional interpolation function for irregularly-spaced data. In *23rd national conference*, pages 517–524, New York, USA. Association for Computing Machinery.

Shiels, D., Leonard, A., and Roshko, A. (2001). Flow-induced vibration of a circular cylinder at limiting structural parameters. *Journal of Fluids and Structures*, 15(1):3–21.

Siemens, P. (2015). Virtual Lab, http://www.plm.automation.siemens.com.

Simms, D., Schreck, S., Hand, M., and Fingersh, L. (2001). NREL Unsteady Aerodynamics Experiment in the NASA-Ames Wind Tunnel: A Comparison of Predictions to Measurements. Technical Report June, National Renewable Energy Laboratory (NREL), Golden, CO.

Simulia, D. S. C. (2008). Abaqus Analysis version 6.8 User's Manual.

Smagorinsky, J. (1963). General Circulation Experiments with the Primitive Equations. *Monthly Weather Review*, 91:99.

Smith, A. M. O. and Cebeci, T. (1967). *Numerical Solution of the Turbulent-boundary-layer Equations*. Report - Douglas Aircraft Co., Douglas Aircraft Division. McDonnell Douglas.

Smith, R. E. (1999). Transfinite Interpolation (TFI) Generation Systems. In Weatherill, N. P. ., Soni, B. K. ., and Thompson, J. F. ., editors, *Handbook of Grid Generation*. CRC Press.

Soni, B. (1985). Two- and three-dimensional grid generation for internal flow applications of computational fluid dynamics. In *7th Computational Physics Conference*, Meeting Paper Archive. American Institute of Aeronautics and Astronautics.

Sørensen, J. N. and Shen, W. Z. (2002). Numerical Modeling of Wind Turbine Wakes. *Journal of Fluids Engineering*, 124(2):393–399.

Sørensen, N. N. (1995). *General Purpose Flow Solver Applied to Flow Over Hills*. Risø-R. Risø National Laboratory.

Spalart, P. and Allmaras, S. (1992). A one-equation turbulence model for aerodynamic flows. In *30th Aerospace Sciences Meeting and Exhibit*, Aerospace Sciences Meetings, pages 1–22. American Institute of Aeronautics and Astronautics.

Spalart, P. R., Deck, S., Shur, M. L., Squires, K. D., Strelets, M., and Travin, A. (2006). A New Version of Detached-eddy Simulation, Resistant to Ambiguous Grid Densities. *Theoretical and Computational Fluid Dynamics*, 20(3):181–195.

Spalart, P. R., Jou, W.-H., Strelets, M., and Allmaras, S. (1997). Comments on the feasibility of LES for wings and on a hybrid RANS/LES approach. In *1st AFOSR International Conference on DNS/LES*, pages 137–147, Rouston.

Spekreijse, S. P. (1995). Elliptic grid generation based on Laplace equations and algebraic transformations. *Journal of Computational Physics*, 118(1):38–61.

Spiker, M. A., Kielb, R. E., Thomas, J. P., and Hall, K. C. (2009). Application of Enforced Motion to Study 2-D Cascade Lock-in Effect. In *47th AIAA Aerospace Sciences Meeting Including The New Horizons Forum and Aerospace Exposition*, Orlando, Florida. American Institute of Aeronautics and Astronautics.

Spiker, M. A., Thomas, J. P., Hall, K. C., Kielb, R. E., and Dowell, E. H. (2006). Modeling cylinder flow vortex shedding with enforced motion using a harmonic balance approach. In *47th AIAA/ASME/ASCE/AHS/ASC Structures, Structural Dynamics, and Materials Conference*, number May, Newport, Rhode Island. American Institute of Aeronautics and Astronautics.

Stadler, D., Kosel, F., Damjan, C., and Lipej, A. (2011). Mesh deformation based on artificial neural networks. *International Journal of Computational Fluid Dynamics*, 25(8):439–448.

Stein, K., Tezduyar, T., and Benney, R. (2003). Mesh moving techniques for fluid-structure interactions with large displacements. *ASME Journal of Applied Mechanics*, 70(1):58.

Storms, B. L. and Jang, C. S. (1994). Lift enhancement of an airfoil using a Gurney flap and vortex generators. *Journal of Aircraft*, 31(3):542–547.

Suárez, J. M. and Doerffer, P. (2015). CFD validated technique for prediction of aerodynamic characteristics on horizontal axis wind energy turbines. In *EWEA Offshore 2015*, pages 1–10, Copenhagen.

Suárez, J. M., Doerffer, P., Szulc, O., and Tejero, F. (2015). Aerodynamic analysis of wind turbine rotor blades. *Task Quarterly*, 19(2):129–140.

Sumner, J., Watters, C. S., and Masson, C. (2010). CFD in wind energy: The virtual, multi-scale wind tunnel. *Energies*, 3(5):989–1013.

Tanida, Y., Okajima, A., and Watanabe, Y. (1973). Stability of a circular cylinder oscillating in uniform flow or in a wake. *Journal of Fluid Mechanics*, 61(04):769–784.

Thomas, J., Dowell, E. H., Hall, K., and Denegri, C. (2004). Modeling Limit Cycle Oscillation Behavior of the F-16 Fighter Using a Harmonic Balance Approach. *45th AIAA/ASME/ASCE/AHS/ASC Structures, Structural Dynamics & Materials Conference*, (April).

Thomas, J., Dowell, E. H., Hall, K., and Denegri, C. (2005). Further investigation of modeling limit cycle oscillation behavior of the F-16 Fighter using a harmonic balance approach. *American Institute of Aeronautics and Astronautics Journal.*

Thomas, J. P., Dowell, E. H., and Hall, K. C. (2002). Nonlinear inviscid aerodynamic effects on transonic divergence, flutter, and limit-cycle oscillations. *AIAA Journal*, 40(4):638–646.

Thomson, L. M. M. (1966). *Theoretical Aerodynamics*. Dover Publication, New York, USA.

Timmer, W. and van Rooij, R. (2003). Summary of the Delft University Wind Turbine Dedicated Airfoils. In *41st Aerospace Sciences Meeting and Exhibit*, pages 1–11, Reno, Nevada USA. American Institute of Aeronautics and Astronautics.

Timoshenko, S. (1921). On the correction factor for shear of the differential equation for transverse vibrations of bars of uniform cross-section. *Philosphical Magazine*, page 744.

Timoshenko, S. (1953). *History of strength of materials*. McGraw-Hill, New York, USA.

Troldborg, N., Zahle, F., and Sørensen, N. N. (2015). Simulation of a MW rotor equipped with vortex generators using CFD and an actuator shape model. In *53rd AIAA Aerospace Sciences Meeting*, Kissimmee, Florida. American Institute of Aeronautics and Astronautics.

Troolin, D., Longmire, E., and Lai, W. (2006). Time-resolved PIV analysis of flow over a NACA 0015 airfoil with gurney flap. *Experiments in Fluids*, 41(2):1–17.

Truong, a. H., Oldfield, C. a., and Zingg, D. W. (2008). Mesh Movement for a Discrete-Adjoint Newton-Krylov Algorithm for Aerodynamic Optimization. *American Institute of Aeronautics and Astronautics Journal*, 46(7):1695–1704.

Tsai, H. M., Wong, A. S. F., Cai, J., Zhu, Y., and Liu, F. (2001). Unsteady flow calculations with a parallel multiblock introduction. *American Institute of Aeronautics and Astronautics Journal*, 39(6).

UpWind Consortium (2011). Design limits and solutions for very large wind turbines. Technical report, European Wind Energy Association (EWEA), Roskilde, Denmark.

Vilmin, S., Lorrain, E., Hirsch, C., and Swoboda, M. (2006). Unsteady Flow Modeling Across the Rotor/Stator Interface Using the Nonlinear Harmonic Method. In *ASME Turbo Expo 2006*, pages 1–11, Barcelona.

Wang, Q. and Hu, R. (2012). Adjoint-based optimal variable stiffness mesh deformation strategy based on bi-elliptic equations. *International Journal for Numerical Methods in Engineering*, 2012(90):659–670.

Wang, Q., Zhou, H., and Wan, D. (2012). Numerical simulation of wind turbine blade-tower interaction. *Journal of Marine Science and Application*, 11(3):321–327.

Weller, H. G., Tabor, G., Jasak, H., and Fureby, C. (1998). A tensorial approach to computational continuum mechanics using object-oriented techniques. *Computers in Physics*, 12(6):620–631.

Wick, T. (2011). Fluid-structure interactions using different mesh motion techniques. *Computers & Structures*, 89(13-14):1456–1467.

Wieselberger, C. (1921). Neuere Feststellungen Über die Gesetze des Flüssigkeits Luftwiderstands. *Phys. Z*, 22:321–328.

Wilcox, D. C. (1988). Reassessment of the scale-determining equation for advanced turbulence models. *American Institute of Aeronautics and Astronautics Journal*, 26(11):1299–1310.

Williamson, C. (1996). Vortex Dynamics in the Cylinder Wake. *Annu. Rev. Fluid. Mech.*, 28:477–539.

Williamson, C. and Govardhan, R. (2004). Vortex-Induced Vibrations. *Annual Review of Fluid Mechanics*, 36(1):413–455.

Winslow, A. M. (1981). Adaptive-mesh zoning by the equipotential method. Technical report, Lawrence Livermore Laboratory.

Wirz, R. E. and Johnson, P. M. (2011). Aero-Structural Performance of Multiplane Wind Turbine Blades. In *29th AIAA Applied Aerodynamics Conference*, number June, Honolulu, Hawaii. American Institute of Aeronautics and Astronautics.

Witteveen, J. A. S. (2010). Explicit and Robust Inverse Distance. In *48th Aerospace Sciences Meeting Including the New Horizons Forum and Aerospace EXposition*, Orlando, Florida. American Institute of Aeronautics and Astronautics.

Yamazaki, W., Mouton, S., and Carrier, G. (2010). Geometry Parameterization and Computational Mesh Deformation by Physics-Based Direct Manipulation Approaches. *American Institute of Aeronautics and Astronautics Journal*, 48(8):1817–1832.

Yang, Z. and Mavriplis, D. J. (2005). Unstructured dynamic meshes with higher-order time integration schemes for the unsteady Navier-Stokes equations. In *41st Aerospace Sciences Meeting and Exhibit*, Reno, USA. American Institute of Aeronautics and Astronautics.

Yates, E. C. (1987). AGARD standard aeroelastic configurations for dynamic response. Candidate configuration I.-wing 445.6. NASA-TM-1000492. Technical report, NASA.

Yelmule, M. and Anjuri, E. (2013). CFD predictions of NREL Phase VI Rotor Experiments in NASA/AMES Wind tunnel. *International Journal of Renewable Energy Research*, 3(2):261–270.

Yigit, S., Schäfer, M., and Heck, M. (2008). Grid movement techniques and their influence on laminar fluid-structure interaction computations. *Journal of Fluids and Structures*, 24(6):819–832.

Yu, D. O. and Kwon, O. J. (2014). Predicting wind turbine blade loads and aeroelastic response using a coupled CFD-CSD method. *Renewable Energy*, 70:184–196.

Zahle, F., Bak, C., Bitsche, R., Kim, T., Hansen, M. H., Yde, A., and Rethore, P. E. (2013). Towards an Integrated Design Complex for Wind Turbines. Design of a 10MW Reference Turbine. Technical report, DTU Wind Energy , Department of Wind Energy.

Zahle, F., Bak, C., Guntur, S., Sørensen, N. N., and Troldborg, N. (2014). Comprehensive aerodynamic analysis of a 10 MW wind turbine rotor using 3D CFD. In *32^{nd} ASME Wind Energy Symposium*, pages 1–15, Maryland, USA. American Institute of Aeronautics and Astronautics.

Zahle, F. and Sørensen, N. N. (2008). Overset grid flow simulation on a modern wind turbine. In *26^{th} Applied Aerodynamics Conference*, Honololulu. American Institute of Aeronautics and Astronautics.

Zahle, F. and Sørensen, N. N. (2011). Characterization of the unsteady flow in the nacelle region of a modern wind turbine. *Wind Energy*, 14(2):271–283.

Zahle, F., Sørensen, N. N., and Johansen, J. (2009). Wind turbine rotor-tower interaction using an incompressible overset grid method. *Wind Energy*, 12(6):594–619.

Zeng, D. and Ethier, C. R. (2005). A semi-torsional spring analogy model for updating unstructured meshes in 3D moving domains. *Finite Elements in Analysis and Design*, 41(11):1118–1139.

Zhou, X. and Li, S. (2013). A new mesh deformation method based on disk relaxation algorithm with pre-displacement and post-smoothing. *Journal of Computational Physics*, 235:199–215.

Zhu, Y., Joseph Teran, E. S., and Brandt, A. (2010). An efficient multigrid method for the simulation of high-resolution elastic solids. *ACM Trans. Graph.*, 29(2):16:1—-16:18.

Zhu, Z., Lacor, C., and Hirsch, C. (1993). A new residual smoothing method for multigrid, multi-stage schemes. In *AIAA 11^{th} Computational Fluid Dynamics Conference*, Fluid Dynamics and Co-located Conferences, pages 657–665, Orlando,FL. American Institute of Aeronautics and Astronautics.

Appendix A

Numerical set-up of previous HAWT CFD studies

Table A.1 summarizes the computational set-up of the wind turbine CFD computations mentioned in the literature review of Section 2.1.6. The acronyms used, ordered by columns, are presented below:

- **WP: Working points**
  - FL: Flutter analysis
  - NOP: Normal operation
  - SS: Standstill
  - YM: Yaw misalignment
- **Type: Simulation type**
  - st: Static simulations
  - dyn: Dynamic simulations
- **Fluid: Flow numerical model**
  - Numerical method
    - ALE: Arbitrary Lagrangian Eulerian formulation [Hughes et al. (1981)]
    - DDES: Delayed Detached Eddy simulation [Spalart et al. (2006)]
    - DDES-SST: Delayed detached eddy simulation based on k-ω SST [Gritskevich et al. (2012)]
    - DES-SST: Zonal detached eddy simulation [Menter and Kuntz (2004)]
    - HR-LES: Zonal hybrid RANS/LES approach [Sanchez-Rocha et al. (2006)]
    - VMS: Residual-based variational multiscale formulation of the Navier–Stokes equations and turbulence modeling [Bazilevs et al. (2007)]
  - Turbulence models

    - ∗ k-ε: Turbulence model of Launder and Sharma (1974)
    - ∗ k-ω: Turbulence model of Wilcox (1988)
    - ∗ k-ω SST: Turbulence model of Menter (1993)
    - ∗ SA: *Spalart-Allmaras* turbulence model of Spalart and Allmaras (1992)

- **Struct.: Blade structural model**
  - BEAM: Non-linear beam-based structural model
  - IGA: NURBS-based *Isogeometric Analysis*
  - MBD: Multi-Body Dynamics
  - ROM: Reduced Order Model of the blade, represented by its natural frequencies and mode shapes
- **Def.: Mesh deformation algorithms**
  - DO: Dynamic overset [Carrica et al. (2007)]
  - ELA: Elastic analogy
  - TFI: Transfinite Interpolation
  - N/A: Not applicable
  - SPRA: Spring Analogy

Table A.1: Summary of the computational set-up for the HAWT simulations presented in Section 2.1.6

HAWT	Author/s	Solvers	Mesh	WP	Type	Fluid	Struct.	Def.
NREL PHASE VI	Le Pape and Lecanu (2004)	elsA	1 blade	NOP	st	RANS, k-ω SST	Rigid	N/A
	Le Pape and Lecanu (2004)	elsA	1 blade	NOP	dyn	URANS, k-ω SST	Rigid	N/A
	Zahle et al. (2009)	Ellypsis3D	2 rotor blades and tower	NOP	dyn	URANS, k-ω	Rigid	N/A
	Lynch (2011)	FUN3D	2 blades, nacelle and tower	NOP	dyn	URANS, k-ω SST	Rigid	N/A
	Lynch (2011)	FUN3D	2 blades, nacelle and tower	NOP,YM	dyn	HR-LES	Rigid	N/A
	Wang et al. (2012)	OpenFoam	2 blades, nacelle and tower	NOP	dyn	URANS, k-ω SST	Rigid	N/A
	Hsu et al. (2014)	In-house	2 blades	NOP	st	ALE-VMS	Rigid	N/A
	Hsu et al. (2014)	In-house	2 blades, nacelle and tower	NOP	dyn	ALE-VMS	Rigid	N/A
	Li (2014)	CFDShip-Iowa	2 blades, approx. nacelle, approx.tower	NOP	dyn	URANS, k-ω SST	Rigid	N/A
	Li (2014)	CFDShip-Iowa	2 blades, approx. nacelle, approx.tower	NOP	dyn	DDES-SST	Rigid	N/A
	Carrión (2014)	HMB2	2 blades, nacelle and tower	NOP	dyn	URANS, k-ω SST	ROM	SPRA+TFI

Continued on next page…

HAWT	Author/s	Solvers	Mesh	WP	Type	Fluid	Struct.	Def.
	Fan and Kang (2009)	FINE™/Turbo	1 blade (infinite hub)	NOP	st	RANS, SA & k-ω SST	Rigid	N/A
	Elfarra et al. (2014)	FINE™/Turbo	1 blade (infinite hub)	NOP	st	RANS, k-ε	Rigid	N/A
	Suárez and Doerffer (2015); Suárez et al. (2015)	FINE™/Turbo	1 blade (infinite hub)	NOP	st	RANS, SA & k-ω SST	Rigid	N/A
MEXICO	Carrión (2014)	HMB2	1 blade (infinite hub)	NOP	st	RANS, k-ω	BEAM	SPRA+TFI
NREL 5MW	Hsu and Bazilevs (2012)	In-house	3 blades, nacelle and tower	NOP	dyn	ALE-VMS	IGA	ELA
	Yu and Kwon (2014)	In-house	1 blade	NOP	st	RANS, k-ω SST	BEAM	SPRA
	Yu and Kwon (2014)	In-house	3 blades, approx. nacelle, tower	NOP	dyn	URANS, k-ω SST	BEAM	SPRA
	Li (2014)	CFDShip-Iowa	3 blades, approx. nacelle, tower and spar buoy	NOP	dyn	URANS, k-ω SST	MBD	DO
SNL-100-00	Corson et al. (2012)	AcuSolve	1 blade, approx, nacelle	NOP	st	RANS, SA	ROM	ELA
	Corson et al. (2012)	AcuSolve	1 blade, approx. nacelle	FL	dyn	DDES	ROM	ELA
DTU 10MW RWT	Zahle et al. (2014)	Ellypsis3D	3 blades (no prebending, no precone)	NOP	st	RANS, k-ω SST	Rigid	N/A

Continued on next page…

HAWT	Author/s	Solvers	Mesh	WP	Type	Fluid	Struct.	Def.
	Zahle et al. (2014)	Ellypsis3D	1 blade (no prebending, no precone)	SS+YM	dyn	DES-SST	Rigid	N/A
SIEMENS 3.6MW	Zahle and Sørensen (2008)	Ellypsis3D	3 blades and tower	NOP	dyn	URANS, k-ω	Rigid	N/A
NKT 500/41	Zahle and Sørensen (2011)	Ellypsis3D	3 rotor blades and nacelle	NOP	st	RANS, k-ω-SST	Rigid	N/A
	Zahle and Sørensen (2011)	Ellypsis3D	3 rotor blades and nacelle	NOP,YM	dyn	URANS, k-ω-SST	Rigid	N/A

Concluded

Appendix B

NLH formulation

In this appendix, the derivation of the baseline NLH formulation is detailed. Let start by considering the unsteady *Reynolds-Averaged Navier-Stokes* equations presented in Section 2.1.2, where the indexes issued from the Reynolds averaging were removed for the sake of simplicity:

$$\frac{\partial}{\partial t}\int_{\Omega} U d\Omega + \oint_{S} \left(\vec{F}_I - \vec{F}_V\right) \cdot d\vec{S} = \int_{\Omega} Q d\Omega \tag{B.1}$$

with:

$$U = \begin{pmatrix} \rho \\ \rho v_x \\ \rho v_y \\ \rho v_z \\ \rho E \end{pmatrix}, \vec{F}_I = \begin{pmatrix} \rho\vec{v} \\ \rho\vec{v}v_x + p\vec{e}_x \\ \rho\vec{v}v_y + p\vec{e}_y \\ \rho\vec{v}v_z + p\vec{e}_z \\ \rho\vec{v}E + p\vec{v} \end{pmatrix}, \vec{F}_V = \begin{pmatrix} 0 \\ \tau_{xx}\vec{e}_x + \tau_{xy}\vec{e}_y + \tau_{xz}\vec{e}_z \\ \tau_{xy}\vec{e}_x + \tau_{yy}\vec{e}_y + \tau_{yz}\vec{e}_z \\ \tau_{xz}\vec{e}_x + \tau_{yz}\vec{e}_y + \tau_{zz}\vec{e}_z \\ \boldsymbol{\tau}\vec{v} + \vec{q} \end{pmatrix} \tag{B.2}$$

Decomposing every variable into time-mean and harmonic contributions:

$$
\begin{aligned}
&\frac{\partial}{\partial t}\int_{\Omega}\begin{pmatrix} \overline{\rho}+\rho' \\ \overline{\rho v_x}+(\rho v_x)' \\ \overline{\rho v_y}+(\rho v_y)' \\ \overline{\rho v_z}+(\rho v_z)' \\ \overline{\rho E}+(\rho E)' \end{pmatrix} d\Omega \\
&+\oint_S \begin{pmatrix} \overline{\rho\vec{v}}+(\rho\vec{v})' \\ \left(\overline{\rho\vec{v}}+(\rho\vec{v})'\right)\left(\overline{v_x}+v_x'\right)+\left(\overline{p}+p'\right)\vec{e}_x \\ \left(\overline{\rho\vec{v}}+(\rho\vec{v})'\right)\left(\overline{v_y}+v_y'\right)+\left(\overline{p}+p'\right)\vec{e}_y \\ \left(\overline{\rho\vec{v}}+(\rho\vec{v})'\right)\left(\overline{v_z}+v_z'\right)+\left(\overline{p}+p'\right)\vec{e}_z \\ \left(\overline{\rho E}+(\rho E)'\right)\left(\overline{\vec{v}}+\vec{v}'\right)+\left(\overline{p}+p'\right)\left(\overline{\vec{v}}+\vec{v}'\right) \end{pmatrix}\cdot d\vec{S} \\
&-\oint_S \begin{pmatrix} 0 \\ \left(\overline{\tau_{xx}}+\tau_{xx}'\right)\vec{e}_x+\left(\overline{\tau_{xy}}+\tau_{xy}'\right)\vec{e}_y+\left(\overline{\tau_{xz}}+\tau_{xz}'\right)\vec{e}_z \\ \left(\overline{\tau_{xy}}+\tau_{xy}'\right)\vec{e}_x+\left(\overline{\tau_{yy}}+\tau_{yy}'\right)\vec{e}_y+\left(\overline{\tau_{yz}}+\tau_{yz}'\right)\vec{e}_z \\ \left(\overline{\tau_{xz}}+\tau_{xz}'\right)\vec{e}_x+\left(\overline{\tau_{yz}}+\tau_{yz}'\right)\vec{e}_y+\left(\overline{\tau_{zz}}+\tau_{zz}'\right)\vec{e}_z \\ \left(\overline{\boldsymbol{\tau}}+\boldsymbol{\tau}'\right)\left(\overline{\vec{v}}+\vec{v}'\right)+\left(\overline{\vec{q}}+\vec{q}'\right) \end{pmatrix}\cdot d\vec{S} \\
&=\int_{\Omega}\left(\overline{Q}+Q'\right)d\Omega
\end{aligned}
\tag{B.3}
$$

Performing intermediate multiplications:

$$
\begin{aligned}
&\frac{\partial}{\partial t}\int_{\Omega}\begin{pmatrix} \bar{\rho}d\Omega+\rho' d\Omega \\ \overline{\rho v_x}d\Omega+(\rho v_x)'d\Omega \\ \overline{\rho v_y}d\Omega+(\rho v_y)'d\Omega \\ \overline{\rho v_z}d\Omega+(\rho v_z)'d\Omega \\ \overline{\rho E}d\Omega+(\rho E)'d\Omega \\ \end{pmatrix} \\
&+\oint_S\begin{pmatrix} \overline{\rho\vec{v}}d\vec{S}+(\rho\vec{v})'d\vec{S} \\ \overline{\rho\vec{v}}\,\overline{v_x}d\vec{S}+\overline{\rho\vec{v}}v'_x d\vec{S}+(\rho\vec{v})'\,\overline{v_x}d\vec{S}+(\rho\vec{v})'\,v'_x d\vec{S}+\bar{p}dS_x+p'dS_x \\ \overline{\rho\vec{v}}\,\overline{v_y}d\vec{S}+\overline{\rho\vec{v}}v'_y d\vec{S}+(\rho\vec{v})'\,\overline{v_y}d\vec{S}+(\rho\vec{v})'\,v'_y d\vec{S}+\bar{p}dS_y+p'dS_y \\ \overline{\rho\vec{v}}\,\overline{v_z}d\vec{S}+\overline{\rho\vec{v}}v'_z d\vec{S}+(\rho\vec{v})'\,\overline{v_z}d\vec{S}+(\rho\vec{v})'\,v'_z d\vec{S}+\bar{p}dS_z+p'dS_z \\ \overline{\rho E}\bar{\vec{v}}d\vec{S}+\overline{\rho E}\vec{v}'d\vec{S}+(\rho E)'\,\bar{\vec{v}}d\vec{S}+(\rho E)'\,\vec{v}'d\vec{S}+\bar{p}\bar{\vec{v}}d\vec{S}+\bar{p}\vec{v}'d\vec{S}+p'\bar{\vec{v}}d\vec{S}+p'\vec{v}'d\vec{S} \end{pmatrix} \\
&-\oint_S\begin{pmatrix} 0 \\ \overline{\tau_{xx}}dS_x+\tau'_{xx}dS_x+\overline{\tau_{xy}}dS_y+\tau'_{xy}dS_y+\overline{\tau_{xz}}dS_z+\tau'_{xz}dS_z \\ \overline{\tau_{xy}}dS_x+\tau'_{xy}dS_x+\overline{\tau_{yy}}dS_y+\tau'_{yy}dS_y+\overline{\tau_{yz}}dS_z+\tau'_{yz}dS_z \\ \overline{\tau_{xz}}dS_x+\tau'_{xz}dS_x+\overline{\tau_{yz}}dS_y+\tau'_{yz}dS_y+\overline{\tau_{zz}}dS_z+\tau'_{zz}dS_z \\ \bar{\boldsymbol{\tau}}\bar{\vec{v}}d\vec{S}+\bar{\boldsymbol{\tau}}\vec{v}'d\vec{S}+\boldsymbol{\tau}'\bar{\vec{v}}d\vec{S}+\boldsymbol{\tau}'\vec{v}'d\vec{S}+\bar{\vec{q}}d\vec{S}+\vec{q}'d\vec{S} \end{pmatrix} \\
&=\int_{\Omega}\bar{Q}d\Omega+Q'd\Omega
\end{aligned}
\tag{B.4}
$$

B.1 Time-mean equations

To derive the NLH mean equations, we consider the time-averaged of Equation B.4:

$$\begin{gathered}\frac{\partial}{\partial t}\int_{\Omega}\begin{pmatrix}\bar{\rho}d\Omega\\ \overline{\rho v_x}d\Omega\\ \overline{\rho v_y}d\Omega\\ \overline{\rho v_z}d\Omega\\ \overline{\rho E}d\Omega\\ \end{pmatrix}+\oint_S\begin{pmatrix}\overline{\rho}\vec{v}d\vec{S}\\ \overline{\rho}\vec{v}\overline{v_x}d\vec{S}+\overline{(\rho\vec{v})'\,v'_x}d\vec{S}+\bar{p}dS_x\\ \overline{\rho}\vec{v}\overline{v_y}d\vec{S}+\overline{(\rho\vec{v})'\,v'_y}d\vec{S}+\bar{p}dS_y\\ \overline{\rho}\vec{v}\overline{v_z}d\vec{S}+\overline{(\rho\vec{v})'\,v'_z}d\vec{S}+\bar{p}dS_z\\ \overline{\rho E}\bar{\vec{v}}d\vec{S}+\overline{(\rho E)'\,\vec{v}'}d\vec{S}+\bar{p}\bar{\vec{v}}d\vec{S}+\overline{p'\vec{v}'}d\vec{S}\end{pmatrix}\\ -\oint_S\begin{pmatrix}0\\ \overline{\tau_{xx}}dS_x+\overline{\tau_{xy}}dS_y+\overline{\tau_{xz}}dS_z\\ \overline{\tau_{xy}}dS_x+\overline{\tau_{yy}}dS_y+\overline{\tau_{yz}}dS_z\\ \overline{\tau_{xz}}dS_x+\overline{\tau_{yz}}dS_y+\overline{\tau_{zz}}dS_z\\ \bar{\boldsymbol{\tau}}\bar{\vec{v}}d\vec{S}+\overline{\boldsymbol{\tau}'\vec{v}'}d\vec{S}+\bar{\vec{q}}d\vec{S}\end{pmatrix}=\int_{\Omega}\bar{Q}d\Omega\end{gathered} \tag{B.5}$$

Considering that the temporal derivative of a time-averaged quantity is null, the first term can be removed:

$$\oint_S\begin{pmatrix}\overline{\rho}\vec{v}d\vec{S}\\ \overline{\rho}\vec{v}\overline{v_x}d\vec{S}+\overline{(\rho\vec{v})'\,v'_x}d\vec{S}+\bar{p}dS_x\\ \overline{\rho}\vec{v}\overline{v_y}d\vec{S}+\overline{(\rho\vec{v})'\,v'_y}d\vec{S}+\bar{p}dS_y\\ \overline{\rho}\vec{v}\overline{v_z}d\vec{S}+\overline{(\rho\vec{v})'\,v'_z}d\vec{S}+\bar{p}dS_z\\ \overline{\rho E}\bar{\vec{v}}d\vec{S}+\overline{(\rho E)'\,\vec{v}'}d\vec{S}+\bar{p}\bar{\vec{v}}d\vec{S}+\overline{p'\vec{v}'}d\vec{S}\end{pmatrix}-\oint_S\begin{pmatrix}0\\ \overline{\tau_{xx}}dS_x+\overline{\tau_{xy}}dS_y+\overline{\tau_{xz}}dS_z\\ \overline{\tau_{xy}}dS_x+\overline{\tau_{yy}}dS_y+\overline{\tau_{yz}}dS_z\\ \overline{\tau_{xz}}dS_x+\overline{\tau_{yz}}dS_y+\overline{\tau_{zz}}dS_z\\ \bar{\boldsymbol{\tau}}\bar{\vec{v}}d\vec{S}+\overline{\boldsymbol{\tau}'\vec{v}'}d\vec{S}+\bar{\vec{q}}d\vec{S}\end{pmatrix}=\int_{\Omega}\bar{Q}d\Omega \tag{B.6}$$

Equation 2.7 is usually written as:

$$\oint_S \begin{pmatrix} \overline{\rho\vec{v}}d\vec{S} \\ \overline{\rho\vec{v}}\overline{v_x}d\vec{S}+\bar{p}dS_x \\ \overline{\rho\vec{v}}\overline{v_y}d\vec{S}+\bar{p}dS_y \\ \overline{\rho\vec{v}}\overline{v_z}d\vec{S}+\bar{p}dS_z \\ \overline{\rho E}\bar{\vec{v}}d\vec{S}+\bar{p}\bar{\vec{v}}d\vec{S} \end{pmatrix} + \oint_S \begin{pmatrix} 0 \\ \overline{(\rho\vec{v})'\,v'_x}d\vec{S} \\ \overline{(\rho\vec{v})'\,v'_y}d\vec{S} \\ \overline{(\rho\vec{v})'\,v'_z}d\vec{S} \\ \overline{(\rho E)'\,\vec{v}'}d\vec{S}+\overline{p'\vec{v}'}d\vec{S} \end{pmatrix} - \oint_S \begin{pmatrix} 0 \\ \overline{\tau_{xx}}dS_x+\overline{\tau_{xy}}dS_y+\overline{\tau_{xz}}dS_z \\ \overline{\tau_{xy}}dS_x+\overline{\tau_{yy}}dS_y+\overline{\tau_{yz}}dS_z \\ \overline{\tau_{xz}}dS_x+\overline{\tau_{yz}}dS_y+\overline{\tau_{zz}}dS_z \\ \bar{\boldsymbol{\tau}}\bar{\vec{v}}d\vec{S}+\bar{\vec{q}}d\vec{S} \end{pmatrix}$$

$$- \oint_S \begin{pmatrix} 0 \\ 0 \\ 0 \\ 0 \\ \overline{\boldsymbol{\tau}'\vec{v}'}d\vec{S} \end{pmatrix} = \int_\Omega \bar{Q}d\Omega \tag{B.7}$$

where the first term is often referred as the *Linearized inviscid fluxes*, the second as the *Inviscid deterministic stress* (present in the time-mean equations due to the non-linearity of the formulation), the third one as the *Viscous fluxes* and $\overline{\boldsymbol{\tau}'\vec{v}'}d\vec{S}$ as the *Viscous deterministic stress*. It is to be observed that the role of the deterministic stresses is to account for the contribution of the flow unsteadiness into the time-mean flow equations, similarly to the function that the Reynolds stresses play in the RANS formulation presented in Section 2.1.2. Equation B.7 is often expressed in terms of the *Enthalpy* variable H, defined as $H = E + pV$:

$$\oint_S \begin{pmatrix} \overline{\rho\vec{v}}d\vec{S} \\ \overline{\rho\vec{v}}\overline{v_x}d\vec{S}+\bar{p}dS_x \\ \overline{\rho\vec{v}}\overline{v_y}d\vec{S}+\bar{p}dS_y \\ \overline{\rho\vec{v}}\overline{v_z}d\vec{S}+\bar{p}dS_z \\ \overline{\rho H}\bar{\vec{v}}d\vec{S} \end{pmatrix} + \oint_S \begin{pmatrix} 0 \\ \overline{(\rho\vec{v})'\,v'_x}d\vec{S} \\ \overline{(\rho\vec{v})'\,v'_y}d\vec{S} \\ \overline{(\rho\vec{v})'\,v'_z}d\vec{S} \\ \overline{(\rho H)'\,\vec{v}'}d\vec{S} \end{pmatrix} - \oint_S \begin{pmatrix} 0 \\ \overline{\tau_{xx}}dS_x+\overline{\tau_{xy}}dS_y+\overline{\tau_{xz}}dS_z \\ \overline{\tau_{xy}}dS_x+\overline{\tau_{yy}}dS_y+\overline{\tau_{yz}}dS_z \\ \overline{\tau_{xz}}dS_x+\overline{\tau_{yz}}dS_y+\overline{\tau_{zz}}dS_z \\ \bar{\boldsymbol{\tau}}\bar{\vec{v}}d\vec{S}+\bar{\vec{q}}d\vec{S} \end{pmatrix}$$

$$- \oint_S \begin{pmatrix} 0 \\ 0 \\ 0 \\ 0 \\ \overline{\boldsymbol{\tau}'\vec{v}'}d\vec{S} \end{pmatrix} = \int_\Omega \bar{Q}d\Omega \tag{B.8}$$

Using a compact finite-volume formulation, Equation B.8 can be written for every cell as:

$$\sum_{cell faces} \overline{\vec{F}_I} \cdot \vec{S} - \sum_{cell faces} \overline{\vec{F}_V} \cdot \vec{S} = \bar{Q}\Omega \tag{B.9}$$

with:

$$\overline{\vec{F}_I} \cdot \vec{S} = \begin{pmatrix} \overline{\rho\vec{v}}\vec{S} \\ \overline{\rho\vec{v}}\,\overline{v_x}\vec{S} + \bar{p}S_x \\ \overline{\rho\vec{v}}\,\overline{v_y}\vec{S} + \bar{p}S_y \\ \overline{\rho\vec{v}}\,\overline{v_z}\vec{S} + \bar{p}S_z \\ \overline{\rho H}\bar{\vec{v}}\vec{S} \end{pmatrix} + \begin{pmatrix} 0 \\ \overline{(\rho\vec{v})'\, v'_x}\vec{S} \\ \overline{(\rho\vec{v})'\, v'_y}\vec{S} \\ \overline{(\rho\vec{v})'\, v'_z}\vec{S} \\ \overline{(\rho H)'\, \vec{v}'}\vec{S} \end{pmatrix} \tag{B.10}$$

$$\overline{\vec{F}_V} \cdot \vec{S} = \begin{pmatrix} 0 \\ \overline{\tau_{xx}}S_x + \overline{\tau_{xy}}S_y + \overline{\tau_{xz}}S_z \\ \overline{\tau_{xy}}S_x + \overline{\tau_{yy}}S_y + \overline{\tau_{yz}}S_z \\ \overline{\tau_{xz}}S_x + \overline{\tau_{yz}}S_y + \overline{\tau_{zz}}S_z \\ \bar{\boldsymbol{\tau}}\bar{\vec{v}}\vec{S} + \bar{\vec{q}}\vec{S} \end{pmatrix} + \begin{pmatrix} 0 \\ 0 \\ 0 \\ 0 \\ \overline{\boldsymbol{\tau}'\vec{v}'}\vec{S} \end{pmatrix} \tag{B.11}$$

A pseudo-time dependence is finally added in Equation B.9 by the introduction of a pseudo-time ς derivative term:

$$\frac{\partial \bar{U}}{\partial \varsigma}\Omega + \sum_{cell faces} \left(\overline{\vec{F}_I} - \overline{\vec{F}_V}\right) \cdot \vec{S} = \frac{\partial}{\partial \varsigma} \begin{pmatrix} \bar{\rho} \\ \overline{\rho v_x} \\ \overline{\rho v_y} \\ \overline{\rho v_z} \\ \overline{\rho E} \end{pmatrix} \Omega + \sum_{cell faces} \left(\overline{\vec{F}_I} - \overline{\vec{F}_V}\right) \cdot \vec{S} = \bar{Q}\Omega \tag{B.12}$$

B.2 Harmonic equations

To derive the set of harmonic equations let consider again Equation B.4, but only retaining first-order fluctuation terms:

$$
\begin{aligned}
&\frac{\partial}{\partial t}\int_{\Omega}\begin{pmatrix} \bar{\rho}d\Omega+\rho' d\Omega \\ \overline{\rho v_x}d\Omega+(\rho v_x)'d\Omega \\ \overline{\rho v_y}d\Omega+(\rho v_y)'d\Omega \\ \overline{\rho v_z}d\Omega+(\rho v_z)'d\Omega \\ \overline{\rho E}d\Omega+(\rho E)'d\Omega \end{pmatrix} \\
&+\oint_S\begin{pmatrix} \overline{\rho\vec{v}}d\vec{S}+(\rho\vec{v})'d\vec{S} \\ \overline{\rho\vec{v}}\,\overline{v_x}d\vec{S}+\overline{\rho\vec{v}}v'_x d\vec{S}+(\rho\vec{v})'\,\overline{v_x}d\vec{S}+\bar{p}dS_x+p'dS_x \\ \overline{\rho\vec{v}}\,\overline{v_y}d\vec{S}+\overline{\rho\vec{v}}v'_y d\vec{S}+(\rho\vec{v})'\,\overline{v_y}d\vec{S}+\bar{p}dS_y+p'dS_y \\ \overline{\rho\vec{v}}\,\overline{v_z}d\vec{S}+\overline{\rho\vec{v}}v'_z d\vec{S}+(\rho\vec{v})'\,\overline{v_z}d\vec{S}+\bar{p}dS_z+p'dS_z \\ \overline{\rho E}\bar{\vec{v}}d\vec{S}+\overline{\rho E}\vec{v}'d\vec{S}+(\rho E)'\,\bar{\vec{v}}d\vec{S}+\bar{p}\bar{\vec{v}}d\vec{S}+\bar{p}\vec{v}'d\vec{S}+p'\bar{\vec{v}}d\vec{S} \end{pmatrix} \\
&-\oint_S\begin{pmatrix} 0 \\ \overline{\tau_{xx}}dS_x+\tau'_{xx}dS_x+\overline{\tau_{xy}}dS_y+\tau'_{xy}dS_y+\overline{\tau_{xz}}dS_z+\tau'_{xz}dS_z \\ \overline{\tau_{xy}}dS_x+\tau'_{xy}dS_x+\overline{\tau_{yy}}dS_y+\tau'_{yy}dS_y+\overline{\tau_{yz}}dS_z+\tau'_{yz}dS_z \\ \overline{\tau_{xz}}dS_x+\tau'_{xz}dS_x+\overline{\tau_{yz}}dS_y+\tau'_{yz}dS_y+\overline{\tau_{zz}}dS_z+\tau'_{zz}dS_z \\ \bar{\boldsymbol{\tau}}\bar{\vec{v}}d\vec{S}+\bar{\boldsymbol{\tau}}\vec{v}'d\vec{S}+\boldsymbol{\tau}'\bar{\vec{v}}d\vec{S}+\bar{\vec{q}}d\vec{S}+\vec{q}'d\vec{S} \end{pmatrix} \\
&=\int_{\Omega}\left(\bar{Q}+Q'\right)d\Omega
\end{aligned}
\tag{B.13}
$$

Expressing the *Inviscid terms* in terms of H:

$$
\begin{aligned}
&\frac{\partial}{\partial t}\int_{\Omega}\begin{pmatrix}\bar{\rho}d\Omega+\rho' d\Omega\\ \overline{\rho v_x}d\Omega+(\rho v_x)'d\Omega\\ \overline{\rho v_y}d\Omega+(\rho v_y)'d\Omega\\ \overline{\rho v_z}d\Omega+(\rho v_z)'d\Omega\\ \overline{\rho E}d\Omega+(\rho E)'d\Omega\end{pmatrix}\\
&+\oint_S\begin{pmatrix}\overline{\rho\vec{v}}d\vec{S}+(\rho\vec{v})'d\vec{S}\\ \overline{\rho\vec{v}}\overline{v_x}d\vec{S}+\overline{\rho\vec{v}}v'_x d\vec{S}+(\rho\vec{v})'\,\overline{v_x}d\vec{S}+\bar{p}dS_x+p'dS_x\\ \overline{\rho\vec{v}}\overline{v_y}d\vec{S}+\overline{\rho\vec{v}}v'_y d\vec{S}+(\rho\vec{v})'\,\overline{v_y}d\vec{S}+\bar{p}dS_y+p'dS_y\\ \overline{\rho\vec{v}}\overline{v_z}d\vec{S}+\overline{\rho\vec{v}}v'_z d\vec{S}+(\rho\vec{v})'\,\overline{v_z}d\vec{S}+\bar{p}dS_z+p'dS_z\\ \overline{\rho H}\bar{\vec{v}}d\vec{S}+(\rho H)'\,\bar{\vec{v}}d\vec{S}+\overline{\rho H}\vec{v}'d\vec{S}\end{pmatrix}\\
&-\oint_S\begin{pmatrix}0\\ \overline{\tau_{xx}}dS_x+\tau'_{xx}dS_x+\overline{\tau_{xy}}dS_y+\tau'_{xy}dS_y+\overline{\tau_{xz}}dS_z+\tau'_{xz}dS_z\\ \overline{\tau_{xy}}dS_x+\tau'_{xy}dS_x+\overline{\tau_{yy}}dS_y+\tau'_{yy}dS_y+\overline{\tau_{yz}}dS_z+\tau'_{yz}dS_z\\ \overline{\tau_{xz}}dS_x+\tau'_{xz}dS_x+\overline{\tau_{yz}}dS_y+\tau'_{yz}dS_y+\overline{\tau_{zz}}dS_z+\tau'_{zz}dS_z\\ \bar{\boldsymbol{\tau}}\bar{\vec{v}}d\vec{S}+\bar{\boldsymbol{\tau}}\vec{v}'d\vec{S}+\boldsymbol{\tau}'\bar{\vec{v}}d\vec{S}+\bar{\vec{q}}d\vec{S}+\vec{q}'d\vec{S}\end{pmatrix}\\
&\qquad=\int_{\Omega}\left(\bar{Q}+Q'\right)d\Omega
\end{aligned}
\tag{B.14}
$$

By casting into the frequency domain, the equations of the h$^{\text{th}}$ harmonic can be written as:

$$
\begin{aligned}
&I\omega_h \int_\Omega \begin{pmatrix} \widetilde{\rho}|_h d\Omega \\ \widetilde{\rho v_x}|_h d\Omega \\ \widetilde{\rho v_y}|_h d\Omega \\ \widetilde{\rho v_z}|_h d\Omega \\ \widetilde{\rho E}|_h d\Omega \end{pmatrix} + \oint_S \begin{pmatrix} \widetilde{\rho\vec{v}}|_h d\vec{S} \\ \overline{\rho\vec{v}}\widetilde{v_x}|_h d\vec{S} + \widetilde{\rho\vec{v}}|_h \overline{v_x} d\vec{S} + \tilde{p}|_h dS_x \\ \overline{\rho\vec{v}}\widetilde{v_y}|_h d\vec{S} + \widetilde{\rho\vec{v}}|_h \overline{v_y} d\vec{S} + \tilde{p}|_h dS_y \\ \overline{\rho\vec{v}}\widetilde{v_z}|_h d\vec{S} + \widetilde{\rho\vec{v}}|_h \overline{v_z} d\vec{S} + \tilde{p}|_h dS_z \\ \widetilde{\rho H}|_h \bar{\vec{v}} d\vec{S} + \overline{\rho H}\widetilde{\vec{v}}|_h d\vec{S} \end{pmatrix} \\
&- \oint_S \begin{pmatrix} 0 \\ \widetilde{\tau_{xx}}|_h dS_x + \widetilde{\tau_{xy}}|_h dS_y + \widetilde{\tau_{xz}}|_h dS_z \\ \widetilde{\tau_{xy}}|_h dS_x + \widetilde{\tau_{yy}}|_h dS_y + \widetilde{\tau_{yz}}|_h dS_z \\ \widetilde{\tau_{xz}}|_h dS_x + \widetilde{\tau_{yz}}|_h dS_y + \widetilde{\tau_{zz}}|_h dS_z \\ \bar{\boldsymbol{\tau}}\widetilde{\vec{v}}|_h d\vec{S} + \widetilde{\boldsymbol{\tau}}|_h \bar{\vec{v}} d\vec{S} + \widetilde{\vec{q}}|_h d\vec{S} \end{pmatrix} = \int_\Omega \widetilde{Q}|_h d\Omega
\end{aligned}
\tag{B.15}
$$

The first term is referred as the *Frequency source term*, the second as the *Inviscid fluxes* and the third as *Viscous fluxes*. ω_h is the angular velocity related to the h$^{\text{th}}$ harmonic. Using a compact finite-volume formulation, Equation B.15 can be written for every cell as:

$$
I\omega_h \widetilde{U}|_h \Omega + \sum_{cellfaces} \widetilde{\vec{F}_I}|_h \cdot \vec{S} - \sum_{cellfaces} \widetilde{\vec{F}_V}|_h \cdot \vec{S} = \widetilde{Q}|_h \Omega \tag{B.16}
$$

where:

$$
\widetilde{\vec{F}_I}|_h \cdot \vec{S} = \begin{pmatrix} \widetilde{\rho\vec{v}}|_h \vec{S} \\ \overline{\rho\vec{v}}\widetilde{v_x}|_h \vec{S} + \widetilde{\rho\vec{v}}|_h \overline{v_x} \vec{S} + \tilde{p}|_h S_x \\ \overline{\rho\vec{v}}\widetilde{v_y}|_h \vec{S} + \widetilde{\rho\vec{v}}|_h \overline{v_y} \vec{S} + \tilde{p}|_h S_y \\ \overline{\rho\vec{v}}\widetilde{v_z}|_h \vec{S} + \widetilde{\rho\vec{v}}|_h \overline{v_z} \vec{S} + \tilde{p}|_h S_z \\ \widetilde{\rho H}|_h \bar{\vec{v}} \vec{S} + \overline{\rho H}\widetilde{\vec{v}}|_h \vec{S} \end{pmatrix} \tag{B.17}
$$

$$
\widetilde{\vec{F}_V}|_h \cdot \vec{S} = \begin{pmatrix} 0 \\ \widetilde{\tau_{xx}}|_h S_x + \widetilde{\tau_{xy}}|_h S_y + \widetilde{\tau_{xz}}|_h S_z \\ \widetilde{\tau_{xy}}|_h S_x + \widetilde{\tau_{yy}}|_h S_y + \widetilde{\tau_{yz}}|_h S_z \\ \widetilde{\tau_{xz}}|_h S_x + \widetilde{\tau_{yz}}|_h S_y + \widetilde{\tau_{zz}}|_h S_z \\ \bar{\boldsymbol{\tau}}\widetilde{\vec{v}}|_h \vec{S} + \widetilde{\boldsymbol{\tau}}|_h \bar{\vec{v}} \vec{S} + \widetilde{\vec{q}}|_h \vec{S} \end{pmatrix} \tag{B.18}
$$

As done for the time-mean equations, a pseudo-time derivative term is finally introduced in Equation B.16:

$$\frac{\partial \widetilde{U}}{\partial \varsigma}\Omega + I\omega_h \widetilde{U}|_h \Omega + \sum_{cellfaces} \widetilde{\vec{F}_I}|_h \cdot \vec{S} - \sum_{cellfaces} \widetilde{\vec{F}_V}|_h \cdot \vec{S} = \widetilde{Q}|_h \Omega \tag{B.19}$$

Appendix C

Turbulence model sensitivity for Rotor-only computations

Due to the absence of an experimental database for DTU 10MW RWT simulations validation, a detailed analysis of the impact of the turbulence modeling was not considered in this research. Because of its simplicity and robustness, all the presented simulations were based on the Spalart-Allmaras turbulence model [Spalart and Allmaras (1992)]. In this section, the results of the application of the so-called k-ω SST turbulence model [Menter (1993)] on the *prebent-precone* computations of Section 5.5 are discussed. The k-ω SST turbulence model was employed for HAWT rotor analysis by many authors, since it is considered a good option when dealing with massive separations and important recirculations [Menter et al. (2003)]. This model combines k-ω and k-ε philosophies for the near wall and the rest of the domain respectively.

The whole 0 deg operating range from Table 5.2 was considered in this study. Both *rigid* and *flexible* configurations were analyzed. For the latter configuration, mesh deformation relied in the *hybrid method* summarized in Section 3.6.

For the *rigid* simulations, same suction and pressure separation bubbles were identified for both turbulence models, as illustrated in Figure C.1 for the 11 ms^{-1} operating point (FT_WSP11).

When accounting for *flexible* blades, the observed deformation differences between the two considered turbulence models was in the order of centimeters (Figure C.2), representing less than 0.1% of the radius of the rotor. Higher discrepancies were found for low wind speeds.

Figure C.3 illustrates the results on rotor performance for both turbulent models. Even if non negligible differences were found, both approaches showed a similar influence of the wind speed evolution and the blade flexibility. This justifies the use of the Spalart-Allmaras model in the present PhD research, which focus was the development of new methodologies for the study of HAWTs aeroelasticity.

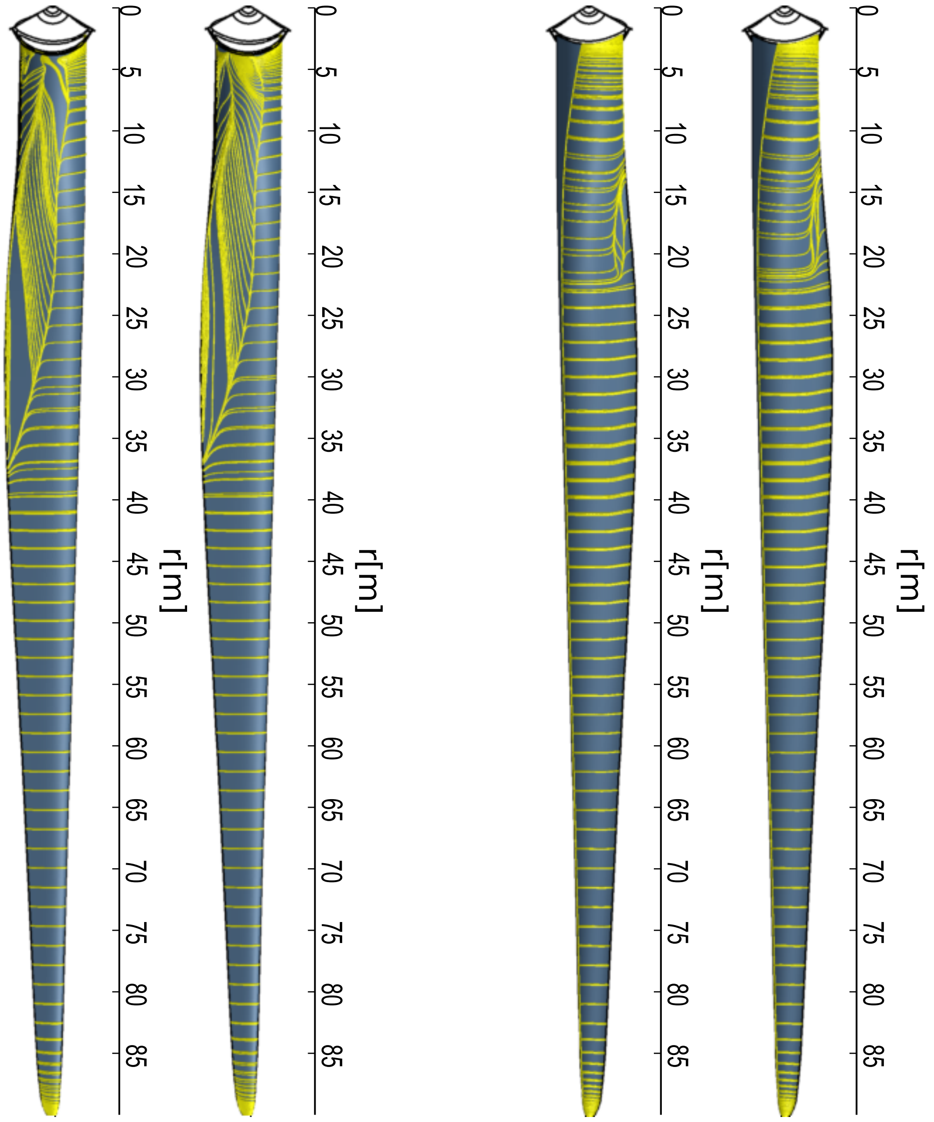

(a) *SS*-SA **(b)** *SS*-SST **(c)** *PS*-SA **(d)** *PS*-SST

Figure C.1: Friction streamlines at 11 ms^{-1} for suction and pressure surfaces (referred as *SS* and *PS* respectively). *Rigid* simulations of *prebent/precone* blade without *Gurney flaps*. SA refers to Spalart-Allmaras turbulence model. SST refers to k-ω SST turbulence model

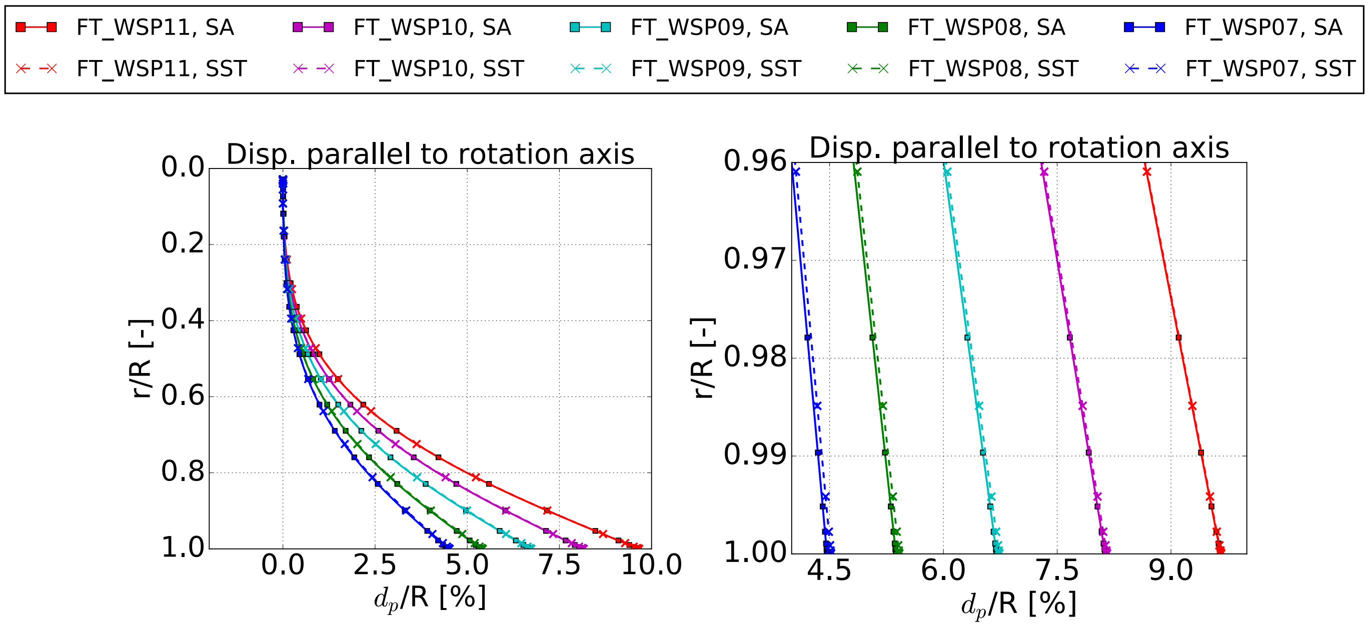

(a) Blade axis displacement, global view **(b)** Blade axis displacement, high span zoom

Figure C.2: DTU 10MW RWT blade deformation parallel to the rotor axis for the *prebent/precone* configuration without *Gurney flaps*. Results are expressed as a function of normalized radius. SA refers to Spalart-Allmaras turbulence model. SST refers to k-ω SST turbulence model

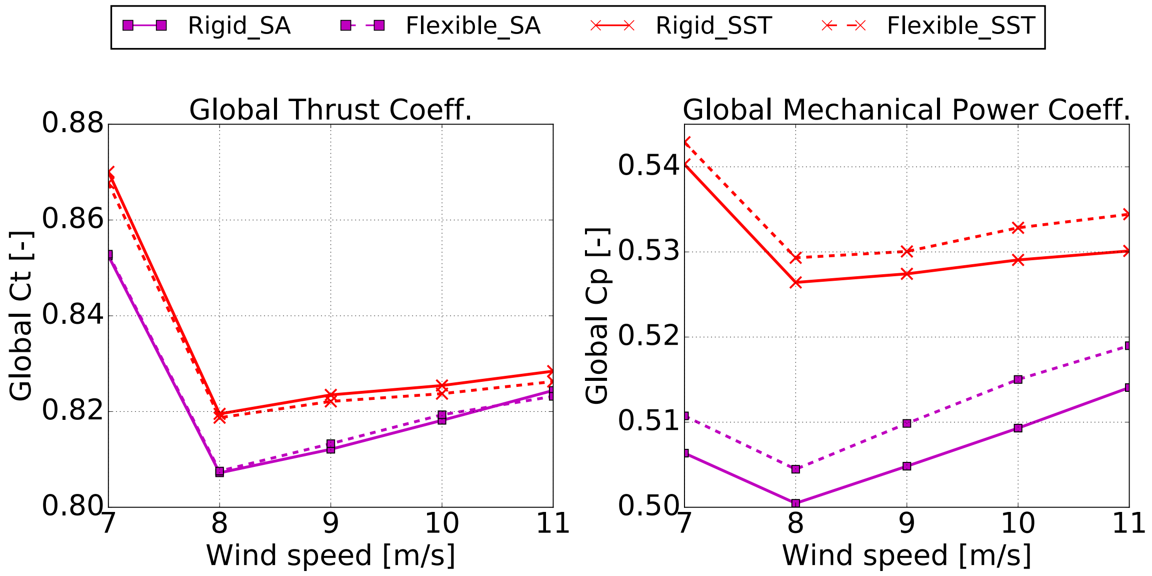

(a) Global thrust coefficient **(b)** Global power coefficient

Figure C.3: DTU 10MW RWT global coefficients versus wind speed, *prebent/precone* blade without *Gurney flaps*. SA refers to Spalart-Allmaras turbulence model. SST refers to k-ω SST turbulence model